UNIVERSITY OF CALIFORNIA
Los Angeles

Numerical Exploration of Rotating Detonation Rocket Engine Chamber Dynamics

A dissertation submitted in partial satisfaction
of the requirements for the degree
Doctor of Philosophy in Mechanical Engineering

by

Mathias Ross

2022

ABSTRACT OF THE DISSERTATION

Numerical Exploration of Rotating Detonation Rocket Engine Chamber Dynamics

by

Mathias Ross
Doctor of Philosophy in Mechanical Engineering
University of California, Los Angeles, 2022
Professor Ann Karagozian, Chair

With efficiencies in conventional rocket designs reaching the limit of theoretical possibility, there has been renewed interest in technologies which may be able to shift the boundaries of efficiency. One such technology is the rotating detonation rocket engine, which has the potential to create highly efficient engines in a small form factor. However, the detonation dynamics and complex flowfields inside the combustion chamber are greatly dependent on geometry; in particular, the downstream nozzle design affects dynamics inside the combustion chamber. In this work, high fidelity large eddy simulations of gaseous methane-oxygen rotating detonation rocket engines are presented for five engine configurations.

The first simulation discussed is a validation case from the AIAA model validation in propulsion workshop. A laser model based on the Beer-Lambert law was developed for comparing simulations with experimental laser absorbance measurements, and used to directly relate the simulation with experimental measurements of temperature, pressure, and CO column density in the exhaust of the engine. The analysis found that the simulation over-predicted pressure and thrust in the engine, as has been the case in other simulations of the engine, but that features in the exhaust flowfield closely matched experimental measurements. Close agreement between simulation and experiment was also seen in the measured CO mole fraction of the exhaust.

The effect of adding a converging-diverging nozzle to a rotating detonation rocket engine was explored in the other four simulations, which consider an engine of two different lengths, with and without a constriction. The geometries matched experimental tests previously conducted at the Air Force Research Laboratory, and the operational modes attained in the simulations were found in all cases to directly relate to experimental observations.

In the unconstricted geometries, flow in the chamber exceeded Mach 1 in pockets upstream of the chamber exit. However, geometries with a diverging-converging nozzle directly followed the Mach-area relationship, with supersonic flow existing only in the diverging regions of the nozzle. This suggests a fundamental difference between the flowfield present in RDRE geometries with and without an area constriction, even though the constriction studied was gradual enough that no reflected shocks were observed travelling upstream.

The formation enthalpy of the flow was measured inside the chamber for all configurations, and demonstrated that the difference in pressures and detonation structures associated with the chamber area constriction did not result in a significant change in the amount of energy released through combustion. Adding a constriction increased the average pressure of the combustion chamber, which would typically result in increased combustive energy release, but no associated release through combustion was observed. As such, although the use of a converging-diverging nozzle increased overall performance, the induced change in operating mode was detrimental to the extraction of energy from the flow.

Changing chamber length was found to have little impact on the operation of an unconstricted rotating detonation rocket engine. However, changing the length of a chamber with a constriction resulted in a change in operating mode, and decrease in the strength of the counter-propagating waves. This suggests that, although unconstricted chamber geometries are likely optimized at short lengths, the length of the chamber is an important parameter to be considered when the engine utilizes a chamber area constriction.

The dissertation of Mathias Ross is approved.

Jeff Eldredge

Mitchell Spearrin

Xiaolin Zhong

Christopher Lietz

Ann Karagozian, Committee Chair

University of California, Los Angeles

2022

To my family.

TABLE OF CONTENTS

LIST OF FIGURES

LIST OF TABLES

List of Symbols

A_j . . . . . Arrhenius pre-exponential factor of reaction j

A_i . . . . . i-component of vector indicating area A

$A_{i,j}$ . . . . . Absorbance area of transitions i for species j

a . . . . . Speed of sound

C_p . . . . . Specific heat at constant pressure

C_v . . . . . Specific heat at constant volume

c . . . . . Speed of light in a vacuum

c_2 . . . . . Planck's second radiation constant

D_k . . . . . Diffusion coefficient of species k

$\tilde{E}$ . . . . . Favre-filtered total internal energy

E_j . . . . . Arrhenius activation energy of reaction j

e . . . . . Internal specific energy

$\mathbf{F}_i$ . . . . . Central-volume i-direction flux vector

G . . . . . LES filter

H^* . . . . . Change in enthalpy of formation, normalized by single-step combustion

H_{equil} . . . . . Change in enthalpy of formation, normalized by equilibrium state

h . . . . . Enthalpy per unit mass

h_k^0 . . . . . Enthalpy of formation per unit mass of species k

h_k . . . . . Internal enthalpy of species k

I_0 . . . . . Initial laser intensity

I_t . . . . . Transmitted laser intensity

I_{sp} . . . . . Specific impulse, in seconds

k . . . . . Boltzmann's constant

k_j . . . . . Arrhenius rate constant of reaction j

L . . . . . Length of laser path

M . . . . . Mach number

$\dot{m}$ . . . . . Mass flow rate, unit mass per unit time

N . . . . . Number of waves

N_j . . . . . Column density of species j

n_j . . . . . Molar density of species j

$\bar{n}_j$ . . . . . Path-averaged molar density of species j

Pr_t . . . . . Turbulent Prandtl number

p . . . . . Pressure

p_i . . . . . Pressure in cell i

$\bar{p}$ . . . . . LES-filtered pressure

Q . . . . . Total partition sum

q . . . . . Heat of reaction per unit mass

q_i . . . . . Indexed component of heat flux

R . . . . . Universal gas constant

R_s . . . . . Specific gas constant

r . . . . . Radius

S . . . . . Linestrength

S . . . . . Vectorized source terms in governing equations

Sc_t . . . . . Turbulent Schmidt number

s . . . . . Entropy

T . . . . . Temperature

$\bar{T}$ . . . . . Species-averaged temperature over a laser path

$\tilde{T}$ . . . . . Favre-filtered temperature

t . . . . . Time

U . . . . . Vector of state variables

u . . . . . Velocity

u_i . . . . . indexed component of velocity field

$\tilde{u}_i$ . . . . . Favre-filtered indexed velocity

v . . . . . Wave velocity

$V_{k,i}$ . . . . . i-component diffusion velocity for species k

W . . . . . Shock velocity

X_s . . . . . Mole fraction of species s

x_i . . . . . indexed spatial coordinate

Y_k . . . . . Mass fraction of species k

$\tilde{Y}_k$ . . . . . Favre-filtered mass fraction of species k

α . . . . . absorbance

β_j . . . . . Arrhenius rate constant for reaction j

γ . . . . . Ratio of specific heats, $\frac{C_p}{C_v}$

γ_{j-s} . . . . . Broadening coefficient for collisional partners j and s

Δ . . . . . Computational cell length

δ_{ij} . . . . . Kronecker delta

ϵ_c . . . . . Contraction ratio

η . . . . . Thermodynamic efficiency

λ . . . . . Local thermal conductivity, as defined by Fourier's law

μ . . . . . Absolute viscosity

μ_s . . . . . Molar mass of species s

ν . . . . . Wavenumber

ν_t . . . . . Turbulent eddy viscosity

ϕ . . . . . Equivalence ratio

φ . . . . . Lineshape function

ρ . . . . . Density

$\bar{\rho}$ . . . . . LES-filtered density

σ_{ij} . . . . . Stress tensor with pressure, $\sigma_{ij} = \tau_{ij} - p\delta_{ij}$

τ_{ij} . . . . . Viscous stress tensor

$\bar{\tau}_{ij}$ . . . . . LES-filtered viscous stress tensor

$\dot{\omega}_k$ . . . . . Reaction rate for species k, mass/volume/-time

$\bar{\dot{\omega}}_k$ . . . . . LES-filtered Reaction rate for species k

List of Acronyms

AIAA . . . . . American Institute of Aeronautics and Astronautics

MVP . . . . . Model Validation for Propulsion

RDRE . . . . . Rotating Detonation Rocket Engine

CTAP . . . . . Capillary Tube Attenuated Pressure

PGC . . . . . Pressure Gain Combustion

AFRL . . . . . Air Force Research Laboratory

PDE . . . . . Pulsed Detonation Engine

RDE . . . . . Rotating Detonation Engine

LES . . . . . Large Eddy Simulation

AHFM . . . . . ALREST High Fidelity Modeling

ALREST . . . . . Advanced Liquid Rocket Engine Scaling Tool

LESLIE . . . . . Large Eddy Simulation with LInear Eddies

RANS . . . . . Reynolds-Averaged Navier-Stokes

C-J . . . . . Chapman-Jouguet

ZND . . . . . Zeldovich-von Neumann-Döring

NASA . . . . . National Aeronatics and Space Administration

CEA . . . . . Chemical Equilibrium with Applications

LIH . . . . . Lavrent'ev Institute for Hydrodynamics

LAS . . . . . Laser Absorption Spectroscopy

CAD . . . . . Computer-Aided Design

DoD . . . . . Department of Defense

HPC . . . . . High-Performance Computer

HPCMP . . . . . High-Performance Computing Modernization Program

ERDC . . . . . Engineer Research and Development Center

DDT . . . . . Deflagration-To-Detonation

NETL . . . . . National Energy Technology Laboratory

FFT . . . . . Fast Fourier Transform

T-S . . . . . Temperature-Entropy

ACKNOWLEDGMENTS

I'm extremely fortunate to have had two incredible advisors during my work on this project, without whom none of what I've accomplished would have been possible. Dr. Ann Karagozian provided support and encouragement every step of the way, and her guidance and patience has made pursuing a PhD during a pandemic somehow seem both feasible and enjoyable. I'm also grateful to Dr. Christopher Lietz, who introduced me to detonation engines, and who helped me work through questions every step of the way.

I'd also like to thank all the members of the RDRE research group at AFRL, for making me feel welcome even when I was just an intern at the lab, and for making it fun to work on RDREs: Dr. Armani Batista, Dr. John Bennewitz, Dr. Eric Paulson, Dr. William Hargus, Dr. Jason Burr, and Blaine Bigler. They've been willing to help me understand new aspects of the project, and have taken the time to explain things to me – even when I was clearly blinded by an ignorance of what goes into actually running experiments.

The other members of the UCLA Energy and Propulsion Research Laboratory have me looking forward to group meeting every Friday, and I learn something new whenever I talk to them. I'd especially like to thank Miguel Plascencia, David Ren, and Andres Vargas, who have helped me feel connected to UCLA even while living in the desert. My understanding of laser spectroscopy also owes much to conversations with Dr. Anil Nair, and the other members of Dr. Spearrin's lab at UCLA.

Lastly, this work was made possible by support from the Air Force Office of Scientific Research (Dr. Chiping Li, program manager), under AFRL Lab Task 20RQCOR63. Support to UCLA has been provided via subcontracts from ERC, Inc. (subcontract PS190051), and from Jacobs Technology, Inc. (subcontracts RAPT1-0000000002 and RAPTR1-0000000001). The work was supported in part by high-performance computer time and resources from the DoD High Performance Computing Modernization Program.

VITA

2019	M.S. (Mechanical Engineering), University of California, Los Angeles
2016	B.S. (Mathematics) and B.A. (Physics), University of Chicago
2019	Research Co-Op, ERC, Inc., AFRL

PUBLICATIONS AND PRESENTATIONS

M. C. Ross, J. Burr, A. Batista, and C. Lietz, "Flow Acceleration in an RDRE with Gradual Chamber Constriction," presented at 28th Int. Colloq. on the Dyn. of Explosions and Reactive Syst. (ICDERS), Naples, Italy, June 2022; under modification for journal submission

M. C. Ross, C. Lietz, and W. A. Hargus, "Synthetic Laser Diagnostics of Simulated RDRE Exhaust." Presented at the AIAA P&E 2021 Forum. Aug. 2021. doi: 10.2514/6.2021-3643.

J. W. Bennewitz, B. R. Bigler, **M. C. Ross**, S. A. Danczyk, W. A. Hargus, and R. D. Smith, "Performance of a Rotating Detonation Rocket Engine with Various Convergent Nozzles and Chamber Lengths," ***Energies***, vol. 14, no. 8, Art. no. 8, Jan. 2021, doi: 10.3390/en14082037.

A. Batista, **M. C. Ross**, C. Lietz, and W. A. Hargus, "Descending Modal Transition Dynamics in a Large Eddy Simulation of a Rotating Detonation Rocket Engine," ***Energies***, vol. 14, no. 12, Art. no. 12, Jan. 2021, doi: 10.3390/en14123387.

A. Nisenoff, V. V. Dwarkadas, and **M. C. Ross**, "Supernova X-Ray Database (SNaX) Updated to Ensure Long-term Stability," ***Res. Notes AAS***, vol. 4, no. 11, p. 195, Nov. 2020, doi: 10.3847/2515-5172/abc6a7.

M. C. Ross, C. Lietz, Y. Desai, J. Hamilton, and W. A. Hargus, "Constriction-Induced Counter-Propagating Behavior in RDREs," presented at the AIAA P&E 2020 Forum. Aug. 2020. doi: 10.2514/6.2020-3873.

M. C. Ross, C. Lietz, Y. Desai, J. Hamilton, and W. Hargus, "Investigation into the impact of an Exit Constriction on Rotating Detonation Rocket Engines, Using Large Eddy Simulations," presented at the 2019 JANNAF meeting. Dec. 2019.

M. C. Ross and V. V. Dwarkadas, "SNaX: A Database of Supernova X-Ray Light Curves," ***The Astronomical Journal***, vol. 153, p. 246, Jun. 2017, doi: 10.3847/1538-3881/aa6d50.

CHAPTER 1

Introduction and Background

As combustion technologies have matured and expanded, it has become both more important and more difficult to find new ways to improve existing technologies. One promising avenue, and the topic of this research, is the use of devices designed around supersonic combustion waves – detonations – as opposed to the more standard subsonic deflagration regime. Although building devices capable of using detonations is not an especially new idea – some of the earliest combustion devices used detonations, even if it wasn't realized at the time – most modern propulsion devices are structured around deflagrative combustion. This is largely because detonations introduce a number of added complications that don't exist when using deflagrations to power an engine. One of the most important is due to the rapid propagation of the reaction wave, which is coupled to a pressure shock, and means that detonation waves are rarely stationary with respect to the engine. However, because the combustion reactions in detonations occur at a higher pressure than in deflagrations of the same reactants, the associated thermodynamic cycles have a higher ideal thermodynamic efficiency. Moreover, detonative reactions occur at a shorter length scale, and so enable geometries that would not be possible using deflagrative combustion.

This study focuses on using detonations in rocket propulsion applications. The specific type of device looked at in this work, a rotating detonation rocket engine (RDRE), was the subject of several studies in the 60s. At that time there was enough difficulty, both in sustaining detonations and in developing designs able to take the extreme stresses of the system, that interest in RDREs largely waned in favor of other avenues open at the time for rapid advances in rocket engine technology. Recent improvements in materials, as well as improved capabilities in computational modeling and diagnostics, have brought renewed

interest in recent years to the possibilities of RDREs.

1.1 Detonations

A focus on the study of combustion propagation rates in the 19th century, motivated by explosions in coal mines, led to the realization that some combustion waves propagate at an extremely rapid rate. The first experimental measurements of a detonation velocity were taken by Frederick Abel in the late 1860s and 1870s: a chronometer designed around using spinning wheels attached to a weight dropping at terminal velocity was used to measure propagation of a detonation in guncotton, and measured wavespeeds in excess of 5000 m/s [1, 2]. Studies of wave velocity were soon extended to gaseous combustion, and a series of experiments conducted by Berthelot and Vieille measured detonation velocities for a variety of fuels and oxidizers [3, 4]. These experiments coincided with work done by Mallard and Le Chatelier as part of a French commission on the use of explosives in the presence of firedamp [5, 6], in which velocity measurements of subsonic combustion waves demonstrated that the same gas could sustain combustion propagation at two very different wave velocities. As an aside, the French commission into firedamp was one of many such commissions into firedamp combustion conducted near the end of the 19th century; separate initiatives were launched in Prussia, Saxony, Austria, and England.

1.1.1 Chapman-Jouguet Conditions

Early work on detonations such as experiments designed by Champion and Pellet to measure detonative concussive forces [7], make it clear that it was largely understood from the outset that detonations are associated with a pressure wave. By 1900 this idea had been further refined to considering a detonation using two separate regions: a shock discontinuity, and a combustion reaction [8]. This perhaps explains why, at the turn of the 20th century the conservation analysis done on shocks by Rankine and Hugoniot [9, 10] was extended to detonations independently by Chapman [11], Jouguet [12], and Mikelson [13]. The works of

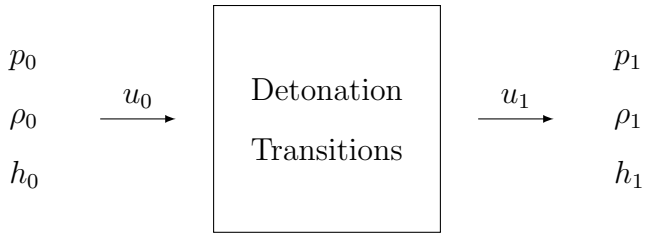

Figure 1.1: One-dimensional flow quantities pressure (p), density (ρ), enthalpy (h), and velocity (u) in the frame of steady detonation reaction, with subscript 0 indicating flow before the reaction, and 1 indicating fully-reacted flow.

Chapman and Jouguet were the best known of these, and so the ideal detonation associated with the following conservation analysis has come to be known as a Chapman-Jouguet, or C-J, detonation.

The conservation analysis begins by considering one-dimensional steady flow in the reference frame of a steady combustion reaction, as in figure 1.1 The conservation equations for pressure p, density ρ, enthalpy h, and velocity u can be written out in a standard form (see e.g. [14]).

$$\rho_0 u_0 = \rho_1 u_1 \qquad \text{(Mass)} \qquad (1.1)$$

$$p_0 + \rho_0 u_0^2 = p_1 + \rho u_1^2 \qquad \text{(Momentum)} \qquad (1.2)$$

$$h_0 + \frac{u_0^2}{2} + q = h_1 + \frac{u_1^2}{2} \qquad \text{(Energy)} \qquad (1.3)$$

The energy equation includes q, the net heat released per mass between the two states. For a chemical reaction this comes from the difference in the energy contained within the bonds for the composition of the mixture, and can be calculated in terms of the enthalpy of formation h_k^0 and species mass fractions Y_k:

$$q = \sum_k^{\text{reactants}} Y_k h_k^0 - \sum_k^{\text{products}} Y_k h_k^0 \qquad (1.4)$$

Note that representing the detonation wave in this way makes no statements about the one-dimensional size or structure of the wave – only that a steady state exists in which

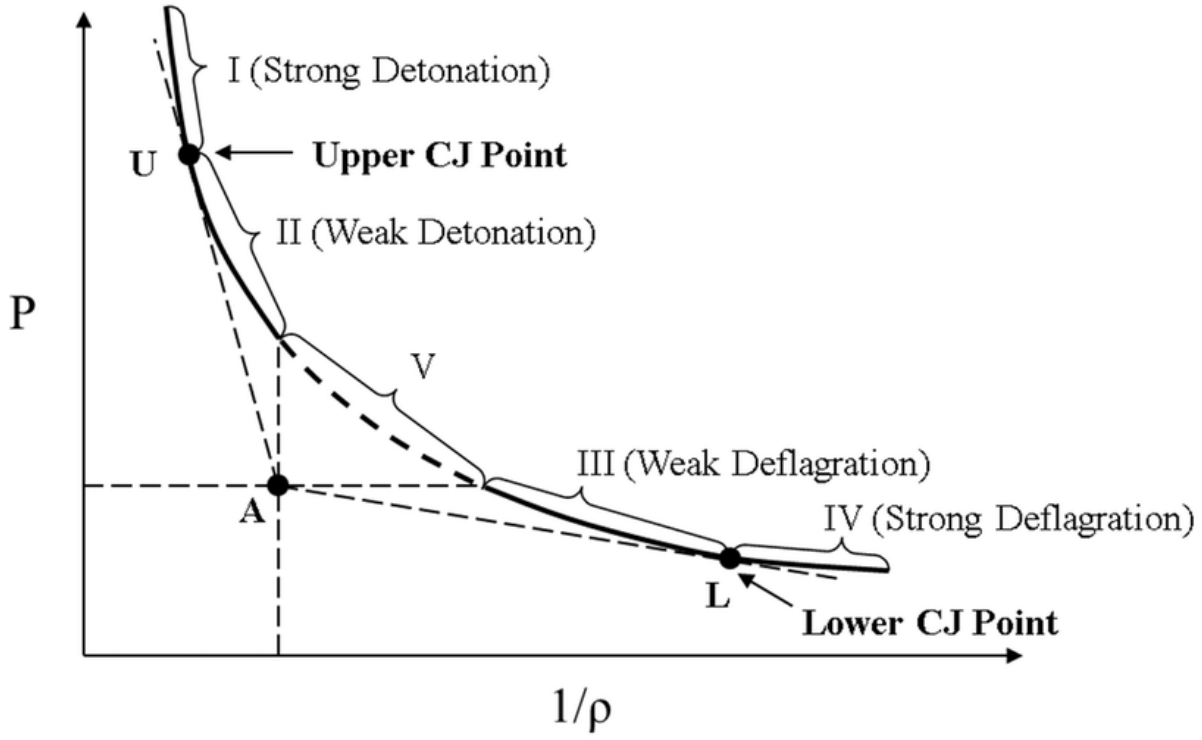

Figure 1.2: Hugoniot curve as represented by equation 1.7, taken from [15]

it travels at a constant velocity, so that it can be considered in a standard inertial frame. Equations for conservation of mass (1.1) and momentum (1.2) can be combined to express velocities in terms of pressure and density:

$$u_{0,1}^2 = \frac{p_{1,0} - p_{0,1}}{\rho_{0,1}\left(1 - \frac{\rho_{0,1}}{\rho_{1,0}}\right)} \tag{1.5}$$

Equations 1.5 can then replace the kinetic energy components of the energy conservation equation 1.3:

$$h_0 + \frac{p_1 - p_0}{2\rho_0\left(1 - \frac{\rho_0}{\rho_1}\right)} + q = h_1 + \frac{p_0 - p_1}{2\rho_1\left(1 - \frac{\rho_1}{\rho_0}\right)} \tag{1.6}$$

which can then be simplified:

$$h_1 - h_0 = \frac{p_1 - p_0}{2(\frac{1}{\rho_1} + \frac{1}{\rho_0})} + q \tag{1.7}$$

Equation 1.7 gives what is known as the Hugoniot curve, shown in figure 1.2. For a given initial condition and final composition, the Hugoniot curve is the space of possible

post-combustion states as represented by the one-dimensional conservation equations. If no reactions were to occur between the two states then q would be 0, and the initial condition would also be on the Hugoniot curve – the Hugoniot curve would give the solution space for one-dimensional shocks.

The straight line which connects an initial state with a solution on the Hugoniot curve is known as a Rayleigh line, and represents the transition between specific states. The Rayleigh line's slope can be expressed in terms of the initial and final state:

$$\text{Slope of Rayleigh Line} = \frac{p_1 - p_0}{\frac{1}{\rho_1} - \frac{1}{\rho_0}} \tag{1.8}$$

However, this can be simplified using conservation of mass and momentum:

$$\begin{aligned}
\text{Slope of Rayleigh Line} &= \frac{p_1 - p_0}{\frac{1}{\rho_1} - \frac{1}{\rho_0}} && (1.9)\\
&= \frac{\rho_0 u_0^2 - \rho_1 u_1^2}{\frac{1}{\rho_1} - \frac{1}{\rho_0}} && \text{Conservation of Momentum} \quad (1.10)\\
&= \rho_0^2 u_0^2 \frac{\frac{1}{\rho_0} - \frac{1}{\rho_1}}{\frac{1}{\rho_1} - \frac{1}{\rho_0}} && \text{Conservation of Mass} \quad (1.11)\\
&= -\dot{m}^2 && (1.12)
\end{aligned}$$

This expression makes it possible to rule out part of the solution space suggested by the Hugoniot curve as nonphysical. Specifically, the region with $p_1 > p_0$ and $\frac{1}{\rho_1} > \frac{1}{\rho_0}$ requires a Rayleigh line with a positive slope, implying that $\dot{m}^2 < 0$. However, $\dot{m} = \rho_0 u_0$, and $\rho_0 > 0$ by definition, so a solution in this space would suggest that the velocity u_0 is nonreal, which isn't physical.

This nonphysical region on the Hugoniot curve separates possible solutions into two distinct regions: Region 1, where $p_1 > p_0$, $\frac{1}{\rho_1} < \frac{1}{\rho_0}$, and region 2, where $p_1 < p_0$, $\frac{1}{\rho_1} > \frac{1}{\rho_0}$. The slope of the Rayleigh line is negative in both regions, but in region 1 the magnitude of the slope is greater than 1; in region 2 the magnitude is less than 1.

The speed of sound a in a calorically perfect gas can be evaluated using γ:

$$a = \sqrt{\gamma R_s T} \tag{1.13}$$

$$= \sqrt{\gamma \frac{p}{\rho}} \tag{1.14}$$

where R_s is the specific gas constant for the mixture.

This relation makes it possible to recast the slope of the Rayleigh line, $-\dot{m}^2$, in terms of the Mach number (M) of the combustion wave as it travels into the unburnt gases, $M_0 = \frac{u_0}{a_0}$:

$$\dot{m}^2 = \frac{p_0 - p_1}{\frac{1}{\rho_1} - \frac{1}{\rho_0}} = \rho_0^2 u_0^2 \tag{1.15}$$

$$= \rho_0^2 M_0^2 a_0^2 \tag{1.16}$$

$$= \rho_0^2 M_0^2 \gamma_0 \frac{p_0}{\rho_0} \tag{1.17}$$

$$= \gamma_0 \rho_0 p_0 M_0^2 \tag{1.18}$$

$$\frac{1 - \frac{p_1}{p_0}}{\frac{\rho_0}{\rho_1} - 1} = \gamma_0 M_0^2 \tag{1.19}$$

It's known that $\gamma > 1$, and so this relation indicates that region 1 corresponds to a combustion wave traveling at Mach number above 1, a detonation solution. Similarly, a final state in region 2 means that the wave speed is below sonic, and corresponds to a deflagration solution.

The slope of the Rayleigh line can also be used to the solutions on the Hugoniot curve for which the Rayleigh and Hugoniot lines are tangent. Doing this reveals that the two tangent solutions correspond to solutions where $M_1 = \frac{u_1}{a_1} = 1$, which is either the minimum velocity in the detonation region or the maximum velocity in the deflagration region. It is also possible to use the Gibbs equation to consider entropy variation along the Hugoniot curve, which would reveal that these two solutions are the minimum-entropy states on the Hugoniot curve. These two solutions are known as the Chapman-Jouguet solutions, and even though this is purely a 1-dimensional conservation analysis, it has been found experimentally that most premixed detonations propagate at a velocity corresponding to the upper C-J point. However, experimental setups in which the detonation is "driven," such as with a

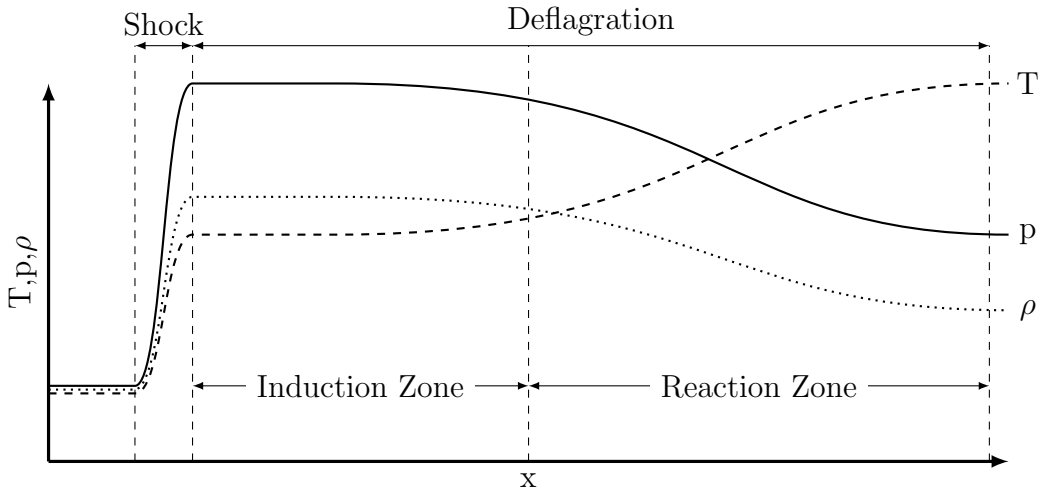

Figure 1.3: Representative variation in temperature, pressure, and density for a one-dimensional detonation with ZND structure.

piston, can force p_1 values above the C-J detonation condition. A detonation of this sort is considered "overdriven," or "strong," and requires some mechanism to continue forcing the wave; the speed of sound in this overdriven region is such that, with nothing else affecting the detonation, an expansion fan would travel into the post-detonation region and reduce the steady-state detonation velocity. In some situations it is also physically possible for "Weak" detonations, solutions in the detonation region of the Hugoniot curve for which the p_1 value is less than the C-J condition, to propagate steadily. One such situation, as analyzed by Von Neumann, occurs when Hugoniot curves corresponding to partially reacted mixtures intersect, such as when the combustion process leads to an initial rapid exothermic reaction followed by a slow endothermic equilibration; such waves are sometimes called "pathological" detonations [16].

1.1.2 One-Dimensional ZND Detonation Structure

Although the Chapman-Jouguet solutions and associated Hugoniot analysis provides a solution for the final conditions of a detonated gas, they do not provide any direct information about the structure of a detonation wave. Attributed to Zeldovich [17], von Neumann [18],

and Döring [19] for work done in the early 1940s, the ZND structure is a formal use of the idea that a detonation wave is structured as a shock followed by a reaction zone. In this case the shock wave can be considered as a discontinuity, since its thickness and associated timescales are much smaller than those associated with reaction heat-release rates [20].

Starting with an unburnt gas at initial conditions, the ZND structure starts with a shock traveling at the same wave velocity as the C-J detonation velocity. The state immediately following the shock is known as the von Neumann condition, by which point the flow has not yet undergone any chemical reactions. However, the post-shock temperature and pressure is high enough to cause radical-generating reactions to start. The radical-generating reactions do not on their own cause large changes in temperature, pressure, or density – this region behind the von Neumann state is called the "induction zone," and is indicated on Fig. 1.3. It is not until enough radical species have built up that the strongly exothermic combustion reactions take off, causing the flow temperature to increase as pressure and density decreases. Although this structure is an extremely simplified steady one-dimensional theory, experiments in the late 50s and early 60s were able to demonstrate for gaseous detonations the existence of a sharp increase in pressure and density, followed by a decrease to C-J conditions [21–24], although in general the spatial resolution of these experiments was not high enough to fully resolve the peak in pressure predicted by the post-shock von Neumann state.

Evaluating the ZND structure that would form for a specific mixture requires knowledge of the associated chemistry. In order to find the C-J conditions that define the limits of the specific ZND structure requires knowledge of the net heat release q which defines the Hugoniot curve; although this can be estimated using single-step complete combustion, in practice this evaluation requires some form of iterative procedure based on possible chemistry equilibria, such as the method used in NASA's Chemical Equilibrium with Applications (CEA) toolset, and discussed in Kuo's book [15]. Once the wave velocity is known, the Rankine-Hugoniot relations for nonreacting shocks can be used to find the von Neumann conditions for the flow. The assumed chemistry can then be used to find the flow properties between completely unreacted (the Neumann condition) and fully reacted (the C-J condition).

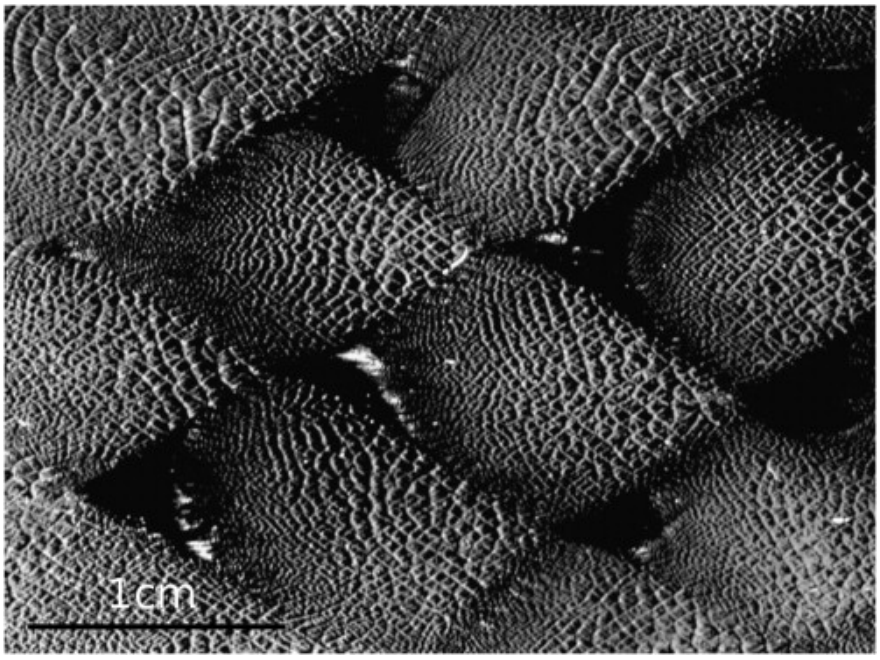

Figure 1.4: Soot foil showing a double-cellular structure from the passage of a detonation in a $H_2 -- NO_{2/}N_2O_4$ mixture, from Joubert et al. [25].

1.1.3 Three-Dimensional Detonation Structure

Although the one-dimensional ZND detonation structure provides a large amount of insight into detonation propagation, in most cases detonations do not have a steady propagation regime. Instead, a physical detonation tends to be both unsteady and highly three-dimensional, even as it sustains propagation into unburnt reactants. This was first realized in 1926, when Campbell and Woodhead observed that detonations in a tube filled with a premixed lean mixture travel in helical pattern, as opposed to a 1-dimensional planar geometry. A technique known as "smoked foil," or "soot foil" can provide a stunning experimental demonstration of the unsteady nature of a detonation propagation, as in Fig. 1.4. As a detonation passes by a plate coated with a layer of soot, it traces a pattern in the soot corresponding to regions of locally high pressure.

This can largely be explained through a detonation's leading shock being nonplanar, and consisting instead of many convex sections. The intersection points of these convex shock sections causes a shock to propagate into the reacting flow region, and this location is often

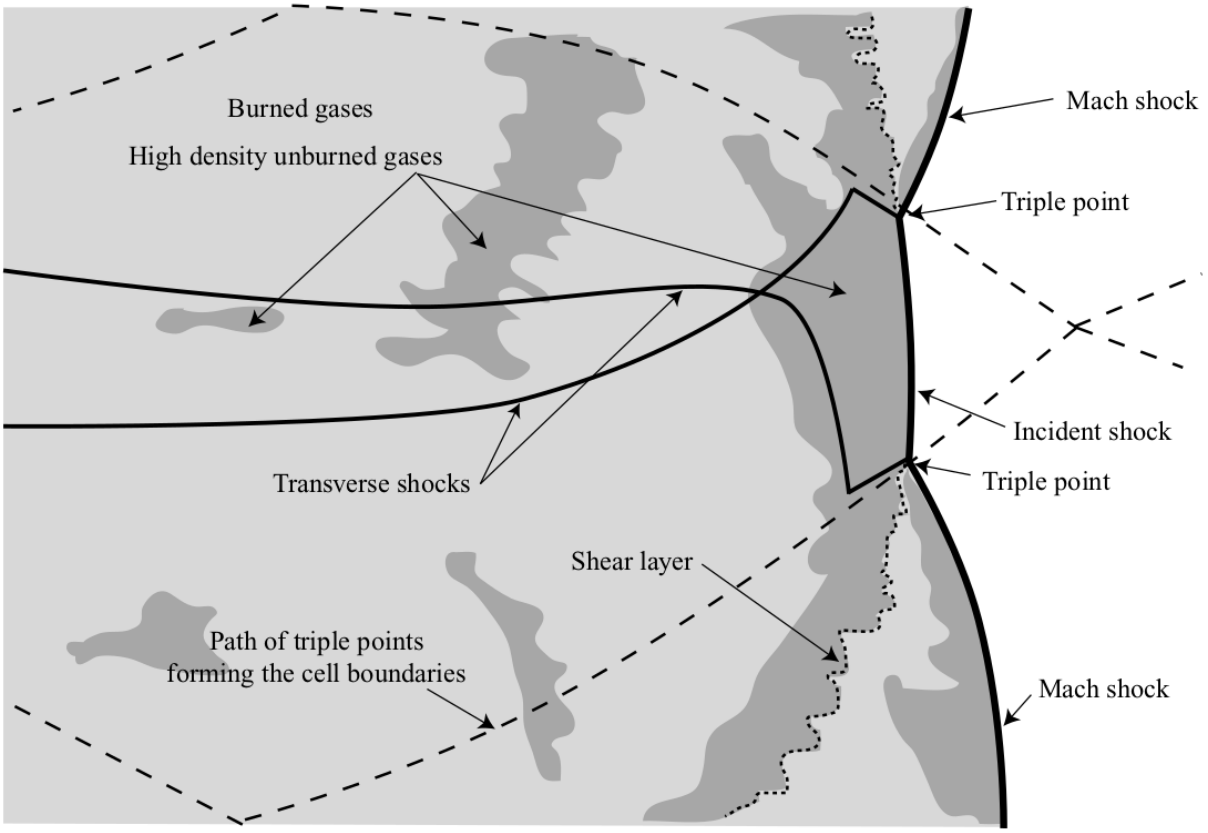

Figure 1.5: Sketch representing two triple-point structures tracing out a cell path, from Radulescu et al. [26]

called a "triple point" due it being a confluence of three separate shock structures. As a detonation propagates, the triple points move along the detonation front, propagating in the transverse direction and tracing out a "cell structure" in a two-dimensional foil, as represented in Fig. 1.5. These cell sizes are often used to compare different unburnt reactants, and give a length that can be considered when analyzing detonation propagation. The formation of these multidimensional unsteady structures can be reproduced numerically, but the complicated structure of even a well-behaved freely propagating pre-mixed detonation gives some indication of the difficulty inherent in developing intuition for detonation behavior.

1.2 Detonation Engines

Although the 19th century saw a number of fanciful designs that used detonations [27,28], it was not until the 20th century that the theoretical understanding was well enough developed to successfully build upon the idea. The modern impetus for a "detonation engine" – a device that uses detonation waves to continuously produce thrust – really only goes back to around 1940, which is when Zeldovich first showed that an ideal detonation cycle could be more efficient for propulsion applications than constant-pressure combustion [29, 30]. Although he did note that there are practical difficulties with designing detonation-based devices, and suggested that loss mechanisms make it impractical to actually achieve performance improvements, there is still hope in Zeldovich's work that the improved theoretical efficiency can be utilized. Moreover, it is still possible that detonations could enable improvements at a system level, even if overall higher I_{sp} is never achieved for a detonation engine; for instance, the reduction in required initial compression may simplify the required turbomachinery and pumping apparatus, greatly reducing overall engine costs [31].

The rapid propagation rate characteristic of detonations must be taken into account when considering the integration of detonations into a functional device. As such, the first proposed geometries were for situations in which a detonation could be stationary in the lab frame as the fluid travels through the device at supersonic rates, such as in a ramjet holding a fixed detonation in the combustion chamber [32]. This is essentially the geometry considered in Zeldovich's thermodynamic analysis, and the idea of using stationary detonations in ramjet-like geometries, usually with an oblique-ramp arrangement, is still an area of active research with applications in hypersonic propulsion [33].

The second approach that was deeply investigated was the idea of designing an engine around constantly re-initiating the detonation, and then allowing the detonation to extinguish or leave the device [34]. There were several variations on this idea, including a series of patents awarded posthumously to Robert Goddard [35–37]. This sort of engine based on repeated initiation of detonation, now called a "pulsed detonation engine" or PDE (not to be confused with partial differential equations), has the advantage that the brief nature of

the detonation reduces the thermal loads on the materials. It also means that PDEs have to constantly purge and re-initiate detonation, and tend to have cycles under 200 Hz [38] – this limits their usability. Although active research into PDEs largely decreased after the 60s, the idea saw a resurgence in the 90s that, by 2008, led to a successful flight test of a PDE-propelled aircraft by the Air Force Research Laboratory [39].

The relative success of PDE research has led to renewed interest in a third approach to detonation engine design: rotating detonation engines (RDEs). The main idea of an RDE is to create a chamber geometry, such as a circular annulus, that allows detonations to continuously travel within the engine. A design of this sort means that, in the lab frame, the engine itself does not need to move, and the injected fluid velocities do not need to be especially high with respect to the engine. This in essence combines the idea of PDEs and oblique detonation engines: operation is periodic – as in a PDE – but the detonation never dies or leaves the engine, and so provides continuous thrust – as in a ramjet with a stationary detonation.

The ability to constrain a detonation to a circular geometry was first demonstrated by Voitskhovskii in 1959, at the Russian Lavrent'ev Institute of Hydrodynamics (LIH) [40]. The aim of their experiment was to create an apparatus that could prevent a detonation from dying out, and so take measurements on timescales larger than the microseconds possible in detonation tubes. Using an annular chamber with an optically-transparent wall, and an oxy-acetyline mixture, Voitskhovskii was able to sustain detonations for 1-1.5 s.

The publication by Voitsekhovskii led the US Air Force, in 1962, to fund James Nicholls and Robert Cullen at the University of Michigan to pursue rotating detonation designs with rocket propulsion in mind. The design of the annular engine design studied at Michigan is shown in figure 1.6, and is remarkably similar to designs used in modern RDRE designs. Unfortunately, they were unable to reproduce Voitsekhovskii's success at sustaining a detonation; although a detonation was initiated in the chamber, it tended to disappear after a single revolution of the annulus. Although the final report by Nicholls et al. is optimistic about the potential for rotating detonation engines, and includes a number of calculations

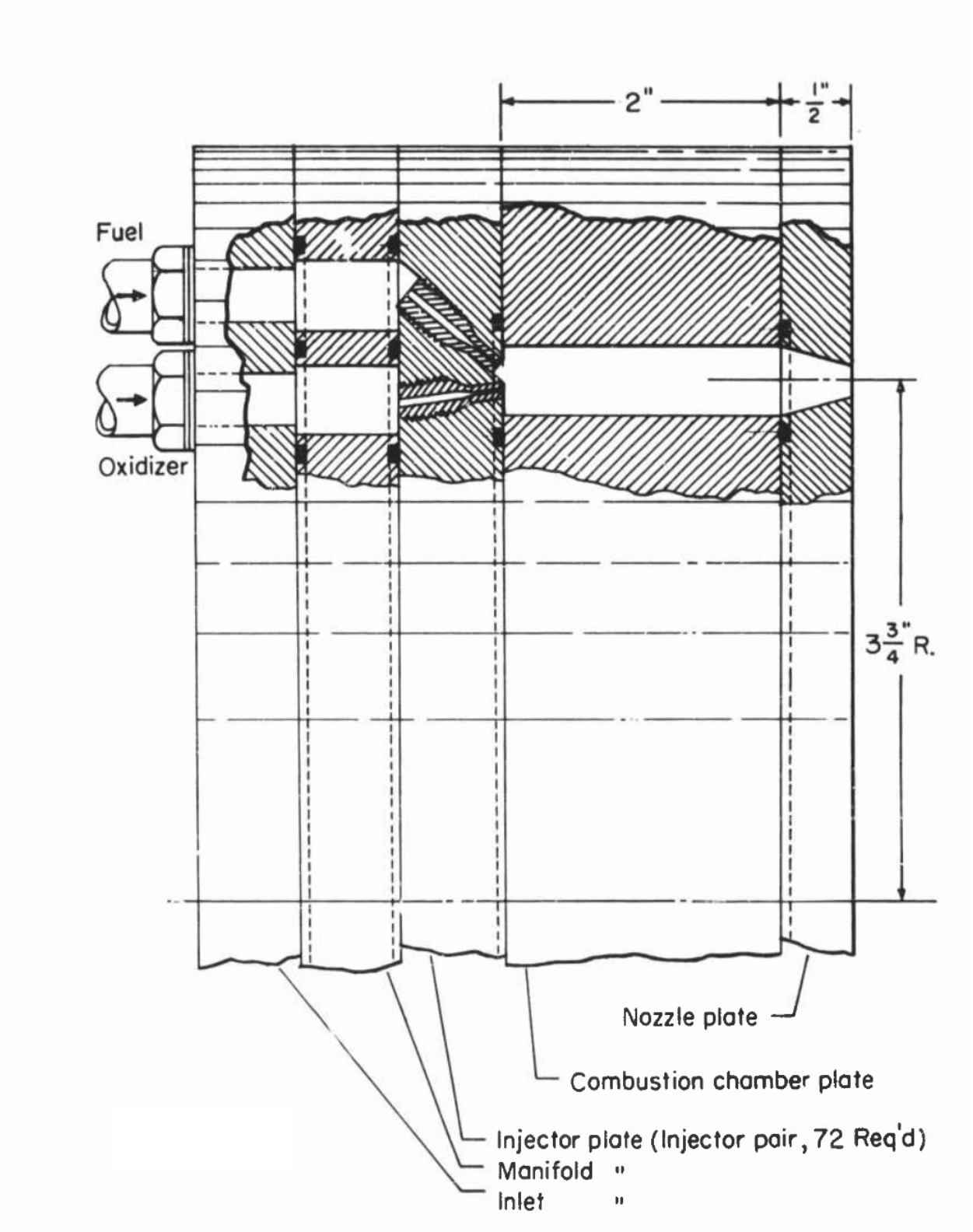

Figure 1.6: Diagram of an annular rotating detonation rocket engine, adapted from Nicholls et al. [41].

suggesting that it should be possible to create a H_2/O_2 RDRE with heat loads similar to a conventional engine design, but with improved performance parameters (such as I_{sp})[1], their difficulty in sustaining detonation damped enthusiasm for the technology in the US [41]. However, the research group at LIH continued to study rotating detonation engines, and most designs currently being studied are based on the extensive series of experiments and analysis conducted at LIH by Bykovskii et al. [42].

There has been a global resurgence in interest in rotating detonation devices in the last 15 years, both as a propulsion technology and as a means of efficient energy generation. The issues sustaining a rotating detonation wave encountered by Nicholls have largely been overcome, with groups in recent years demonstrating detonative behavior using a wide range of propellants and operating conditions. Recent maturation of the technology was emphasized in 2021, when the Japan Aerospace Exploration Agency (JAXA), in collaboration with several Japanese universities, successfully tested a rotating detonation rocket engine as part of a sounding rocket [43]. However, there remain a number of outstanding challenges to be overcome with rotating detonation technology, and the community is still chasing the goal of a detonation-based engine that demonstrably outperforms a deflagrative counterpart.

1.2.1 Thermodynamic Cycle

Modern pressure gain combustion (PGC) engine work is largely driven by thermodynamic analysis similar to that done by Heiser and Pratt, which compares a detonation-based cycle to a deflagration engine [44]. Traditional deflagration engines can be closely approximated by a Brayton cycle, consisting of three parts: adiabatic and isentropic compression, constant pressure combustion, and an adiabatic isentropic expansion. Detonation engines still require the initial compression and expansion stages, but – unlike deflagrative combustion – cannot be approximated as a constant-pressure process. Instead, as suggested by the ZND structure represented in figure 1.3, detonation cycles include a shock compression region that increases the pressure at which combustion reactions occur. It is not uncommon for the overall com-

[1] Although they did calculate that their brass engine would melt after 2s of operation.

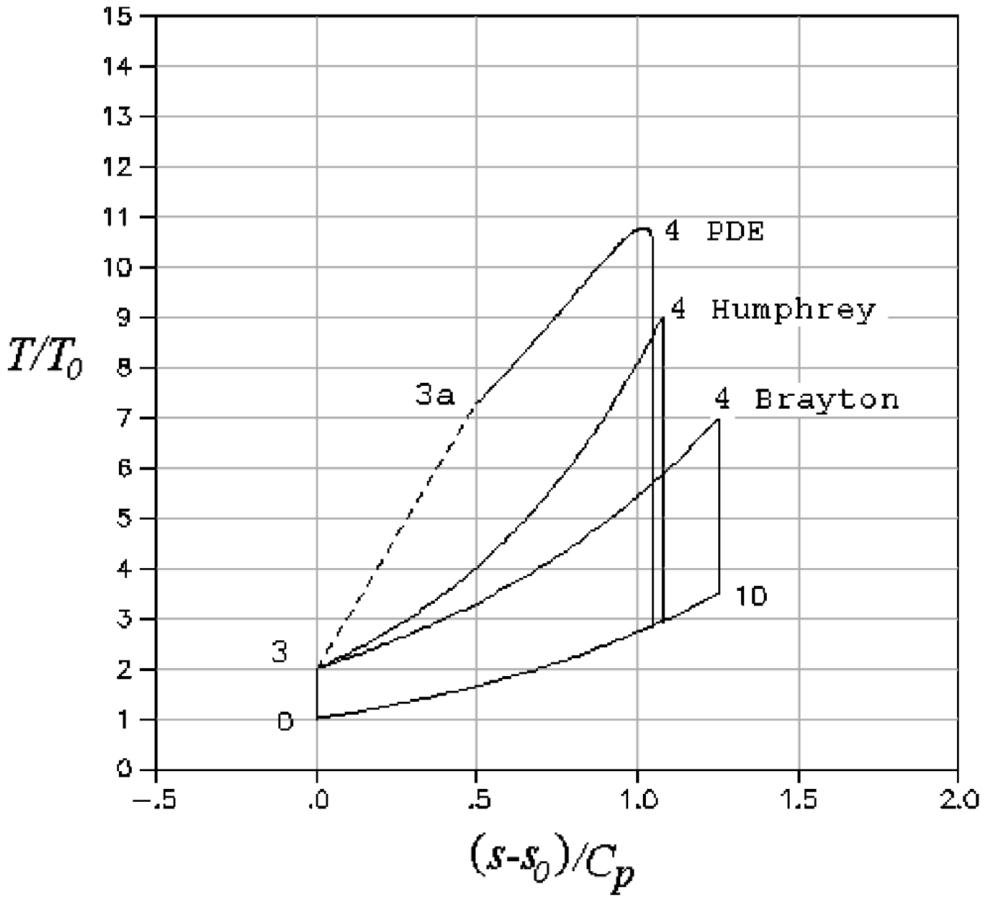

Figure 1.7: Temperature-entropy diagrams for ideal thermodynamic cycles with equivalent initial compression stages, from Heiser et al. [44].

bustion process in a detonation engine to be approximated as constant-volume combustion, as in a Humphrey cycle, but it is also possible to more accurately construct a thermodynamic cycle which uses the ZND structure as a basis.

Figure 1.7 shows an idealized cycle for a detonation-based process, both using the idealized Humphrey cycle and a ZND-based PDE cycle, in order to compare with the standard Brayton cycle. All three cycles consider an initial isentropic compression (from 0 to 3) and conclude with an isentropic expansion (from 4 to 10). The differences occur in the combustion process occurring between points 3 and 4; for a Brayton cycle it can be assumed to be constant pressure, while in a detonation there is an initial shock compression (3 to 3a). The Humphrey cycle is a commonly used approximation of the PDE cycle, in which heat

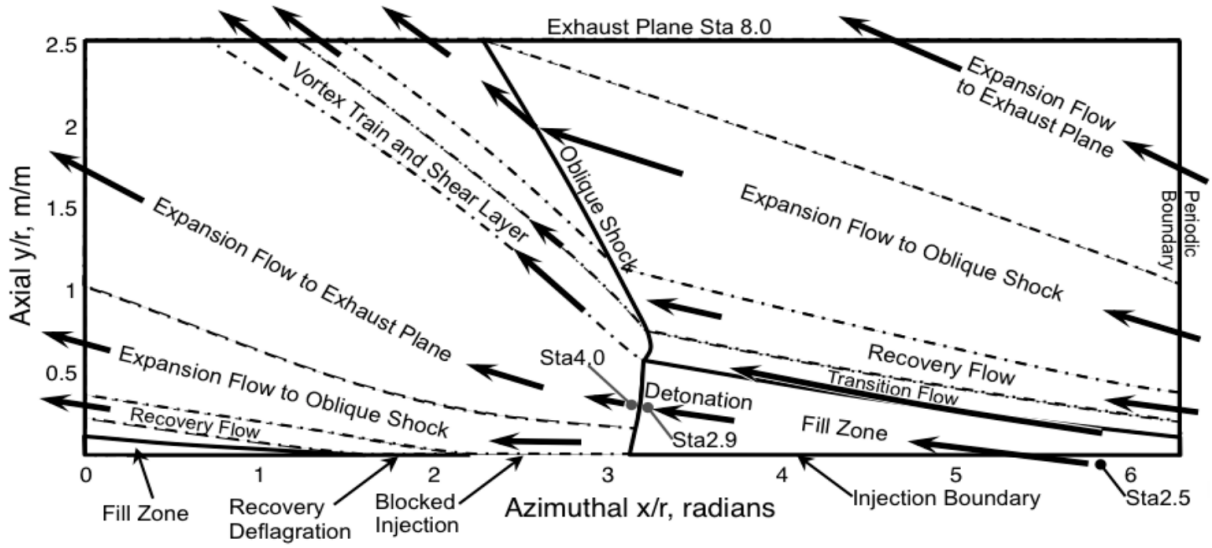

Figure 1.8: Diagram of a canonical rotating detonation wave structure in an unwrapped two-dimensional chamber, taken from Nordeen [45].

addition occurs as a constant volume process. On the T-S diagram it can be seen that the detonation process increases the work done by the cycle, while decreasing the energy lost to the medium; the result is an increased thermal efficiency (η), defined as the ratio of external work done by the cycle to energy added to the cycle's working substance. In an engine, this translates to improved thrust and specific impulse [44], as well as a reduction in the pressure ratio that must be created by upstream turbomachinery to enable engine operation [31].

1.2.2 Idealized 2-D Rotating Detonation

The central idea of a rotating detonation engine is to allow the detonation to continuously travel within the combustion chamber. Figure 1.8 represents how this is done, and represents the major flow features in what has become the standard representation of an RDE chamber: a steady single-wave propagating in an unwrapped two-dimensional annulus. The y-direction in Fig. 1.8 is parallel to the axis of the represented annulus, with the x-direction representing azimuthal position up to periodic boundaries on the left and right of the figure. In this case the chamber is represented in the detonation frame, for a detonation that would be traveling left-to-right in the laboratory reference, with fluid injected from the bottom of the figure and

exiting the top. Unburnt reactants are injected from the bottom of the chamber, forming a triangular "fill zone" of detonable mixture. The detonation continuously travels into the fill zone, transforming the unburnt mixture into a region of high-temperature, high-pressure products.

Because the chamber is longer than the detonation height – as is required to allow detonative combustion of all the reactants – the fill zone does not extend to the top of the chamber. The detonation structure does not have anything to burn in the section of the chamber consisting of products, and so only the shock part of the detonation remains. Without the combustion reactions driving the wave forward, this shock structure lags behind the detonation. The result is a continuously generated oblique shock, which travels out of the chamber in the exhaust along with the products.

The oblique shock formed by the detonation travels into the hot products, increasing the pressure of the already-detonated mixture. A shear layer forms between the just-detonated products and the detonated-and-shocked products, and can result in a classical Kelvin-Helmholtz instability. If it does, the resultant vortex train traveling into the exhaust region originates at the point where the detonation transitions into an oblique shock.

This two-dimensional model also represents two features that have become some of the most important complications being considered in the development of rotating detonation combustors. The first is that the boundary of the fill zone includes an interface between unburnt detonable mixture and high temperature burnt gases, which can result in combustion of the unburnt reactants even before the detonation reaches that section of the mixture, marked as the "transition flow" in Fig. 1.8. This combustion is in a deflagrative mode; the central aim of a detonation engine is to utilize the detonation-based thermodynamic cycles, and so any deflagration of the reactants is considered a loss. Emphasizing the negative nature of this burning, non-detonative combustion in the chamber is commonly referred to as "parasitic" in the literature [46, 47].[2]

[2]Occasionally the phrase "commensal combustion" is used to specify deflagration outside of the detonation, but in the high-pressure region [46].

The second complication hinted at by Fig. 1.8 is the fact that the high pressure of the detonation is likely enough to prevent injection of unburnt reaction. In a worst-case scenario, this may even reverse the injector pressure gradient enough to trigger reverse flow, forcing hot products into the injection system. Even if the detonation does not reverse flow, the interruption of injection prevents the clean re-establishment of a fill zone after the detonation passes. The interruption may further lead to parasitic deflagration. This suggests that, in order for the detonation engine to have a cleaner, closer-to-ideal operation, stiffer (higher-diodicity) injection is required. Typically, stiffer injection is accomplished physically by decreasing injector area and increasing pressure at the start of the injection system; using Fig. 1.7, this refers to an increased initial compression in the cycle. Injection design is one of the major tradeoffs in RDRE design: the goal is to achieve better performance at lower initial compression ratios, but the lower the compression ratio is the further the combustor fill zone is from ideal.

1.2.3 Further Complications

Although section 1.2.2 already alludes to some of the complications that can occur in a real device, there are several phenomena observed in real RDREs that are not captured by the 2D model.

One such observation is that most rotating detonation rocket engines do not operate in a single wave mode; ignition forms an unsteady transient, which eventually leads to several waves travelling around the annulus. Experimentally, it has been found that the engine tends to "lock in" to a repeatable number of waves, which depends on engine design and flow conditions (e.g. mass flow rate). In some cases an engine may not have all its detonations traveling in the same direction, resulting in a "counter-propagating" regime with detonations constantly colliding and interacting. Even in "co-rotating" cases, where all the detonations travel in the same azimuthal direction, transition regions have been observed: flow conditions at which the same engine can operate with two different numbers of waves. Usually there is hysteresis in the operation (i.e. it locks in to one of the two wave modes and then

doesn't change), but there also exist experiments in which an engine reached an apparently stable operational condition before transitioning into a different number of waves. Rocket engines, using pure oxygen and fuel, generally observe more waves than air-based engines. This is likely due to the combustion timescales, which affect both how fast the detonation propagates and how much deflagration occurs in the fill zone/burnt product interface, and seem to largely influence the number of waves.

There is currently no comprehensive theory able to predict the number of waves an engine will lock into during operation. Conservation laws, such as the Wolanski criterion [48], can be used in the ideal case to relate detonation height, wave speed, and injection flow rates; however, while this establishes relations that exist for a specific number of waves, conservation relations of this sort cannot on their own predict the number of waves that will develop. There have been attempts to fill the missing link using empirical knowledge of detonation cell sizes, which forms a connection to the combustion timescales; however, these techniques have not yet managed to fully predict the number of waves at which an engine design will operate. The unpredictability in number of waves forms the basis for two of the questions for which the community is most ardently seeking answers: how does one predict the number of detonations an engine will have during operation, and what number yields the best performance. [3]

Figure 1.8 hints at the effect of detonations stopping the injection of reactant. The complication of this is exacerbated by the impracticality of injecting premixed reactants into the combustion chamber of a real RDRE: the detonation wave would travel into the feed system, turning the engine into a bomb. Instead, fuel and oxidizer are injected separately, creating a three-dimensional mixing field within the chamber. It is this field of partially mixed reactants that the detonation actually interacts with as it propagates, and which dictates both the detonation structure and the thermodynamic cycle being utilized by the engine. Moreover, the cyclic nature of the device means that the fill zone is also affected

[3]The number of detonations an RDE has during operation is often referred to as the "wave number" of the engine. This must not be confused with other uses of the term, such as the wave number that comes from the classical wave equations.

by the passage of the preceding wave, so the fill zone may have hot products and partially deflagrated reactants mixed in – all of which are affected by the turbulent structure behind the preceding detonation, and by the unblocking behavior of the specific injection design.

1.2.4 Detonation Engine Simulation

Even without considering the complications of a detonation engine, detonation simulations come with a list of technical challenges. Detonation simulation requires the ability to capture shock structures, in flows that also contain turbulence and chemical reactions on a range of timescales. Attempting to run direct numerical simulations becomes untenable even in extremely small geometries, with some recent studies using more than 1×10^9 cells to simulate 3 cm^3 [49].

Until recently, most simulations of RDREs used two-dimensional domains based on Euler equations and single-step chemistry [50–52]. Although there is a lot that can be gained from such studies, they are unable to capture effects caused by three-dimensional mixing fields; such simulations tend to propagate at C-J velocities, with an unchanging number of waves that all propagate in the same direction. As such, there has been a move in the last several years to use three-dimensional domains, which can more fully capture geometric effects [53–55]. Three-dimensional simulations with non-premixed injections avoid the issue of developing C-J detonations, and more closely model experimental results. However, it's still largely unknown to what extent engine operation depends on choices of model for chemistry or turbulence.

1.2.5 Nozzle Design

Any practical device using an RDE will require some form of nozzle at the end. However, the unsteady nature of the flow fields complicates the design of an optimal nozzle beyond what would be the case for a traditional deflagration-based engine. It has also been shown, both experimentally and numerically, that changes in geometry and flow conditions can greatly impact the steady state detonation mode of an RDRE [56–59]. These changes manifest in a

variety of ways: the number of detonation waves may change, the wave speeds may shift, and the engine may even begin to sustain waves propagating in both azimuthal directions. Further investigation into the effect that engine geometry has on detonation mode is necessary to fully understand how RDRE design impacts performance.

The addition of a constriction to the exit of an RDRE annulus is one such geometric effect that requires further study; when designing nozzles for use with an RDRE it will be vital to understand what effect the constriction has on combustion within the chamber. Previous work on air-breathing hydrogen detonation engines has shown that a constriction typically increases the average chamber pressure, and can also increase the number of detonation waves [56]. It has also been observed that a constriction can increase the amount of parasitic deflagration present in the annulus [60].

The reasons behind these changes in detonation dynamics are still largely unknown. It has been proposed [56] that a large component is an increase in average chamber pressure expected from the addition of a constriction, as it also changes the reactivity of the gases involved. Prior experiments with constrictions have also determined that there frequently exist associated pressure reflections, which travel towards the injection plane. It has also been hypothesized [57] that any pressure waves returning to the injection region may influence the injector response, and a small change in injection behavior may be enough to greatly affect detonation dynamics. Any study which looks at the creation of non-ideal engine operation is partially aimed at explaining this change in behavior.

Although it's known that reducing the length of an unconstricted chamber minimally affects the detonation dynamics of an annular RDE [50], the effects of changing chamber length are less well known when a constriction is present. Prior experimental work has demonstrated that certain lengths can trigger longitudinal pulsing, and that a difference in length can affect the presence of counter-propagating behavior [57]. Any deviation from the idealized plane detonation is likely to prevent the device from reaching theoretical efficiencies, and so a study of any such phenomenon is warranted. The pressures, temperatures, and heats associated with PGC typically limit what can be measured experimentally; numerical studies

do not run into the same issues, and so are well suited to an investigation of detonation dynamics within a rocket's combustion chamber.

1.3 Research Objectives and Overview

This study is a numerical analogue to experimental tests conducted at the Air Force Research Laboratory. As such, each of the five simulations presented in this work have direct experimental analogues with which the simulated engine operation can be compared. Once comparisons with experiment have been made, the simulations are used to further understanding of phenomena inside the combustion chamber by close examination of parts of the flowfield which cannot be measured experimentally.

The first part of this work, chapters 3 and 4, considers a rotating detonation rocket engine geometry that was selected as part of the AIAA model validation in propulsion (MVP) workshop. Chapter 3 examines the in-chamber behavior associated with the engine operating mode, and compares global measurements of the engine with both experimental results and with other simulation results from groups that have simulated the engine as part of the validation workshop. In chapter 4 a physics-based approach is developed for comparing simulation data with laser absorbance measurements. The simulated laser measurements are then compared to experimental measurements of the engine's exhaust, and the simulation is used to explore what would be necessary to take laser measurements inside the engine.

The second part of this work, chapters 5 and 6, focuses on the experimental observation that changing chamber geometries impacts the engine's operating mode. Chapter 5 considers two geometries, to show what occurs inside the chamber when a converging-diverging nozzle is added to an RDRE. The simulation flowfield is used to consider whether the changes in operating mode caused by the nozzle constriction are detrimental to engine performance. The study is from 5 is then extended in chapter 6 to consider chambers with different length, and establish whether length must be considered when developing RDRE nozzles. Finally, results are summarized in chapter 7, and potential avenues for further research are discussed.

CHAPTER 2

Simulation Setup

2.1 Governing Equations

The flow within an RDRE is governed by standard compressible-flow conservation equations: conservation of mass, momentum, and energy. However, because the flow is affected by a combustion reaction, chemical reaction processes come into play and must also be tracked; the result is a reaction rate term that impacts what species exist in the flow, as well as controlling how much energy is converted from the combustion.

2.1.1 Mass Conservation

The overall mass conservation law is not directly impacted by individual species reaction rates, and so conservation of mass can be represented by the standard continuity equation:

$$\frac{\partial \rho}{\partial t} + \frac{\partial}{\partial x_i}\left(\rho u_i\right) = 0 \tag{2.1}$$

Equation 2.1 uses index summation notation for vectors, where the i subscript in x_i indicates which spatial coordinate, and u_i similarly denotes a component of the velocity field. ρ denotes density of the mixture of gases.

2.1.2 Momentum Conservation

Conservation of momentum is represented as the Navier-Stokes equation (neglecting body forces):

$$\frac{\partial}{\partial t}(\rho u_i) + \frac{\partial}{\partial x_j}(\rho u_j u_i) = -\frac{\partial p}{\partial x_i} + \frac{\partial \tau_{ij}}{\partial x_j} \tag{2.2}$$

Equation 2.2 includes pressure p and viscous stress tensor τ_{ij}, where the stress tensor depends on viscosity μ:

$$\tau_{ij} = -\frac{2}{3}\mu\frac{\partial u_k}{\partial x_k}\delta_{ij} + \mu\left(\frac{\partial u_i}{\partial x_j} + \frac{\partial u_j}{\partial x_i}\right) \tag{2.3}$$

The δ_{ij} term in equation 2.3 is the Kronecker delta.

2.1.3 Energy Conservation

Conservation of energy within a flow can be considered either by directly tracking energy, or by considering the flow's entropy. One way of following the flow's energy is to directly consider the specific internal energy of the flow e; this form is an energy per unit mass, and does not include kinetic terms.

The result, after using continuity to simplify a material derivative, is in equation 2.4:

$$\rho\frac{D}{Dt}(e) = \frac{\partial}{\partial t}(\rho e) + \frac{\partial}{\partial x_i}(\rho u_i e) = -\frac{\partial}{\partial x_i}q_i + \sigma_{ij}\frac{\partial}{\partial x_j}u_i \tag{2.4}$$

One thing to note about equation 2.4 is that, because the equation tracks internal energy using a material derivative, a change in form due to combustion reaction does not add an explicit term. Instead, energy is either transferred to kinetic energy through the σ_{ij} tensor:

$$\sigma_{ij} = \tau_{ij} - p\delta_{ij} \tag{2.5}$$

or through the heat flux term, which takes into account both a conductive heat flux term and a diffusive term:

$$q_i = -\lambda\frac{\partial T}{\partial x_i} + \rho\sum_{k=1}^{N} h_k Y_k V_{k,i} \tag{2.6}$$

The conductive term in equation 2.6 is based on the local thermal conductivity λ, affected by temperature T according to Fourier's law. Energy lost to diffusion requires keeping track of individual species, because different species may have different formation energies, which

affects internal enthalpy h_k of species k. Mass fraction is denoted Y_k, and it is necessary to also track diffusion velocities $V_{k,i}$.

2.1.4 Species Conservation

As is apparent in the effect of diffusion on energy conservation, the governing equations of reacting flow must take variation in species composition into account. Species are converted throughout reacting regions within a flow according to chemical reaction rate $\dot{\omega}_k$, but total mass must be conserved. The conservation of mass requirement must be enforced for every species k:

$$\frac{\partial}{\partial t}\left(\rho Y_k\right) + \frac{\partial}{\partial x_i}\left(\rho Y_k\left(u_i + V_{k,i}\right)\right) = \dot{\omega}_k \tag{2.7}$$

Note that equation 2.7 reduces to the overall continuity equation when summed over all species in the system.

2.1.5 Diffusion Velocities

Both the conservation of energy and the conservation of species requires tracking diffusion, which is represented in equations 2.7 and 2.6 by the diffusion velocities V_k. This can be modeled using Fick's law:

$$V_{i,k} = \frac{D_k}{Y_k}\frac{\partial Y_k}{\partial x_i} \tag{2.8}$$

where D_k is a diffusion coefficient for species k, which is calculated using a chemkin transport database.

2.1.6 Equation of State

Even in a reacting flow model it is usually possible to use the ideal gas equation of state:

$$p = \rho R T \tag{2.9}$$

A standard compressible-flow simulation tool is to couple the ideal gas law with a calori-

cally perfect gas assumption. However, when there are large temperature ranges involved the heat capacity values for a single species can vary. Fortunately, for many species of interest this variation has been measured and tabulated, such as in the NASA curvefits database [61] – and so a thermally perfect gas assumption can be invoked to improve accuracy in a reactive flow.

2.2 Combustion Chemistry

The reaction rates $\dot{\omega}_k$ are present in the species conservation equations for a reacting flow, e.g. 2.7, and so must be determined. The first step is to determine which reactions to consider for a given simulation; unfortunately, choosing the appropriate chemistry is not easy. One instinct is to attempt to simulate an exhaustive list of possible reactions, but for most applications an exhaustive list would include hundreds – or even thousands – of reactions, and is not at all feasible to simulate. Instead, it is more common to use a reduced chemistry developed to represent all the dominant species and reactions for a given regime. One such chemistry model is given in appendix A, which discusses FFCMy-12 – a chemistry with 12 species and 38 reactions designed for methane-oxygen detonation reaction, and based on the foundational fuel chemistry model (FFCM) [62].

Simply knowing which reactions and species to consider is not enough to calculate $\dot{\omega}_k$; although it is possible to determine individual reaction rates from first principles, doing such calculations using quantum mechanical descriptions of atomic and molecular structures is generally not necessary. Instead, reaction rates are generally well-modeled according to an Arrhenius law:

$$k_j = A_j T^{\beta_j} e^{-\frac{E_j}{RT}} \tag{2.10}$$

where Arrhenius constants A_j, β_j and activation energy E_j are determined empirically for each reaction and tabulated for the model. FFCMy-12 also includes several third-body reactions which depend on pressure; these reactions are modeled using either Lindemann's

approach [63] or using Troe's form [64, 65], depending on the reaction.

2.3 LES Filtering

In 1922, Richardson observed that turbulent flows exhibit an energy cascade, in which energy is transferred from larger scales to smaller ones:

> Big whorls have little whorls,
> Which feed on their velocity;
> And little whorls have lesser whorls,
> And so on to viscosity
> (in the molecular sense)

Although it is generally unfeasible to directly simulate everything in a flow, the observation in a large eddy simulation (LES) is that it is possible to take advantage of these varying length scales: it's possible to fully simulate the large whorls, and then model the behavior of small scales using something less intensive than a full simulation. To do this, the first step in LES is to define a filtering operation that separates the length scales:

$$\overline{f}(\mathbf{x}, t) = \int G(\mathbf{x}, \mathbf{r}) f(\mathbf{x} - \mathbf{r}, t)\, d\mathbf{r} \tag{2.11}$$

In this case, G is a general filter that is yet to be chosen; for it to not also scale the flow properties it must be normalized:

$$\int G(\mathbf{x}, \mathbf{r})\, d\mathbf{r} = 1 \tag{2.12}$$

With this operation, every flow property can be separated into filtered and residual components; e.g., for flow velocity $\mathbf{u}$:

$$\mathbf{u} = \overline{\mathbf{u}} + \mathbf{u}' \tag{2.13}$$

From this form it isn't immediately obvious what a good choice of G would be. However, one observation is that simply discretizing a continuous field to a mesh, as is standard for numerical schemes, is already the application of a filter. This implicit approach is used for this study. For a uniform 3D mesh, of cell length Δ, the filter due to the cell discretization is represented as a "top hat," or "box" filter:

$$G(\mathbf{x}, \mathbf{r}) = \prod g\left(x_i - r_i\right)$$

$$g(x) = \begin{cases} \frac{1}{\Delta} & |x| < \frac{\Delta}{2} \\ 0 & \text{otherwise} \end{cases}$$

Some notes on this filter: Because the filter definition is a purely spatial convolution, the operation commutes with temporal differentiation:

$$\overline{\frac{\partial}{\partial t} f} = \frac{\partial}{\partial t} \overline{f} \tag{2.14}$$

Also, because of the choice of filter the operation also commutes with the spatial derivative:

$$\frac{\partial}{\partial x_i} \overline{f} = \overline{\frac{\partial}{\partial x_i} f} + \int f(\mathbf{x} - \mathbf{r}, t) \frac{\partial}{\partial x_i} G(\mathbf{x}, \mathbf{r}) \, d\mathbf{r} \tag{2.15}$$

$$\frac{\partial}{\partial x_i} \overline{f} = \overline{\frac{\partial}{\partial x_i} f} + 0 \tag{2.16}$$

This is useful, because it allows for easy conversion of the governing equations. For continuity, this becomes:

$$\frac{\partial \overline{\rho}}{\partial t} + \frac{\partial}{\partial x_i} \left(\overline{\rho u_i}\right) = 0 \tag{2.17}$$

Because $\overline{\rho u_i} \neq \overline{\rho}\, \overline{u_i}$, at this stage a mass-weighted Favre filter is also introduced, $\overline{\rho u_i} = \overline{\rho} \tilde{u_i}$, so that:

$$\frac{\partial \overline{\rho}}{\partial t} + \frac{\partial}{\partial x_i} \left(\overline{\rho} \tilde{u_i}\right) = 0 \tag{2.18}$$

The other conservation equations can then also be filtered, for example momentum:

$$\frac{\partial \overline{\rho}\tilde{u}_i}{\partial t} + \frac{\partial}{\partial x_i}(\overline{\rho}\tilde{u}_j\tilde{u}_i) = -\frac{\partial \overline{p}}{\partial x_j} + \frac{\partial}{\partial x_i}\left[\overline{\tau}_{ij} - \overline{\rho}(\widetilde{u_i u_j} - \tilde{u}_i\tilde{u}_j)\right] \tag{2.19}$$

Although these filtered equations are mostly similar in form to the unfiltered versions, there are a number of extra terms; for example, the Favre filtered Reynold's stress $\widetilde{u_i u_j}$ in equation 2.19. The added terms must be modeled in order to close the system of equations, corresponding to modeling the small scales.

2.3.1 Subgrid Closure Model

Rewriting conservation of mass, momentum, energy, and species in a form that makes explicit the subgrid-scale terms introduced by the LES filter:

$$\frac{\partial \overline{\rho}}{\partial t} + \frac{\partial}{\partial x_i}\left(\overline{\rho}\tilde{u}_i\right) = 0 \tag{2.20}$$

$$\frac{\partial \overline{\rho}\tilde{u}_j}{\partial t} + \frac{\partial}{\partial x_i}\left[\overline{\rho}\tilde{u}_j\tilde{u}_i + \overline{p}\delta_{ij} - \overline{\tau}_{ij} + \tau_{ji}^{\text{sgs}}\right] = 0 \tag{2.21}$$

$$\frac{\partial \overline{\rho}\tilde{E}}{\partial t} + \frac{\partial}{\partial x_i}\left[\overline{\rho}\tilde{u}_i\tilde{E} + \overline{p}\tilde{u}_i + \overline{q_i} - \tilde{u_j}\overline{\tau_{ij}} + H_i^{\text{sgs}} + \sigma_i^{\text{sgs}}\right] = 0 \tag{2.22}$$

$$\frac{\partial \overline{\rho}\tilde{Y_k}}{\partial t} + \frac{\partial}{\partial x_i}\left[\overline{\rho}\left(\tilde{Y_k}\tilde{u}_i + \tilde{Y_k}\tilde{V_{i,k}}\right) + Y_{i,k}^{\text{sgs}} + \Theta_{i,k}^{\text{sgs}}\right] = \overline{\dot{\omega}_k} \tag{2.23}$$

where the subgrid-scale terms which require further modeling are marked "sgs":

$$\tau_{ij}^{\text{sgs}} = \overline{\rho}\left(u_i\tilde{u}_j - \tilde{u}_i\tilde{u}_j\right) \tag{2.24}$$

$$H_i^{\text{sgs}} = \overline{\rho}\left(\widetilde{Eu_i} - \tilde{E}\tilde{u}_i\right) + \left(\overline{u_i p} - \tilde{u}_i\overline{p}\right) \tag{2.25}$$

$$\sigma_i^{\text{sgs}} = \left(\overline{u_j\tau_{ij}} - \tilde{u}_j\overline{\tau_{ij}}\right) \tag{2.26}$$

$$Y_{i,k}^{\text{sgs}} = \overline{\rho}\left(\widetilde{u_i Y_k} - \tilde{u}_i\tilde{Y}_k\right) \tag{2.27}$$

$$\Theta_{i,k}^{\text{sgs}} = \overline{\rho}\left(\widetilde{V_{i,k}Y_k} - \tilde{V_{i,k}}\tilde{Y}_k\right) \tag{2.28}$$

$$\tag{2.29}$$

This work uses a one-equation eddy viscosity closure model, which relates a characteristic length scale to the subgrid kinetic energy $\mathrm{k}^{\text{sgs}} = \frac{1}{2}\left(\widetilde{u_i u_j} - \tilde{u}_i\tilde{u}_j\right)$. Specifically, using the cell length as a characteristic length scale and C_ν as a modeled coefficient, an eddy viscosity can be defined as

$$\nu_t = C_\nu \Delta\sqrt{k^{\text{sgs}}} \tag{2.30}$$

Using this allows rewriting the subgrid-scale stress tensor τ^{sgs} in a form analogous to the standard viscous stress tensor:

$$\tau_{ij}^{\text{sgs}} = -2\overline{\rho}\nu_t\left(\tilde{S_{ij}} - \frac{1}{3}\tilde{S_k}k\delta_{ij}\right) + \frac{2}{3}k^{\text{sgs}}\delta_{ij} \tag{2.31}$$

In order to close the LES-filtered momentum equation, the evolution of the subgrid-scale kinetic energy is modeled as a single differential equation:

$$\frac{\partial\overline{\rho}k^{\text{sgs}}}{\partial t} + \frac{\partial}{\partial x_i}\left(\overline{p}\tilde{u}_j k^{\text{sgs}}\right) = T^{\text{sgs}} + P^{\text{sgs}} - D^{\text{sgs}} \tag{2.32}$$

In this form, T^{sgs} represents diffusion, P^{sgs} represents production, and D^{sgs} represents dissipation:

$$T^{\text{sgs}} = \frac{\partial}{\partial x_i}\left[\left(\overline{\rho}\nu_t + \mu\right)\frac{\partial k^{\text{sgs}}}{\partial x_i} + \frac{\overline{\rho}\nu_t\tilde{R}}{\mathrm{Pr}_t}\frac{\partial\tilde{T}}{\partial x_i}\right] \tag{2.33}$$

$$P^{\text{sgs}} = -\tau_{ij}^{\text{sgs}}\frac{\partial\tilde{u}_j}{\partial x_i} \tag{2.34}$$

$$D^{\text{sgs}} = \frac{\overline{\rho}C_\epsilon\left(k^{\text{sgs}}\right)^{\frac{3}{2}}}{\Delta} \tag{2.35}$$

C_ν	C_ϵ	Pr_t	Sc_t
0.067	0.916	0.4	1

Table 2.1: Coefficients used in subgrid-scale closure model.

Although there exist dynamic approaches to evaluating the coefficients C_ν, C_ϵ, and the turbulent Prandtl number Pr_t, constant coefficients are used in this study; see Table 2.1.

The subgrid-scale energy transport terms are modeled together:

$$H_i^{\mathrm{sgs}} + \sigma_i^{\mathrm{sgs}} = -\left(\overline{\rho}\nu_t + \mu\right)\frac{\partial k^{\mathrm{sgs}}}{\partial x_i} - \frac{\overline{\rho}\nu_t C_p}{\mathrm{Pr}_t}\frac{\partial \tilde{T}}{\partial x_i} + \tilde{u}_j \tau_{ij}^{\mathrm{sgs}} \tag{2.36}$$

And eddy-diffusion is also used to model subgrid species diffusion, using a turbulent Schmidt number as in Table 2.1:

$$Y_{i,k}^{\mathrm{sgs}} = -\frac{\overline{\rho}\nu_t}{\mathrm{Sc}_t}\frac{\partial \tilde{Y}_k}{\partial x_i} \tag{2.37}$$

In general, the choice of model for turbulent chemical reaction rates, $\overline{\dot{\omega}}$, can greatly affect LES solutions. However, there is not yet a standard model shown to behave appropriately over the large range of conditions at which combustion may occur in an RDRE, and so the simplest model is used for this study:

$$\overline{\dot{\omega}} = \dot{\omega}(\tilde{Y}_k, \tilde{T}) \tag{2.38}$$

In this case the Arrhenius rate laws are still used, but the rate calculations are done directly using the filtered variables. This is the equivalent of the assumption that turbulent time scales are much smaller than combustion timescales, which – although not a generally applicable assumption for RDREs – has been used with success in a number of RDRE simulations [66–68].

2.4 Numerical Formulation

The simulations were run using ALREST High Fidelity Modeling (AHFM), which is a commercially-maintained version of the Large Eddy Simulation with Linear Eddy (LESLIE) solver developed at the Georgia Institute of Technology [69]. The solver has previously been validated for a wide range of turbulent and reacting flows, and recently has been used with success in other detonation engine studies [68, 70–75]. AHFM uses a structured multi-block hexahedral mesh, and solves the fully-reacting LES-filtered Navier-Stokes equations with a single-equation turbulent closure based on a subgrid-scale turbulent kinetic energy model [71]. In order to parallelize the solution, the domain was separated into separate blocks that could be solved for independently, with communication between the blocks at each timestep conducted using a message passing interface. Timestepping was accomplished using a 2nd-order MacCormack scheme, with an additional third-order MUSCL shock-capturing method based on a hybrid HLLC/HLLE Riemann solver [76–80]. The thermally-perfect ideal gas equation of state was used, with thermodynamic properties based on 7-parameter NASA polynomials and the JANAF thermochemical tables [81].

2.4.1 Central Scheme

In order to numerically solve the equations of section 2.1, the relations are first combined into a vector form:

$$\frac{\partial \mathbf{U}}{\partial t} + \frac{\partial \mathbf{F}_i}{\partial x_i} = \mathbf{S} \tag{2.39}$$

where the terms $\mathbf{F}_i$ and $\mathbf{S}$ are functions of U, according to the models of section 2.1. The conservation equations, including subgrid kinetic energy closure, then give the form of the vectors:

$$\mathbf{U} = \begin{bmatrix} \overline{\rho} \\ \overline{\rho}\tilde{u_i} \\ \overline{\rho}\tilde{E} \\ \overline{\rho}k^{\text{sgs}} \\ \overline{\rho}\tilde{Y_k} \end{bmatrix}, \mathbf{F}_i = \begin{bmatrix} \overline{\rho}\tilde{u_i} \\ \overline{\rho}\tilde{u_j}\tilde{u_i} + \overline{p}\delta_{ij} - \overline{\tau}_{ij} + \tau_{ji}^{\text{sgs}} \\ \overline{\rho}\tilde{u_i}\tilde{E} + \overline{p}\tilde{u_i} + \overline{q_i} - \tilde{u_j}\overline{\tau_{ij}} + H_i^{\text{sgs}} + \sigma_i^{\text{sgs}} \\ \overline{p}\tilde{u_j}k^{\text{sgs}} - \left((\overline{\rho}\nu_t + \mu)\frac{\partial k^{\text{sgs}}}{\partial x_i} + \frac{\overline{\rho}\nu_t \tilde{R}}{\text{Pr}_t}\frac{\partial \tilde{T}}{\partial x_i} \right) \\ \overline{\rho}\left(\tilde{Y_k}\tilde{u_i} + \tilde{Y_k}\tilde{V_{i,k}} \right) + Y_{i,k}^{\text{sgs}} + \Theta_{i,k}^{\text{sgs}} \end{bmatrix} \tag{2.40}$$

Note that, although conservation of momentum is represented as a single row with directional indices, because the solver takes three dimensions into account there are actually three rows for conservation of momentum. Similarly, the number of rows keeping track of species conservation depends on the number of species. The source term, $\mathbf{S}$, is nonzero because of both the LES subgrid model, and the possibility of changes in species through chemical reactions:

$$\mathbf{S} = \begin{bmatrix} 0 \\ 0 \\ 0 \\ P^{\text{sgs}} + D^{\text{sgs}} \\ \overline{\dot{\omega_k}} \end{bmatrix} \tag{2.41}$$

A cell-centered finite volume formulation of the conservation equations was used, in which the vector form of equation 2.39 is integrated for the computational cell, and then Green's theorem is applied to separate the state vector $\mathbf{U}$ from the flux terms $\mathbf{F}_i$:

$$\frac{\partial}{\partial t}\int_\Omega \mathbf{U}\, dV + \int_{\partial\Omega} \mathbf{F}_i\, dA_i = \int_\Omega \mathbf{S}\, dV \tag{2.42}$$

The form of equation 2.42 leads to tracking a change in state, d$\mathbf{U}$, evaluated in a cell based on the flux terms, source terms, mesh geometry, and time step dt. The specifics are discussed in Genin et. al [71, 80], and lead to a change d$\mathbf{U}$ that can be marched in time according to

$$\mathrm{d}\mathbf{U} = -\frac{\mathrm{dt}}{\Delta}\sum \mathbf{F}_{i,l} A_{i,l} + \mathbf{S}\mathrm{dt} \tag{2.43}$$

where A indicates the area of one of the sides of the hexahedral mesh. Although further notation is left out for convenience, the values of $\mathbf{U}$ and $\mathbf{S}$ being tracked are now the averages of the cell, based on the integration of equation 2.42. The MacCormack predictor-corrector approach is applied to the state $\mathbf{U}$, with

$$\mathbf{U}^{\overline{n+1}} = \mathbf{U}^n + \mathrm{d}\mathbf{U}^n \tag{2.44}$$

$$\mathbf{U}^{n+1} = \frac{1}{2}\left[\mathbf{U}^n + \mathbf{U}^{\overline{n+1}} + \mathrm{d}\mathbf{U}^{\overline{n+1}}\right] \tag{2.45}$$

In order to evaluate the values of $\mathbf{F}_i$ at the interfaces, forward and backward extrapolation of $\mathbf{U}$ is used alternately in the predictor and corrector steps. The result is a scheme with second order accuracy in space and time.

2.4.2 Shock Capturing

The central scheme introduces dispersive error in the vicinity of shocks, which are widespread in the types of flows being considered. To deal with this problem, the central-volume fluxes are calculated differently when in the vicinity of a shock. This is a determined using a smoothness parameter for cell i, $\lambda_{p,i}$.

$$\lambda_{p,i} = \begin{cases} \frac{|p_{i+1}-2p_i+p_{i-1}|}{|p_{i+1}-p_i|+|p_i-p_{i-1}|} - \lambda_p^{th} & |p_{i+1}-2p_i+p_{i-1}| \geq 0.05p_i \\ -\lambda_p^{th} & |p_{i+1}-2p_i+p_{i-1}| < 0.05p_i \end{cases} \tag{2.46}$$

where λ_p^{th} is a threshold for pressure smoothness; 0.125 was used. A parameter based on density, λ_ρ, is also calculated; the calculation is equivalent to that used for pressure, but with p in equation 2.46 replaced with ρ. A density threshold, λ_ρ^{th}, of 0.5 was used.

If the interface for which the flux was being calculated had a smoothness factor greater than 0, based on either pressure or density, a Reimann problem was evaluated to determine relevant values of $\mathbf{F}_i$. The left and right states of the Riemann problem are evaluated as:

$$U^L_{i+1/2} = U_i + \frac{1-\xi_i}{4}\left[\frac{2}{3}\Delta^+_{i-1/2} + \frac{4}{3}\Delta^-_{i+1/2}\right] \tag{2.47}$$

$$U^R_{i+1/2} = U_{i+1} - \frac{1-\xi_{i+1}}{4}\left[\frac{4}{3}\Delta^+_{i+1/2} + \frac{2}{3}\Delta^-_{i+3/2}\right] \tag{2.48}$$

where ξ is a flattening parameter based on Collela et. al [78], and $\Delta^{\pm}_{i+1/2}$ denotes the difference in state $\mathbf{U}$ between cells i and i+1:

$$\Delta^{\pm}_{i+1/2} = (\mathbf{U}_{i+1} - \mathbf{U}_i)\,\phi\left(r^{\pm}_{i+1/2}\right) \tag{2.49}$$

with

$$r^+_{i+1/2} = \frac{\mathbf{U}_{i+2} - \mathbf{U}_{i+1}}{\mathbf{U}_{i+1} - \mathbf{U}_i} \tag{2.50}$$

$$r^-_{i+1/2} = \frac{\mathbf{U}_i - \mathbf{U}_{i-1}}{\mathbf{U}_{i+1} - \mathbf{U}_i} \tag{2.51}$$

and a monotonized central limiter is used for $\phi(r)$:

$$\phi(r) = \max\left(0, \min\left(2r, 2, \frac{1+r}{2}\right)\right) \tag{2.52}$$

The flattening term ξ_i is based on the pressure gradient,

$$\xi_i = \begin{cases} \max(\tilde{\xi}_i, \tilde{\xi}_{i+1}) & \text{if } p_{i+1} - p_{i-1} < 0 \\ \max(\tilde{\xi}_i, \tilde{\xi}_{i-1}) & \text{if } p_{i+1} - p_{i-1} > 0 \end{cases} \tag{2.53}$$

where

$$\tilde{\xi}_i = \max\left(0, \min\left(1, 10\left(\frac{p_{i+1} - p_{i-1}}{p_{i+2} - p_{i-2}} - 0.75\right)\right)\right) \tag{2.54}$$

In order to solve the resultant Riemann problem, a hybrid extension of the HLL (Harten, Lax, and van Leer, [82]) type of solvers are used. In most of the region for which an HLL solver is used, as controlled by equation 2.46, a three-wave HLLC solver is used [79, 83] which solves for a contact surface as well as the main left-running and right-running waves of the Riemann problem. However, the HLLC solver develops instabilities in the vicinity of shocks; to solve this, Quirk [84] suggests using two-wave solver in regions where this poses

a problem. A hybrid solver of this form is used, where a two-wave HLLE (Harten, Lax, van Leer, Einfeldt) solver is used in the vicinity of a shock [85, 86].

In order to switch between HLLC and HLLE solvers, conditions based on pressure and velocity are considered:

$$\frac{|p_{i+1} - p_{i-1}|}{\min(p_{i+1}, p_{i-1})} - \frac{1}{3} < 0 \tag{2.55}$$

$$u_{i+1} - u_{i-1} < 0 \tag{2.56}$$

If both conditions are true, in either the j or k direction, then the flux $\mathbf{F}$ in the i direction is solved for using the HLLE approach; otherwise, the HLLC approach is used. This hybrid approach is more thoroughly discussed and verified in Genin and Menon [71].

CHAPTER 3

Validation Geometry

Modern high-fidelity simulations of rotating detonation engines do an ever-improving job at replicating experimental results, but there remain major differences between what is seen experimentally and what exists in simulations. No group is able to use simulations to consistently and precisely predict the number of waves or wave speeds that a given engine would sustain. Simulated pressures also tend to be higher than what is seen experimentally.

The large amount of knowledge still to be gained about RDREs, both in terms of the relevant physics and in terms of what must is necessary to create accurate models, led to the selection of an RDRE as a focus for the AIAA model validation for propulsion (MVP) workshop. Work on the current MVP validation case is discussed within the community each year at the AIAA SciTech conference, with the focus switching from bluff body premixed flames to RDREs in SciTech 2020. The workshop aims to foster collaboration on specific validation cases, encouraging modelers to research what elements of a simulation affect a well-defined problem, while at the same time encouraging experimentalists to work toward a large body of trusted data that can be compared with experiment. Several research groups, with several different LES implementations, have simulated the MVP-geometry RDRE, and make it possible to consider a simulation of the geometry across multiple groups and experiment [66, 87, 88].

3.1 Simulation Setup

In order to ensure all groups participating in the MVP project worked with the same specifications, geometry CAD files of the engine were available to those interested in running

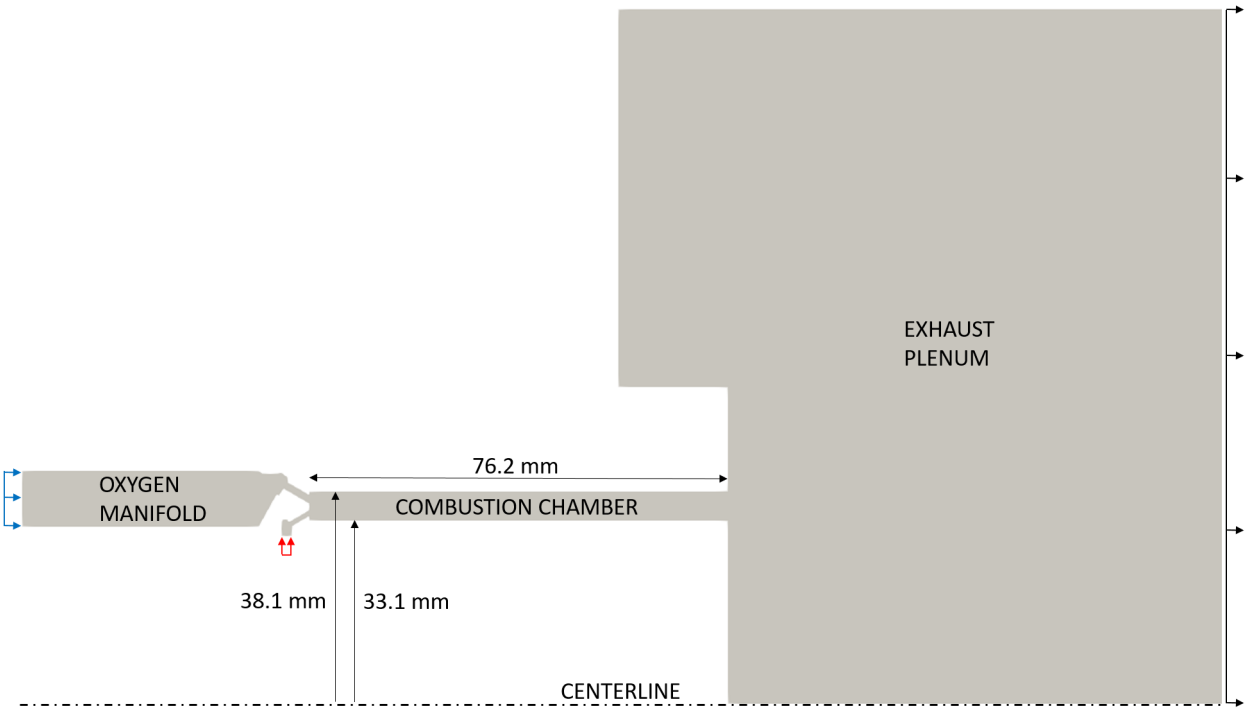

Figure 3.1: Schematic representing MVP-geometry simulation domain.

the simulation. Similarly, a document describing boundaries and flow conditions ensured consistency between numerical groups working on the project. The focus of this chapter is the "nominal" MVP RDRE validation case, referring to injecting methane-oxygen propellant with a flow rate of 0.267 kg/s, and an equivalence ratio of 1.16.

3.1.1 Engine Geometry

The MVP RDRE geometry uses an annular combustion chamber, akin to the engine used by Nicholls et al., sketched in Fig. 1.6. A schematic of the simulation domain is shown in Fig. 3.1. Fuel and oxygen enter the domain separately, into isolated manifolds upstream of the detonation chamber. Propellant manifolds are connected to the annular combustion chamber through 72 discrete impinging injectors, with dimensions shown in Fig. 3.2. The injector arrangement is further represented in Fig. 3.3. Once injected into the annular combustion chamber, the propellants are able to mix and combust. A downstream exhaust plenum was also included in the domain, to provide separation between the exit boundary condition and

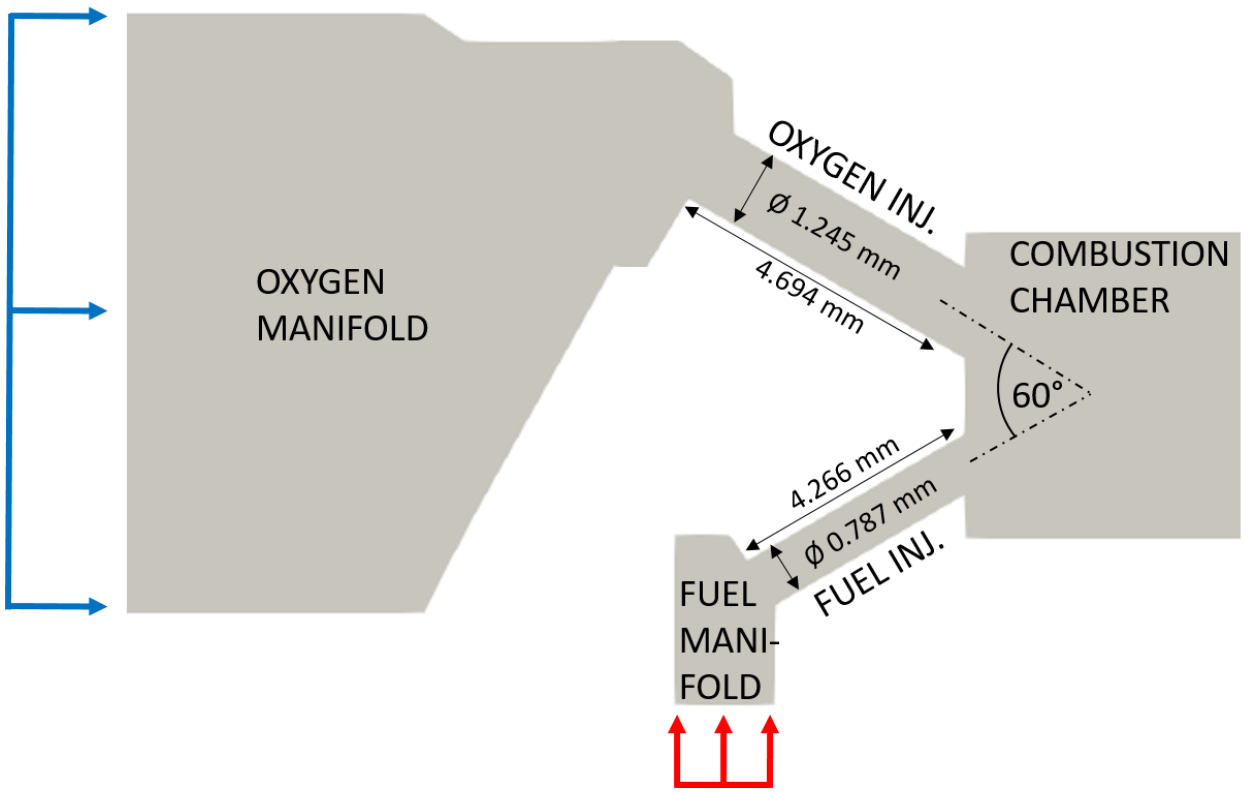

Figure 3.2: Schematic showing injector geometry for a single injector pair.

the regions of interest in the combustion chamber.

Although directly analogous to experimental geometries, the geometry as simulated did necessarily have some differences from experimental apparatus targeted for comparisons. In order to initiate detonation, experimental designs utilize a detonation tube attached to the combustion chamber through a port in the annulus outerbody. Similarly, experimental designs typically have instrumentation ports built into the engine; for the experimental component of the MVP effort, ports designed to take pressure measurements inside the chamber were added to the experimental engines, at locations 8.9 mm, 28.6 mm, and 65.5 mm axially downstream of injection.

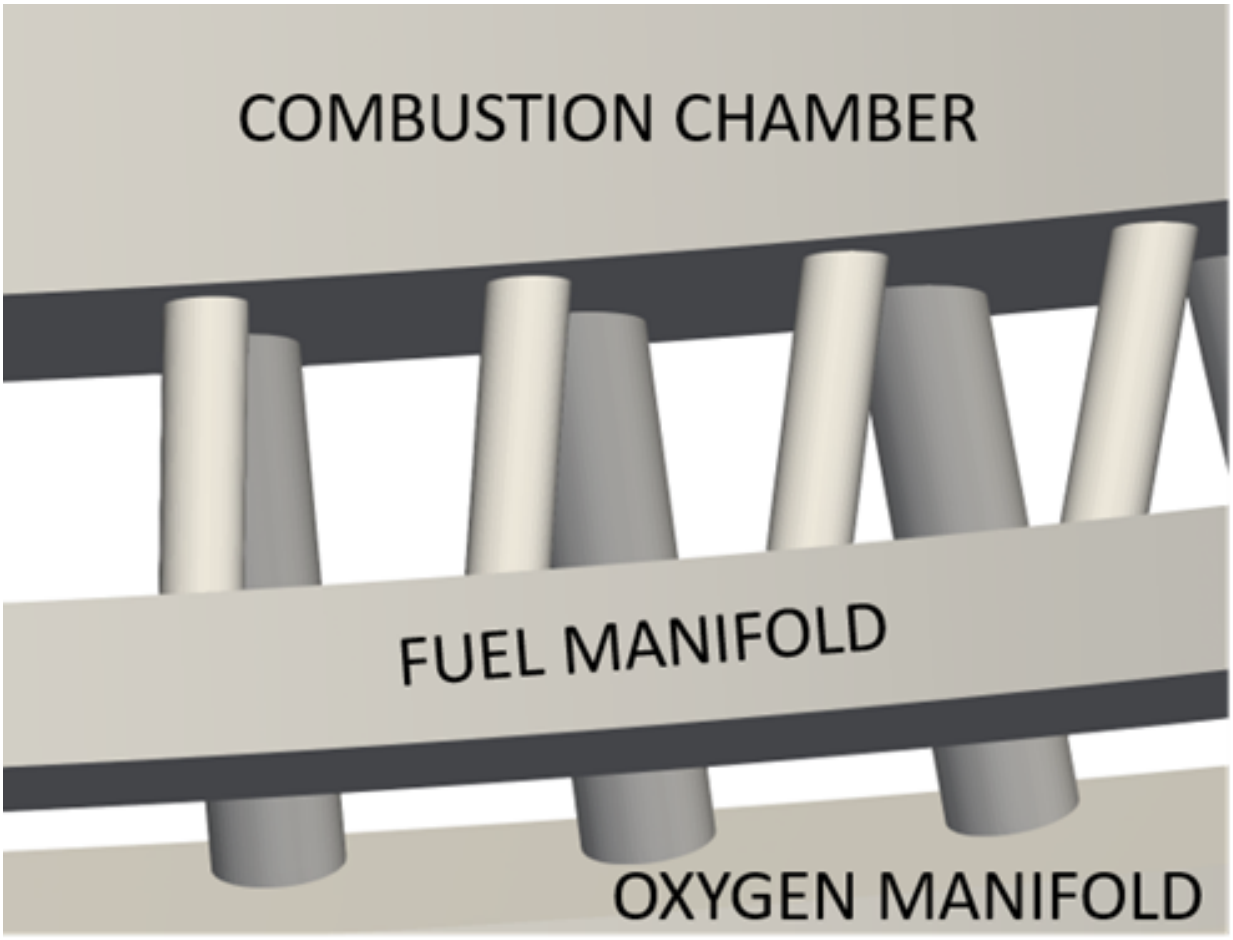

Figure 3.3: Isometric view of simulation-domain injector region, with discrete injector pairs visible.

3.1.2 Simulation Conditions

The simulation was run using AHFM, as described in chapter 2. A hexahedral mesh was used to model the geometry shown in Fig. 3.1, using 150 million cells. Methane-oxygen chemistry was modeled using FFCMy-12, with nonreacting N_2 added as a 13th species in order to approximate transport properties in the exhaust region.

In order to match the specified flow conditions, simulation boundary conditions specified that CH_4 was injected radially into the fuel manifold at a fixed rate of 0.060 kg/s, at 300 K. Pure O_2 was injected axially into the oxidizer manifold, with a rate of 0.207 kg/s and a temperature of 300 K. Adiabatic, non-slip walls were used for the engine walls, with adiabatic slip walls in effect at the boundaries of the exhaust plenum. A coflow was used in the exhaust region, axially injecting N_2 with a velocity of 10 m/s (and a temperature of 300 K). The characteristic boundary condition in the simulation outflow was set to use a farfield pressure of 0.10 MPa in subsonic regions.

The simulation was initialized with air (by mass fraction 0.77 N_2, 0.23 O_2) in the exhaust region, as well as in the chamber at all axial distances greater than 20 mm from the injection plane. The region in the chamber near injection was set to stoichiometric CH_4 and O_2, with fuel and oxidizer injectors initialized to pure CH_4 and O_2, respectively. Pressure in the exhaust was plenum was initialized at 0.10 MPa, and the chamber pressure was set as a linear gradient from 0.10 to 1 MPa. Fuel and oxidizer injectors were initialized to 1.31 MPa and 1.20 MPa respectively, corresponding to previously-measured experimental static pressures during operation.

Ignition was triggered using a 3000 K, 4MPa kernel in the stoichiometric portion of the combustion chamber. The kernel was located near the injection plane, spaced between two injector pairs, with a height of 5 mm, a radial width of 5 mm (the full channel width), and an azimuthal length of 2 degrees.

The simulation was run on the onyx HPC, an intel-based CRAY machine owned by the army's Engineer Research and Development Center (ERDC), and managed by the DoD

high-performance computing and modernization program (HPCMP). Additional processing of the data was conducted on the centennial and narwhal systems, also part of the DoD HPCMP.

3.2 Startup

The ignition kernel triggered a multistep startup process, which eventually led to operation conditions. A startup process of this sort is consistent with prior studies, and has been shown to lead to a operating conditions approximating the experimental result without requiring the imposition of a number of waves. A representation of the process is shown in Fig. 3.4, in which the region of the chamber within 15 mm of the injection plane was separated into 360 one-degree regions. Spatial averages of properties in each region were then calculated, and represented in time as a colormap. The resultant θ-t diagrams are simulation analogs to experimental detonation surface plots, constructed from chemiluminescence data taken using high-speed cameras [89].

At the start of the simulation, the high pressure of the kernel caused shock waves to expand azimuthally in both directions, visible in the pressure plot of Fig. 3.4. The increased temperature of the kernel eventually led to symmetric combustion waves, expanding azimuthally into the stoichiometric region of the chamber in both directions. After about 0.2 ms, the combustion wave visibly underwent the start of a deflagration-to-detonation (DDT) process, with new pressure shocks forming with the combustion wave. The resultant wave structures accelerated, indicated by the change in slope in the θ-t diagrams, until the two waves eventually collided at an azimuthal position 180 degrees shifted from the initial kernel. Discrete secondary structures were visible in the pressure field behind the combustion wave during this time period, 0.2 - 0.4 ms from the start of the simulation; these discrete pressure waves were likely due to interactions with the injectors.

At the wave collision, 0.4 ms from simulation start, there is a feature visible in the temperature field of Fig. 3.4 corresponding to a decrease in the high-temperature part of the

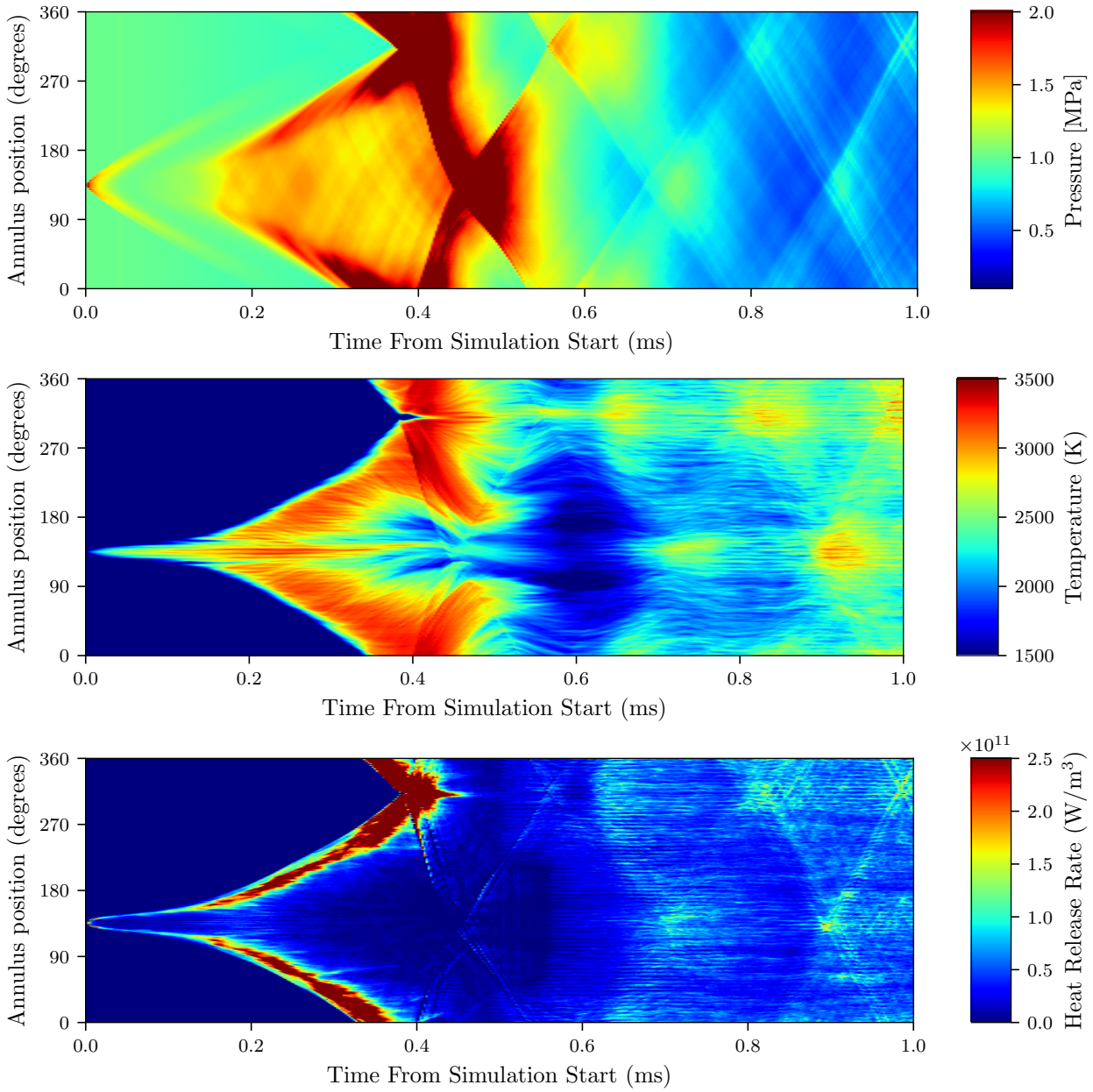

Figure 3.4: θ-t diagrams of pressure, temperature, and heat release, during the startup transient, averaged over the 15 mm immediately downstream of injection.

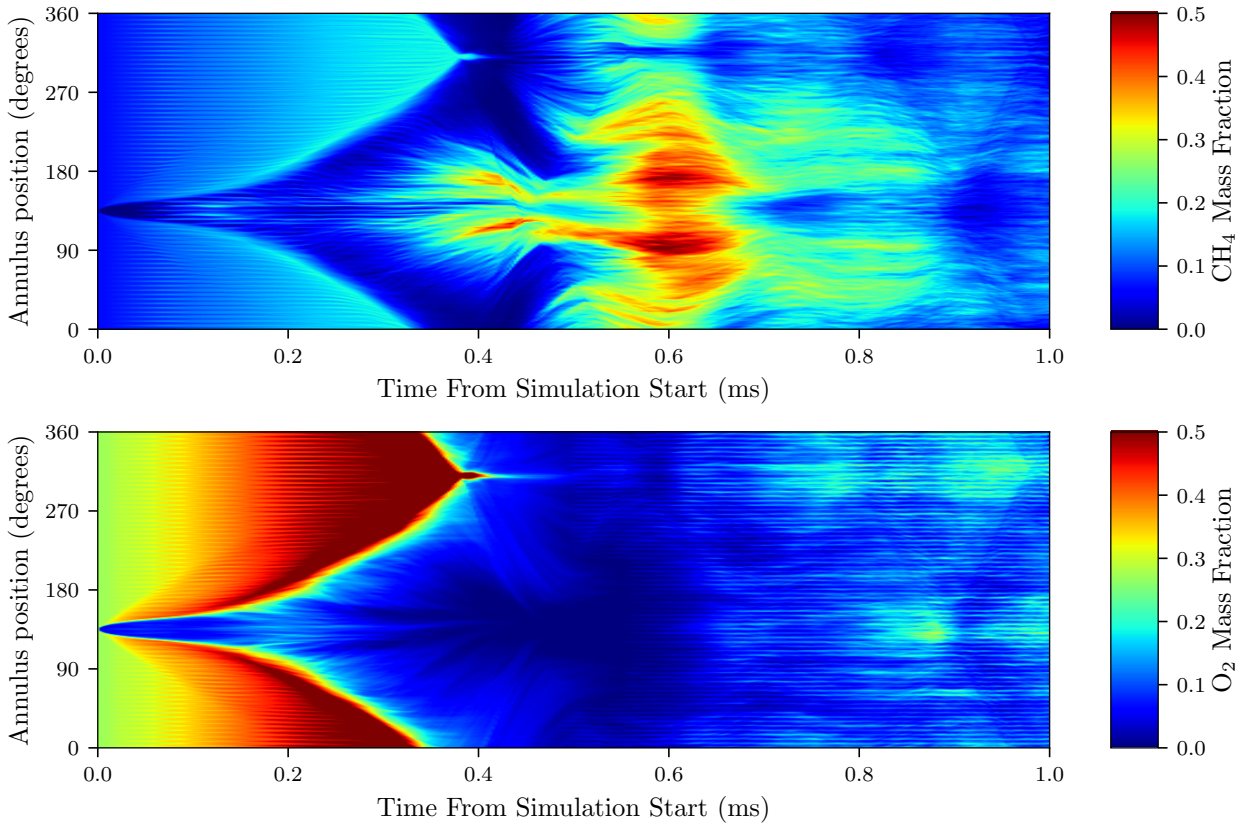

Figure 3.5: θ-t diagrams showing amounts of reactant in the chamber(CH_4 and O_2) during the startup transient, averaged over the 15 mm immediately downstream of injection.

combustion wave. This was due to the change in flow velocity caused by the shock collision. When the nearly-symmetric shocks collided, the azimuthal component of velocity went to near zero in the post-collision region. The slight spatial separation between pressure shock and hot products, corresponding to the combustion wave's induction zone, was exacerbated by this change in velocity. As a consequence, the region at collision exhibited a delay between the rapid increase in pressure and the arrival of high-temperature products. The delay was further represented by the continued presence of CH_4 and O_2 in this region, as in Fig. 3.5.

By a time 0.5 ms after simulation start, most of the reactant in the chamber had been used up. This meant that the pressure waves were no longer being fed by rapid combustion reactions, and the large-magnitude pressure shocks began to lessen in magnitude. Eventually, 0.8 ms after the simulation started, the large initial shock pair had attenuated to pressure

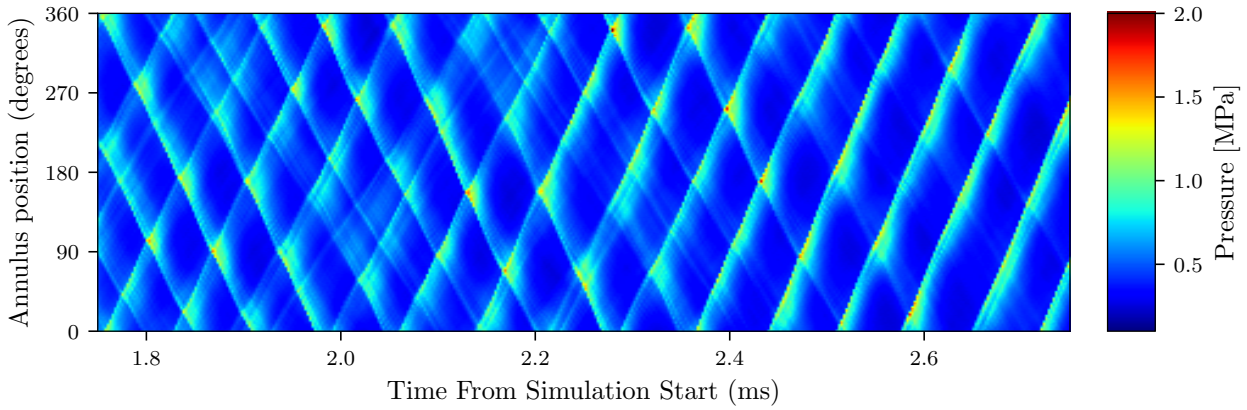

Figure 3.6: θ-t diagram showing pressure during transition to quasi-steady operation, averaged over the 15 mm immediately downstream of injection.

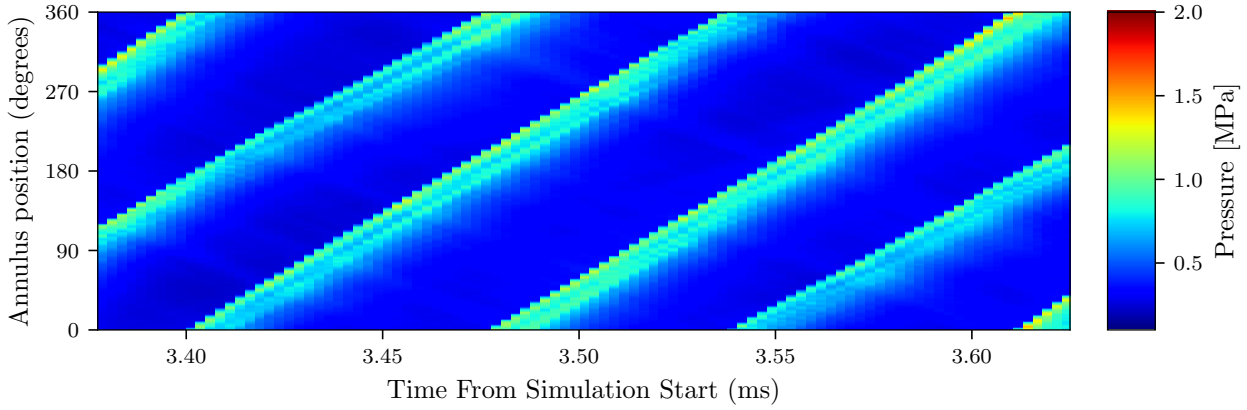

Figure 3.7: θ-t diagram showing pressure after wave cascade process, averaged over the 15 mm immediately downstream of injection.

peaks similar in magnitude to the large number of discrete smaller waves travelling in both directions. This marked the start of a cascade process, in which the large number of waves gradually coalesced, eventually resulting in a sustained two-wave mode. A time period near the end of this cascade process is represented in Fig. 3.6.

3.2.1 Post-Cascade Transients

Although the number of waves stabilized, the simulation never reached an operating mode with constant velocities. It seemed close: after having run for 3 ms of physical time, operation

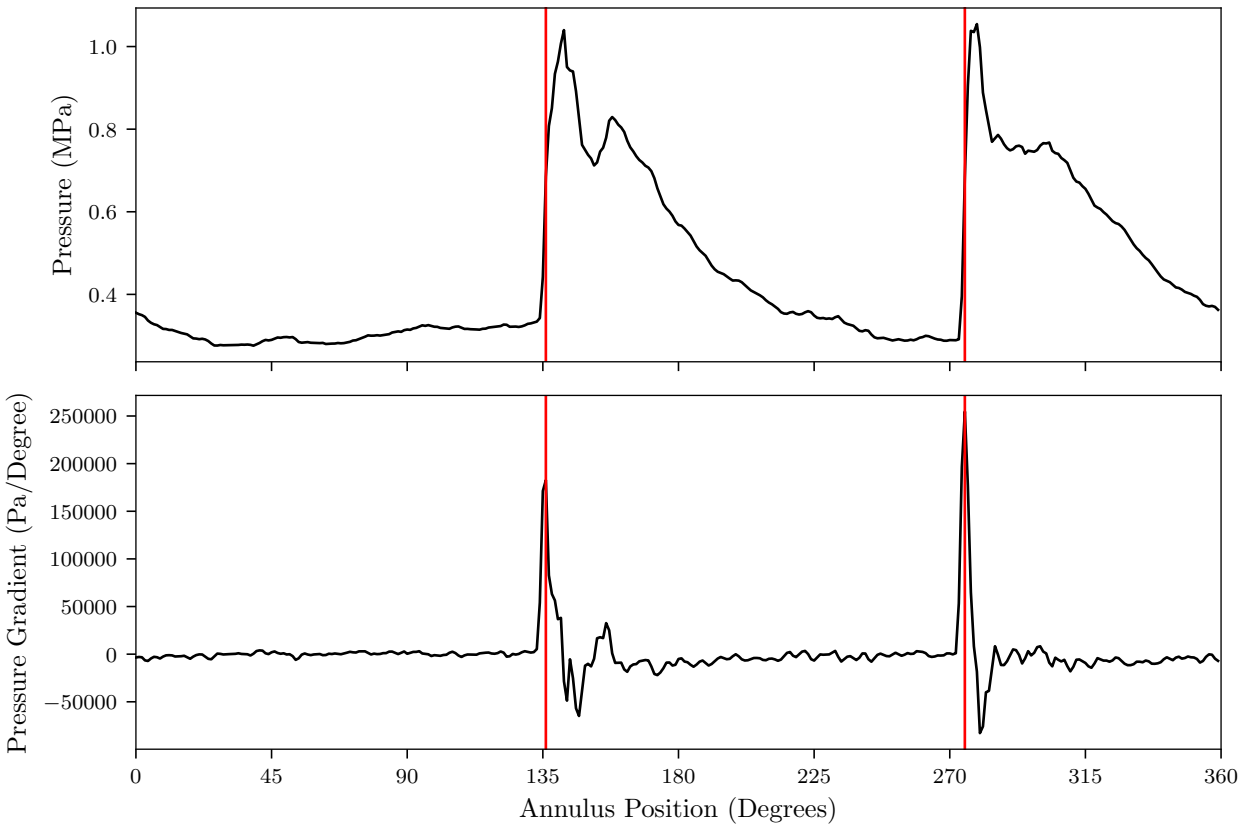

Figure 3.8: Example of instantaneous wave tracking using peak prominence in pressure gradients, based on the data used to generate θ-t diagrams.

had settled in to two waves. An example of this time period is shown in Fig. 3.7. By visual inspection, it seemed to be operating close to a stable manner: two waves, approximately evenly spaced.

However, the waves were not maintaining a constant velocity. At each instant for which the 1-degree averages were calculated, it was possible to use the measurement of pressure as a function of angular position to identify the location of each wave to within a degree. An example of this sort of instantaneous wave tracking is shown in Fig. 3.8. Because the pressure waves are extremely steep-fronted, the spatial derivative of the pressure is large at the wave front, and the signal is well-suited to a peak-finding algorithm. Scipy's prominence-based algorithm was used in this case [90], which evaluates the topographic prominence of each location in the evaluated pressure gradient, with the prominence of a peak defined as

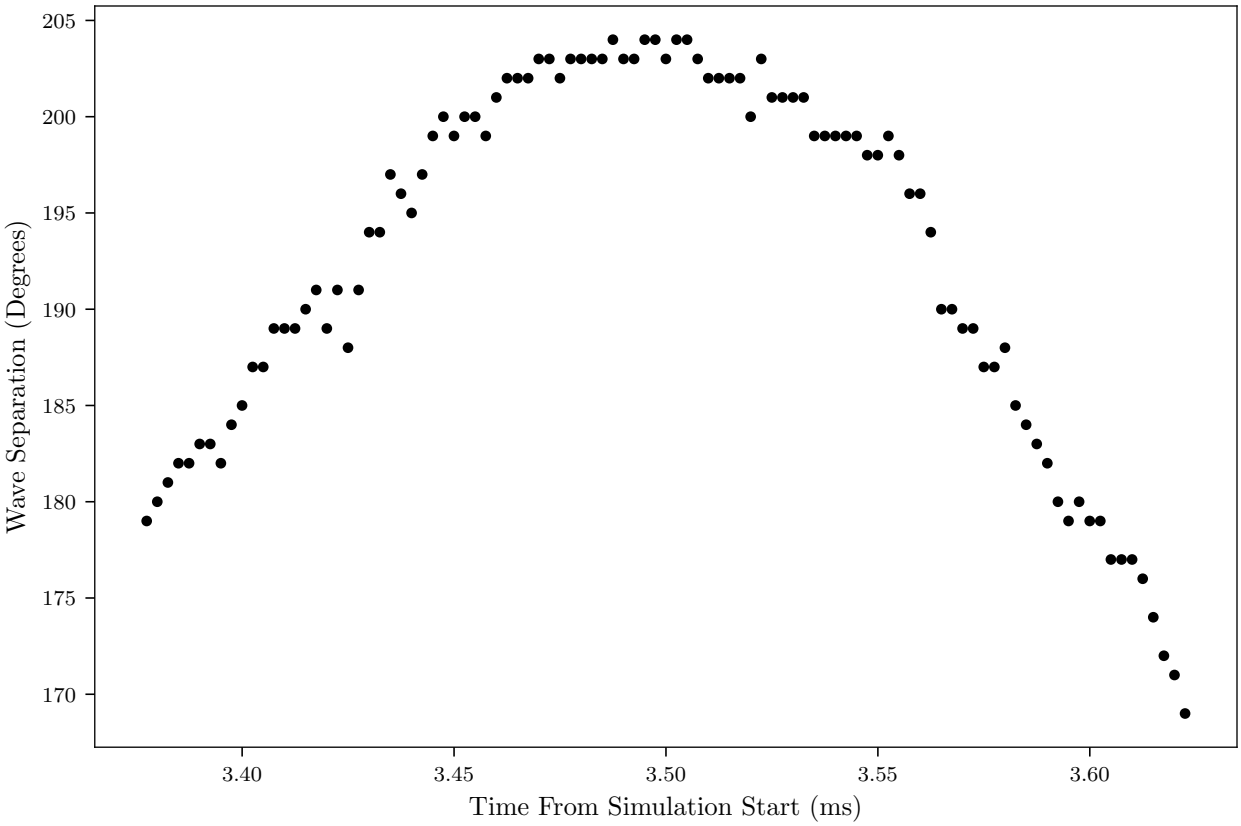

Figure 3.9: Angular separation between the two waves, for the time period displayed in Fig. 3.7.

the least difference in magnitude necessary to reach a peak of greater magnitude. The two most prominent locations in the instantaneous pressure gradient profile corresponded to the locations of the two waves.

Fig. 3.9 shows the separation between waves, calculated by tracking pressure gradients in the data displayed in Fig. 3.7. At this time period, ending more than a full millisecond after the end of the wave cascade process, the waves were undergoing significant changes in velocity as part of a paired galloping phenomenon. The waves alternated between accelerating and decelerating, resulting in an oscillating wave separation. The galloping behavior may be part of a startup transient – experimental measurements for these operating conditions do not show galloping in this engine during operation at equivalent flow conditions. However, there have been experimental demonstrations of engines that operate in two-wave modes

Figure 3.10: Snapshot of exhaust pressure, taken at the end of the cascade process, 2.75 ms after simulation start.

with analogous galloping behavior [91].

It was also discovered that the startup process had increased the pressure in the exhaust manifold, from 0.1 MPa to 0.3 MPa. The pressure in the exhaust manifold after the startup process is shown in Fig. 3.10. Although the subsonic outflow boundary was based on a 0.1 MPa condition, it had not been enough to keep the pressure down in the manifold during startup. It is likely that continuing to run the simulation would have lowered the pressure; however, the size of this simulation meant that each millisecond of simulation was calculated using 3.5 million CPU hours. Instead of waiting for the pressure to drop on its own, the exhaust-region was modified manually in the solution, with a gradual drop in pressure that ended at a simulation time 3.9 ms from the initial start, with a set pressure of 0.12 MPa.

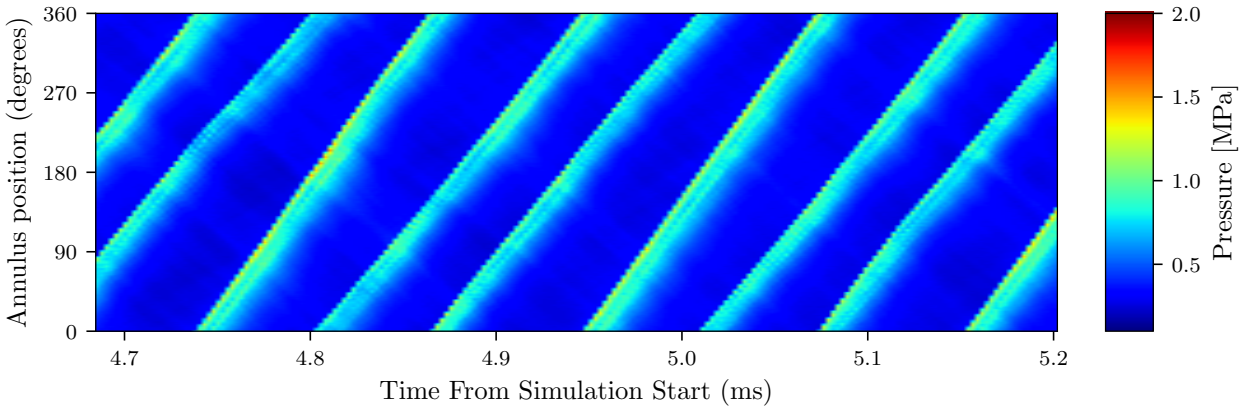

Figure 3.11: θ-t diagram showing pressure during the galloping regime, averaged over the 15 mm immediately downstream of injection.

3.3 Galloping Regime

As the simulation continued to run, the galloping behavior did not disappear; galloping was still occurring over the time shown in Fig. 3.11. Not only did the behavior not disappear, the amplitude grew from a wave separation 204 ° at 3.5 ms, to a peak of 214° at a time 4.91 ms after the simulation start. The changing amplitude during the period represented in Fig. 3.12 does not make it clear whether or not the galloping behavior was part of the startup transient. However, even though the behavior seems unusual, the continuing two-wave operation suggests that the regime was near quasi-steady operating conditions and that measurements could be taken for comparison to experiment.

The pressure in the exhaust was artificially lowered at a simulation time of 3.9 ms, and then without further intervention the pressure decreased further toward the subsonic outflow condition of 0.10 MPa. At a time 5.08 ms after the simulation start, as shown in Fig. 3.13, pressure in the exhaust was near the targeted atmospheric condition. The time shown in Fig. 3.13 also shows a low pressure inside the chamber in the lower annulus segment shown in the slice. This change in pressure is due to the location of the oblique shocks; at this instant in time, an oblique shock is visible as a sudden drop in pressure inside the chamber in the lower section, while in the upper portion the slice shown does not intersect a shock.

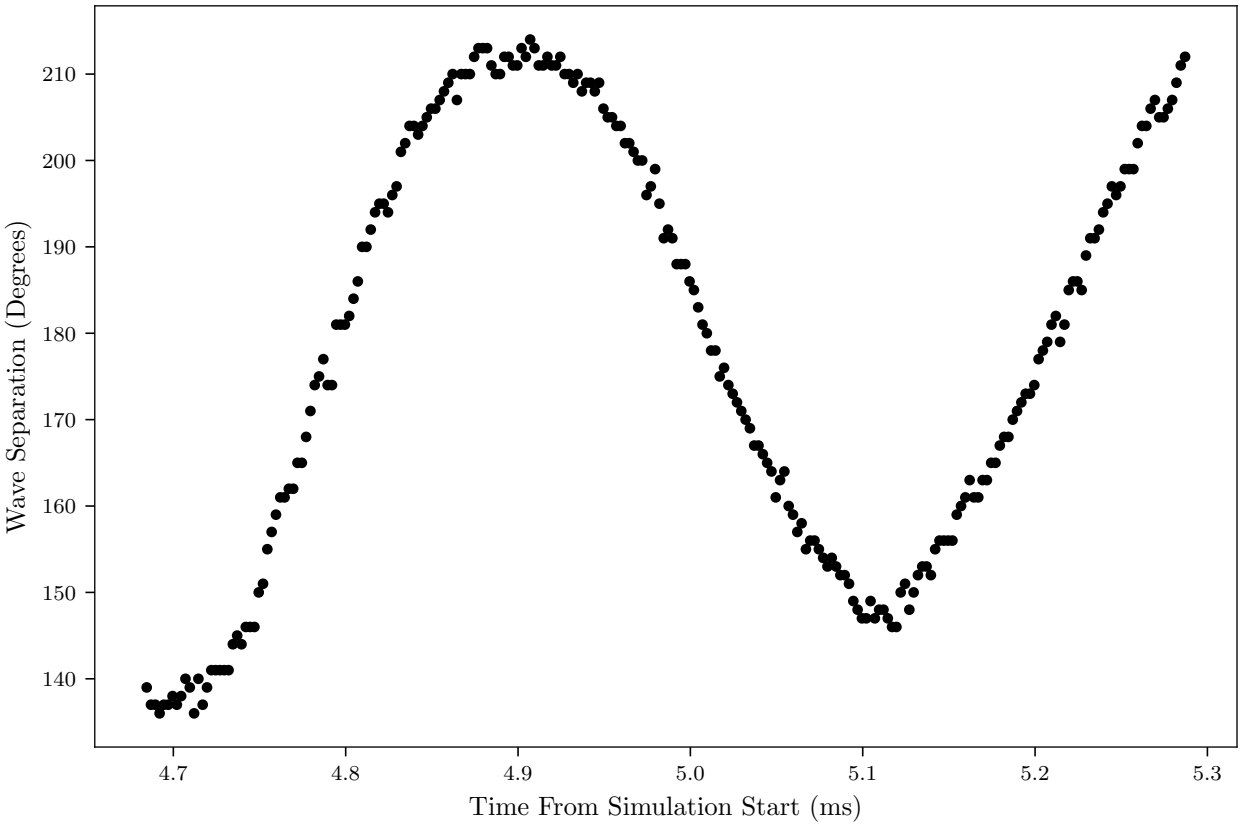

Figure 3.12: Angular separation between waves, with instantaneous wave positions evaluated as in Fig. 3.8.

Figure 3.13: Snapshot of pressure in the exhaust at a simulation time of 5.08 ms from simulation start, 1.18 ms from being manually set to 0.12 MPa.

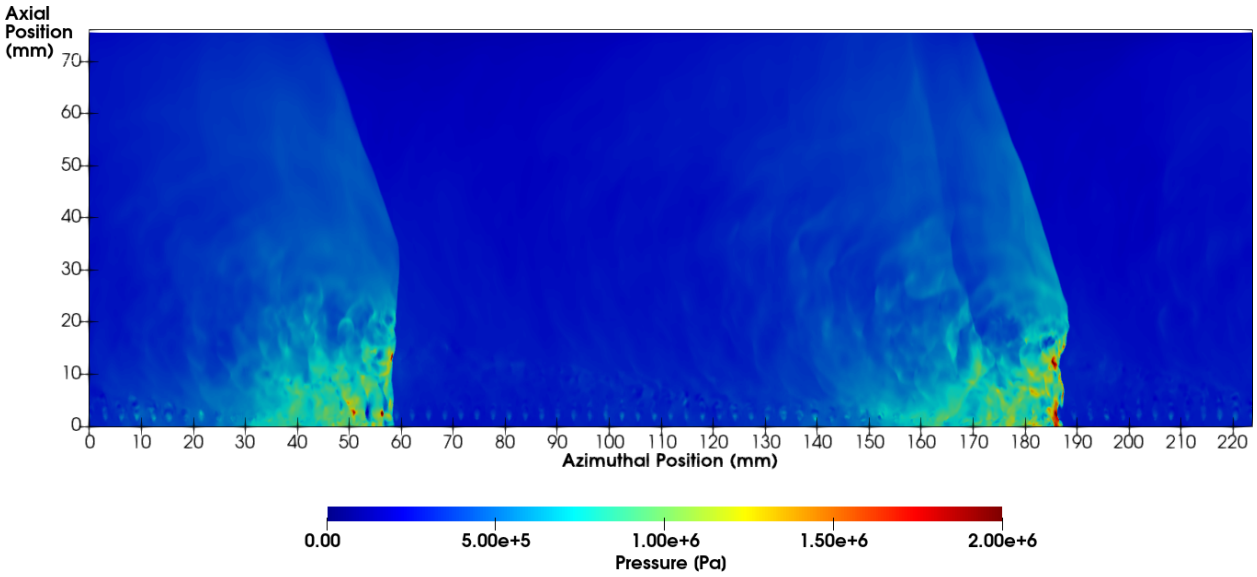

Figure 3.14: Instantaneous snapshot of pressure in the chamber, shown at the center-channel radius of 35.6 mm at a simulation time of 5.08 ms from simulation start.

3.3.1 Field Snapshots

A visualization of the pressure inside the chamber is shown in Fig. 3.14, the unwrapped cylinder corresponding to the middle of the combustion channel (a radius of 35.6 mm). The injection plane in Fig. 3.14 is the bottom surface, with fuel injected from bottom up, as is the case in the two-dimensional idealization in Fig. 1.8.

The shock structure was largely as predicted in the two-dimensional model: near injection, where the waves were fed by unburnt propellant, two detonation structures travelled azimuthally around the annulus (left-to-right in Fig. 3.14. These detonation were essentially perpendicular to the injection plane, with wrinkling suggestive of triple points in a detonation cellular structure. Further from injection, the detonation curved into an oblique shock where there was no fresh propellant to feed the wave. The galloping behavior is evident in Fig. 3.14 as an asymmetry between the two waves, most notably in a height difference.

Instantaneous visualizations of temperature, as in Fig. 3.15, show some of the limitations of premixed conceptualizations of RDREs. Although the general form of the fill region in front of the wave was the triangular shape expected by premixed models, there existed

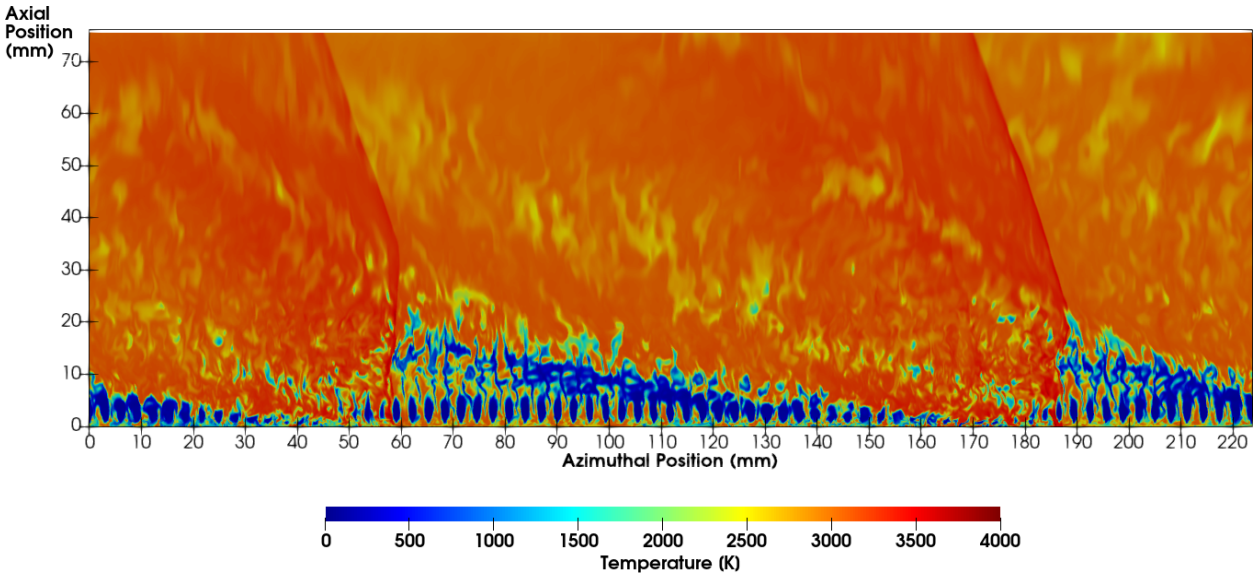

Figure 3.15: Instantaneous snapshot of temperature in the chamber, shown at the center-channel radius of 35.6 mm at a simulation time of 5.08 ms from simulation start.

high-temperature burnt pockets between each injector pair. This is further indicated in Figs. 3.16 and 3.17, which show that the cold pockets corresponded to regions of unburnt reactant. The non-premixed injection also meant that regions near the injection plane were less mixed than the regions further downstream, and even as the detonation passed there remained low-temperature propellant in the near-injection region. The passing of the wave did eventually cause these pockets of reactant to mix and burn, with the disappearance of the low-temperature pockets lagging three-four injectors behind the leading shock. This unburnt region seemed to broaden the high pressure post-detonation zone, leading in the right wave of Fig. 3.14 to a secondary detonation/shock structure behind the leading wave.

The heat release field of Fig. 3.18 tells largely the same story as the temperature field. As expected for a detonation, a large amount of the heat release corresponded with the traveling pressure shocks. Burning also occurred in the regions where low-temperature reactant encountered high-temperature products, with flame-holding in the low-pressure fill region corresponding to parasitic deflagration. A small amount of heat release was present throughout the high-pressure region.

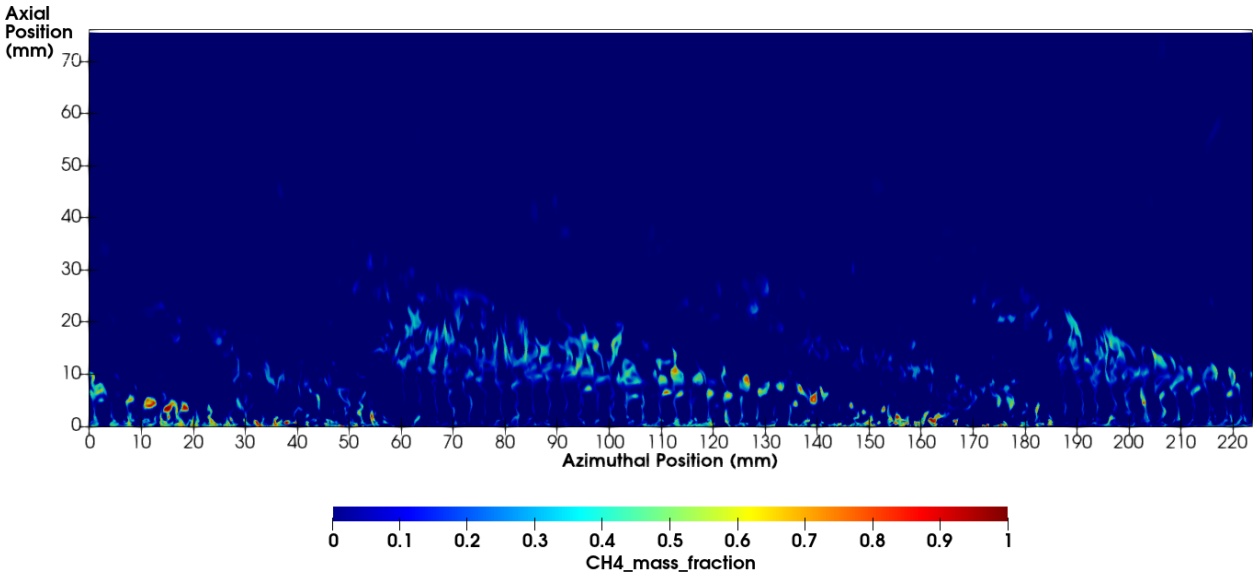

Figure 3.16: Instantaneous snapshot of CH_4 in the chamber, shown at the center-channel radius of 35.6 mm at a simulation time of 5.08 ms from simulation start.

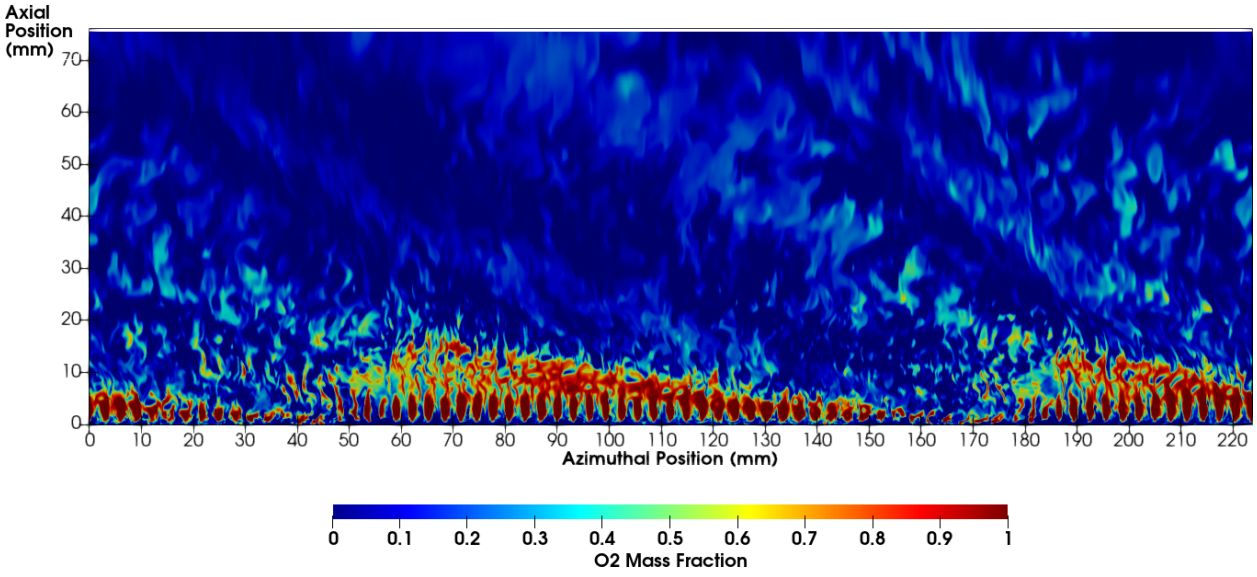

Figure 3.17: Instantaneous snapshot of O_2 in the chamber, shown at the center-channel radius of 35.6 mm at a simulation time of 5.08 ms from simulation start.

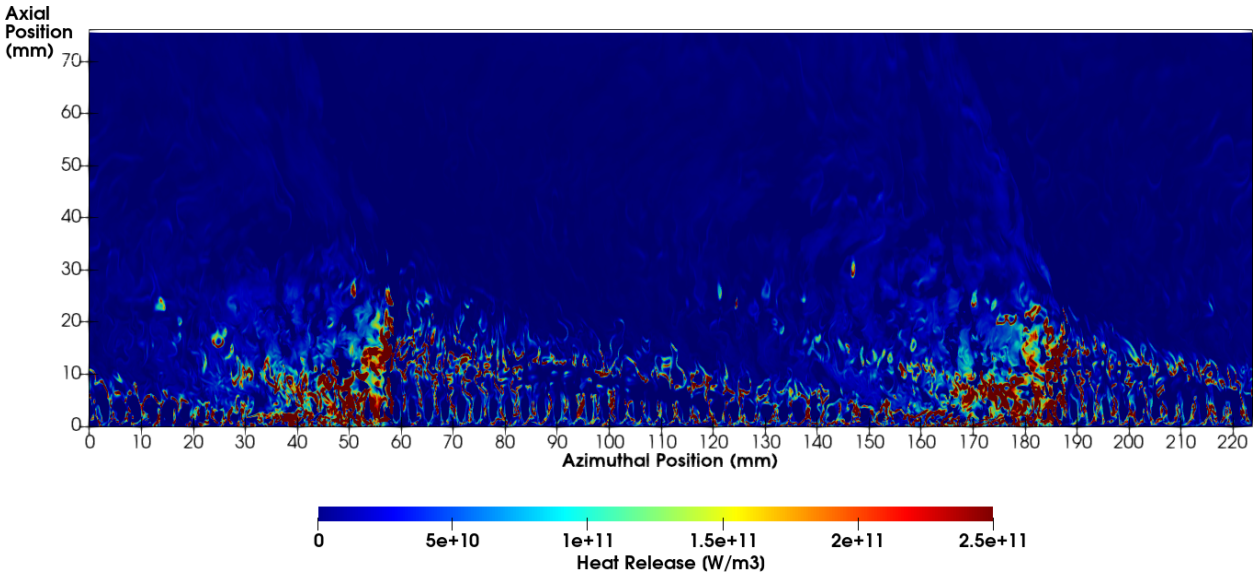

Figure 3.18: Instantaneous snapshot of pressure in the chamber, shown at the center-channel radius of 35.6 mm at a simulation time of 5.08 ms from simulation start.

The reaction zone behind the detonation – but near injection – was quite broad, coinciding with the regions of unburnt reactant evident in 3.15. There also existed a band of heat release behind both waves, coinciding with the high-methane region shown in Fig. 3.16. This band was likely due to an uneven blocking of injection, with fuel injection recovering sooner than oxygen injection. The result was a region of fuel-rich combustion following the passing of the wave.

Axis-normal snapshots of pressure and temperature, for the same instant in time, are shown in Fig. 3.19. With the way the images are oriented, the leftmost wave in the unwrapped-cylinder images corresponds to the wave on the left in the axis-normal representation. In general, the fields shown in Fig. 3.19 are as suggested by Fig. 3.14 and Fig. 3.15: lower pressure in front of the detonation–shock structure, with striated pockets of unburnt reactant in front of the waves. However, there the axis-normal representation shows that there was significant radial variation in the flow at this height, with cold reactants present only near the inner wall of the annulus. This meant that the detonation structure, as indicated by the large pressure ratio, travelled primarily along the inner radius.

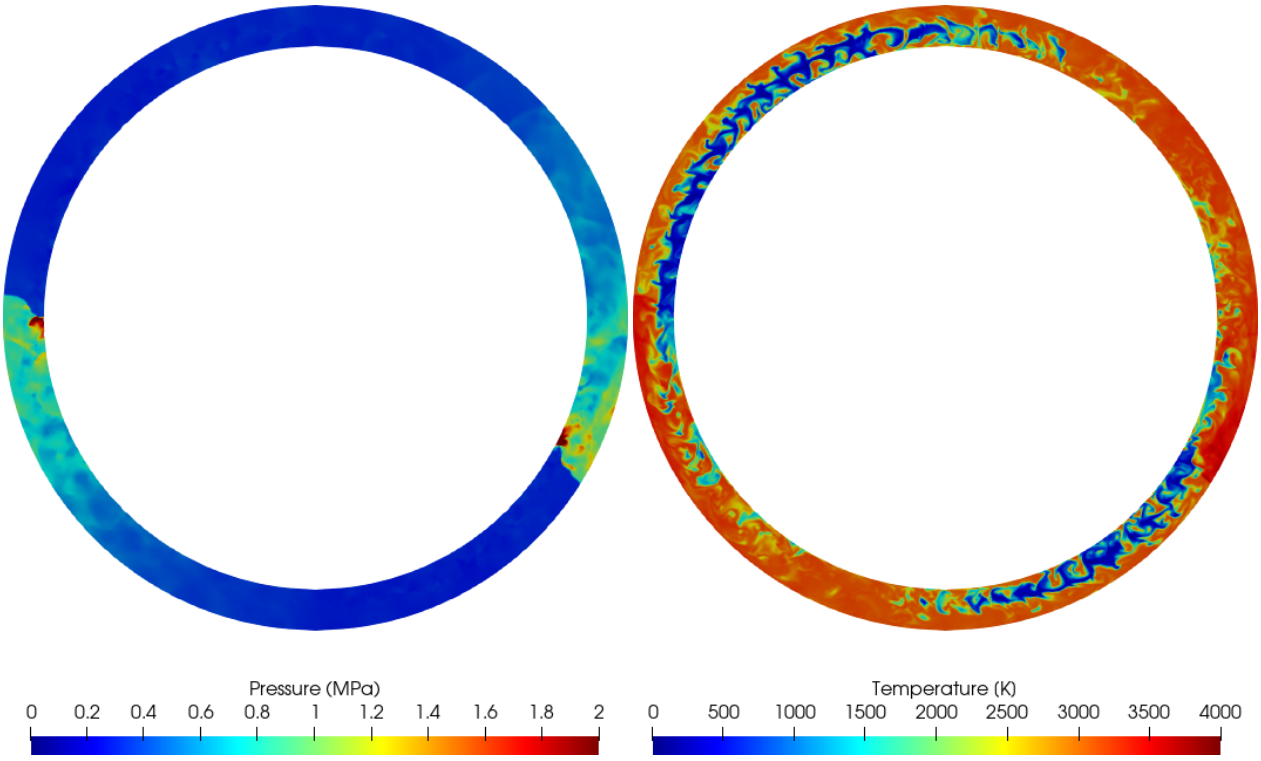

Figure 3.19: Instantaneous snapshot of pressure and temperature, in the chamber, shown for an axis-normal slice at a distance 9 mm from the injection plane, at a simulation time 5.08 ms from simulation start.

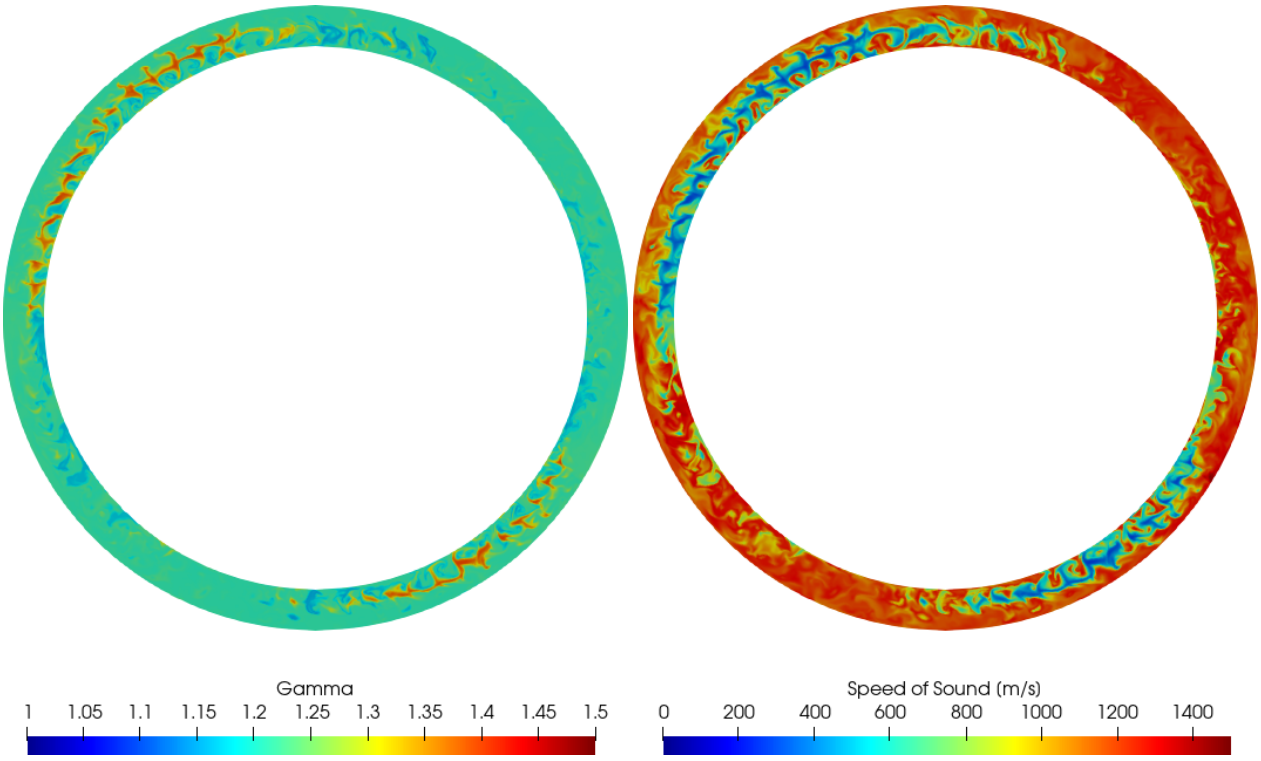

Figure 3.20: Instantaneous snapshot of ratio of specific heats, γ, and speed of sound in the chamber, shown for an axis-normal slice at a distance 9 mm from the injection plane, at a simulation time 5.08 ms from simulation start.

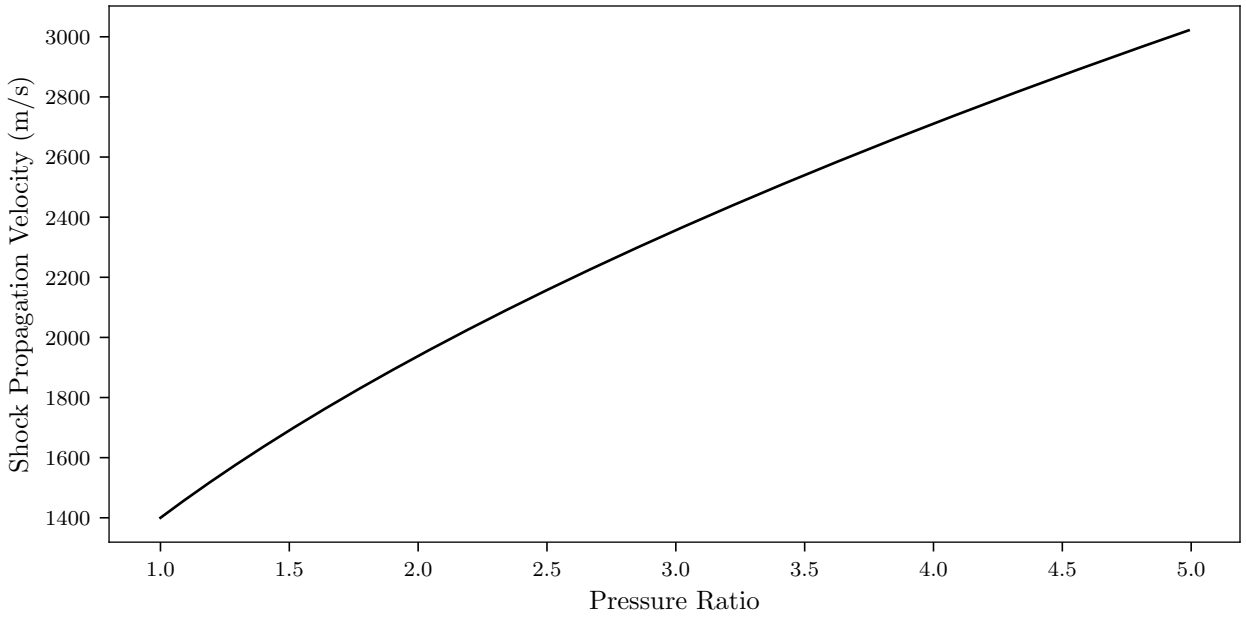

Figure 3.21: Velocity of a planar shock wave, traveling into quiescent flow with $\gamma = 1.2$ and speed of sound of 1400 m/s.

The pressure field also shows that the detonation portion of the structure along the inner wall lagged behind the shock near the outer wall. Although initially unintuitive, the relation can be understood by considering the difference in speeds of sound between the reactant and hot product region. As the detonation's shock travelled into the portion of the channel without reactant, it accelerated due to the increased speed of sound in the outer region, as in Fig. 3.20. The acceleration can be considered in the context of flow velocity for a traveling shock [14]:

$$W = a_1 \sqrt{\frac{\gamma + 1}{2\gamma} \left(\frac{p_2}{p_1} - 1 \right) + 1} \tag{3.1}$$

where W denotes the shock velocity, a_1 the speed of sound in the fluid the shock is traveling into, and $\frac{p_2}{p_1}$ the pressure ratio associated with the shock. Measurements of pressure near the outer wall, as in Fig. 3.22, suggest the pressure ratio of the shock ranged between 2 and 5 in the outer region.

Using the values of Fig. 3.20 to suggest a representative sound speed of 1400 m/s and

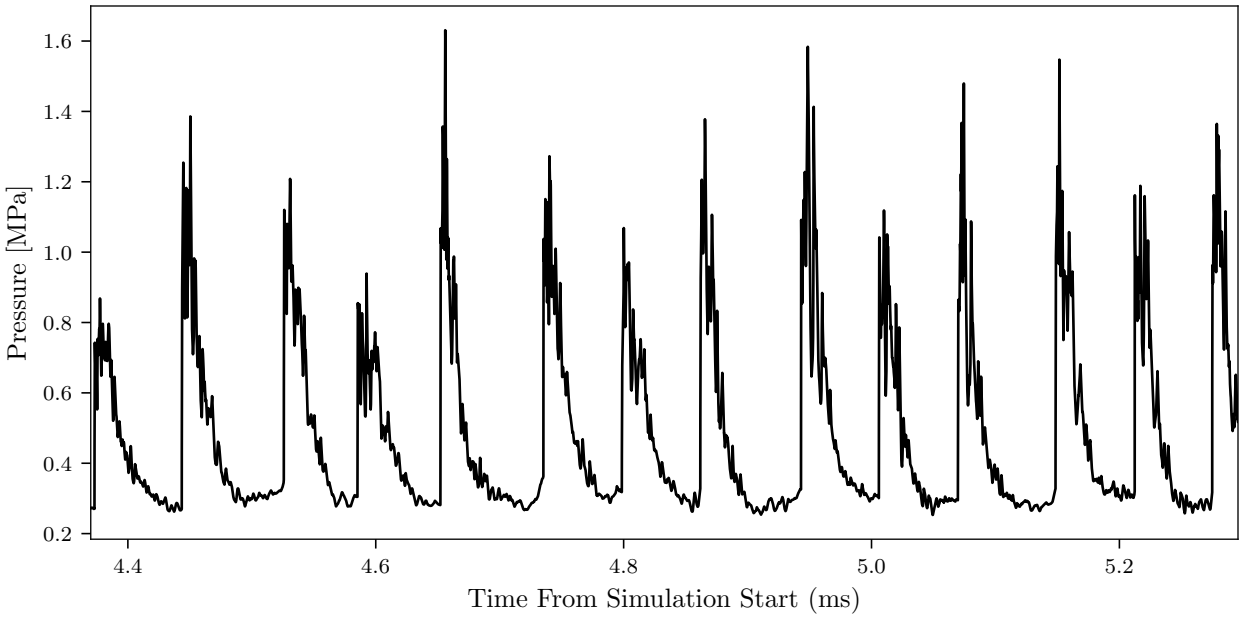

Figure 3.22: Pressure in a simulation cell, at a location 8.89 mm downstream of injection, and 0.01 mm from the outer wall.

product γ of 1.2 in the outer region, the velocity of the non-detonative shock can be estimated as in Fig. 3.21. The initial strength of the wave was enough to cause the wave in the outer region to lead ahead of the wave near the inner wall. However, without detonation reactions to feed the wave, the shock velocity decelerated as it travelled further from the detonation, resulting in a single structure moving at the same rate around the annulus.

3.3.2 Pressure Measurements

Experimental measurements are typically taken inside the chamber of an RDRE using capillary-tube attenuated pressure measurements: the pressure probe is placed at one end of a long sealed tube, and the other end of the tube is placed in the chamber's instrumentation port. With a large enough ratio of length over width in the tube, the chamber's pressure fluctuations are attenuated before being read by the sensor [92]. It's the resultant measurement of average pressure that is quoted as the chamber's CTAP measurement.

In order to extract an analogous measurement from the simulation, the pressure inside

the chamber near the outer wall was considered. An example of this form of pressure signal is plotted in Fig. 3.22, taken at the approximate location of one of the experimental CTAP instrumentation ports. Each passing shock caused a large steep-fronted increase in pressure, which then decayed until the arrival of the next wave. In order to relate this signal to experimental CTAP measurements, the signal was time-averaged. This simple time-average is analogous to a perfect CTAP measurement, with a tube length much larger than width and a measurement taken for a long test. Experimental measurements, with tube lengths on the orders of a meter, are likely close to these idealizations [93].

3.3.3 Wave Velocities

There are several experimental approaches to measuring wave velocities. When the number of waves is known, an average velocity v can be extracted from the Fourier transform of a pressure measurement, such as from a microphone near the engine. This extracts an operational frequency f, which can then be converted to velocity using the known annular radius:

$$v = \frac{f 2\pi r}{N} \tag{3.2}$$

where N is the number of waves. Note that equation 3.2 refers to a single radius r; for the experimental comparisons in this study the centerline radius was used, r = 35.6 mm. Choosing a different radius, such as the inner or outer radius for the channel, can shift the measured value of wavespeed 10% in each direction for this geometry. The same approach can be directly applied to localized pressure measurements in the simulation, such as those shown in Fig. 3.22. However, the computational expense of large simulations limits the number of periods that can measured; for a fast Fourier transform (FFT), the bin width is related to the sampling frequency and the number of samples:

$$\text{FFT bin width (Hz)} = \frac{\text{Sampling frequency (Hz)}}{\text{Number of samples}} \tag{3.3}$$

For 1 ms of simulated time and a simulation timestep of 1 ns, the frequency bin width of this approach would be 1 KHz, corresponding to a velocity spread on the order of 100 m/s for this engine. As a consequence, the computational expense of these high-fidelity simulations means that foregoing the Fourier transform, and measuring operational periods according to time between wave passes is more precise. However, when the wave velocity is not constant, as in the galloping phenomenon observed here, it is hard to account for the unsteady velocities using only peak-to-peak measurements.

θ-t representations of the chamber, as in Fig. 3.11, or in experimental high-speed photography of the chamber exit, allow for extraction of the wave velocities even when the number of waves and wave directions is more difficult to determine. A 2D Fourier transform of a θ-t representation of the chamber allows for measurements of the number of waves in each direction, as well as the dominant frequency associated with each direction [89]. The experimental values in table 3.1 were calculated using this method. Simulation θ-t diagrams, such as in Fig. 3.11, can be analyzed in the same way to extract the number of waves in each direction; however, the simulation sampling rate again means that measuring velocity using the FFT would again not be as precise as desired.

Fortunately, the simulation data presented in θ-t diagrams can be used in a separate way to calculate velocities. Because the angular positions can be calculated as in Fig. 3.8, the locations can be used to directly calculate velocities. Two measurements of wave location to within a degree, spaced 250 μs apart, provides a measurement of average velocity with a precision on the order of 1 m/s. However, the real benefit of measuring instantaneous wave positions is the ability to use position measurements for a range of times, when the average velocity can be measured using a linear fit on the coordinate measurements.

3.3.4 Thrust

For the purposes of comparing across simulations, the MVP effort defined thrust as specifically a metric of combustor performance. In order to do this, the volume of interest for considering conservation of momentum was defined to extend from injection to the exit

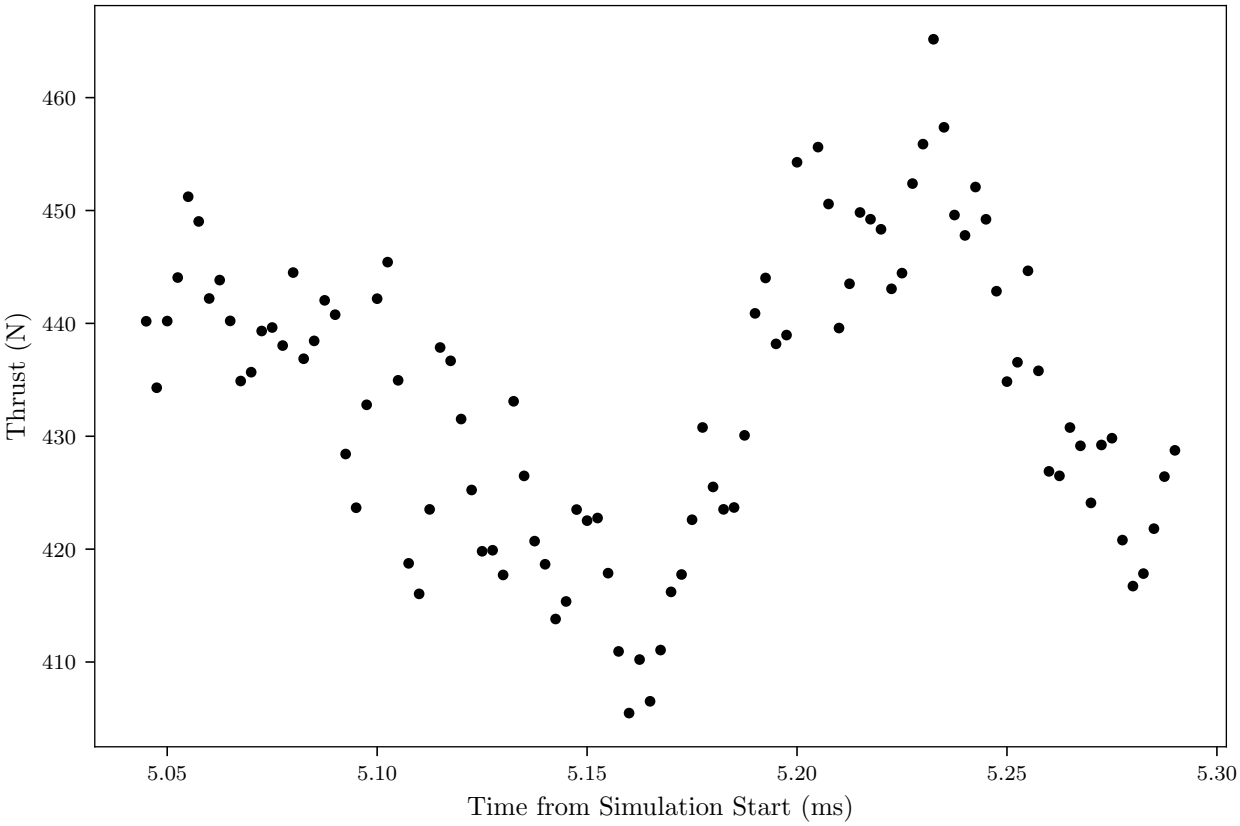

Figure 3.23: Instantaneous thrust measurements, according to equation 3.4.

plane of the combustor:

$$\text{Thrust} = \int_{\text{Chamber Exit}} (\rho \mathbf{u}\mathbf{u} \cdot d\mathbf{A} + p\, d\mathbf{A}) - \int_{\text{Injectors}} (\rho \mathbf{u}\mathbf{u} \cdot d\mathbf{A} + p\, d\mathbf{A}) \tag{3.4}$$

In equation 3.4, the directions of the two surface normals are both defined in the same direction. This representation means that the thrust is produced by the combination of the viscous drag on the chamber walls and the force due to pressure on the backstep at the injector plane. The definition is primarily useful for comparing predicted thrust between simulations, by considering only what's happening within the chamber. It does not work as a direct comparison to experiments, since in this case the definition does not take into account any of the pressures on the outer surface of the engine or the thrust due to cold-flow of the pressurized injection.

The form of equation 3.4 does not include any time-varying terms, and so the measurement must be taken as an average in time. Instantaneous measurements of thrust calculated in this manner are shown in Fig. 3.23, which gives a sense of the spread in thrusts in time. Although the average thrust measurement over 0.25 ms is 433 N, there was a spread of more than 50 N in that time span.

3.3.5 Comparing with Other Groups

Several research groups have participated in the MVP workshop, and so it is possible to compare measurements from the simulation with both experimental results and other codes. Table 3.1 is a subset of the community that has simulated this engine, but shows that all simulation groups were able to sustain the two-wave operation that was seen experimentally. To my knowledge, no groups have observed sustained wave galloping, further suggesting that the effect may be part of a startup transient.

When compared to experiment, the simulations have all shown the same trend: reduced wavespeeds, with higher pressures and thrusts. It's currently unclear what caused the drop in simulation wavespeeds, or why they're so inconsistent between groups. One explanation

	Experiment	Simulation	U. of Michigan [66]	Argonne [87]	NETL [88]
Number of Waves	2	2	2	2	2
Wavespeed (m/s)	1810	1613*	1357	1511	1780
Pressure 1 (MPa)	0.38	0.47	0.48	0.42	0.44
Pressure 2 (MPa)	0.30	0.34	0.37	0.33	0.30
Thrust (N)	356	433	472	365	458
I_{sp} (s)	139	165	177	137	172

Table 3.1: Table comparing measurements taken from simulations conducted at a variety of institutions, as compared with experiment. Pressure 1 and Pressure 2 refer to CTAP measurements, taken at axial positions of 8.9 mm and 28.6 mm respectively. *:Average velocity in galloping regime

might be the choice of chemistry. All groups represented in Table 3.1 used FFCMy-12, which could be underpredicting wavespeeds due to some aspect of the engine regime. It was shown by Badillo-Rios that FFCMy-12 does a poor job of estimating ignition delay when compared to full mechanisms [94], which may be related to underpredictions in wave speeds. The wide spread in velocities could be tied in some way to the observed galloping behavior, but more investigation would be required to understand whether there's a connection.

The increased pressure may largely be due to the use of adiabatic wall conditions inside the engine for all listed simulations; the comparative consistency in the simulation results suggests that the increased pressure was not purely due to the overpressurization in exhaust manifold observed in this work, although it would be worth investigating how much the overall operation and pressure is affected by changes in engine backpressure. All groups saw higher thrust than the experimental values, but the thrust being calculated was not a direct comparison to experiment. Although the simulations from different groups appear to have vastly different thrusts, the thrusts as measured are actually within 10% of those predicted by the University of Michigan and NETL, which is on the same order as the oscillations in time shown in Fig. 3.23. The present predictions, as well as those from Argonne, are closer

to the experimental value of overall thrust. It's also important to note that the trends in measured and computed wavespeeds do not correlate with the trends in thrust, suggesting that the amount of non-detonative combustion, likely the parasitic deflagration in the fill region, varied among the simulations.

CHAPTER 4

Simulated Laser Absorption Measurements

The high frequencies associated with RDREs, as well as the temperatures and pressures involved, make it challenging to design diagnostics capable of extracting information from the chamber flowfield. High-speed cameras can be used to track chemiluminescence associated with various species, giving information on the number of waves and wave velocities. Frequency information can also be measured using a microphone near the engine, which – when coupled with image data – provides another measurement of wavespeed. Further chamber measurements tend to be time-averaged, such as capillary tube attenuated pressure measurements which give averaged measurements of pressure. The use of a thrust stand provides an overall thrust measurement, and when coupled with injection-system diagnostics can provide I_{sp} measurements of the engine – but thrust measurement timescales are usually on the order of an entire RDRE firing, and provide very little in the way of time-resolved information about the engine.

Recent advances in laser diagnostics have extended the range of both frequency and pressure that can be measured using laser absorption spectroscopy (LAS) [95]. These advances make it possible to measure temperatures, pressures, and species concentrations at the high temporal resolution that is required to capture the behavior of an RDRE during operation [96, 97]. The ability to measure temporally-resolved temperature, pressure, CO, and CO_2 in the exhaust of an RDRE, with MHz resolution, was demonstrated by the Spearrin Lab in 2019, as part of a collaboration between UCLA and the Air Force Research Laboratory (AFRL) [97, 98]. The engine used was the same geometry discussed in chapter 3, and so the simulation results can be directly compared to the experimental laser measurements.

Not only do temporally-resolved measurements of an operating RDRE provide valuable insights on their own into what is happening inside the combustion chamber, they can also be considered alongside simulation results. Simulation data contains information about the rest of the flowfield, and can be used to explain experimentally-observed phenomena; in the case of exhaust measurements, simulations can help to connect what was observed experimentally in the exhaust with what occurred in the upstream detonation-region of the engine. Further, the simulation results can help to show which regions of the engine are likely to fall within the capabilities of the diagnostic, and aid in the development of future experiments. Considered in the other direction, highly resolved experimental measurements help explore the limitations of current RDRE simulations, and directly assist the aims of the AIAA MVP effort.

4.1 Laser Absorption Theory

In order to directly compare simulation data with experimental laser measurements, it is necessary to know how the diagnostic would be expected to operate for a given simulation flowfield. This was accomplished by extracting "synthetic" laser measurements of the flowfield in the simulation, taking into account the variation in flowfield encountered over a single laser path. Two different models were used to represent the synthetic laser. The first approach calculated path integrals at instants in time to consider ideal measurements of the instantaneous flowfield. The second used the spectroscopic properties of the flow to estimate absorbances for specific wavelengths, directly modeling the absorption characteristics measured by an experimental laser. These synthetic absorbance measurements were then used the same way experimental measurements of absorbance would be used to extract flow properties [95, 97].

4.1.1 Ideal Laser Measurement

The end result of a laser diagnostic such as the one used experimentally is a measurement of flow properties based on the region of gas that interacts with the laser. The laser for this diagnostic was designed to target the absorbance of CO and CO_2, and so gives measurements of the amount of these species encountered by the laser's beam as the light travels between the laser and the sensor. As such, one targeted measurement is of the amount of species that is encountered – a molar density, e.g. of moles per meter^3, that is the result of a path-integration of the moles of the targeted species present in the gas. The average molar density $\bar{n_j}$ of species j taken with a laser path of length L then depends on the local molar density n_j by a direct integral relation:

$$\bar{n}_j L = N_j = \int_0^L n_j \, dl \tag{4.1}$$

Similarly, experimental measurements of temperature are based on the absorbance characteristics of the species, and so are again based on a species-weighted path-integration. For temperature T, the comparable measurement is an average (denoted $\bar{T}$):

$$\bar{T} = \frac{\int_0^L n_j T \, dl}{N_j} \tag{4.2}$$

The experimental diagnostics being targeted are interpreted as this sort of line integration, and so in regimes where the diagnostics are well established these forms of instantaneous integrations are sufficient to model a laser measurement. This can be taken advantage of in simulations, since N_j and $\bar{T}$ are both easy to calculate as derived quantities based on simulation species and temperature outputs. The largest difficulty in an instantaneous path integration approach is simply in saving the necessary data, since the large size of these 3D simulations can make saving and processing full datasets intractable at MHz resolutions. Fortunately, only a small physical region needs to be saved for a single linepath, and so it is possible to customize output for a targeted laser.

Wavenumber (cm^-1)	Transition	S (cm^-1/(molecule cm^-2))	E (cm^{-1})
2008.422	P(2,20)	1.149 $\times 10^{-28}$	5051.74
2008.525	P(0,30)	2.668 $\times 10^{-22}$	1901.13
2008.552	P(3,14)	2.877 $\times 10^{-32}$	6742.87

Table 4.1: Parameters for calculating linestrength of targeted transitions of $^{12}C^{16}O$ at reference temperature 296 K according to equation 4.4 and as tabulated in HITEMP [99].

4.1.2 Beer-Lambert Absorbance Model

Although a synthetic laser approach following equations 4.1 and 4.2 is often enough to model an experimental diagnostic, the instantaneous integration approach cannot capture temporal effects caused by features with timescales similar to that of the laser sampling rate, and do not provide insight into the validity of a specific diagnostic design for a new regime. In order to closely consider a specific diagnostic design, instead of assuming perfect measurements of the integrated flow field, it is possible to create a more physically-motivated model by considering the Beer-Lambert law, which relates the absorbance α of a laser at wavenumber ν traveling through a species j due to transition i :

$$\alpha_{i,j}(\nu) = -\log\left(\frac{I_t}{I_0}\right) = \int_0^L n_j S_{i,j} \varphi_{i,j}(\nu)\, dl \tag{4.3}$$

where I_0 is initial intensity, I_t is transmitted intensity after traveling through the gas, n_j is the molar density of species j, S is the linestrength of transition i, and φ is the lineshape function. The simulation tracks species concentrations, and so n_j can again be directly taken from simulation data. For the wavenumber being considered, the derived quantities of φ and S can be calculated for each transition, and the absorbance due to each transition can be calculated as in equation 4.3. Although experimentally the individual transition absorbances would be separated out by fitting a Voigt profile to measured transmittance, the synthetic laser calculates the absorbance for each transition directly.

The linestrength S is a function of temperature, and has been tabulated for a number of

species and regimes, making it straightforward to calculate as a derived quantity in the simulation. The high-temperature spectroscopic absorption parameters (HITEMP) database, maintained at the Harvard-Smithsonian Center for Astrophysics, was used for this study [99]. HITEMP models linestrength as a function of temperature T:

$$S_i\left(T\right) = S_i\left(T_{ref}\right) \frac{Q\left(T_{ref}\right) \exp\left(-c_2 E_i/T\right)}{Q\left(T\right) \exp\left(-c_2 E_i/T_{ref}\right)} \frac{1-\exp\left(-c_2\nu/T\right)}{1-\exp\left(-c_2\nu/T_{ref}\right)} \tag{4.4}$$

where Q is the total partition sum as a function of temperature (which is also tabulated in literature for relevant isotopologues), E_i denotes energy of the lower state, T_{ref} is a reference temperature (296 K for HITEMP), and c_2 is the second radiation constant,

$$c_2 = 1.43877 \text{ cm K} \tag{4.5}$$

Calculating lineshape φ from the simulation is less straightforward than evaluating linestrength, as φ depends on temperature, pressure, and composition at each location. In particular, the lineshape function can be modeled as a Voigt profile, which requires taking the convolution of collisional and Doppler broadening effects (referred to in the following as L and G, respectively):

$$\varphi_{i,j}\left(\nu\right) = \int_{-\infty}^{+\infty} G(x) L(\nu - x)\, dx \tag{4.6}$$

Assuming a Maxwellian distribution, Doppler broadening G(x) is a Gaussian centered at the transition linecenter $\nu_{0,i}$, with a full width at half maximum, $\Delta\nu_G$, dependent on temperature:

$$G_i(x) = \frac{2}{\Delta\nu_G}\sqrt{\frac{\log(2)}{\pi}} \exp\left[-4\log(2)\left(\frac{\nu-\nu_{0,i}}{\Delta\nu_G}\right)^2\right] \tag{4.7}$$

$$\Delta\nu_G = \nu_{0,i}\sqrt{\frac{8kT\log 2}{mc^2}} \tag{4.8}$$

where k is the Boltzmann constant, m is the particle's mass, and c is the speed of light. Note that this neglects the Doppler shift that stems from the bulk motion of the fluid, requiring flow to be perpendicular to the laser path.

The collisional broadening effect is modeled as a Lorentzian, with a width that depends on local pressure, temperature, and composition. Specifically,

$$L(\nu) = \frac{1}{2\pi} \frac{\Delta\nu_L}{(\nu - \nu_{0,i})^2 + \left(\frac{\Delta\nu_L}{2}\right)^2} \tag{4.9}$$

where

$$\Delta\nu_L = 2p\gamma_{j-mix} \tag{4.10}$$

$$= 2p \sum_s X_s \gamma_{j-s} \tag{4.11}$$

The broadening coefficients γ_{j-s} depend on temperature, and are modeled according to a power law. CO broadening coefficients for collisional partners CO, H_2O, N_2, and O_2 are tabulated in Hartmann et al. [100], and γ_{CO-H2} is tabulated in Sur et al. [101]. Coefficients for collisional partners present in the simulation, but which we were unable to find in the literature, were modeled according to the N_2 optical collision diameter scaling approach described in Nair et al. [97].

The Voigt convolution described in equation 4.6 is the most computationally expensive part of this form of synthetic laser. For the present work this calculation was done using the Fadeeva package built into scipy [90, 102], but could likely be sped up using a less exact numerical approximation should the application call for it. Fortunately, since these laser measurements are only required for locations defined by the laser path being looked at, it is not prohibitively expensive to run these calculations even in large simulations.

The wavenumber ν for which absorbance is measured along the laser path is swept in time, with a period dictated by the desired measurement sampling rate and an amplitude large enough to capture the broadened lineshape. For the simulated model, a sinusoidal sweep with a period of 1 μs and an amplitude of 0.3 cm^{-1} were used. Although an experimental laser measurement must consider the relation between voltage, intensity, and wavenumber, but the wavenumber can be directly set when taking synthetic laser measurements of a simulation. This gives, for each transition, the absorbance as a function of wavenumber where the wavenumber is a function of time $\alpha_{i,j}(\nu)$, and directly models the effect that the

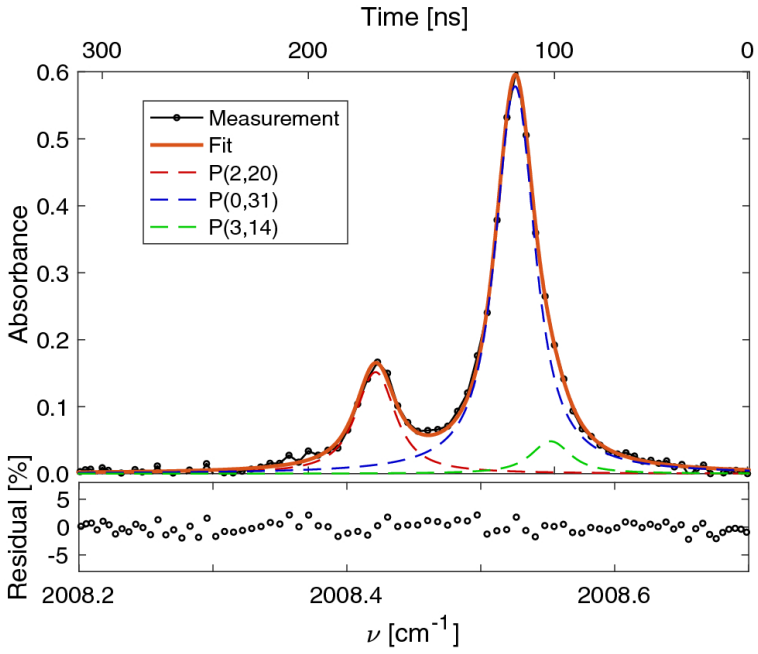

Figure 4.1: Absorbance for a representative wavenumber sweep, measured in the exhaust of an RDRE by Nair et al. [97].

sampling rate timescale has on the measurement. The overall absorbance at an instant in time for the simulation, as a function of wavenumber, is then the sum of the absorbances for all transitions being considered.

Once the absorbances were calculated, the procedure for taking measurements of temperature, pressure, and species concentration were directly analogous to what would be done experimentally, such as is described in Nair et al. [97]. The first step was to fit the measured overall absorbance to Voigt profiles for the targeted transitions. An example of an experimental absorbance measurement targeting the transitions listed in table 4.1 is shown in Fig. 4.1, for which estimates of temperature, Voigt halfwidth, and peak wavenumber were converged using an iterative procedure [97]. In a simulation-based absorbance measurement there is no uncertainty in the peak wavenumber for each absorbance line, and initial guesses can be based on the simulation data. These differences make the fitting step much faster using simulation data than when processing experimental measurements, but have the side effect that simulation-based absorbance measurements can be fit even in regimes that would

be difficult to match accurately using experimental data. This is a consequence of using a model to fit data generated using the same model.

Once the overall absorbance has been fit to the expected Voigt profiles, the absorbance areas A_i associated with each profile are known:

$$A_{i,j} = \int_{-\infty}^{+\infty} \alpha_{i,j}(\nu)\, d\nu = \int_{-\infty}^{+\infty} \int_{0}^{L} n_j S_{i,j} \varphi_{i,j}(\nu)\ dl\, d\nu \tag{4.12}$$

Relating these absorbances to the desired physical quantities requires the assumption that the average of the linestrengths over the path is the same as the linestrength of the average temperature:

$$\frac{\int_0^L n_j S\, dl}{N_j} = S(\bar{T}) \tag{4.13}$$

Equation 4.13 holds whenever the linestrength S is related linearly to the temperature within the linepath. Using the assumption of equation 4.13, and that $\int_{-\infty}^{+\infty} \varphi(\nu)\, d\nu = 1$ by definition, reversing the order of integration in equation 4.12 allows the simplification:

$$A_{i,j} = N_j S_{i,j}(\bar{T}) \tag{4.14}$$

Linestrengths are tabulated in HITEMP, and so the ratios of absorbance areas for a given $\bar{T}$ are related by a known function R:

$$R(\bar{T}) = \frac{S_{1,j}(\bar{T})}{S_{2,j}(\bar{T})} = \frac{A_{1,j}}{A_{2,j}} \tag{4.15}$$

The measurement of temperature $\bar{T} = R^{-1}(A_{1,j}/A_{2,f})$ then also gives the measurement of column density for species j: $N_j = A_{i,j}/S_{i,j}(\bar{T})$. Pressure can also be measured, using the width of a Voigt profile according to equation 4.10.

4.2 Laser Paths

The simulation geometry and flow conditions used for laser measurements of the RDRE field were the same as those discussed in chapter 3. However, there were a couple of differences

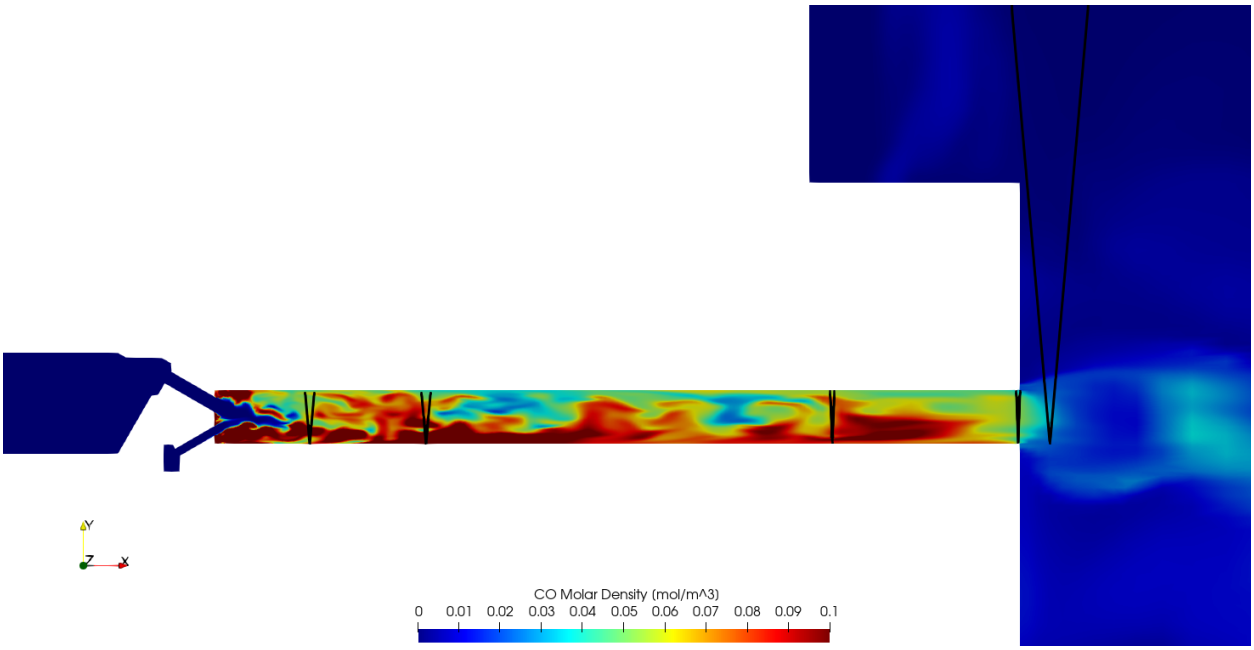

Figure 4.2: Cross-section of simulated chamber, indicating with black lines the locations of laser paths saved at runtime. A sample instantaneous CO molar density field is also shown in simulation cross-section.

in the experimental setup. The annulus centerbody was extended, in order to provide a reflecting surface for the laser; the physical extension was not included in the simulation. In order to minimize the effect of atmospheric CO interfering with the laser, N_2 was blown between the laser emitter and the chamber exhaust in the experiment. In the simulation, the addition of N_2 was approximated through the use of pure nonreacting N_2 in the co-flow inflow, so that all CO present in the simulated plume originated in the engine exhaust.

In order to take measurements using the absorbance-based synthetic laser, data along the laser path was saved at each simulation timestep – a much higher rate than would be practical to save full datasets. As such, paths of interest were defined prior to running the simulation. The pre-defined paths used for calculating laser measurements from the simulation are indicated in Fig. 4.2.

The experimental laser was most closely approximated by a path centered 3 mm downstream of the chamber exit, with a half-angle of 5° – the rightmost path in figure 4.2.

However, the lack of reflective surface meant that laser path reflection was not associated with a wall boundary. It is hoped that future experiments will move the laser location further upstream inside the engine, and so data at further locations inside the chamber were also saved. A laser path 58 mm from injection matches the geometry of an already-designed experimental setup, with a half-angle of 2.4°. Additional data were saved in the detonation region, with laser paths 9 mm and 20 mm from injection both using a half-angle of 5°.

For this study the laser was assumed 1-dimensional, with no effects caused by beam thickness. The absorbance model was only calculated for targeted measurements of CO. However, with the simulation data saved the study could be extended in future to consider other species, as well as other sweep patterns and sampling rates.

4.3 Exhaust Measurements

Experimental LAS measurements of the engine exhaust from Nair et al. [97] are shown in Fig. 4.3. Wave-passage events are most clearly seen in visible in measurements of pressure, where steep-fronted shocks are evident. Measurements of temperature are much less dominated by the shock structure, with many fluctuations that resemble noise but have much larger magnitude than the experimental uncertainty. Similarly, although CO column densities do show rises at the shock front, corresponding to the increase in density, a number of secondary structures are observed in the experimental data. One such structure is the second peak that appears in CO column density, occurring between each passing wave.

4.3.1 Full-Path Measurement

The full-length path centered 3mm from the chamber exit, as in Fig. 4.2, was the location measured in the simulation most directly analogous to the experimental measurements shown in Fig. 4.3. However, synthetic laser measurements in the simulation for the exhaust path, as shown in Fig. 4.4, demonstrate issues that arose with the exhaust laser path. The two synthetic laser models showed a major discrepancy in this location between absorbance-

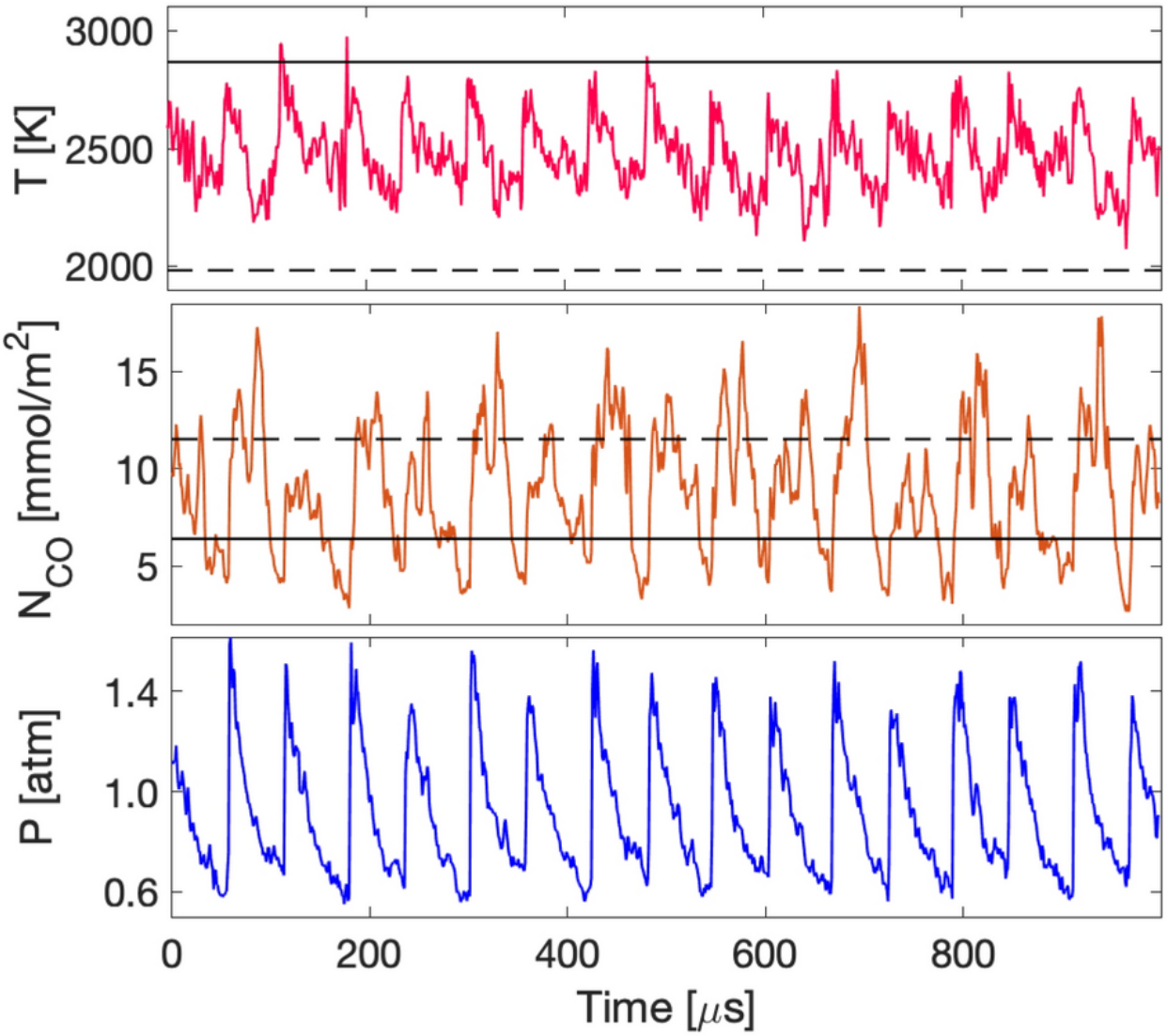

Figure 4.3: Experimental laser measurements of temperature, pressure, and CO column density at the engine exhaust, from Nair et al. [97]. Horizontal lines indicate predicted measurements for an ideal detonation expanded to atmospheric, assuming either frozen (dashed) or equilibrium (solid) flow.

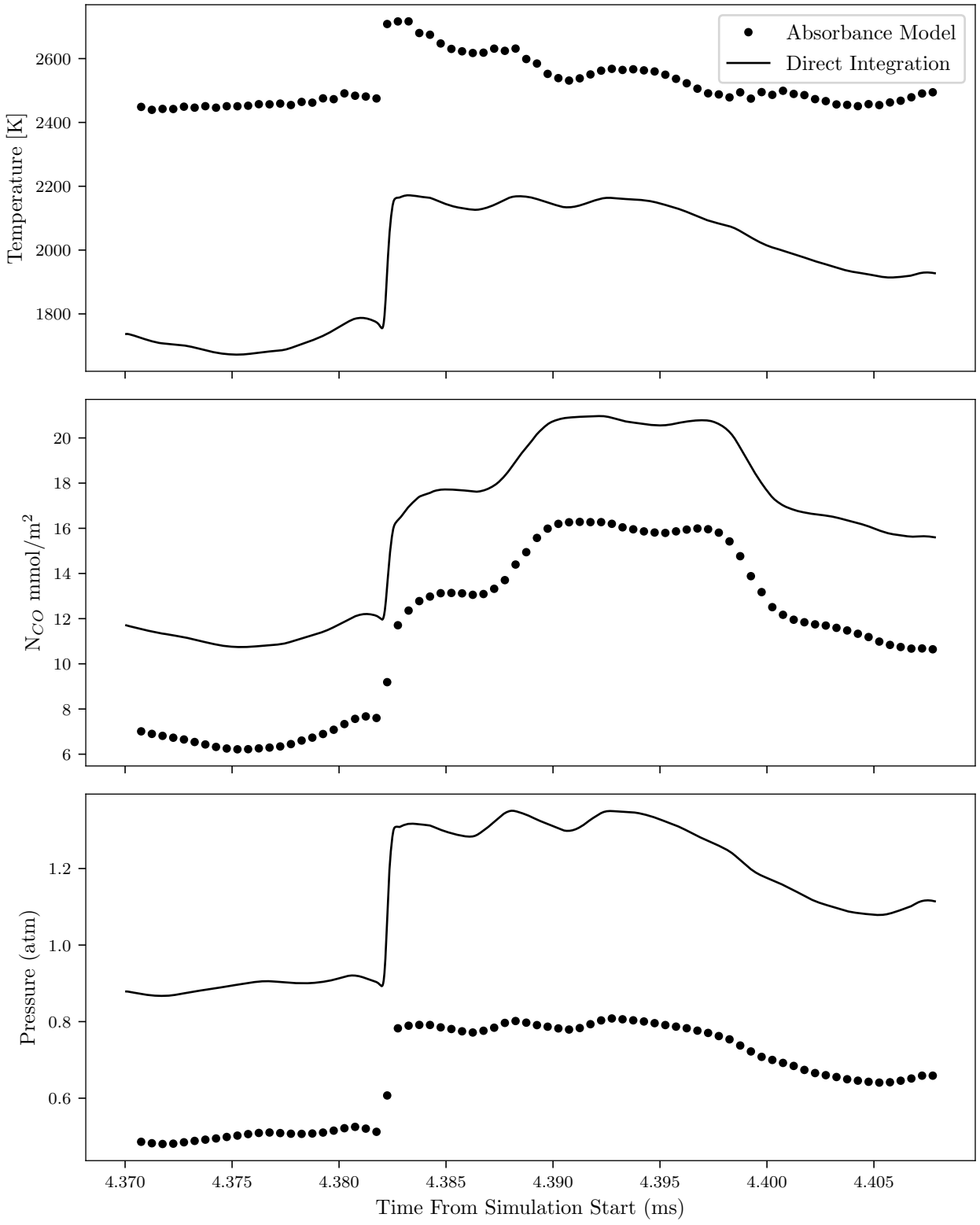

Figure 4.4: Synthetic laser measurements of temperature, CO column density, and pressure in simulation exhaust, with path intersecting outerbody recirculation zone. Results are shown for the two approaches to modeling synthetic laser measurements.

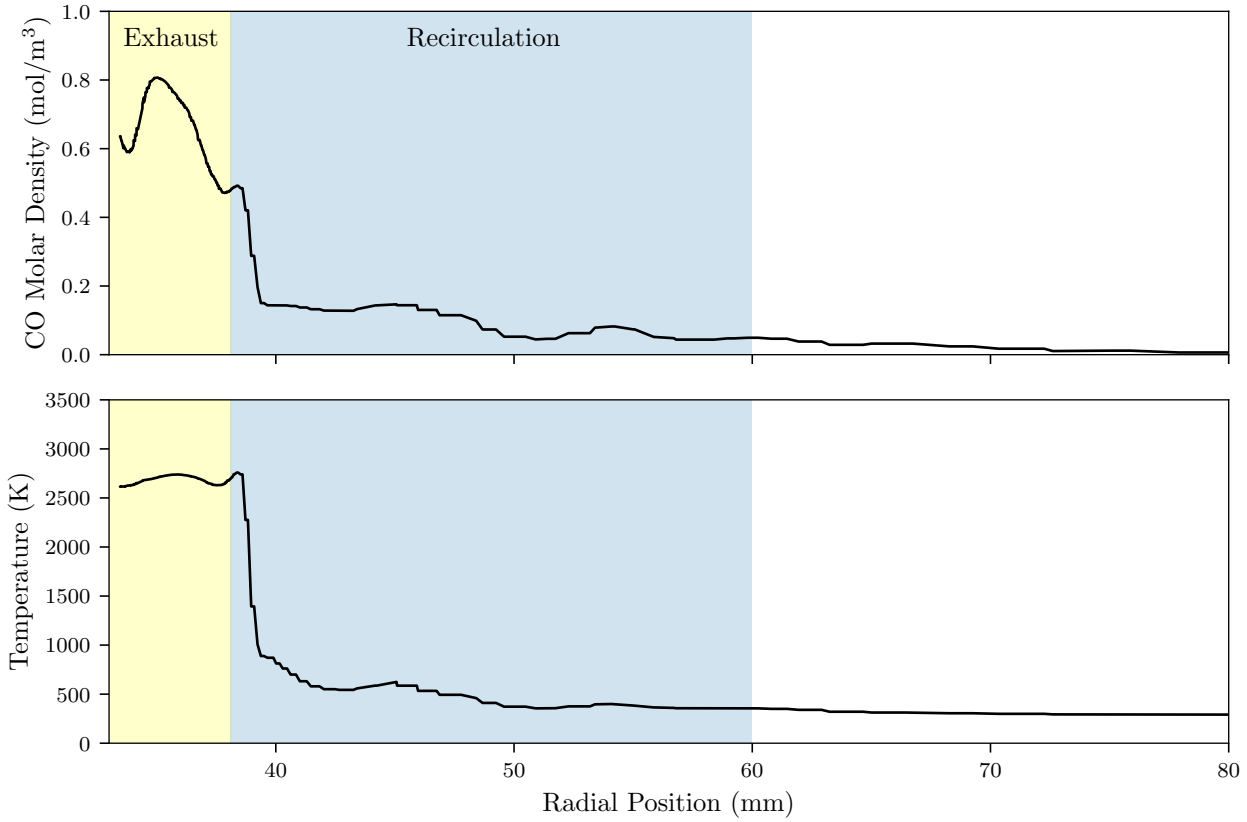

Figure 4.5: Instantaneous values of temperature and CO molar density along a single leg of the exhaust laser. Post-channel exhaust radius designated by yellow region, region behind engine outerbody indicated in blue.

based measurements, as described in section 4.1.2, and direct species-weighted integration as in section 4.1.1.

The discrepancy in Fig. 4.4 can be understood by considering the regions of the flow with which the path intersected. As shown in Fig. 4.5, there existed a region adjacent to the engine outerbody that contained a significant amount of CO. The presence of CO meant that this recirculation zone was detected by both types of synthetic laser, and increased the integrated measurements of pressure and CO column density.

The recirculation zone, located at a radial distance between 38 mm and 60 mm from the centerline, was at a lower temperature than the exhaust. Consequently, integrated measurements of temperature were affected by this low-temperature region. The low temperature

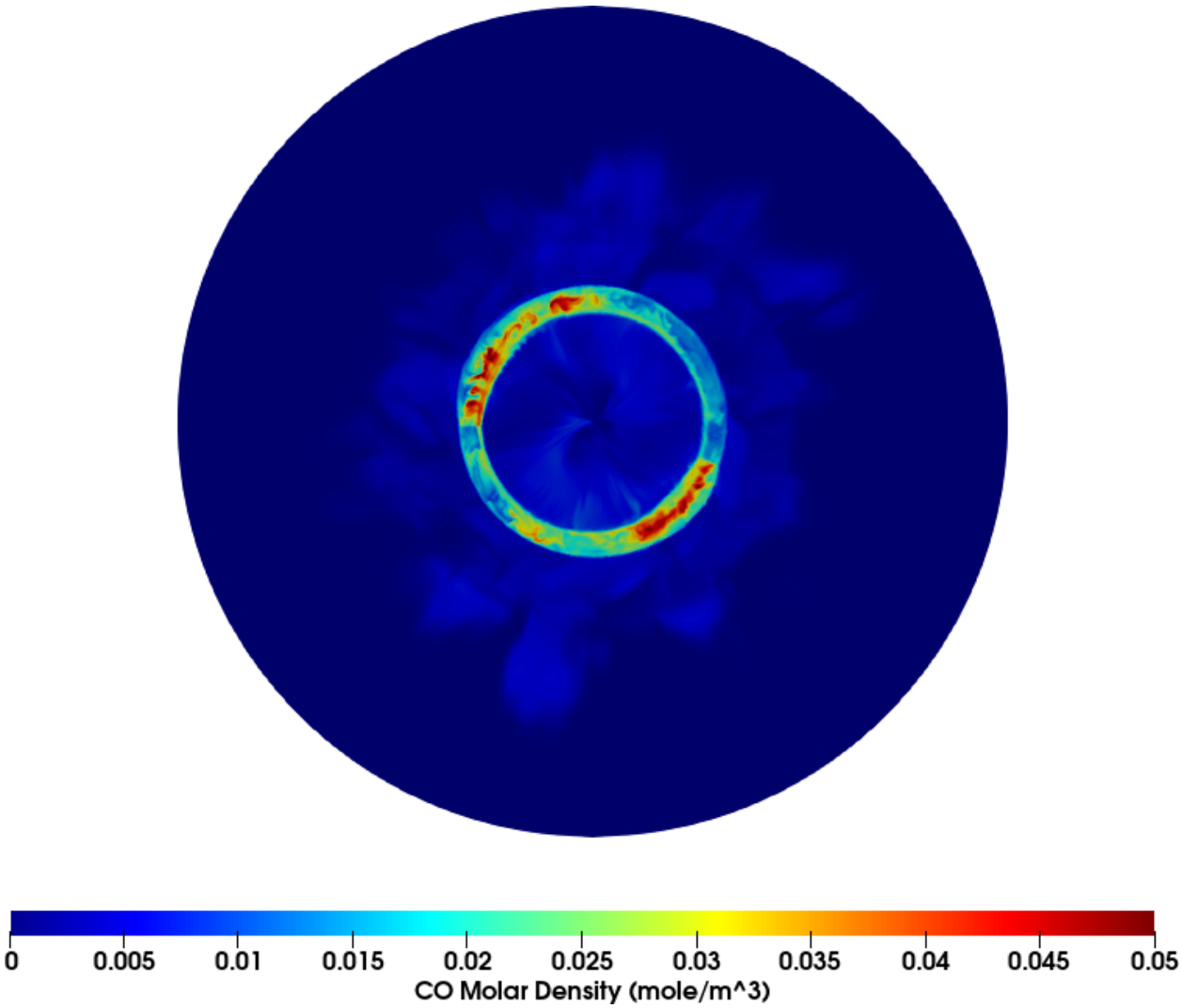

Figure 4.6: Axis-normal snapshot showing CO molar density in the exhaust plenum at an axial distance 3 mm from channel exit.

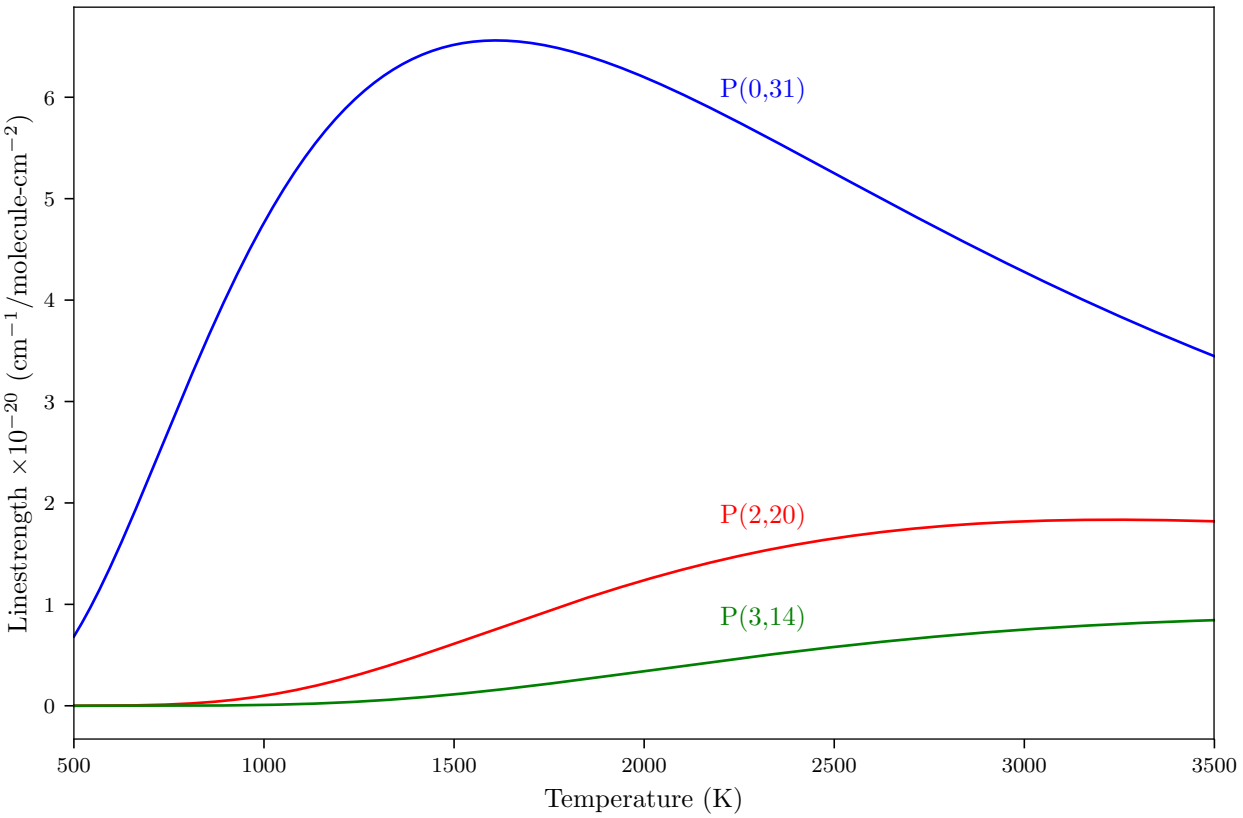

Figure 4.7: Linestrength as a function of temperature for the three targeted CO transitions, based on equation 4.4 and parameters from HITEMP tabulated in 4.1.

also affected the usability of absorbance-based measurements, as the measurement assumed the relation of equation 4.13, as holds for a linear relationship between linestrength and temperature. As shown in Fig. 4.7, the temperatures in the recirculation zone were low enough that the linear relationship, in evidence above 1500 K, did not apply. Consequently, the measurements using the absorbance model differed from those based on direct integration.

It's difficult to tell to what extent the experimental data of Nair et al. are affected by similar recirculation zone effects, but it's likely that the impact was much greater in the simulation than in the experiment. As mentioned, the simulation did not directly model the specific setup of the nitrogen jet, part of the experimental apparatus which was specifically targeted at reducing the impact of non-exhaust CO. The physical engine geometry also included mounting hardware which were not modeled, including bolts which possibly affect the formation of recirculation zones.

4.3.2 Exhaust-Only Laser Path

In order to consider laser measurements of only the engine exhaust, without the influence of the recirculation zone, synthetic laser measurements of the simulation were taken for a path centered 3 mm axially downstream of the chamber exit, but only extending to a radial distance 38 mm from the centerline. This was the same path as discussed in section 4.3.1, but shortened such that only the region immediately downstream of the chamber exhaust is included. Synthetic laser measurements for this exhaust-only laser path are shown in Fig. 4.8, and are likely more directly analogous to the experimental results of Nair et al. than the measurements in Fig. 4.4.

Qualitative features of the synthetic laser measurements on the shortened laser path match what was seen experimentally, as in Fig. 4.3. As in the experiment, passages of the wave in the simulation were primarily visible in the steep-fronted pressure. Synthetic laser measurements of temperature also showed steep-fronted shocks, but then showed large oscillations during the cycle, as in the experiments. Simulations also reproduced the double-peak structure of the experimental measurements of CO column density.

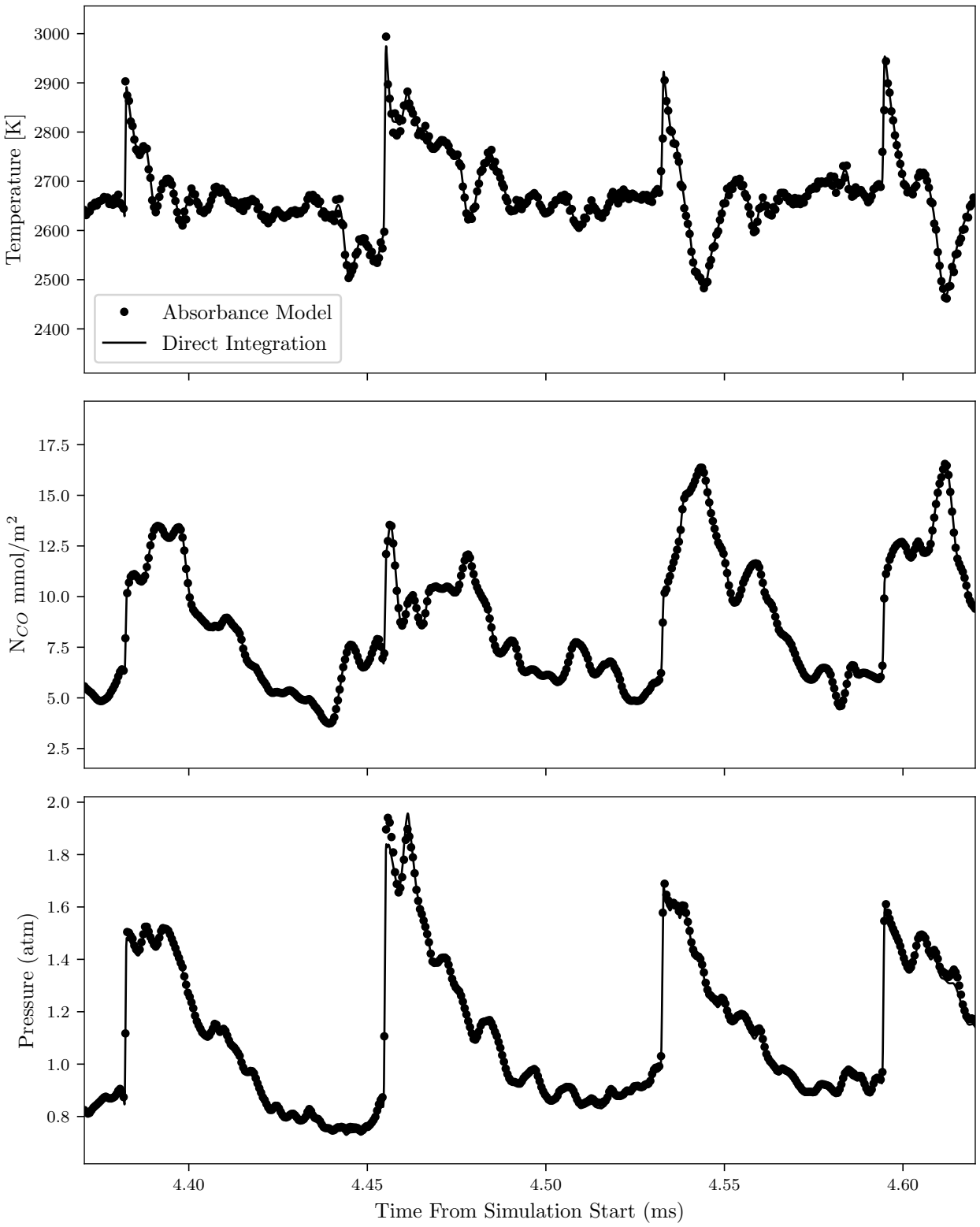

Figure 4.8: Synthetic laser measurements of pressure in simulation exhaust

Unlike in the recirculation region, temperatures in the exhaust were high enough that equation 4.13 applied, and the absorbance-based synthetic laser measurements closely matched direct integration measurements of the simulation in the exhaust region. The only minor deviations in measurement between the two laser models occurred during passages of the wave, such as the passage in Fig. 4.8 that occurred shortly after 4.45 ms. This deviation occurred because the temperature rise due to the shock was at a much smaller timescale than the 0.5 μs used to sweep through wavenumbers, and the absorbance areas of the latter half of the scan were scaled by the increased temperature. Measurements of temperature were based on a ratio of absorbance areas, as in equation 4.15, and an increase in the absorption area for the second scanned transition resulted in a scaled temperature. The direction of the shift in temperature depended on whether the measurement was taken using an upscan or a downscan.

The amount of variation from cycle to cycle, in both the simulation and experiment, suggests that a direct comparison of the two signals would depend on the specific cycle chosen for comparison It is possible to ameliorate this issue by using cycle-averages of the two measurements instead, as in Fig. 4.9. In order to do this, the start of each cycle was determined algorithmically using the pressure profile, and then the measurements were averaged between cycles. Only measurements from the direct integration model were used for determining cycle averages in the simulation data.

The simulation averages of Fig. 4.9 were conducted for only 13 cycles, and so are not as smooth as the experimental averages. However, even with a small number of cycles, the general trends in evolution may be compared between simulation and experiment. Overall, the simulation ran at a higher pressure than the experiment, consistently about 0.3 atm higher throughout the cycle. This is consistent with the CTAP measurements in chapter 3. Comparing synthetic laser measurements with Fig. 4.3 suggests that the simulation exhaust was at a higher temperature than in the experiment, a difference that may be directly connected to the use of adiabatic walls in the simulation.

In order to compare species measurements, CO mole fraction is displayed in Fig. 4.9.

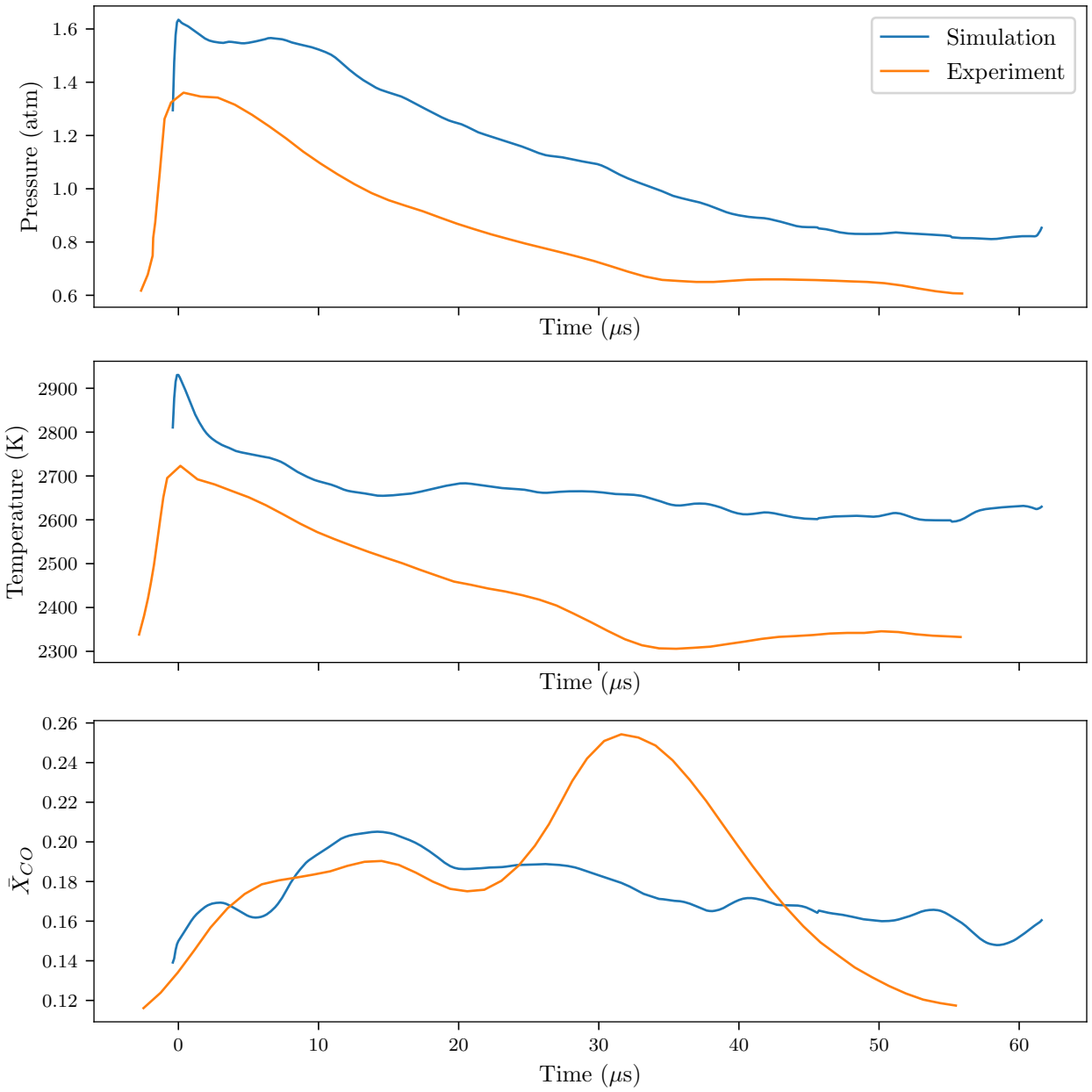

Figure 4.9: Cycle-averaged measurements of pressure, temperature, and CO mole fraction at engine exhaust, as compared with experimental measurements from Nair et al. [97].

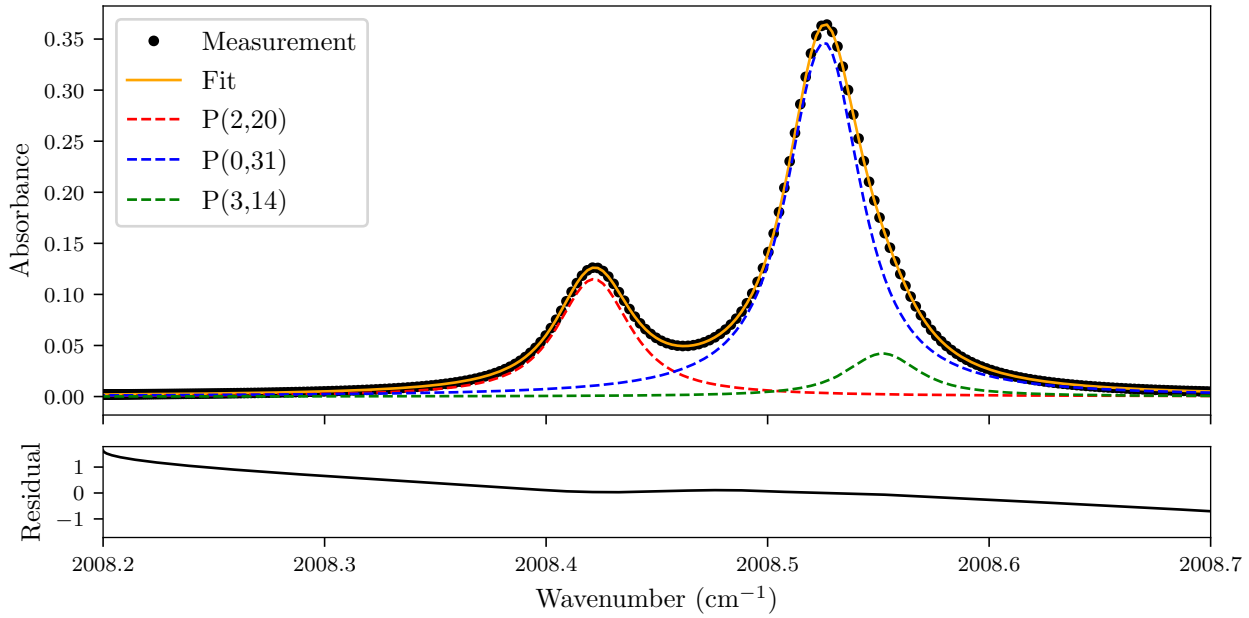

Figure 4.10: Absorbance for a representative simulation wavenumber sweep, for a laser path in the exhaust excluding recirculation region.

Mole fraction is used because the column density is proportional to the local density along the path, and calculating average mole fraction allows the effect of density to be scaled out of the comparison. For both the simulation and the experiment the average mole fraction was measured using measurements of $\bar{T}$ and N_{CO}:

$$\bar{X}_{\mathrm{CO}} = \frac{N_{\mathrm{CO}} k \bar{T}}{pL} \tag{4.16}$$

The scaling shows that, for much of the cycle, the simulated composition closely matched the amount of CO seen in the experiment. However, the cycle-averaging in the simulation did not demonstrate the significant peak in $\bar{X}_{\mathrm{CO}}$ observed experimentally, nor did the simulation demonstrate the associated dips in temperature and pressure. It is likely that this feature would appear if the average were taken over more simulated cycles: simulation column density of CO in Fig. 4.8 shows secondary peaks in the simulation, but the delay between cycle start and CO peak is inconsistent; with only 13 cycles, taking the average washes out the secondary peak.

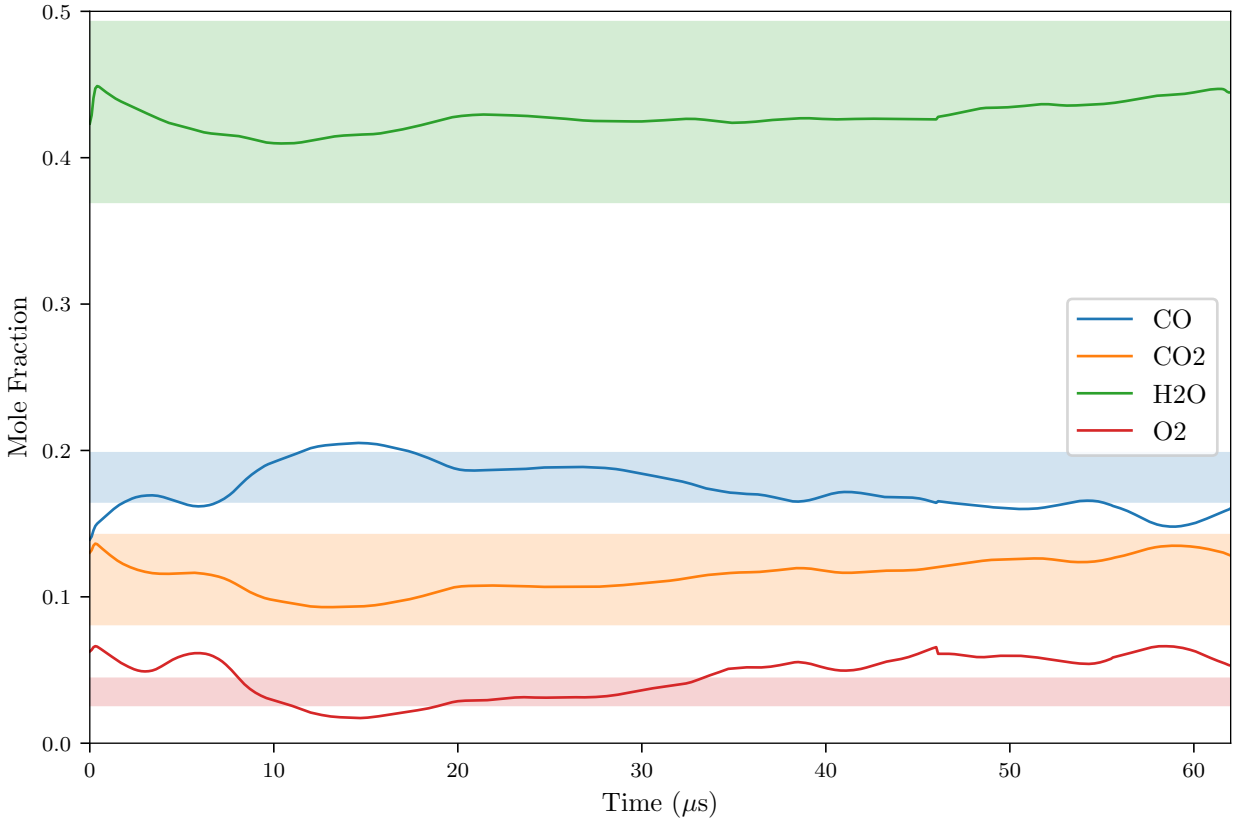

Figure 4.11: Cycle-averaged composition for the four most prevalent species at simulation exhaust, measured as $\bar{X}_j$. Bands show post-CJ composition of a 300 K, 1 atm methane-oxygen detonation, with a ϕ of 1.16, for both frozen flow and equilibrium flow isentropically accelerated to a pressure of 1 atm, calculated using CEA.

Fig. 4.10 shows representative simulation absorbance for one sweep of wavenumbers. Qualitatively the shape was quite similar to the experimental absorbance in Fig. 4.1, and demonstrated the expected features: large peaks due to the P(2,20) and P(0,31) transitions, with a small contribution from the P(3,14) transition. The difference in peak height between simulation and experiment is consistent with the changes in pressure and temperature: pressure broadening caused a decrease in peak height, and in this regime an increase in temperature corresponded with a decrease in linestrength for the P(0,31) peak (as in Fig. 4.7). As such, the decrease in simulation peak height is as dictated by the Beer-Lambert law (Eq. 4.3).

Cycle-averaged composition at the exhaust is shown in Fig. 4.11, for the four most prevalent species in the exhaust. These generally match compositions expected for post-detonative equilibrium, as demonstrated by the frozen-flow and equilibrium-flow compositions indicated in Fig. 4.11. Variation through the cycle is likely due both to non-uniform injection and mixing, and to differing equilibrium conditions caused by changes in pressure within a cycle. Based on Fig. 4.11, regions of high CO correspond to regions of low CO_2 – and regions of low CO correspond to regions of increased O_2.

4.3.3 Relating CO Measurements to Instantaneous Field

The simulated data makes it possible to relate structures measured in the exhaust to the flowfield inside the chamber. In order to understand how the double peak in CO column density measured at the exhaust relates to upstream CO generation regions, Fig. 4.12 aligns instantaneous laser measurements with an unwrapped cylinder inside the engine. The column density in the figure is measured by integrating laser paths centered 76 mm from the injection plane at a single instant in time, for a sweep of azimuthal locations. Because the measurement is instantaneous, the column density shown in Fig. 4.12 directly corresponds to snapshots of the engine; in this case, the mole fraction of CO is shown.

Based on Fig. 4.12, for each wave there were two regions with high amounts of CO generation: the top of the fill zone, and the area behind the wave but near injection. Although they're both places with high CO generation, the combustion occurs at very different pressures. In both cases, the regions of high CO corresponded to regions high in CH_4, as in Fig. 3.16. This is an indication that the variation in mole fraction of CO at the exhaust was directly related to the mixing fields caused by injection.

At the instant shown in Fig. 4.12, the secondary peaks in CO column density occurred at angles of 75° and 296°, corresponding to contact-surface deflagration. Because the contact-surface deflagration occurred at the region between the fill zone and the hot products, the streamlines were such that the region with increased CO corresponded with the shear layer dividing singly-shocked products from twice-shocked products. This feature could be useful

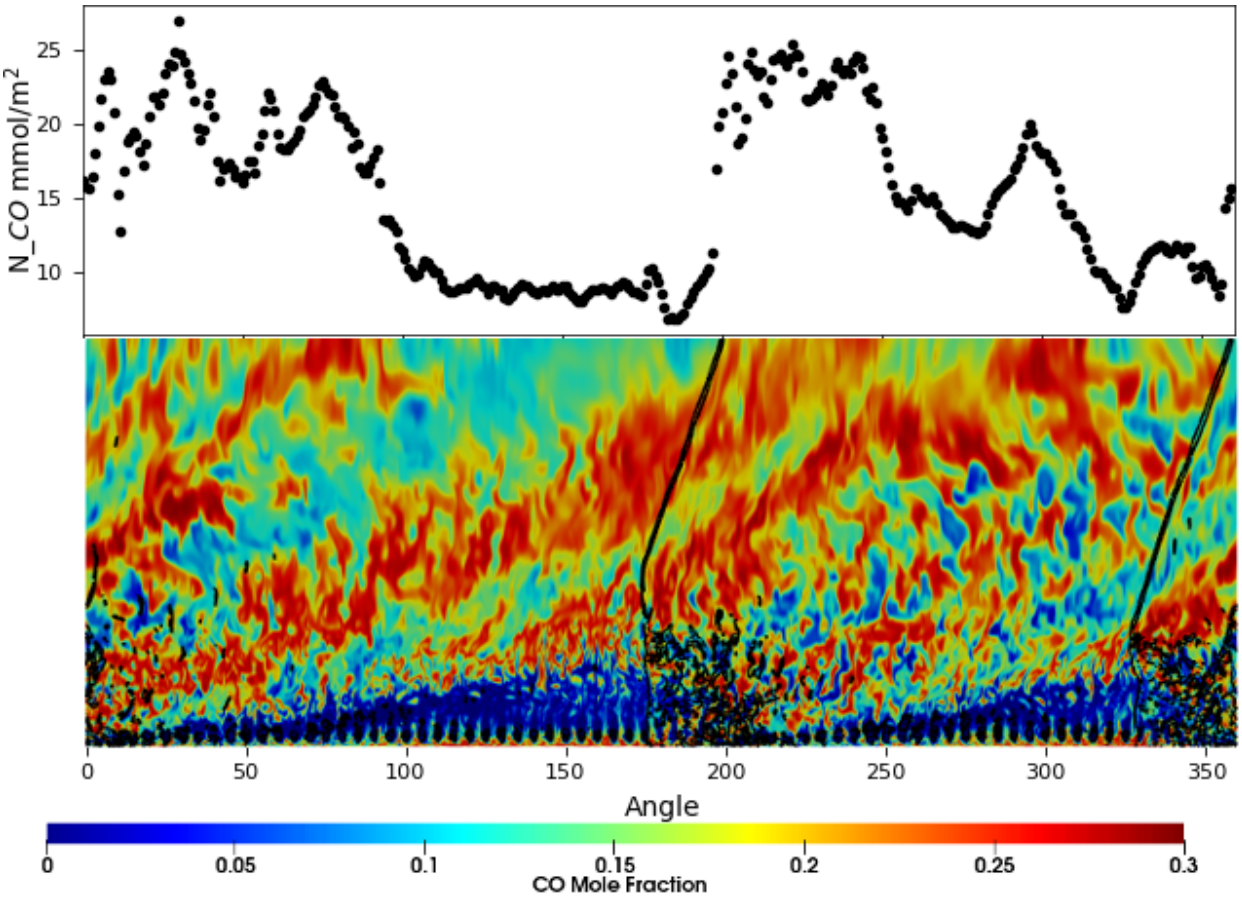

Figure 4.12: Mole fraction of CO in the center of the channel, aligned with a plot of CO column density for laser paths at the exit of the chamber, at multiple angular positions. Shock location is represented using pressure gradient, with the black isocontour showing a gradient of 1×10^8 Pa/m^2.

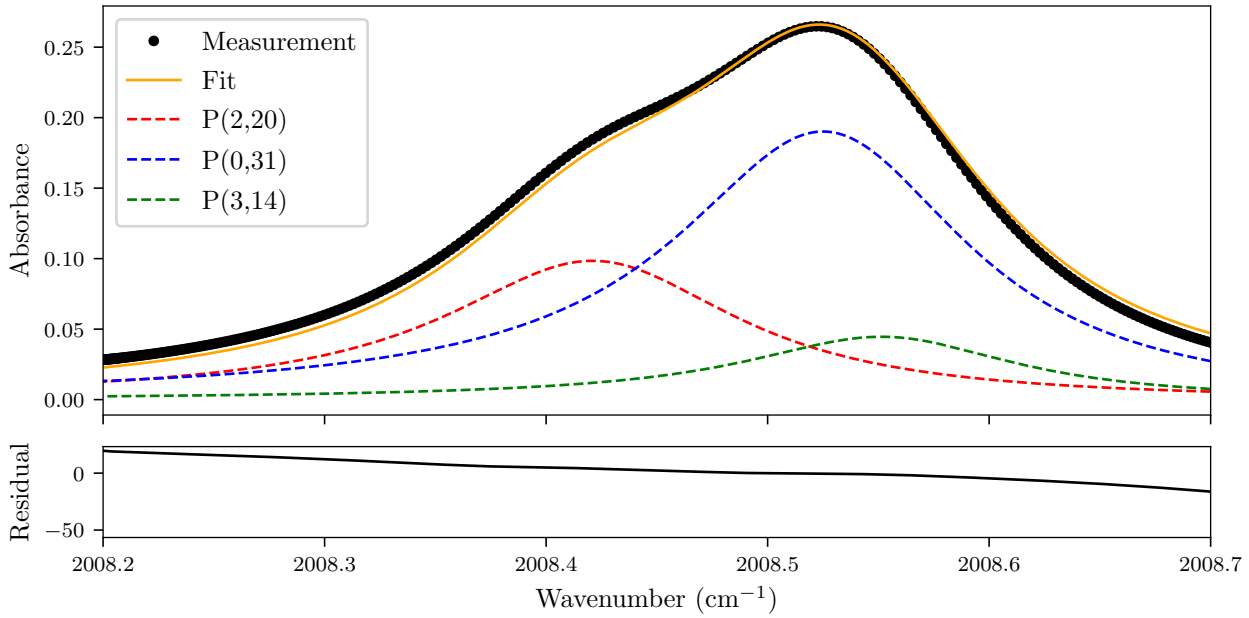

Figure 4.13: Example absorbance for a measurement taken inside the chamber, 58 mm axially downstream of injection.

in analyzing future diagnostics measurements, as it suggests that the location of the shear layer can be determined by measurements of species.

4.4 Inside the Chamber

A recent experimental collaboration between AFRL and UCLA took further experimental measurements inside the chamber, 58 mm downstream of injection; those data are still being analyzed, but in anticipation of that study, simulation laser measurements were also taken inside the chamber. Increases in pressure inside the chamber broadened the absorbance shape, with pressure increasing as the laser path moved further upstream toward injection. The absorbance-based synthetic laser can be used to consider these effects, and consider what flow features may appear in experimental measurements of RDRE flowfields inside the chamber.

4.4.1 Downstream of Detonation

The diagnostic location does not need to be far upstream for pressures to greatly broaden the lineshapes associated with targeted transitions. An example of such broadening is shown in Fig. 4.13, a representative absorbance measurement for a laser path centered 58 mm axially downstream of injection inside the RDRE combustion chamber. This location was already approaching the limits of what can be easily fit to take LAS measurements of the flow using the targeted CO transitions. The absorbance-based synthetic laser procedure was able to fit a Voigt shape in Fig. 4.13, but even with simulated absorbances – that can be fit much more easily than noisy experimental data – the residual of the fit was quite large. This suggests that, although it would be possible to take LAS measurements inside of the engine using these targeted CO transitions, there is a limit to how far upstream the diagnostic would work at the flow condition being considered.

Beyond an increase in pressure, it is expected that laser measurements of the in-chamber oblique shock region downstream of detonation would give similar structures to what is seen in the exhaust. Simulation results of Fig. 4.14 show that this was largely the case: increased pressures and temperatures when compared to the exhaust (Fig. 4.8), but similar structures. As before, the absorbance-based measurements closely followed direct integration except near sudden increases in temperature. At this axial location the measurement of pressure revealed a secondary pressure shock traveling behind the main shock structures. The secondary shocks, which did not coincide with the secondary rises in CO, also appear in flow-field snapshots of the simulation.

The secondary pressure shocks were also visible in cycle-averaged measurements for this location, shown in Fig. 4.15. The existence of a rise in CO concentration 50 μs after the start of the cycle also comes out in the cycle average, along with an associated drop in temperature.

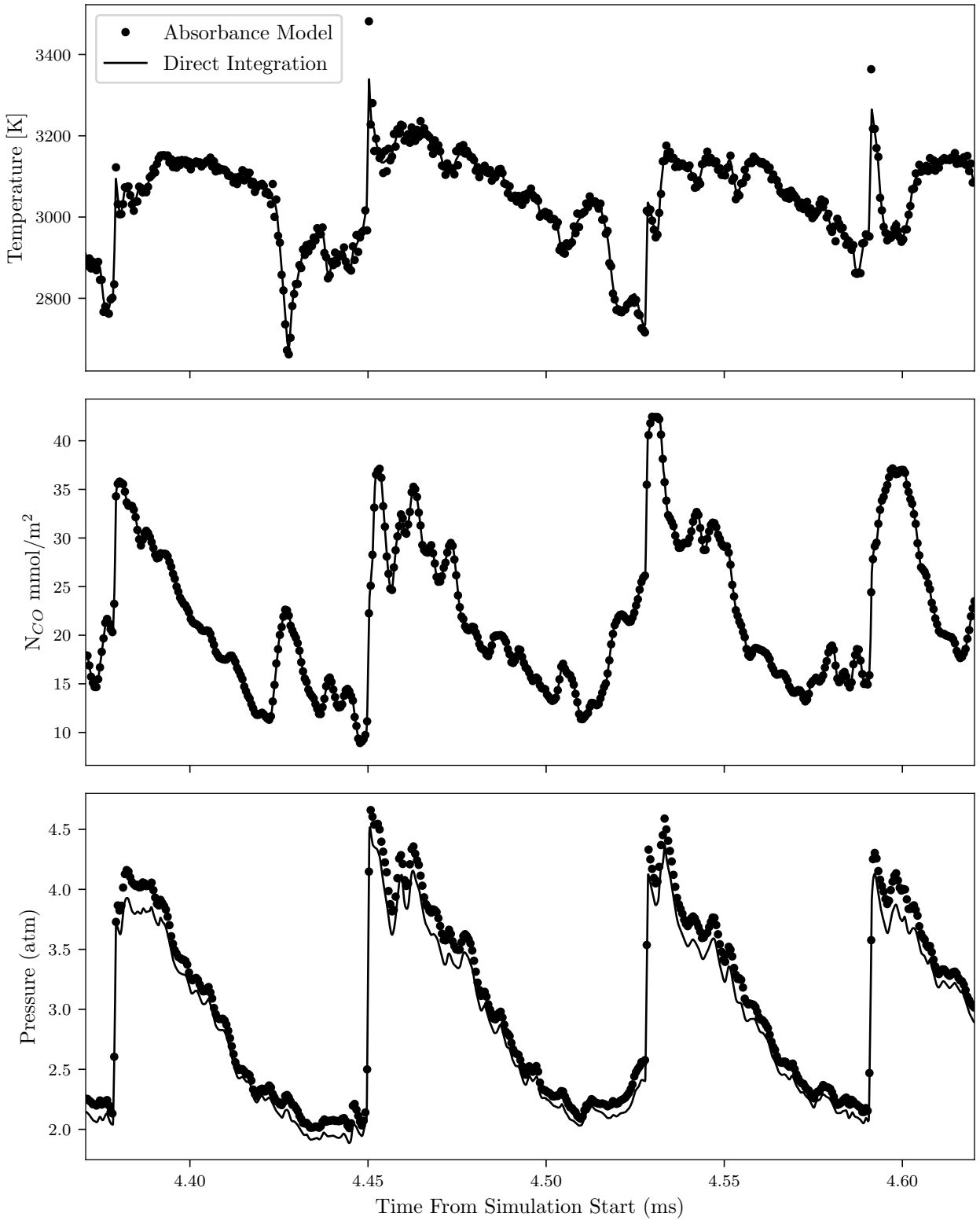

Figure 4.14: Synthetic laser measurements inside the chamber, for a path centered 58 mm axially downstream of injection.

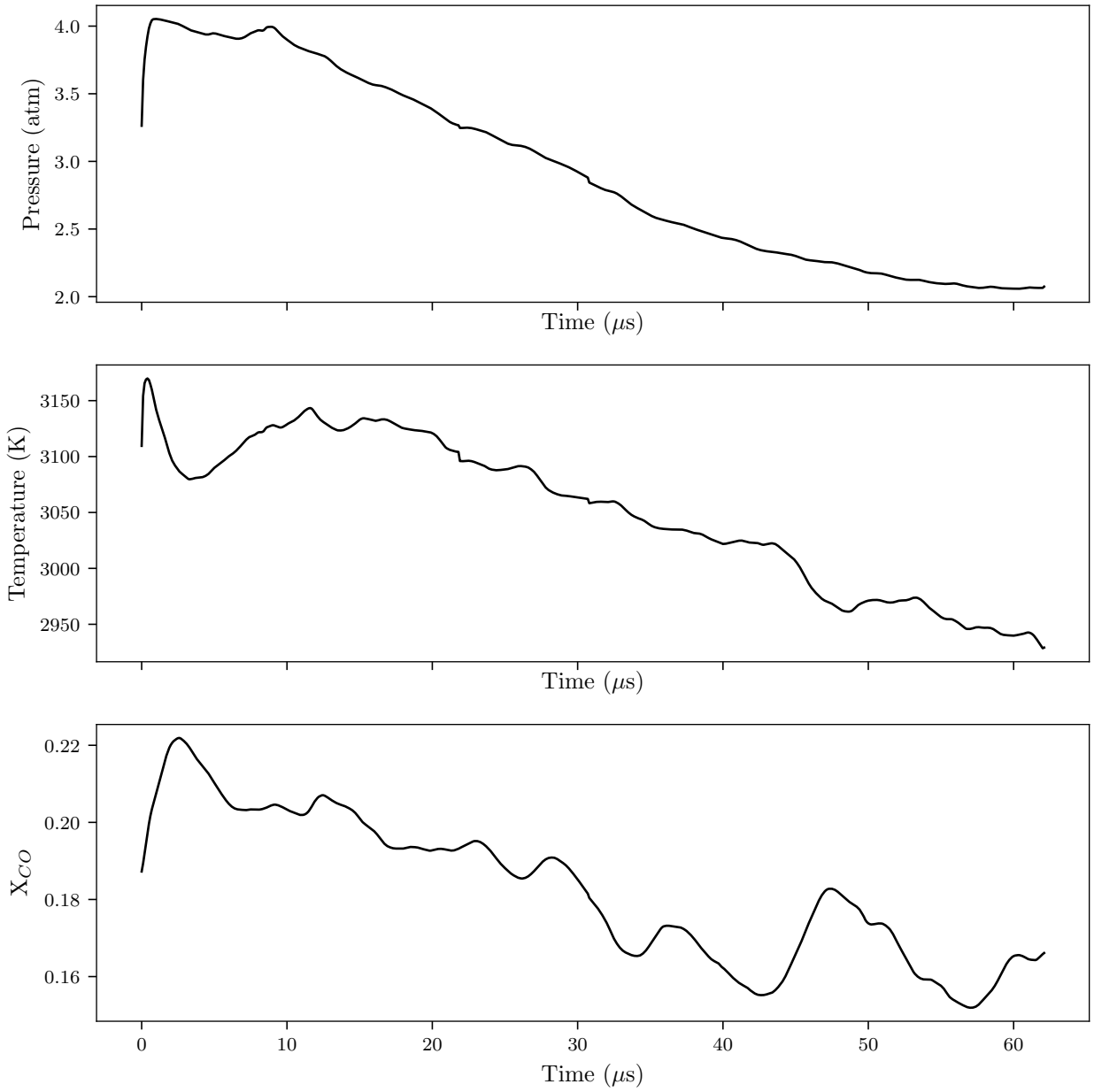

Figure 4.15: Cycle-averaged synthetic laser measurements of pressure, temperature, and X_{CO} inside the chamber, for a path centered 58 mm axially downstream of injection.

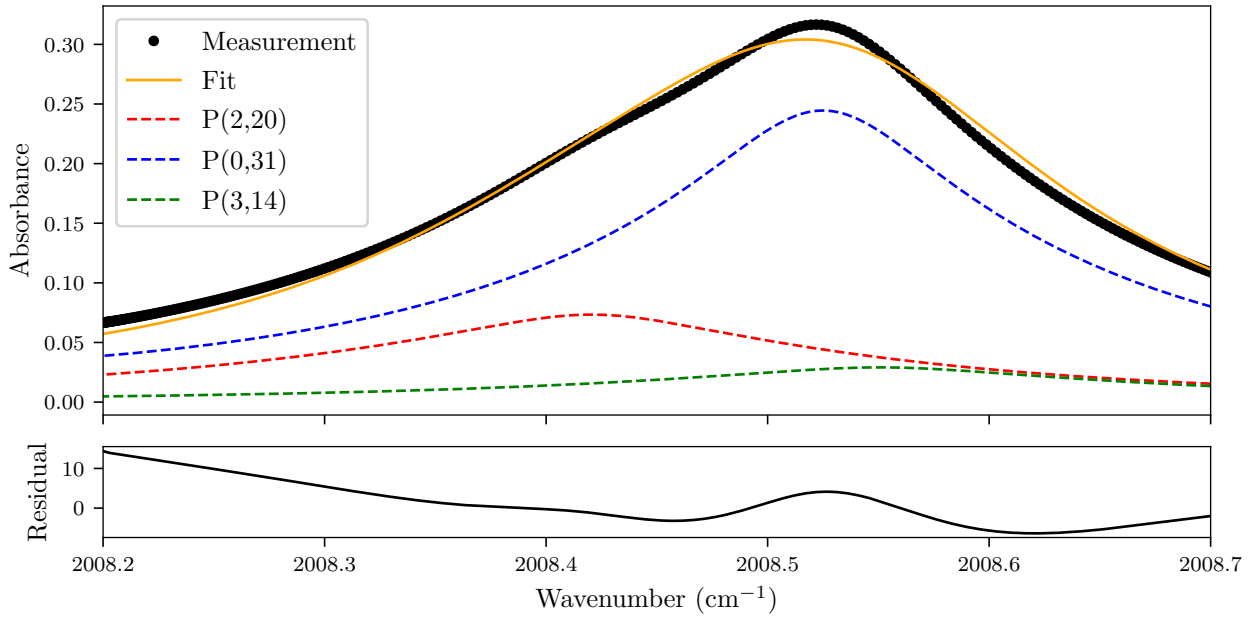

Figure 4.16: Example absorbance for a measurement taken near the detonation, 9 mm axially downstream of injection.

4.4.2 In the Detonation Region

In order to further understand RDRE operation, it would be ideal to take time-resolved measurements inside the detonation. Fig. 4.17 represents using the same synthetic-laser approach to evaluate flowfields in the region 9 mm from injection, a location that would capture passing detonations. Although the absorbance-based synthetic laser measurements were still able to fit Voigt profiles at these extremely high pressures, as in Fig. 4.16, this was an extreme overestimate of the pressures that can be used for accurate measurements of the selected CO-transitions.

However, even with perfect initial conditions, the absorbance model diverged from direct integration in the low-temperature portions of the cycle in Fig. 4.17. This occurred for much the same reason as in the recirculation zone: the injected fill region was at a low temperature, and entrained enough CO from the combustion products to shift the two measurements. As indicated in Fig. 4.19, injector mixing fields led to a large radial variation in flowfield near injection, meaning that a single beam path reflecting off of the centerbody in this region

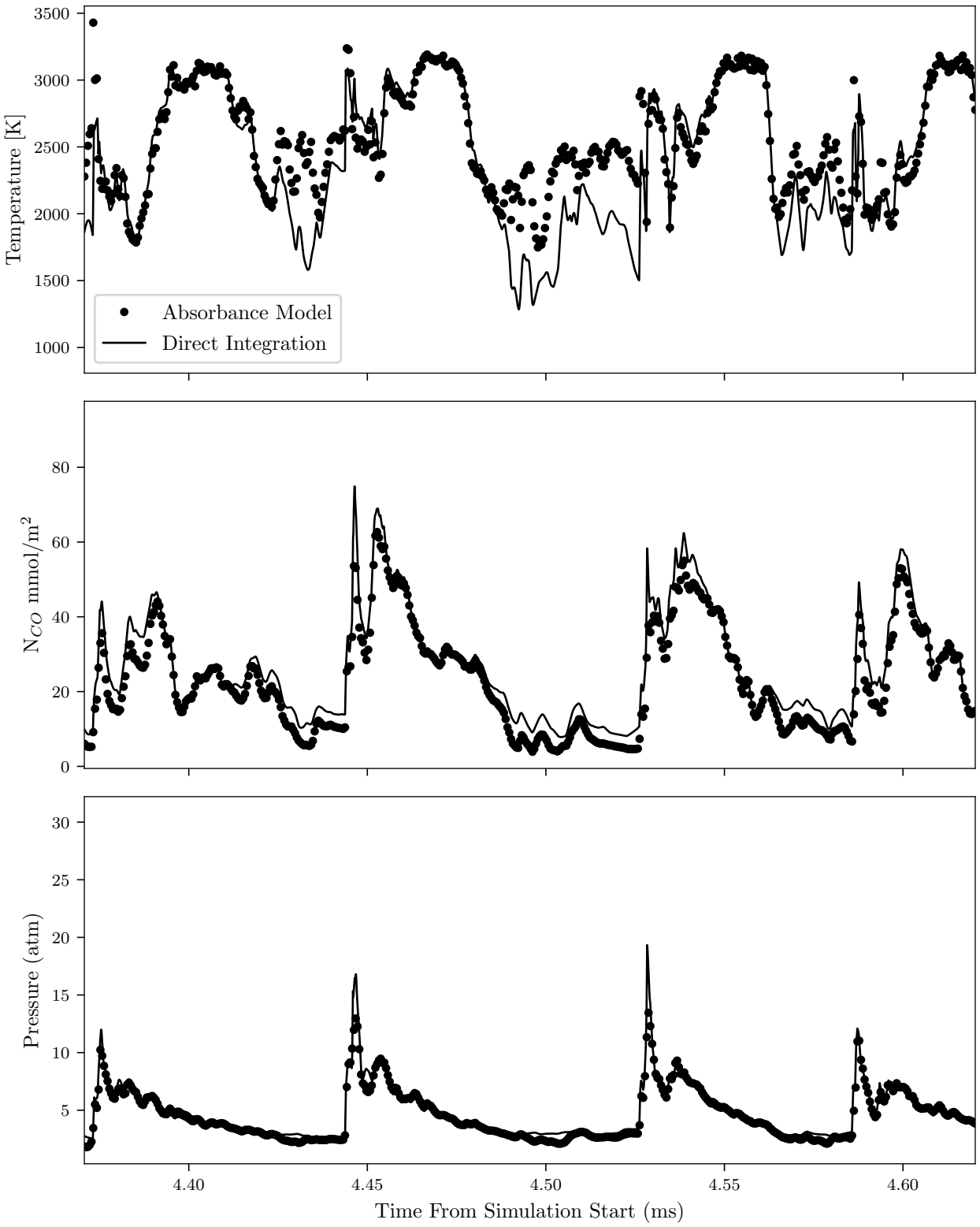

Figure 4.17: Synthetic laser measurements of pressure, 9 mm from injection.

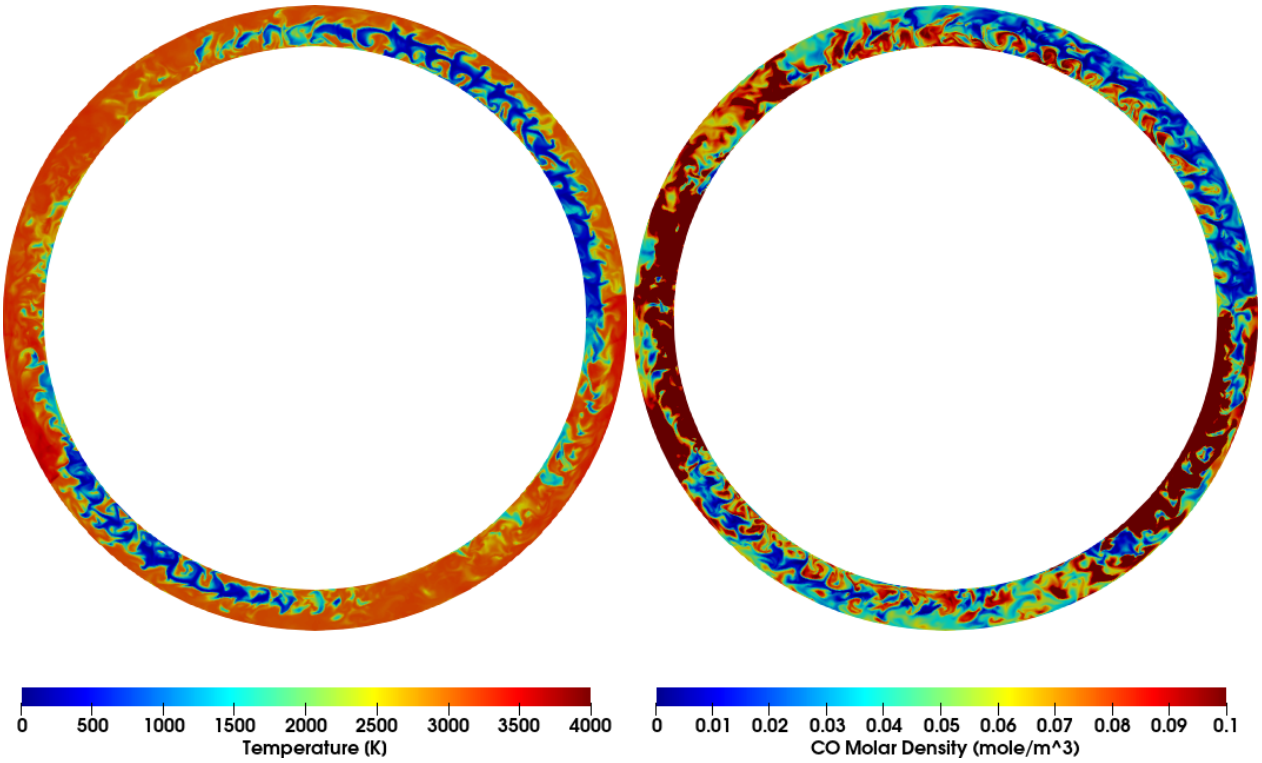

Figure 4.18: Instantaneous snapshot at an axial distance of 9 mm from injection, showing radial distribution of temperature (left) and CO mole density (right).

would travel through an extreme change in regimes (more than 2000 K difference between hot products and cold reactants). The range also means that an integrated measurement with weight in both regimes would not have much useful meaning, since the single integrated measurement would not be indicative of the flowfield at any specific location. Instead, any linepath-based diagnostic targeting the detonation-region of an RDRE would likely need to specifically target one part of the flow, and exclude either the product region or the reactants from the measurement. One candidate species for isolating fill temperature is CH_4, which Fig. 4.20 suggests was present in large amounts in the low temperature region, but not in the hot region.

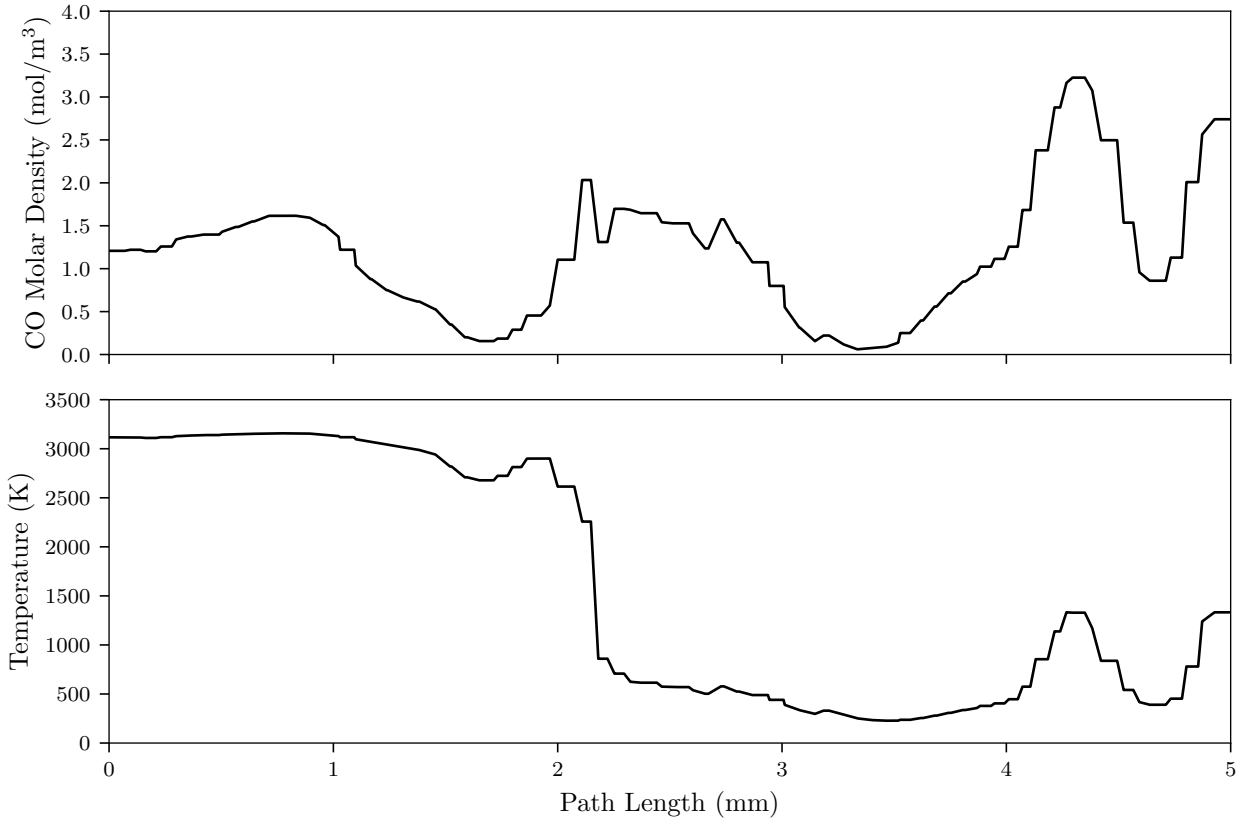

Figure 4.19: Temperature and CO molar density along one leg of a laser path centered at an axial distance 9 mm from injection.

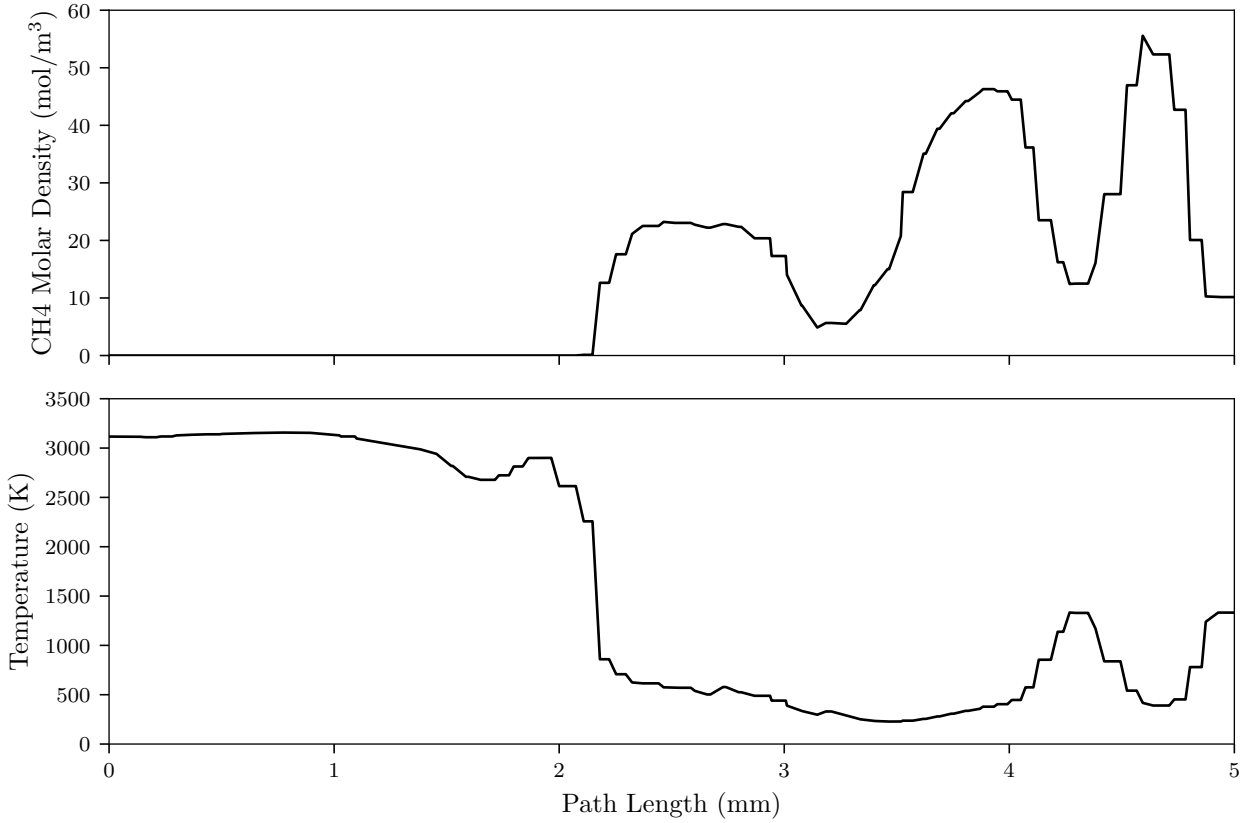

Figure 4.20: Temperature and CH4 molar density along one leg of a laser path centered at an axial distance 9 mm from injection.

CHAPTER 5

Effect of a Converging-Diverging Nozzle

Some of the information in this chapter is taken with slight modification from the article *J. W. Bennewitz, B. R. Bigler, M. C. Ross, S. A. Danczyk, W. A. Hargus, and R. D. Smith, "Performance of a Rotating Detonation Rocket Engine with Various Convergent Nozzles and Chamber Lengths," Energies, vol. 14, no. 8, Art. no. 8, Jan. 2021, doi: 10.3390/en14082037.*

In deflagration based engines, the use of converging-diverging nozzles is well established, and unsurprisingly it has been shown that adding constrictions to annular RDRE chambers has been shown to increase thrust. Adding a constriction is also a standard mechanism for increasing the chamber pressure, and has been shown to reduce the net loss in stagnation pressure [103, 104]. There also exists potential to use a nozzle constriction to attenuate the fluctuations in exhaust pressure that are characteristic of rotating detonation engines [105]. However, the addition of a constriction to the chamber exit is also coupled to the upstream detonation dynamics. It has been shown experimentally that a sharp constriction results in the reflection of shockwaves back toward the upstream injectors [56, 60]. Constrictions have also been shown to change the number of detonation waves present in the chamber, and in some cases have been shown to trigger longitudinal pulsing inside the chamber [54, 58].

Simulations have been used successfully to understand RDRE nozzle design. Zhdan et al. demonstrated, using inviscid, quasi-two-dimensional simulations, that the flow field behind the oblique shock in an unconstricted annular RDRE can be supersonic, and observed that a purely-expanding nozzle is sufficient to increase thrust [50]. Nordeen et al. used three-dimensional simulations to show that changing the constriction ratio affects the local amount

of swirl in the exhaust field, even while conserving angular momentum [106]. Experimentally-observed unsteadiness has been reproduced in numerical studies, which show that the addition of a nozzle may introduce instabilities into the detonation structure, and can reproduce the transition to longitudinal pulsing observed with certain nozzle designs [54,107]. Progress has also been made toward combining simulations with optimization techniques to design nozzles, by treating the chamber and nozzle as a decoupled problem [108, 109].

An experimental study was previously conducted in AFRL that tested a gaseous methane–oxygen RDRE over a range of flow rates and equivalence ratios [110]. The engine's modular design allowed the addition of a converging-diverging nozzle without the modification of any other engine features, and it was shown that the addition of a gradually-converging centerbody can induce counter-propagating wave behavior inside the RDRE chamber. Two geometries from that experiment were chosen for this section to be simulated. One geometry is based on the prototypical annular detonation engine design, with an unconstricted channel that exhausts over a straight aerospike. The second simulation considered the same flow conditions, but instead included a converging-diverging nozzle which experimentally demonstrated counter-propagating waves. The use of simulations makes it possible to track the energy content of the flow, enabling an analysis of the major differences that exist between an unconstricted RDRE chamber and one which includes a gradual constriction.

5.1 Case Description

Geometry and flow conditions were chosen to match experimental measurements taken during an AFRL RDRE testing campaign, in which a gaseous methane-oxygen RDRE was tested with a variety of converging-diverging configurations [110]. The engine hardware was designed by Smith and Stanley, and featured a modular design to enable the testing of individual geometric features [111]. Two specific experimental geometries were simulated, both using a 76 mm combustion chamber, 33 mm inner radius, and 5 mm channel width. The difference focused on a geometric change in engine centerbody: one geometry was unconstricted, with a constant-area channel that remained 5 mm over the entire chamber length.

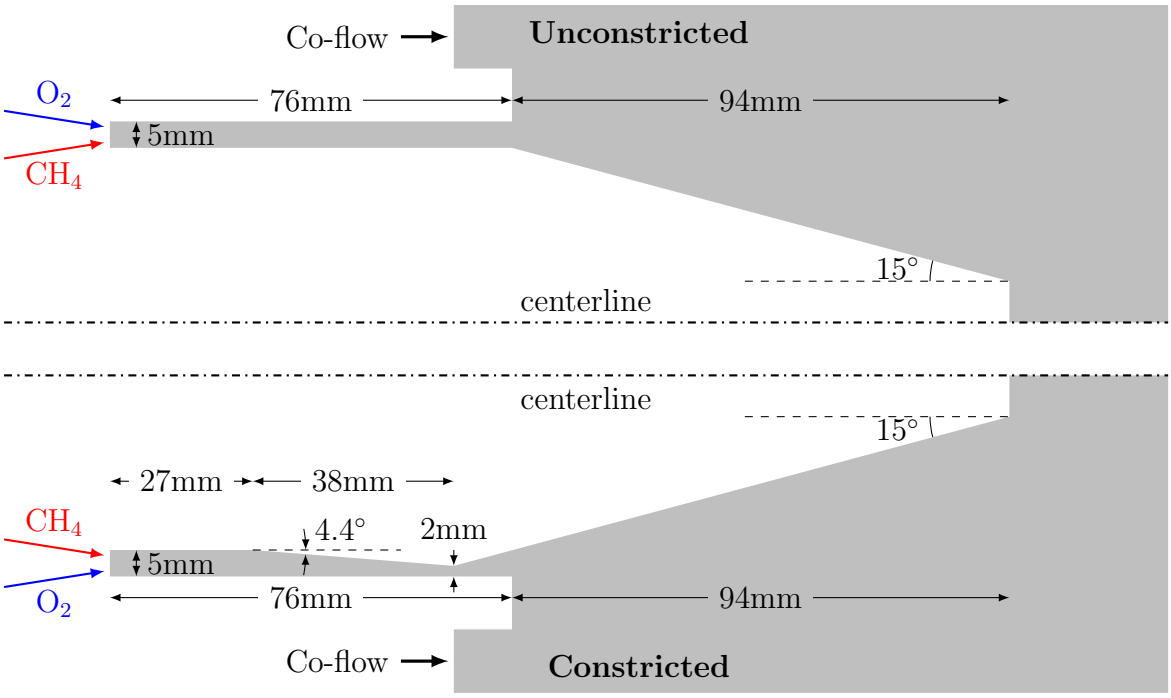

Figure 5.1: Domain diagram, with simplified injector geometry, for both an unconstricted geometry (top) and a chamber with a gradual constriction (bottom).

The second simulation considered a constricted converging-diverging geometry, in which the inner body was shaped to turn the flow 4.4 degrees; this resulted in a 2 mm wide throat located 65 mm from the injection plane. A simplified diagram of the engine geometry is shown in Fig. 5.1 for both cases. Although not shown in Fig. 5.1, the simulation domains also included a large chamber exhaust region and the full injector geometry: 72 discrete impinging injector pairs, connected to upstream injection plena.

Non-slip, adiabatic boundary conditions were enforced at the engine walls, with slip conditions at the walls of the downstream exhaust plenum. Injector plenum inflow conditions were chosen to produce a methane–oxygen equivalence ratio (ϕ) of 1.1, and a mass flow rate ($\dot{m}$) of 0.27 kg/s; enforced parameters are listed in Table 5.1. An exhaust pressure of 92 KPa was chosen for subsonic outflow regions, in keeping with experimental gauge pressures at AFRL.

The mesh for both cases consisted of 136 million hexahedral cells, with sizing chosen to

Enforced Condition	**Value**
Fuel Mass Flux (kg/s)	0.06
Fuel Temperature (K)	300
Oxidizer Mass Flux (kg/s)	0.21
Oxidizer Temperature (K)	300
Co-flow Velocity (m/s)	1
Co-flow Temperature (K)	300
Subsonic Outflow Pressure (KPa)	92

Table 5.1: Boundary conditions enforced at flow inlets and outlets.

	Unconstricted	Constricted
CH_4 Plenum (MPa)	2.3	2.4
O_2 Plenum (MPa)	2.1	2.2

Table 5.2: Initial feed pressures set in injector plenum regions, based on experimental measurements.

ensure cell lengths less than 50 μm in regions where detonations are likely to occur. This allows for multiple cells within an induction length, which for methane/oxygen combustion at an equivalence ratio of 1.1 and reactant pressure of 3 atm have an experimental induction length of 100 μm and a cell size on the order of 1500 μm [112]. 3 atm is higher than the targeted reactant pressures for these designs, and so the chosen cell sizing ensured at least two simulation cells per induction length, and 10 simulation cells per detonation length – sizing which is consistent with other numerical detonation engine simulations [53, 66]. This does mean that the detonation Von-Neumann peak was not spatially resolved in the simulations, but this level of sizing has been demonstrated to capture the physics of interest in RDREs; this model requires 6 million CPU-hours to simulate 2 ms of physical time, and so the benefits of increased spatial accuracy must be weighed against practicality.

Initiation of the detonation was accomplished using a symmetric high-pressure, high-

temperature kernel inside the combustor at the start of simulation, similar to the process described in chapter 3. Initial pressures in the rest of the domain were based on the experiments, with an exhaust region initialized to 92 KPa, and injector plenum pressures initialized to static pressure measurements taken during engine operation, as listed in Table 5.2. The combustion chambers of both simulations were prefilled with stoichiometric methane–oxygen, in order to undergo rapid deflagration-to-detonation (DDT) transition when exposed to the small 6 MPa and 4000 K detonation kernel. A symmetric kernel of this sort results in a process with direct analogs to an experimental spark ignition: the kernel establishes strong detonations in both directions, which then break apart into a large number of pressure waves. The waves then undergo an unsteady cascade process, characterized by a continuous change in the number of waves and the associated wave speeds, before eventually reaching a steady wave mode. A startup of this sort has been used successfully in previous studies to develop the quasi-steady-state wave dynamics of an RDRE without artificially imposing the number of waves, but does require running the simulation for an extended period of time in order to allow the starting transient to stabilize [67].

The simulations were run using Department of Defence High Performance Computing Modernization Program machines. Specifically, the CRAY supercomputer Onyx was used, with the AHFM solver parallelized to run on 16060 cores. Post-processing of simulation data was done using a combination of Python and ParaView [113].

5.2 Startup Transient

Both simulations were initialized with the same form of symmetric kernel, and in both simulations the initial symmetric pressure wave led to a secondary symmetric detonation structure, which underwent DDT. As seen in Fig. 5.2, the symmetric structures collided at a position 180 degrees offset from the initial kernel, and then continued around the annulus until colliding again at the initial location of the kernel. By the time of the second collision, 0.33 ms after initialization, the combustion waves had consumed all of the available methane in the chamber (Fig. 5.3), and in both simulations the detonation structures weakened,

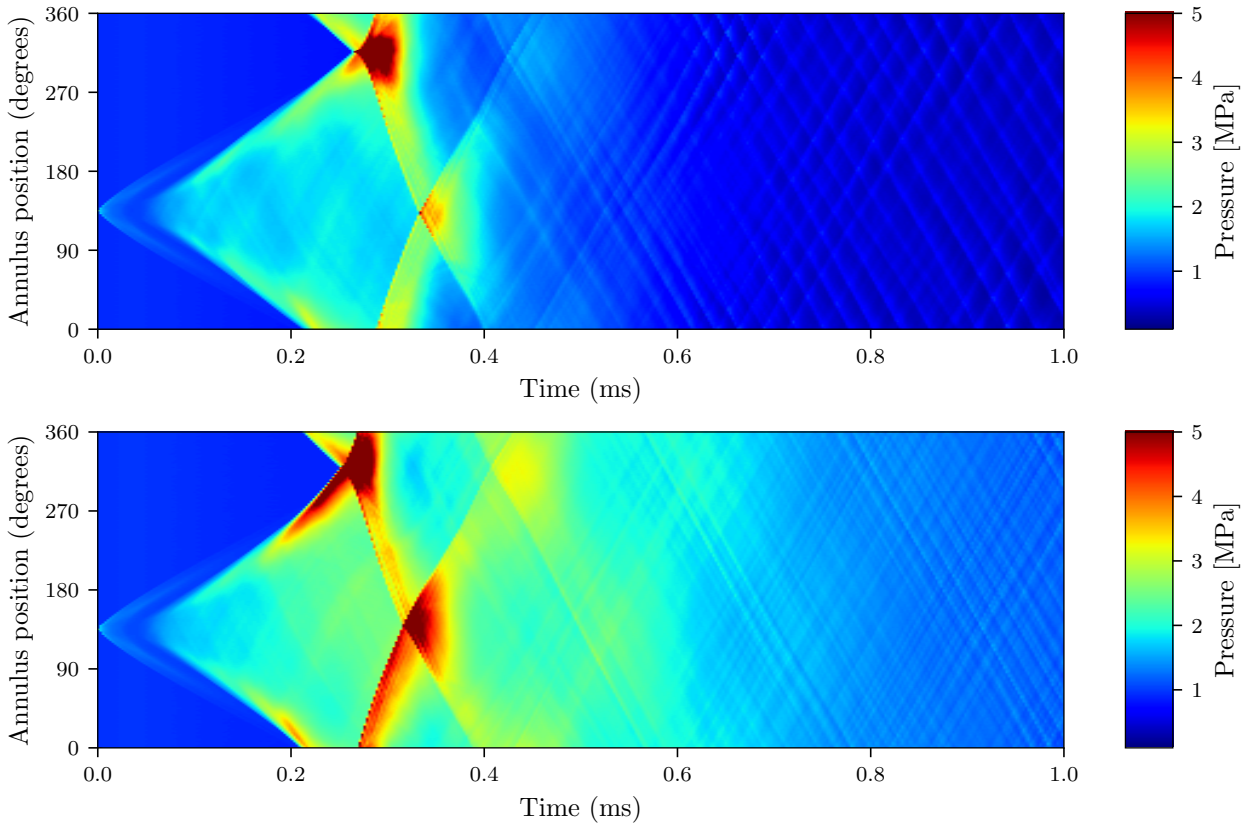

Figure 5.2: θ-t diagrams of pressure during the startup transient, averaged over the 15 mm immediately downstream of injection, for both the unconstricted simulation (top) and constricted simulation (bottom).

eventually becoming purely pressure shock waves. Although the pressures after the initial revolution of the wave structures were higher in the constricted case, the two cases were qualitatively quite similar to one another at a time 0.5 ms from initialization: the initial waves resulted in a large number of pressure waves traveling in both azimuthal directions, with no obvious detonation structure remaining in the chamber.

5.3 Characterizing the Quasi-Steady Operating Mode

Both simulations were considered to have reached quasi-steady operation once the waves completed a full revolution of the azimuthal chamber without significantly changing number

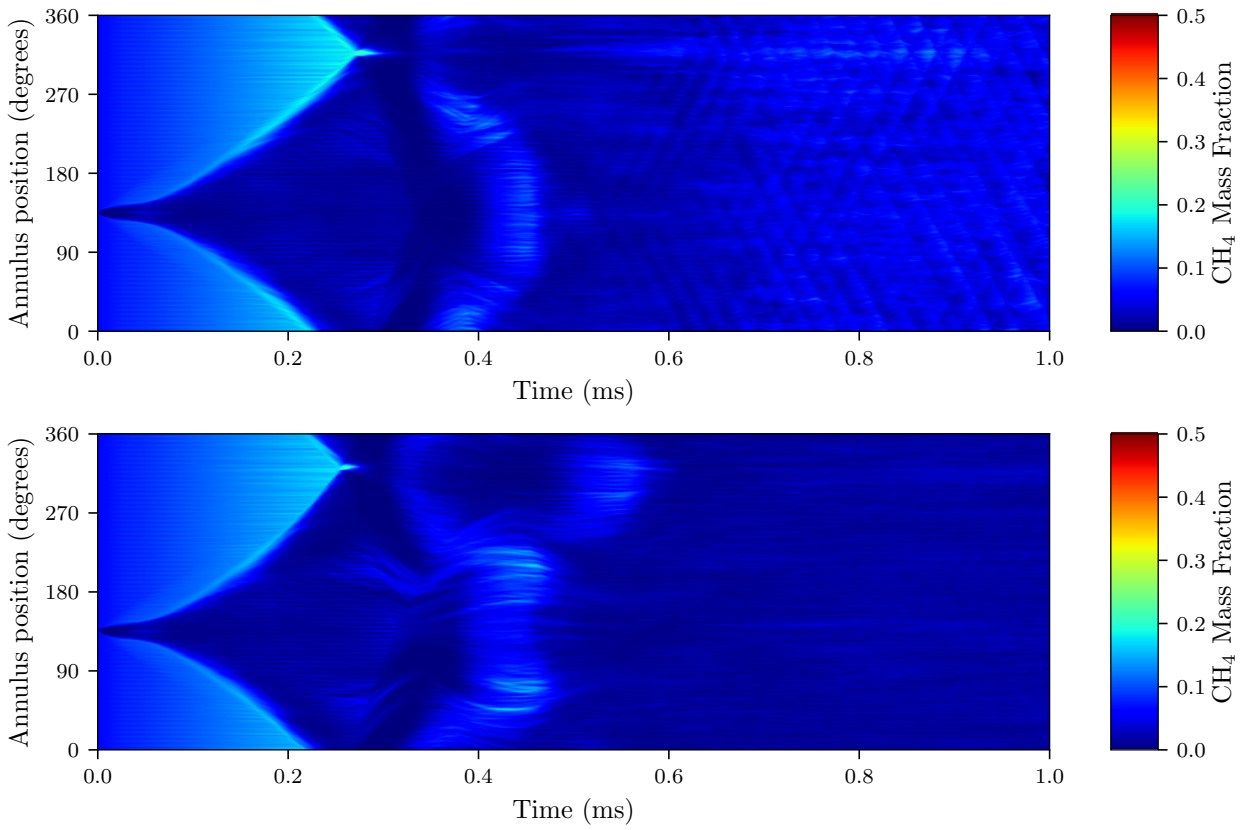

Figure 5.3: θ-t diagrams of CH_4 mass fraction during the startup transient, averaged over the 15 mm immediately downstream of injection, for both the unconstricted simulation (top) and constricted simulation (bottom).

of waves or wave speeds. The end of the wave cascade triggered by the initial transient is shown in Fig. 5.4 for both simulations. From Fig. 5.4 it is immediately apparent that the constricted simulation operated at a higher average chamber pressure, and stabilized with a larger number of waves in both directions.

5.3.1 Comparisons With Experiment

A summary of the quasi-steady-state conditions attained in the simulation is shown in table 5.3. The addition of a converging-diverging nozzle increased thrust and I_{sp}, while also increasing pressure inside of the chamber. In this case, thrust was extracted from the simulation using just the rocket equation on the exit plane 76 mm from injection, using a far-field

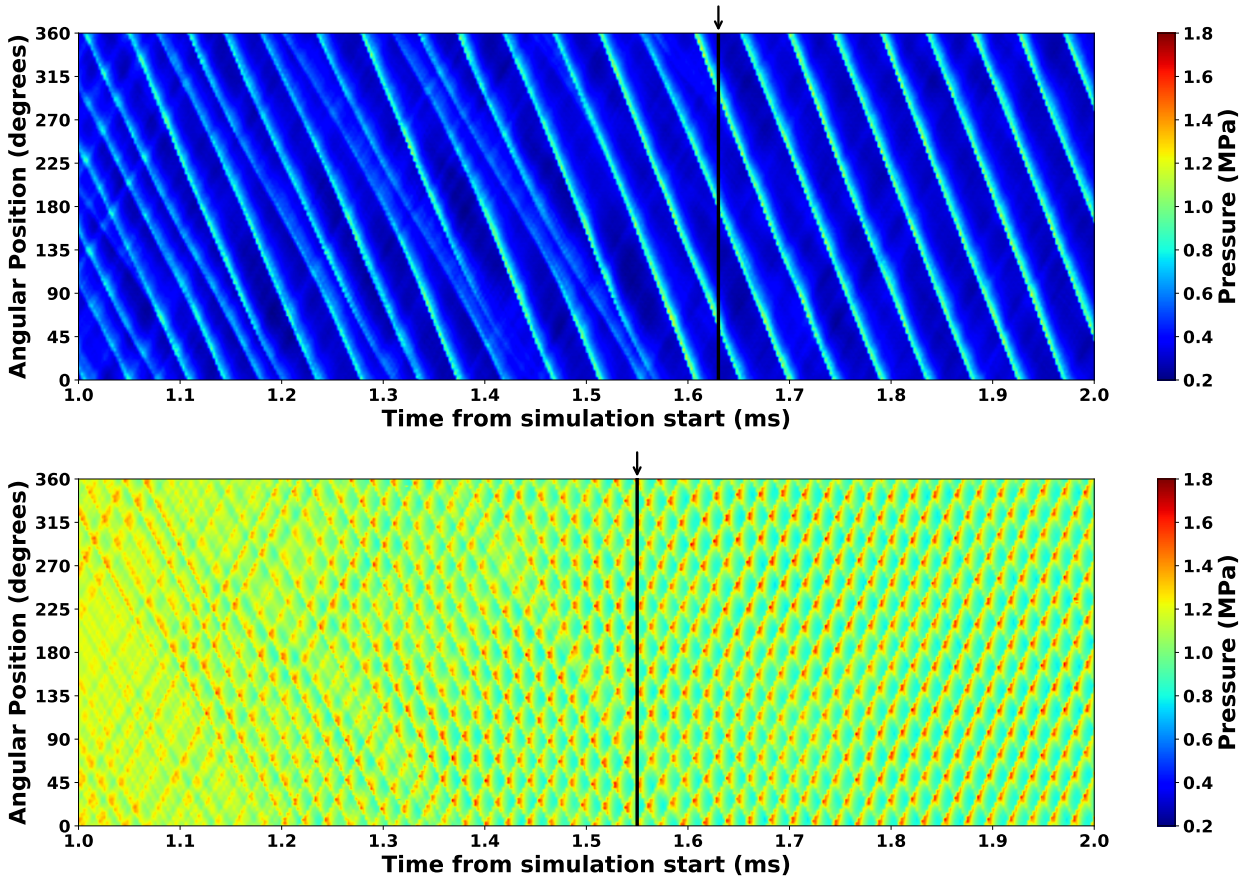

Figure 5.4: θ-t diagrams of pressure in the detonation region of both the unconstricted simulation (top) and constricted simulation (bottom). Arrows indicate where the simulations were considered to reach quasi-steady operation.

pressure of 0.09 MPa. The simulations also captured the effect seen experimentally, that the constricted geometry sustained counter-propagating modes not present in an unconstricted geometry at the same flow conditions. The overall number of waves matched closely between experiment and simulation, with only a slight decrease in the number of waves sustained in the simulations, and wave speeds were overpredicted in both geometries. The simulations also overpredicted both thrust and I_{sp}, which may be largely due to the use of adiabatic conditions. Taken as a whole, Table 5.3 indicates that the simulations reproduced the dominant physics and trends which dictate detonation behavior inside the engine.

	Unconstricted		Constricted	
	Simulation	Experiment	Simulation	Experiment
Number of Waves	3/-	4/-	8/8	8/9
Wavespeeds (m/s)	1632/-	1477/-	1316/1291	1275/1202
Pressure 1 (MPa)	0.43	0.36	1.06	0.99
Pressure 2 (MPa)	0.34	0.31	1.05	1.00
Thrust (N)	513	431	629	543
I_{sp} (s)	189	162	231	208

Table 5.3: Summary of quasi-steady mode achieved in both simulations. Counter-propogating waves were sustained in the constricted case, and so number and wavespeeds are separated by direction in that case. Pressure 1 is a temporally average measurement taken 9 mm from the injection plane, and Pressure 2 is the same measurement 29 mm from the injection plane, locations chosen to coincide with experimental capillary tube attenuated pressure measurements taken by Bennewitz et al. [110].

5.3.2 θ-t Measurements of Detonation Region

θ-t diagrams, of the sort used in section 5.2 to evaluate the startup transient, are also useful in assessing the quasi-steady operating mode of the engine. The most straightforward of these is pressure, shown in Fig. 5.5, which demonstrates that the unconstricted simulation had three large pressure waves travelling azimuthally in a dominant direction. The diagram also demonstrates the existence of pressure waves travelling in the opposing azimuthal direction in the unconstricted geometry, much weaker in magnitude than the waves in the dominant direction. Wave behavior in the constricted simulation was qualitatively quite different: 8 waves in each direction, with a comparatively-small difference in magnitude between pressure waves in the dominant and the secondary direction. The similarity in magnitude resulted in large increases in pressure at intersection locations, locations which – because of the similarity in wavespeeds and number of waves – occur at similar angular positions every cycle.

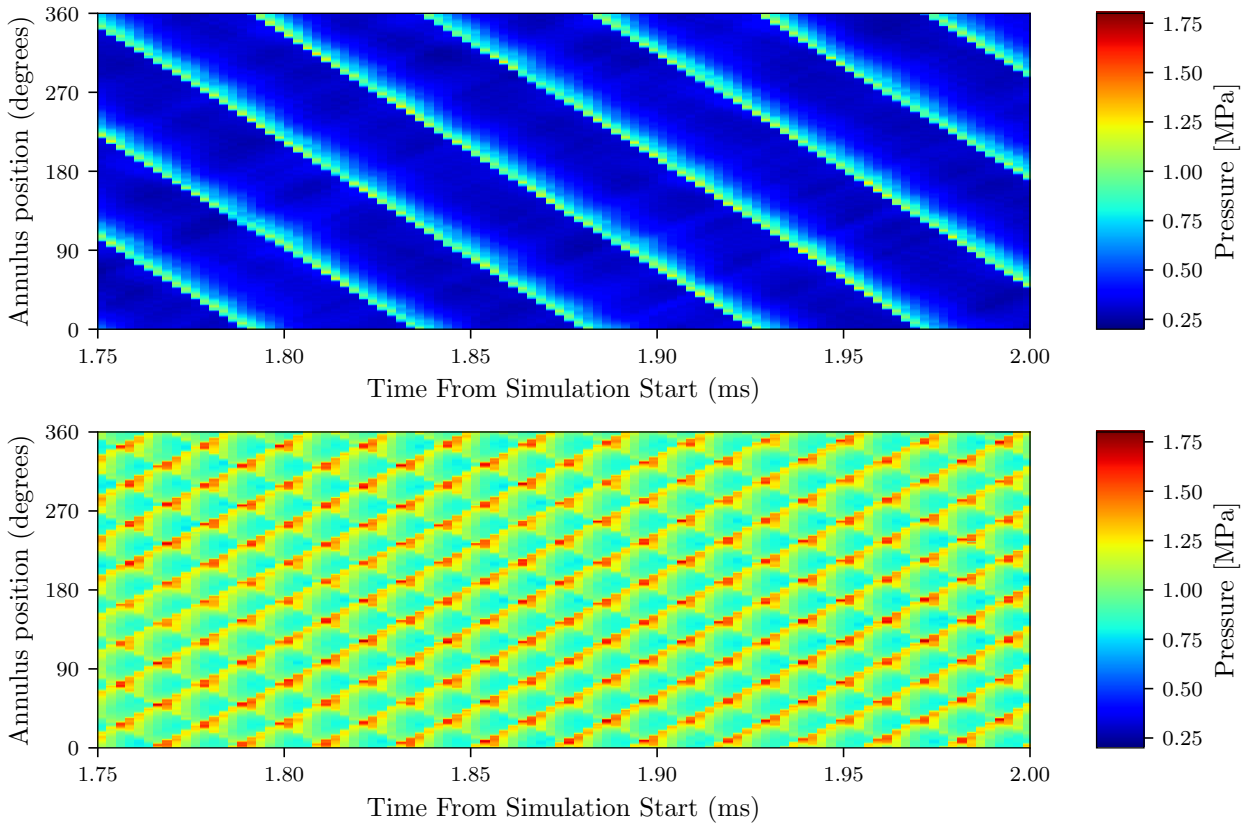

Figure 5.5: θ-t diagrams of pressure during quasi-steady operation, averaged over the 15 mm immediately downstream of injection in 1-degree wedges, for both the unconstricted simulation (top) and constricted simulation (bottom).

Comparing the pressure waves of Fig. 5.5 to the simulation heat release shown in Fig. 5.6, it can be seen that the secondary-direction pressure waves in the unconstricted case did not coincide with any major heat release; instead, the majority of the unconstricted heat release was colocated with the dominant-direction waves. The location of heat release in the unconstricted geometry demonstrates that the secondary-direction pressure waves were able to sustain themselves without being fed by a constant detonative combustion reaction. In the constricted simulation there was also a large amount of heat release corresponding to waves in the dominant direction. However, waves in the secondary direction in the constricted simulation are visible in measurements of heat release, an indication that the constricted simulation did truly exhibit counter-propagating combustion waves, and not just the pres-

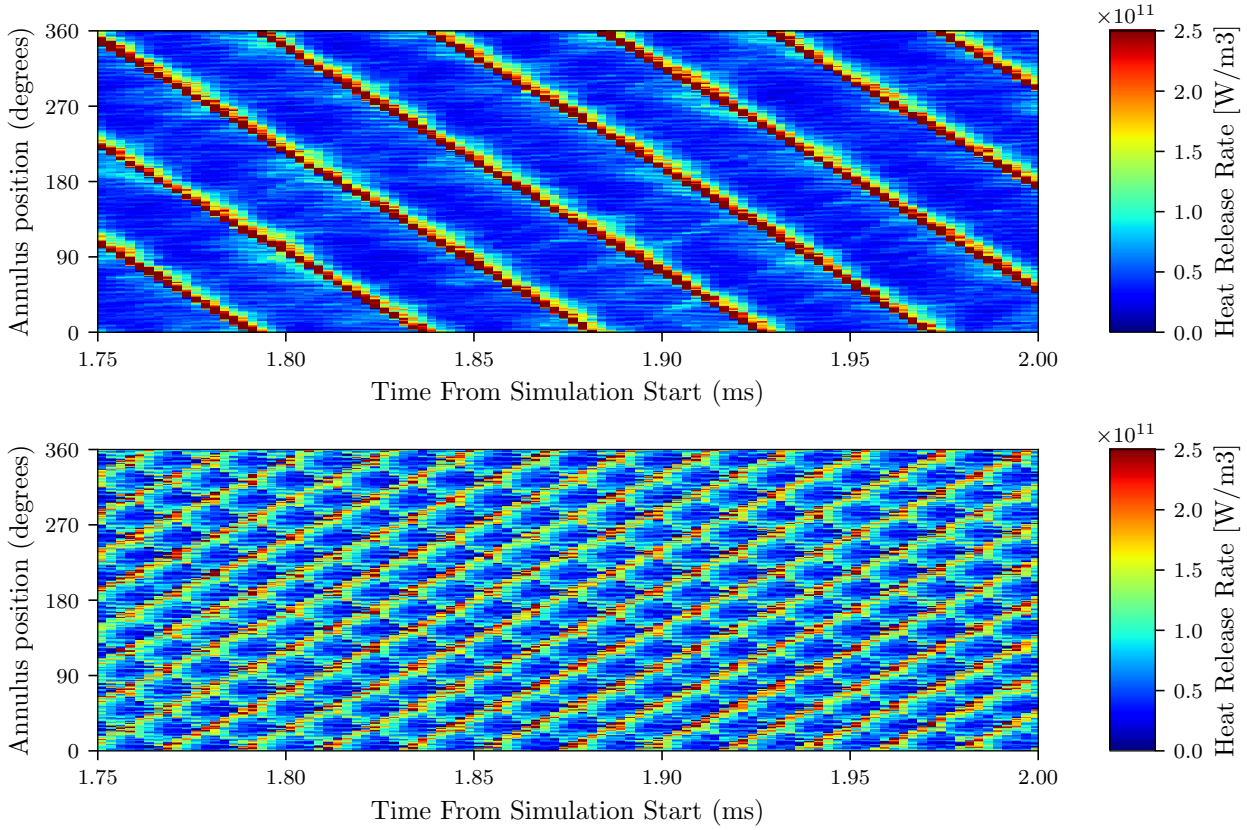

Figure 5.6: θ-t diagrams of heat release during quasi-steady operation, averaged over the 15 mm immediately downstream of injection in 1-degree wedges, for both the unconstricted simulation (top) and constricted simulation (bottom).

sure waves seen in the unconstricted geometry. Horizontal streaks in Fig. 5.6 indicate combustion reactions in a stationary azimuthal location, and correspond to the geometric injector locations. This is probably due to the increased reactability at injection sites, but may suggest that both the constricted and unconstricted geometries exhibited some amount of flame holding at the injectors, one cause of deflagrative combustion.

The amount of reactant present in the first 15 mm of the chamber, as shown in Fig. 5.7, is consistent with the measurement of heat release in Fig. 5.6. In the unconstricted simulation the amount of methane increased until a wave hit, at which time the methane was consumed by the accompanying combustion reaction. In the constricted case this same phenomenon occurred, but with combustion waves travelling in both azimuthal directions. Although in

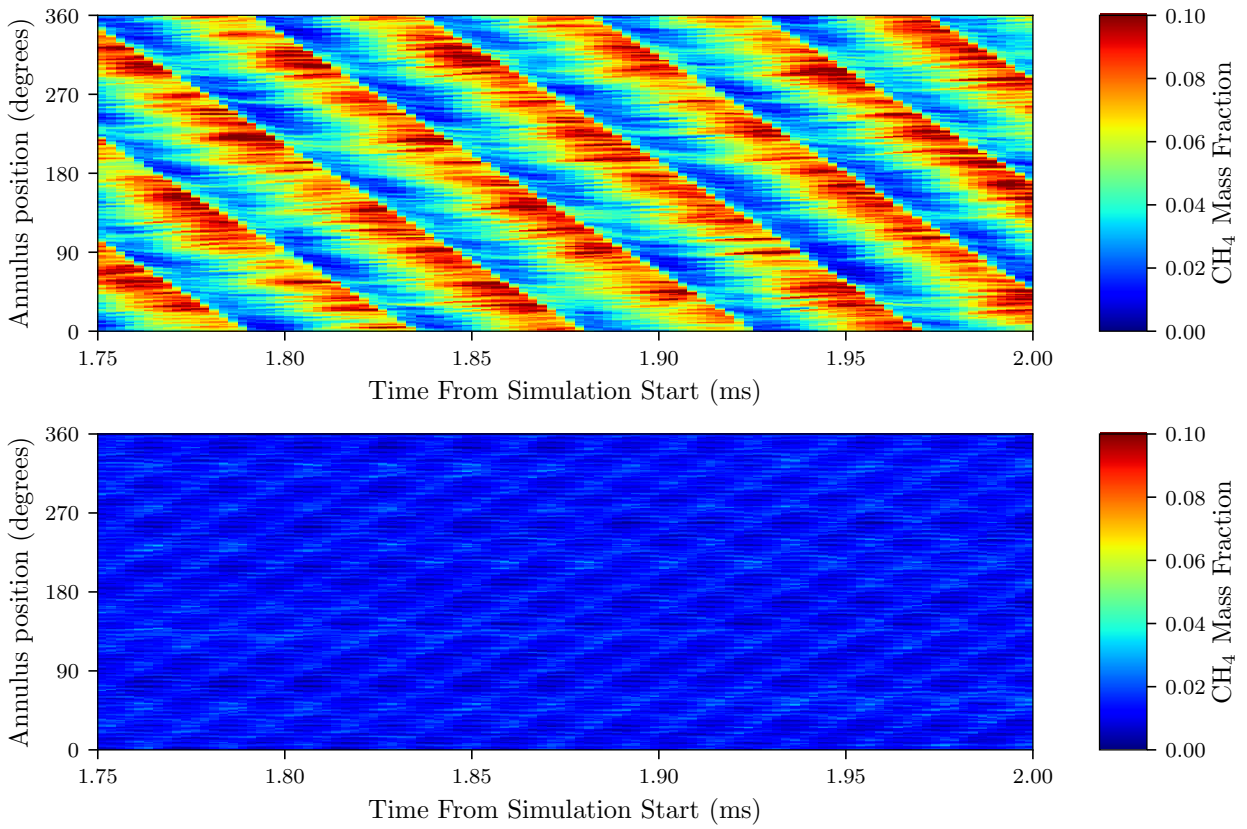

Figure 5.7: θ-t diagrams of mass fraction of CH4 during quasi-steady operation, averaged over the 15 mm immediately downstream of injection in 1-degree wedges, for both the unconstricted simulation (top) and constricted simulation (bottom).

Fig. 5.7 the magnitude of methane mass fraction appears smaller in the constricted case, this is actually as expected for the increased number of waves: these θ-t diagrams are spatial averages, and with an increase in the number of waves a smaller fraction of each integrated volume consisted of unreacted propellant.

5.3.3 Axial Measurements

Composition of the fluid inside the chamber can be seen in Fig. 5.9 for the 5 most prevalent species by mass. The displayed mass fractions are temporally averaged over 0.25 ms, and

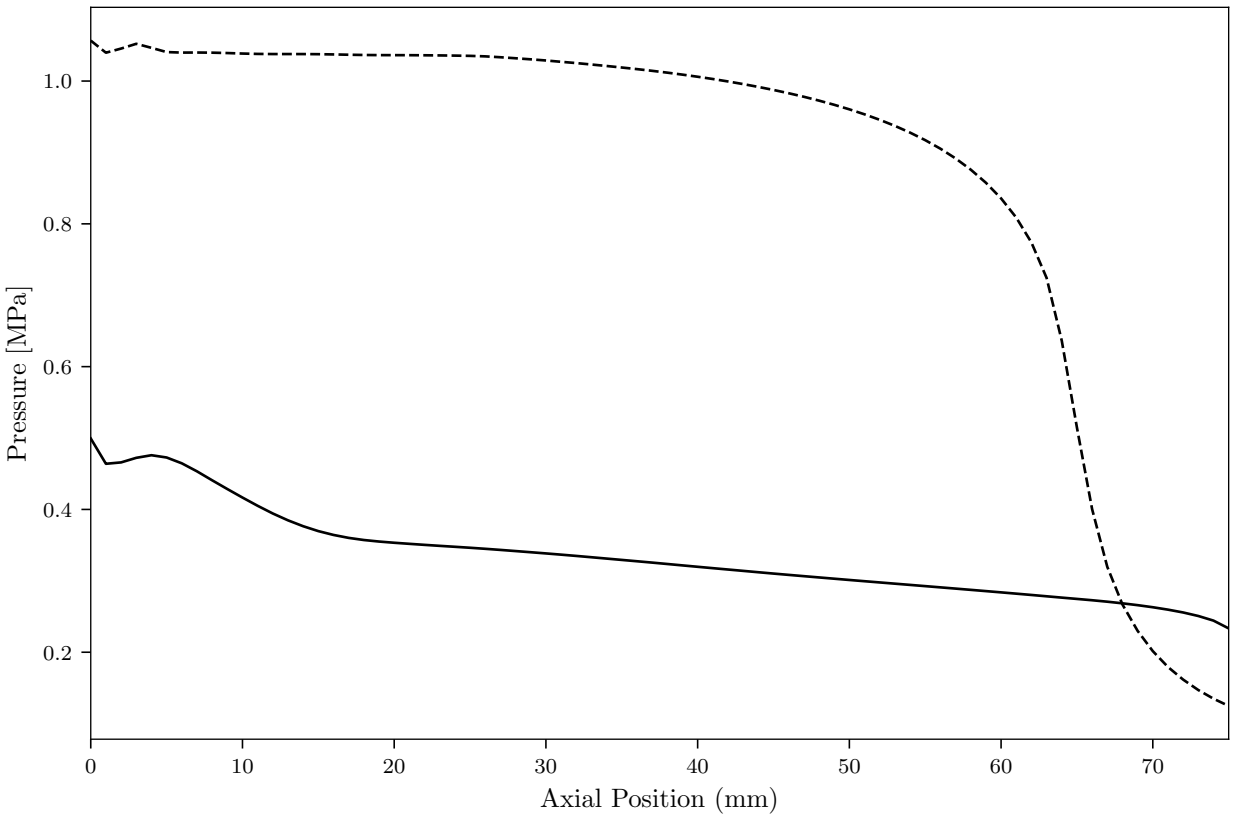

Figure 5.8: Time-averaged static pressure, as a function of axial distance from chamber injection. Dashed line denotes constricted geometry, and solid line denotes unconstricted geometry.

given in a mass-flux-averaged form:

$$\bar{Y}_\mathrm{s} = \frac{\int_A \rho u Y_\mathrm{s}\, dA}{\int_A \rho u\, dA} \tag{5.1}$$

This form has the useful quality that it reproduces the overall mass fraction of the flow at this location, properly normalized so that $\sum_s \bar{Y}_\mathrm{s} = 1$.

Methane serves as a good indicator in Figure 5.9 for the consumption of reactant in both cases, since oxygen is an expected equilibrium product of methane–oxygen detonation, but methane is expected to be completely consumed. The increased number of detonation waves in the constricted case reduced the size of the fill zone, resulting in negligible amounts of methane at an axial distance 10 mm from the injection plane. This is in contrast to the unconstricted simulation, in which methane was still present until an axial distance 20

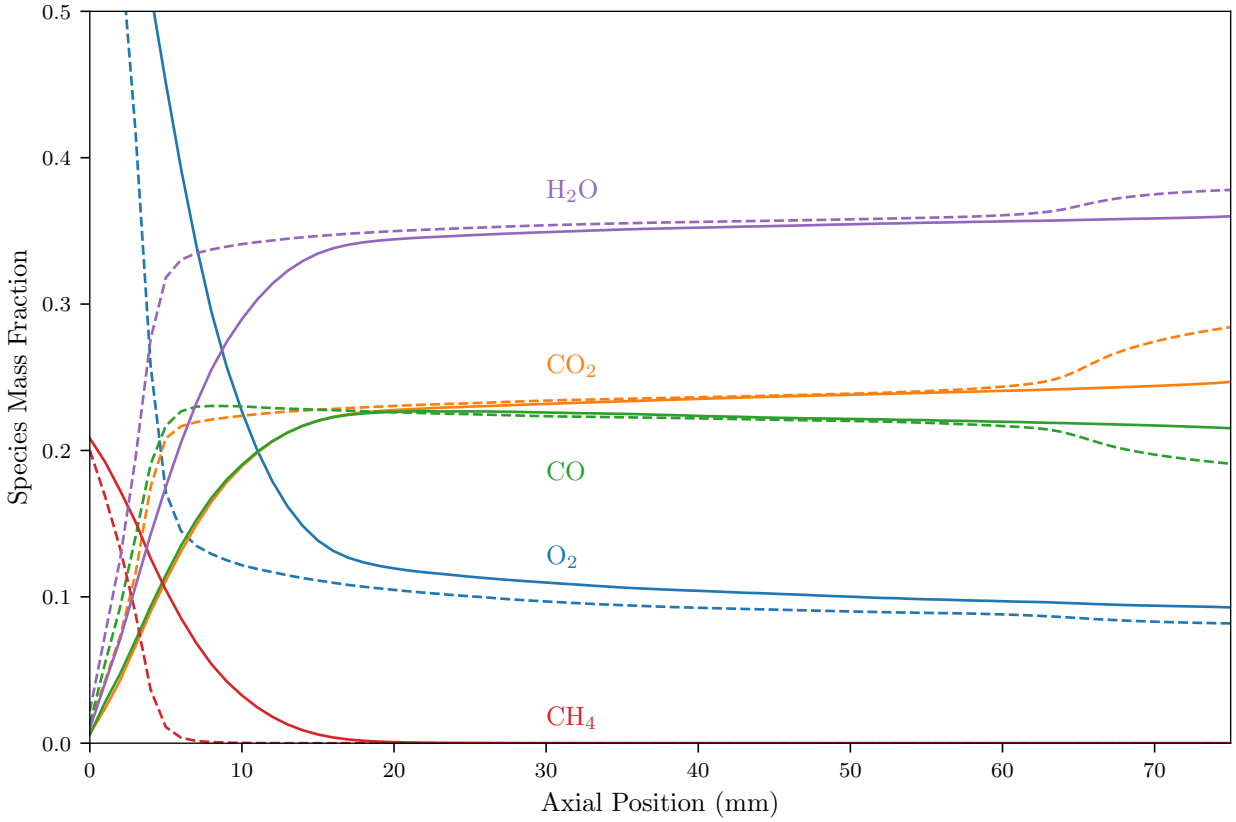

Figure 5.9: Time-averaged mass fractions for the most prevalent species inside the chamber, as a function of distance from injection plane. Dashed line indicates constricted geometry, solid lines denote the unconstricted chamber.

mm from the injection plane. The post-detonation composition, located at axial distances between 20 mm and 60 mm from the injection plane, were largely similar in the two cases – with the notable exception of oxygen, which at every axial location had a greater mass fraction in the unconstricted simulation. The post-throat diverging expansion region (axial positions greater than 65 mm in Fig. 5.9) was represented in species composition as an increased amount of H_2O and CO_2, along with a decrease in CO. This change in composition corresponds to the decreased temperature and pressure in the accelerating flow, and can be explained by the change in equilibrium reaction rates; the equilibrium conditions are further discussed in section 5.5.

5.3.4 Looking for Shock Reflections

Previous experimental results have demonstrated that reflections are sometimes present off of the throat in geometries with sudden constrictions. Such a reflection would travel back into the injection and mixing regions of the combustion chamber, and would have the potential to greatly affect detonation behavior; as such, large scale reflected shocks are one possible mechanism for the creation of counter-propagating behaviors [110]. However, unlike most other studies that exhibit strong reflections of shocks off of a throat, the geometry in this study did not have a sudden constriction, and no strong shock reflections are discernible in a cursory look at the constricted simulation pressure field (as in Fig. 5.10). This absence of easily visible shock reflections incentivizes a closer look at whether or not the constricted geometry exhibits large-scale shock reflections during the quasi-steady operating regime.

The expected wave reflections are caused by shock structures; consequently, pressure gradients reveal associated waves more clearly than static pressure. The scalar field calculated by finding the magnitude of the gradient of the pressure is displayed in figure 5.11. Several secondary wave structures are visible in the figure, both in the unconstricted case and in the constricted simulation. One such structure appears to be formed by pressure waves reflecting off of the discrete injectors. In the unconstricted geometry these waves formed parallel lines, travelling upstream in the annulus until interacting with the detonation's shear layer. Counter-propagating behavior in the constricted case caused these structures to appear as a "cross-hatch" pattern between the detonations and oblique shocks. However, the snapshots of pressure gradient do not reveal any large-scale shock waves travelling downstream in the constricted chamber.

One difficulty with the visualization presented in figure 5.11 is that it is a static snapshot: it is difficult to tell which direction the structures are travelling. This is a major shortcoming when attempting to find wave reflections propagating towards the injectors. Figure 5.12 does a better job, by representing pressure variations at several axial positions (with 1 mm spacing); the horizontal axis denotes time, and the vertical axis denotes axial position. One consequence of the time axis is that the direction of structures visible in 5.11 is indicated by

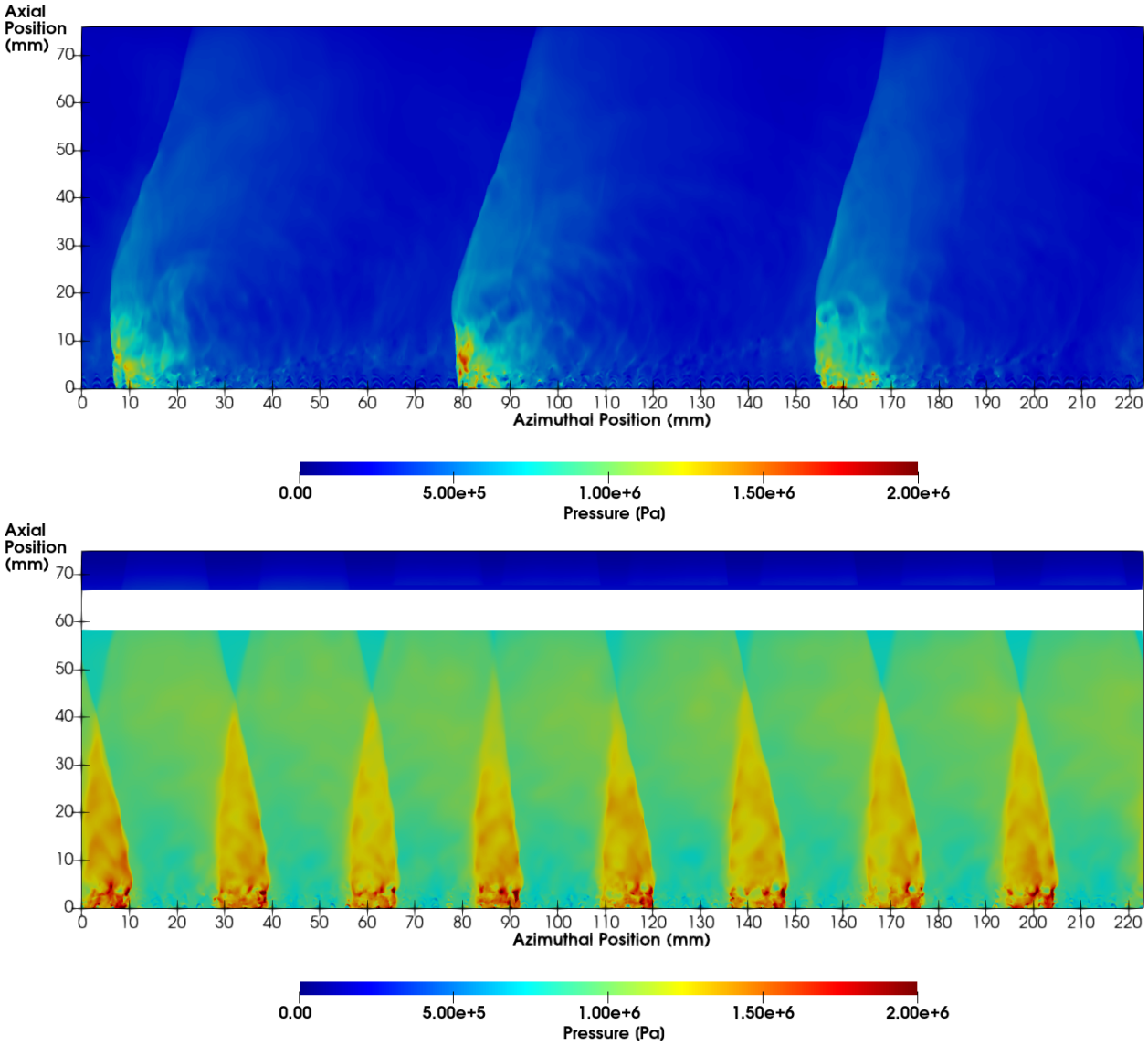

Figure 5.10: Snapshots of unwrapped center-channel pressure fields, for the unconstricted (top) and constricted (bottom) simulations. White space in constricted field is due to intersection of nozzle with channel-center plane.

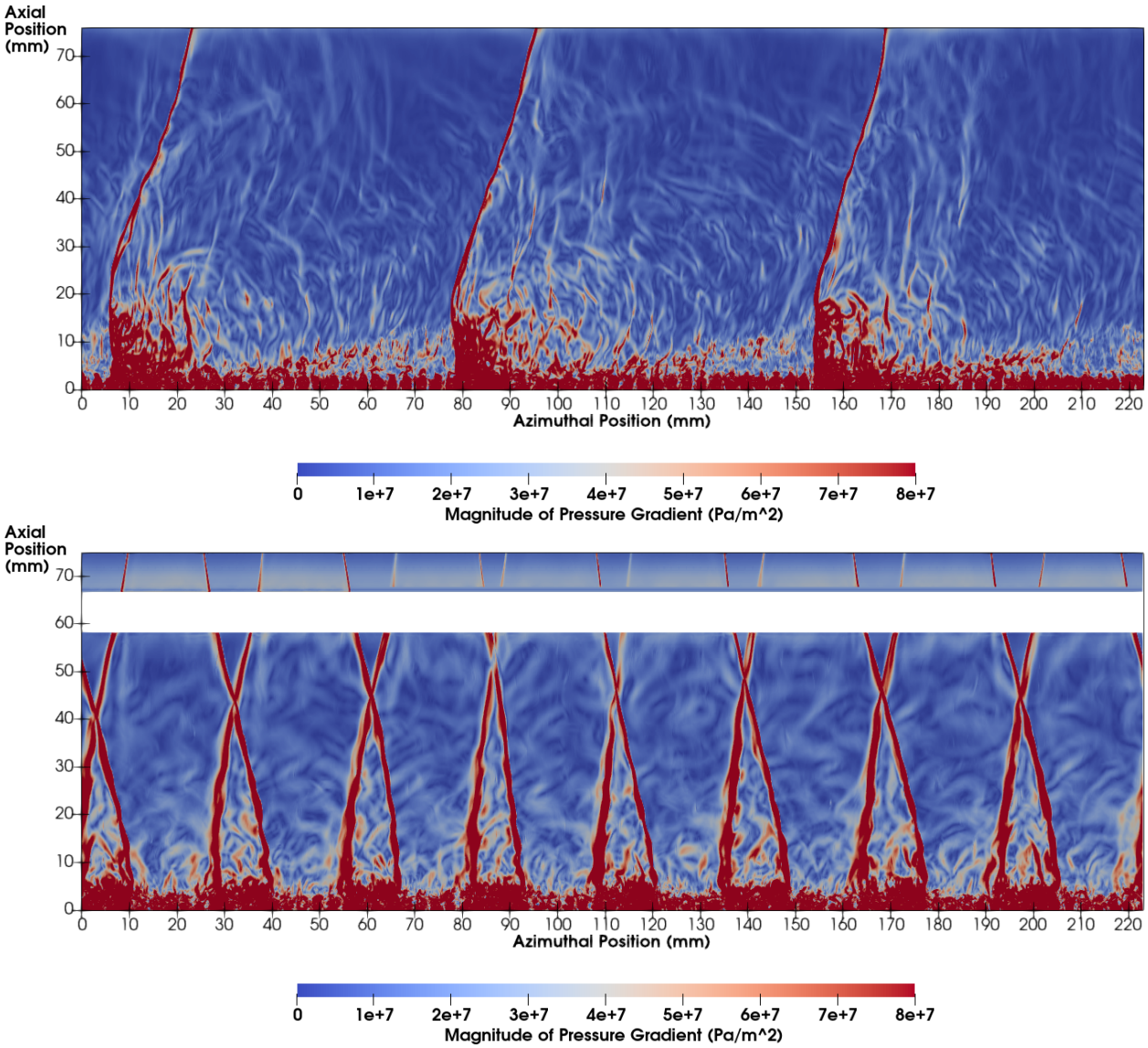

Figure 5.11: Snapshots of unwrapped center-channel pressure gradient fields, for the unconstricted (top) and constricted (bottom) simulations. White space in constricted field is due to intersection of nozzle with channel-center plane.

the associated line's slope in figure 5.12: a wave travelling downstream toward the chamber exit appears as a positive slope. The lack of azimuthal representation in figure 5.12 means that, although the detonation waves are represented in pressure, the azimuthal direction of each wave cannot be determined using these axes alone: waves in the constricted case appear to be the same shape, even when they are traveling in different azimuthal directions.

Secondary wave structures structures in figure 5.12 can again be isolated by calculating a gradient. Although this approach does emphasize flow features, as is shown in 5.13, one dimension of the gradient is in time; magnitudes should not be directly compared to the purely spatial gradients in figure 5.11. However, both the constricted and unconstricted cases show a large number of background waves propagating towards the exit of the annulus, and these are likely the same features revealed by the gradients in figure 5.11.

Any wave reflections off the throat in figure 5.13 should appear as lines with negative slope, propagating down from where shocks intersect the throat. Although there are some features that may correspond to this sort of reflections, the flow is primarily dominated by structures traveling towards the exit. This does not disprove the existence of acoustic features influencing the dynamics of the engine, but any large scale effects caused by pressure reflections must be due to a buildup of a large number of small periodic waves, e.g. some resonance effect or creation of a longitudinal mode, as opposed to something caused by a single large pressure wave.

5.4 Flow Acceleration

The Mach number of the flow inside the combustion chamber is presented in Fig. 5.14 for both simulations. In the unconstricted RDRE, the flow transitioned from subsonic to supersonic in pockets behind the oblique shock structure. This is consistent with the 2D results of Zhdan et al. [50], and has been seen in other numerical works. Many previous results forced supersonic conditions in the chamber outflow; by contrast, this simulation included a large exhaust plenum in the simulation domain, and so there is no numerical

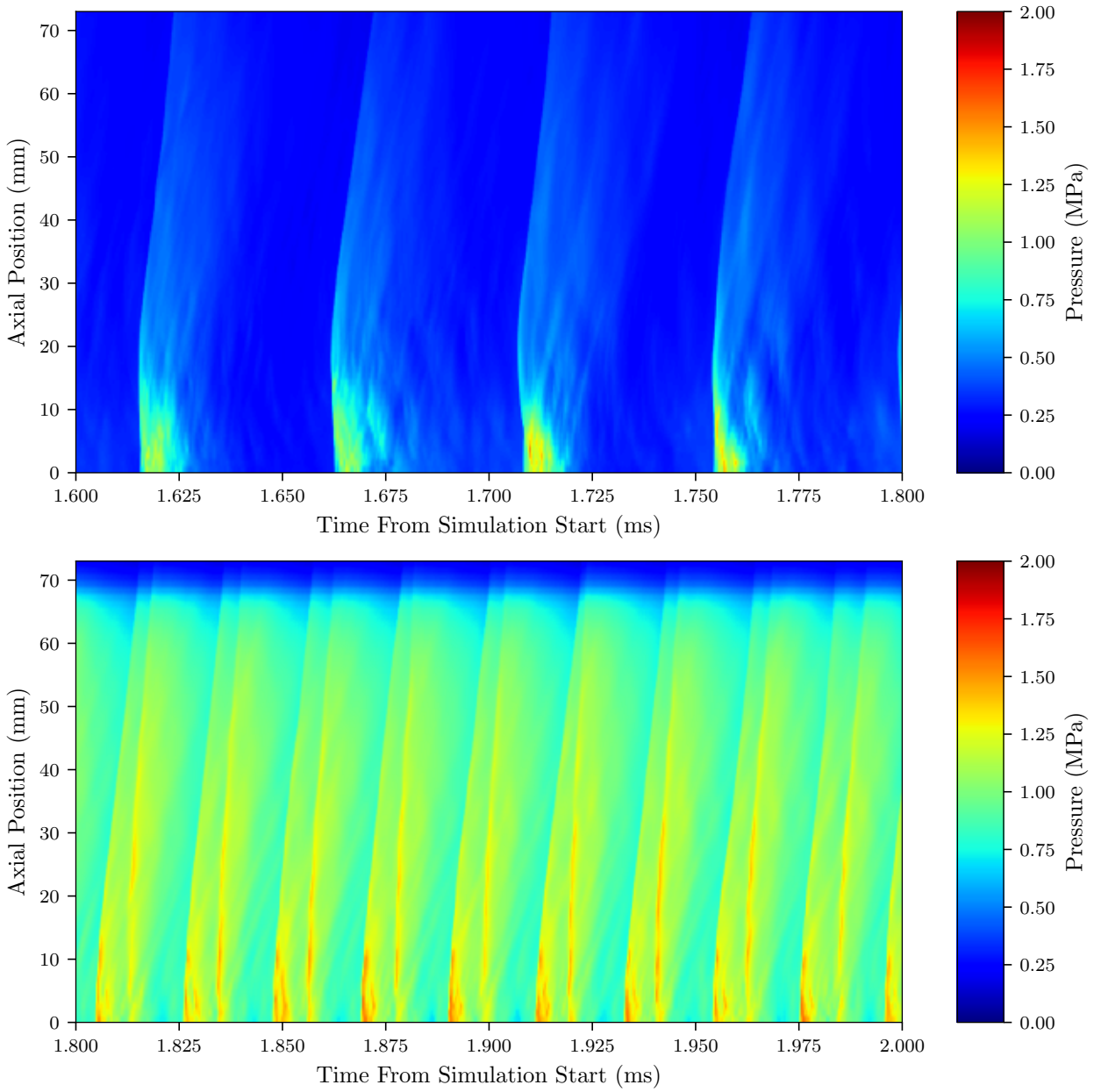

Figure 5.12: Visualization of pressure variation 1 mm from the outer wall, at a single azimuthal location but varying in axial position. Shown for the unconstricted simulation (top) and constricted simulation (bottom).

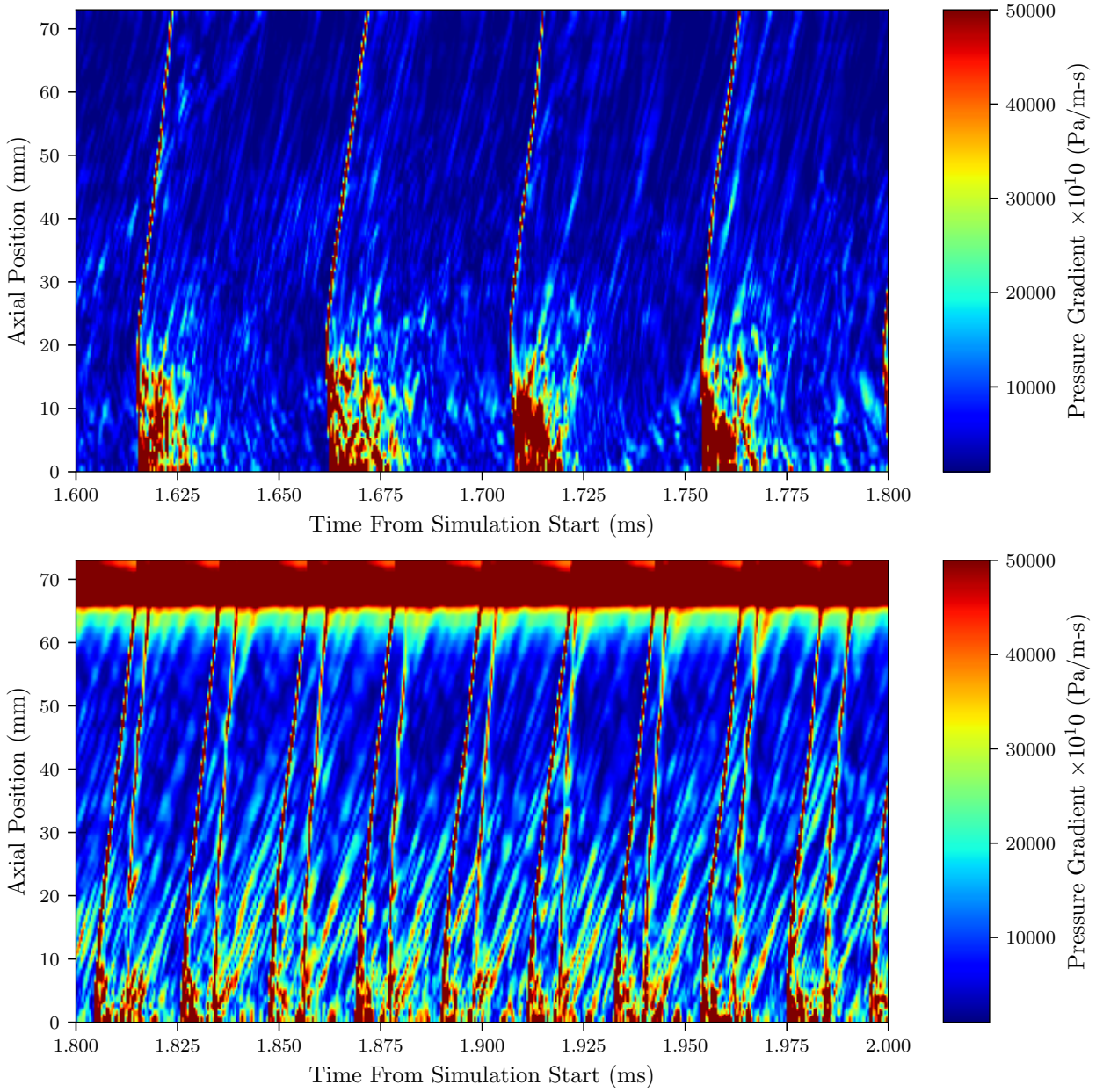

Figure 5.13: Visualization of gradient in pressure variation, 1 mm from the outer wall, at a single azimuthal location but varying in axial position. Shown for the unconstricted simulation (top) and constricted simulation (bottom).

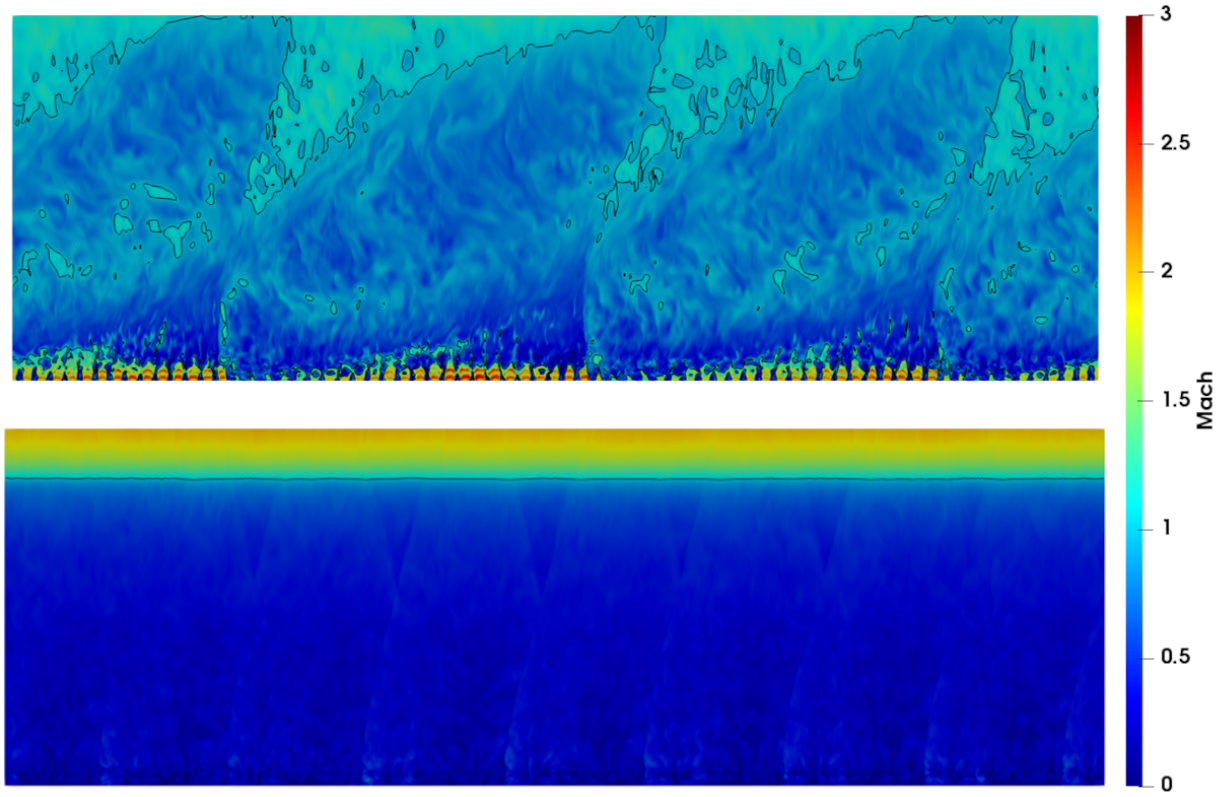

Figure 5.14: Chamber Mach fields, for the center-channel of an unconstricted RDRE (top) and the throat-center of a constricted RDRE (bottom). Black line represents sonic isocontour.

condition forcing the flow to reach Mach 1 at the exit of the chamber. The amount of the flow which chokes before leaving the engine is indicated in Fig. 5.15, which shows the percentage of the flow which is supersonic at each axial location,

$$\frac{\int_{A_{supersonic}} \rho u \, dA_{supersonic}}{\int_A \rho u \, dA} \tag{5.2}$$

In the unconstricted simulation the majority of the flow was thermally choked before reaching the exit of the chamber – however, Fig. 5.15 suggests that an engine with a shorter length may be partially subsonic at the chamber exit.

In both cases there existed a region of supersonic flow near the injection region of the chamber. This was a consequence of the injection scheme, in which usually-choked injection of reactants was followed by expansion inside the chamber. The post-injection expansion accelerates the flow, as visible in Fig. 5.14, and accounts for the near-injection supersonic regions in Fig. 5.15.

In the simulation with gradual constriction, the flow reached Mach 1 only at the physical throat. Unlike in the unconstricted case, there were no pockets of supersonic flow behind the oblique shock. Instead, the flow transitioned in its entirety from subsonic to supersonic at the physical throat location; this is a direct application of the classical Mach-area relationship, which requires that the cross-sectional area be neither increasing nor decreasing when the flow reaches the sonic condition.

That the Mach-area relation holds so completely for an RDRE with converging-diverging nozzle shows a fundamental difference between designs with and without a gradual constriction: the gradual constriction changes the acoustic conditions of the chamber, effectively enforcing an acoustic length in the axial direction in accordance with the throat. This is something that needs to be taken into account when considering the detonation dynamics of an RDRE – while the severity of a constriction may change properties of reflected shock waves traveling into the chamber, this means a gradual constriction can affect detonation dynamics even without considering reflections of the oblique shock structure. Although there are complicated dynamics associated with constricted RDRE detonations, this effect may

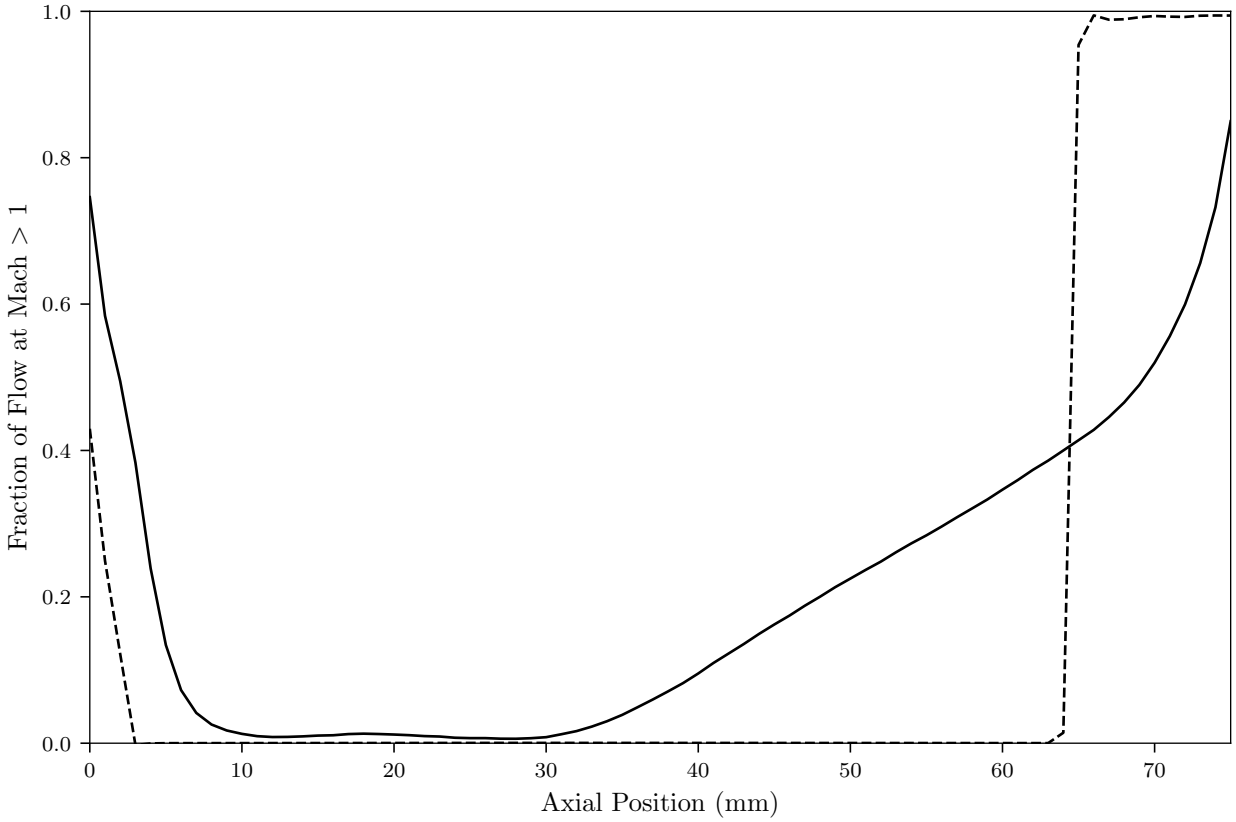

Figure 5.15: Fraction of the flow which is supersonic at each axial position for an unconstricted RDRE, time averaged over 250 μs, for both the unconstricted (solid line) and constricted (dashed line) geometries. Fraction of total mass flux is defined in equation 5.2.

provide utility when designing a practical device; moreover, the complete choking with a gradual constriction is useful when designing simulations that require supersonic boundary conditions.

5.4.1 Idealized Analytic Model

The Mach field shown in Fig. 5.14 for unconstricted geometries is consistent with previous simulations: the field in the lab frame is supersonic behind the oblique shock, with a subsonic hot product region separated from the supersonic zone by a slip line. The setup of a flowfield of this sort, in which the flow upstream of the shock is subsonic but the flow downstream of the shock is supersonic, is only possible because the shock is not stationary in the lab frame.

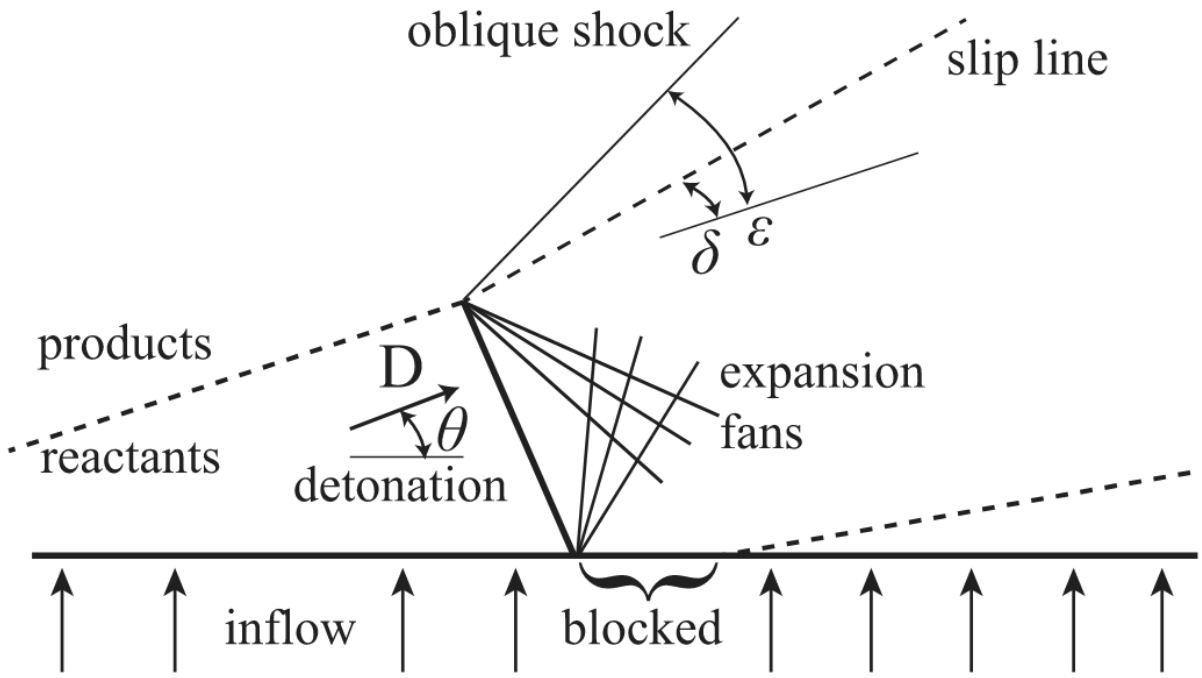

Figure 5.16: Diagram of model for 2D analysis of an RDE field, from Fievisohn and Yu [114].

In the detonation frame, there is no contradiction: the flow is supersonic upstream of the oblique shock, then is turned by an oblique shock. The turn of the flow is enough to make the flow supersonic in the lab frame.

5.4.1.1 Ideal Post-Oblique Mach Number

The turning of the flow field by the oblique shock, and the effects of the change in frame, can be examined using simplified analytic models of an RDRE flow field. One useful model was discussed by Fievisohn and Yu as a building block for the development of a method of characteristics solver for evaluating flow fields [114]. By assuming that all combustion occurs in a Chapman-Jouguet detonation zone, that the post-detonation flow is turned by two centered expansion fans, and that pressures match across contact surfaces, determining the post-shock flowfield reduces to a system of nonlinear equations. Following the geometry in Fig. 5.16, there are three main regions of the flowfield: the reactant fill zone, post-detonation products, and the post-oblique region. For this model all combustion is considered to occur

in the detonation wave, so that the three regions can be considered calorically-perfect frozen flow.

Considered in the detonation frame, the fill zone is separated from post-detonation region by a contact surface and by a tilted C-J detonation; the flow in this region travels at an angle θ, which is dictated in the axial direction by injection velocity and in the angular direction by the frame-shift velocity required to keep the C-J detonation stationary. Although in this geometry the detonation is travelling axially downstream into the injectors, the effect of that reflection is not directly considered. The contact surface separating reactants from products allows for a pressure-matching condition between the two regions.

The post-detonation region contains two centered expansion fans, and it is possible to fully evaluate this region using a method of characteristics solver. However, it can also be assumed that on the product side of the contact surface the flow is in the same direction as the reactant zone. This is a simplifying assumption equivalent to saying that the product streamline near the contact surface goes through both centered expansion fans, resulting in negligible net change in angle. The post-detonation region is separated from the post-oblique region by a slip line, and the pressure along the slip line is dictated by the Prandtl-Meyer expansion.

The oblique shock relations further connect flow in the post-detonation region to flow in the post-oblique region. Putting all of these relations together creates a closed system of equations for solving the flow in the post-oblique-shock region. If the injection velocity, premixed composition, and pressure are known, the angle θ and post-detonation pressure p_{e2} comes from the C-J solution. The expansion fans turn the flow, and in the C-J solution the post-detonation Mach number is 1, so the pre-oblique Mach number M_{e3} is related by the Prandtl-Meyer function ν:

$$\delta = \nu(M_{e3}) \tag{5.3}$$

The pressure in the pre-oblique section of the post-detonation region is an isentropic

expansion from p_{e2} to p_{e3}, M_{e3} using the post-detonation ratio of specific heats γ_e

$$p_{e3} = p_{e2}\left[\frac{1+\frac{\gamma_e-1}{2}}{1+\frac{\gamma_e-1}{2}M_{e3}^2}\right]^{\frac{\gamma_e}{\gamma_e-1}} \tag{5.4}$$

The post-expansion Mach number is the value number going into the oblique shock, and can be used in the oblique shock relations:

$$\tan(\delta) = 2\cot\epsilon\left[\frac{M_{e3}\sin^2\epsilon - 1}{M_{e3}^2(\gamma_e + \cos 2\epsilon) + 2}\right] \tag{5.5}$$

Matching pressures using shock relations, C-J solution, and contact surfaces then turns this into a system of equations that can be solved. The velocities can then be converted back into the lab frame, allowing Mach numbers to be calculated for either frame in any of the regions.

The post-oblique shock flow calculated with this approach is most precisely related to the streamline closest to the detonation and the detonation/oblique shock transition; even in this simplified geometry, the streamlines elsewhere are curved according to the centered expansion fans. However, in a real engine, the post-oblique field at that location is also a region greatly affected by non-ideal features of the flow; injector dynamics, burning across the contact surface, Kelvin-Helmholtz instabilities, and mixing-field effects that change the detonation shape can all impact the flow characteristics in this region. The model is useful as an analysis tool for evaluating overall trends and relationships between flow regions, but beyond that is of limited utility without further machinery (e.g. a method of characteristics solver, injector properties, parasitic deflagration modeling, etc.).

The result of this idealized model, using $\phi = 1.1$ and reactant temperature of 300 K, is shown in Fig. 5.17, in which the calculation is performed for a range of premixed reactant pressures. Considering Fig. 5.17 in the context of Fig. 5.8, which has average pressures that can be used as upper bounds of reactant pressures, the pressures in these engines would lead to supersonic flow behind the oblique shock in an ideal RDRE. Although this model greatly simplifies many of the features present in a real flow – there's no consideration of mixing fields, curved shocks, non-centered expansion fans, or three-dimensional effects – it

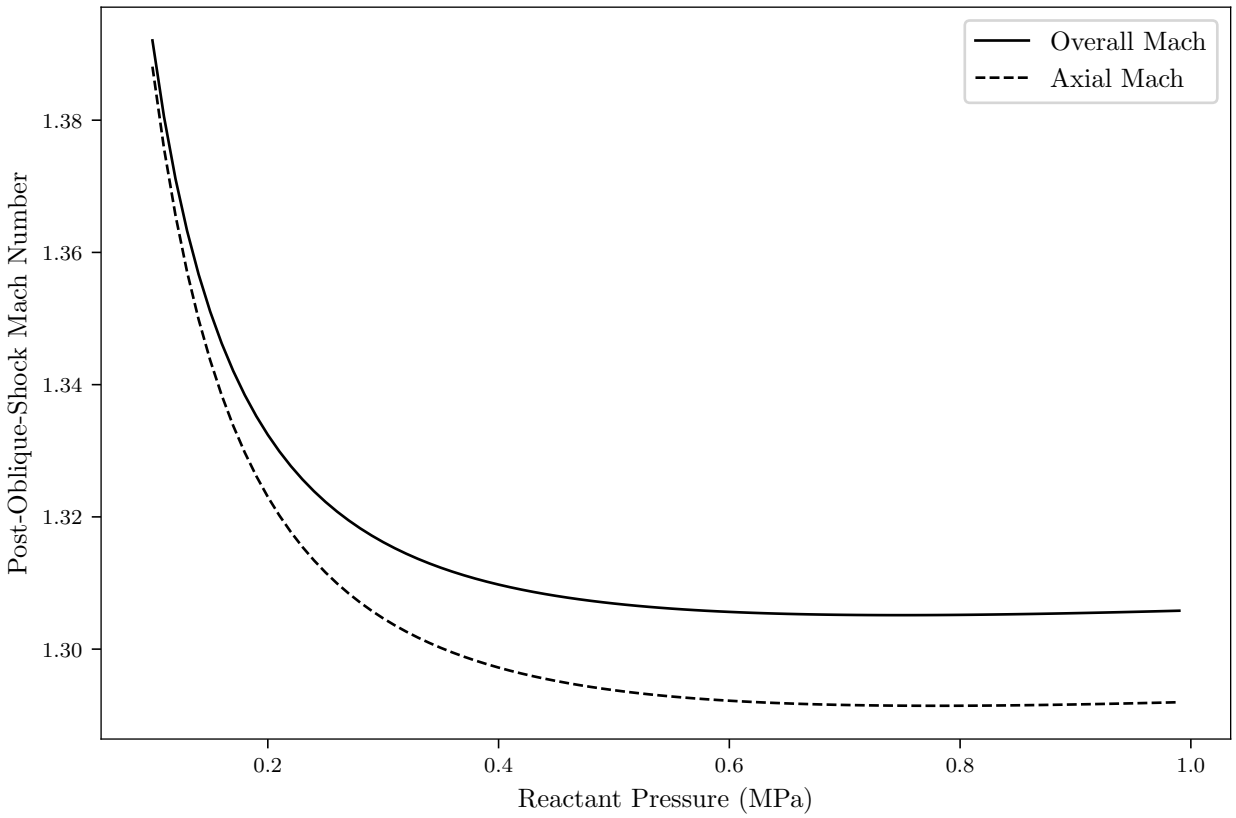

Figure 5.17: Mach number behind the oblique shock of an ideal RDRE geometry, with C-J detonation of premixed methane-oxygen reactants at $\phi = 1.1$ and 300 K.

does predict supersonic flow in the post-oblique region, as is seen in the simulation of an unconstricted engine.

5.4.2 Considering Parasitic Deflagration

The constricted geometry is not as straightforward to assess using ideal two-dimensional models. Considered in three dimensions, a supersonic region upstream of a constriction would necessitate the formation of a shock to turn the flow. The formation of a new set of shocks would not in itself prevent regions of axial supersonic flow from existing upstream of the chamber constriction in an RDRE, but it does demonstrate that the addition of a converging section to an RDRE chamber necessitates large changes in the flowfield, and may be another mechanism for unsteadiness in converging nozzles with the potential to affect the field in the detonation region. However, in the constricted simulation presented in this work, no supersonic regions were detectable behind the oblique shocks during quasi-steady operation. On a qualitative level, this may be made possible by the counter-propagating phenomenon: each streamline traveled through a large number of shocks, each of which decelerated the flow – even though the pre-detonation pressures are still at the levels examined in Fig. 5.17.

The lack of supersonic regions in the constricted simulation raises a question: what is necessary for an RDRE to operate without supersonic regions in the combustion chamber? Although the model used in Fig. 5.17 to consider the turning of a flow is not suitable for direct application to any engine with large counter-propagating behavior, the model can be extended to consider what would be required for a co-rotating engine to reach stable operation with no post-oblique supersonic region.

One feature of RDREs that has a large impact on operation is the tendency of the reactants to combust before the arrival of the detonation. If this parasitic combustion is modeled as occurring uniformly in the fill region prior to the arrival of the shock, the partially-combusted flow can be used as the starting condition when considering the ideal flow turning within an RDRE. Fig. 5.18 is the result of using the same idealized model, but starting with the injection of partially-combusted reactants: assuming injected 300 K, 0.1 MPa, $\phi = 1.1$

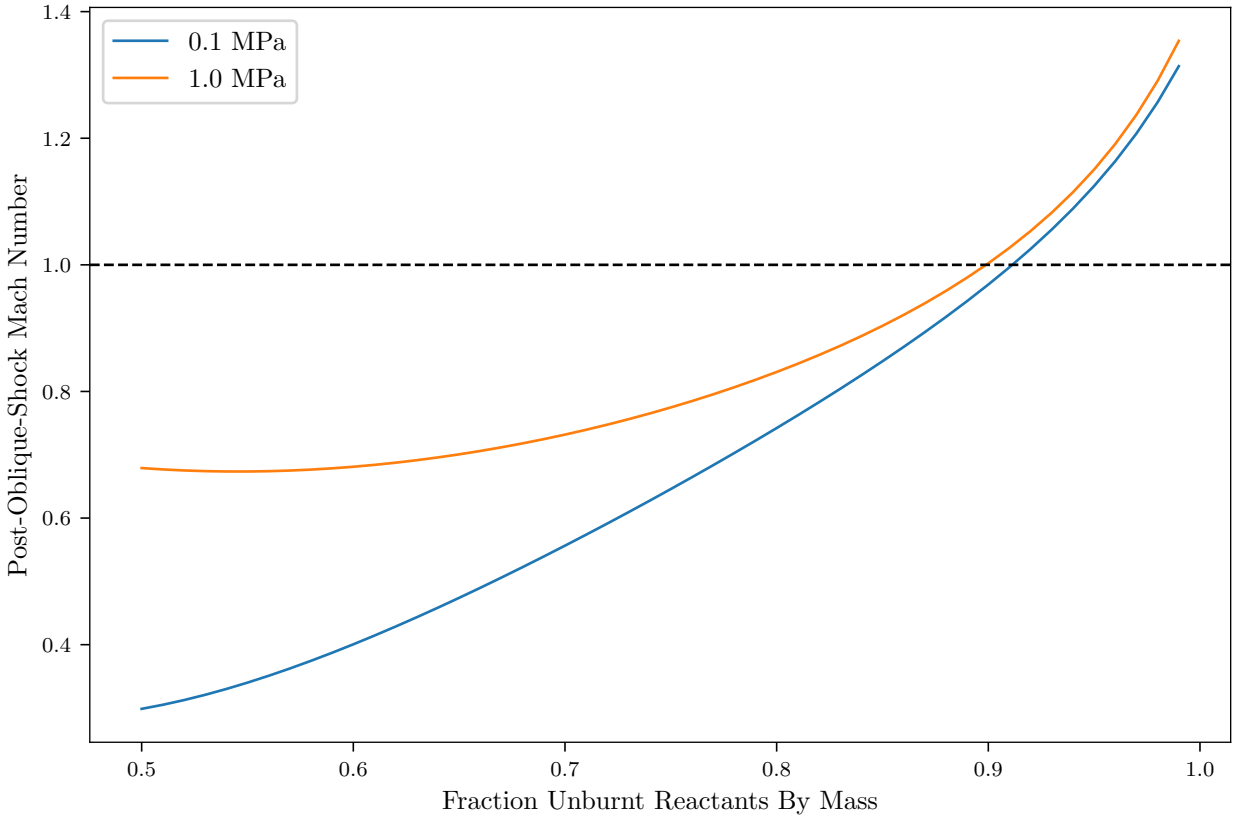

Figure 5.18: Mach number behind the oblique shock for an ideal RDRE operating with an injection of partially combusted methane/oxygen at $\phi = 1.1$, plotted for two reactant pressures: 101 KPa and 506 KPa.

methane/oxygen flow, deflagrated propellant is assumed to completely mix with unburnt reactants before the arrival of a C-J detonation. Although the specific geometry of the model is over-idealized, Fig. 5.18 demonstrates that stable operation of an RDRE may be made possible without supersonic post-oblique regions when the engine contains a large amount of parasitic deflagration. Counter-propagating behavior likely contributes to this: each detonation interacts with partially preburnt propellant, which even in the case of an ideal C-J detonation has the potential to weaken the detonation enough to prevent supersonic flow in the post-oblique region.

The model used to generate Fig. 5.18 does not explain how counter-propagating waves develop, or what sustains the behavior. Instead, it demonstrates that there are situations in which an RDRE may operate without supersonic flow in the post-oblique region; the discussion aims to provide some intuition into how an RDRE may operate without any supersonic regions upstream of a physical constriction. Parasitic deflagration provides one mechanism that can decelerate the post-oblique flowfield, and may contribute to flow accelerating from subsonic to supersonic in the classic De-Laval fashion.

5.5 Enthalpy Conversion

A nozzle's acceleration of the flow increases thrust, and so it becomes difficult to determine to what extent the performance of an RDRE with a nozzle is affected by any change in detonation dynamics. One way to approach this is to consider what is meant by performance: on a fundamental level, the goal of a rocket engine is to convert the propellant's latent energy into a kinetic form. Combustion changes the composition of the propellant, which releases energy that can then be used to accelerate the flow. In a simulation, the energy released by this change in composition can be tracked directly by considering the change in formation enthalpy inside the chamber.

The change in formation enthalpy due to reactions inside the engine can be evaluated by considering the composition flowing through a surface S inside the engine:

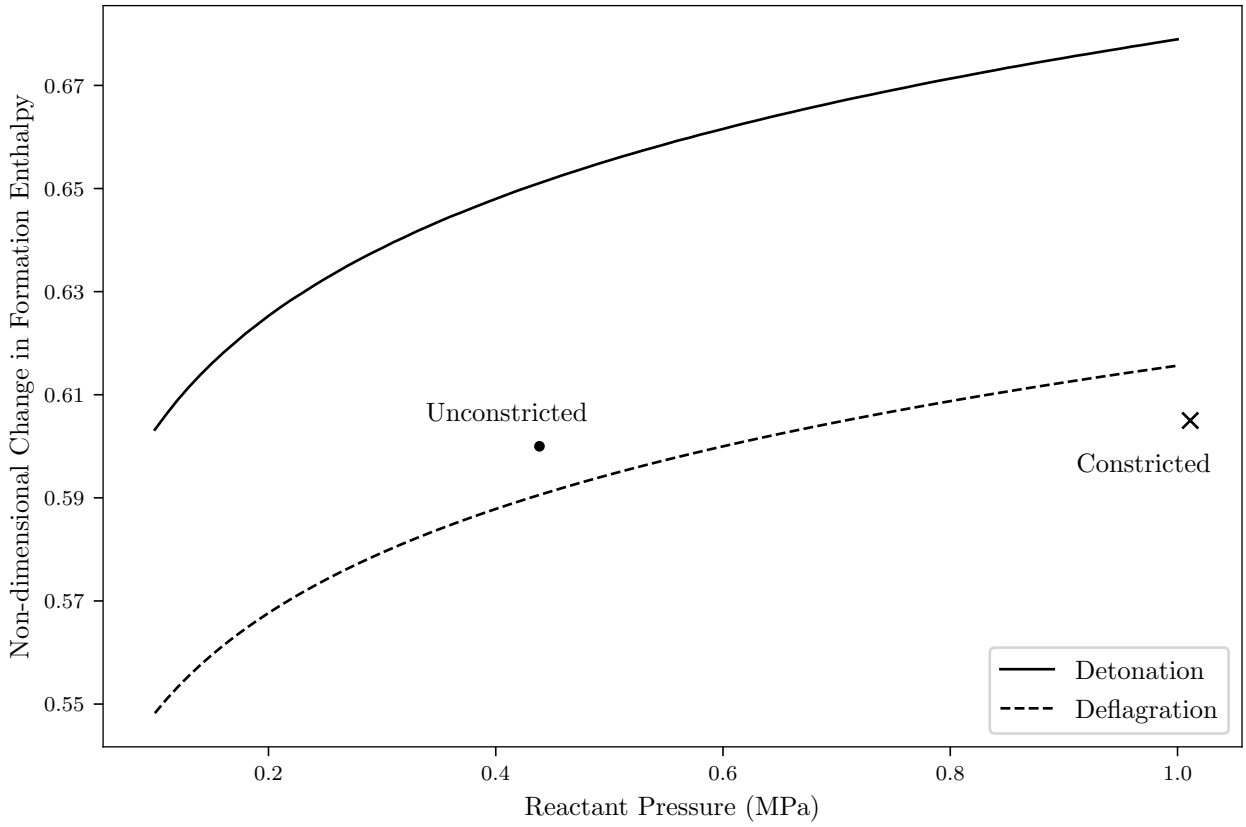

Figure 5.19: Change in formation enthalpy expected for constant-pressure combustion of methane–oxygen flow, starting $\phi = 1.1$ and T=300 for a range of combustion pressures, and non-dimensionalized by the amount expected for complete combustion, as in Eq. 5.7. Measurements from the simulations are also plotted, with values of the change in formation enthalpy taken 20 mm downstream of injection.

$$\Delta H^0 = \int_S \sum_s \left(\frac{Y_s}{\mu_s} h_s^0\right) \rho \mathbf{u} \cdot d\mathbf{S} - \left(\dot{N}_{CH_4} h_{CH_4}^0 + \dot{N}_{O_2} h_{O_2}^0\right) \tag{5.6}$$

where Y_s is the mass fraction of species s, μ_s is the molar mass, h_s^0 is formation enthalpy per mole of species s, $\dot{N}_s$ is moles per second, ρ is density, and $\mathbf{u}$ is the fluid velocity. The value of ΔH^0 can be nondimensionalized using the change in enthalpy due to complete single-step combustion,

$$H^* = \frac{\Delta H^0}{\Delta H^0_{\text{complete}}} \tag{5.7}$$

where $\Delta H^0_{\text{complete}}$ comes from the single-step reaction $CH_4{+}2O_2 \rightarrow 2H_2O{+}CO_2$:

$$\Delta H^0_{\text{complete}} = \dot{N}_{O_2} h^0_{H_2O} + \frac{1}{2}\dot{N}_{O_2} h^0_{CO2} + \left(\dot{N}_{CH_4} - \frac{1}{2}\dot{N}_{O_2}\right) h^0_{CH_4} - \left(\dot{N}_{CH_4} h^0_{CH_4} + \dot{N}_{O_2} h^0_{O_2}\right) \tag{5.8}$$

Fig. 5.19 lends some intuition to what the nondimensionalized change in formation enthalpy metric means. Calculated using Cantera, the figure displays the values of H^* for ideal combustion of methane–oxygen at an equivalence ratio of 1.1, starting at 300 K. Ideal deflagration was modeled using constant-pressure equilibration, while ideal detonative combustion was modeled using a Newton-Raphson iterative solver to determine post-CJ conditions, and then those conditions were expanded back to the initial velocity. This analysis demonstrates for both forms of combustion that the higher the reactant pressure the more energy is released through changes in composition. The gap between solid and dashed line in Fig. 5.19 represents the difference in energy release between an ideal constant-pressure engine and a detonation-based device; the goal of an RDRE is to operate between the two lines.

Comparing the two simulations using equation 5.7 and Fig. 5.19 requires choosing a location to measure the enthalpy, and evaluating the reactant pressure prior to combustion. Reactant pressures inside the chamber were measured by evaluating the average pressure in the simulation for regions that are primarily reactant,

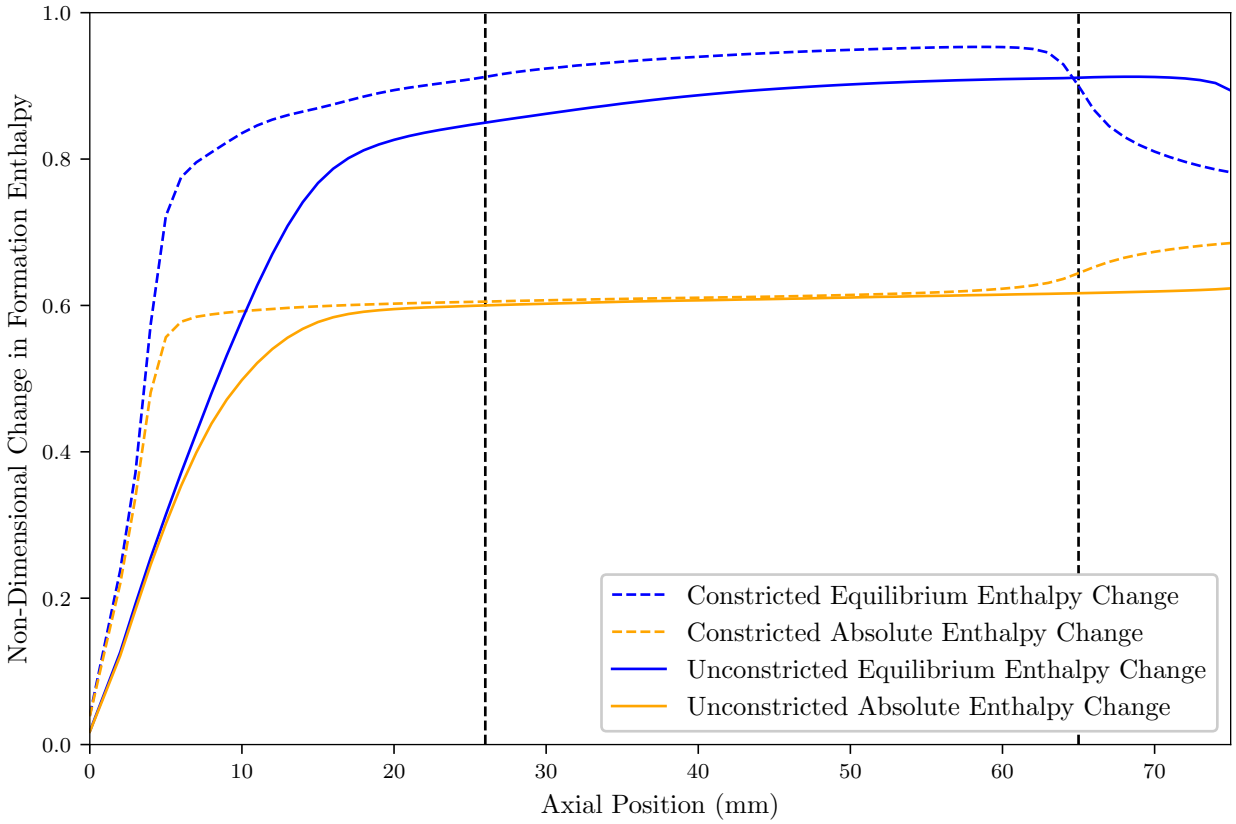

Figure 5.20: Change in enthalpy of formation of the two geometries, given in non-dimensional forms scaled against idealized combustion and compared to equilibrium conditions, as defined in equations 5.7 and 5.10 . Vertical lines at 26 mm and 65 mm indicate constriction start and constriction throat, respectively.

$$p_{\text{reactant}} = \frac{\int_V \rho p \, dV}{\int_V p \, dV} \tag{5.9}$$

where V indicates the volume inside the chamber where $Y_{CH_4} + Y_{O_2} \geq 0.8$. Fig. 5.20 suggests that the choice of axial distance from injection does not affect the value H^* all that much, as long as the enthalpy of formation is evaluated downstream of the detonation region but upstream of the throat; an axial distance of 20 mm was chosen for comparison.

The composition of the unconstricted simulation at 20 mm corresponds to a change in formation enthalpy (H^*) of 0.600, which is equivalent to ideal constant pressure combustion at 0.58 MPa. Similarly, the constricted simulation's composition at 20 mm corresponded to an absolute change in formation enthalpy of 0.605, which would be achieved using constant pressure combustion at 0.68 MPa. This means that, for an analogous ideal constant-pressure device, the difference in enthalpy extraction through combustion between the constricted and unconstricted engines would correspond to an increase in chamber pressure of only 0.1 MPa. This is true even though the average pressures, as in Fig. 5.8, were nearly 0.5 MPa higher in the constricted geometry. This is one indication that, although the addition of the converging-diverging nozzle increased both thrust and I_{sp}, the associated change in combustion dynamics caused the constricted geometry to operate further from the ideal detonative cycle targeted by RDRE technology.

As defined in equation 5.7, H^* compares with one-step complete combustion – which is useful as a nondimensionalization, but ignores the fact that combustion products do not normally equilibrate to pure water and CO_2. When considering the completeness of combustion, it is often preferable to compare to a possible equilibrium condition instead of to the overall ideal. Equilibrium can be considered using a different nondimensionalization,

$$H_{\text{equil}} = \frac{\Delta H^0}{\Delta H_{\text{equil}}} \tag{5.10}$$

where ΔH_{equil} refers to the formation enthalpy that would have been released if the flow was allowed to equilibrate – i.e., H_{equil} is a measure of how close the flow is to equilibrium. In this form a zero again means that no energy has been released due to combustion, but a one

means that the combustion reaction is as complete as is possible for the local equilibrium conditions.

The equilibrium quantity, H_{equil}, was calculated using Cantera for local conditions, and is shown in Fig. 5.20. The higher pressure and temperature in the constricted case mean that, for the same energy released from combustion, the flow is closer to the local equilibrium conditions. However, the nozzle acceleration near the throat is large enough to partially freeze the flow – bringing the amount of released energy further from what would occur at the local equilibrium condition. The sonic condition in the constricted case occurs at the throat, and so instead of comparing the equivalent axial location between the two geometries it makes sense to compare the sonic location of 76 mm in the unconstricted case to 65 mm in the constricted case – at which location the equilibrium change in absolute enthalpy is the same in both cases.

5.6 Scalar Fields in the Wave Vicinity

Figure 5.21 displays instantaneous scalar fields centered on a wave structure, for both the unconstricted and constricted annulus cases. The slices shown were 75 mm from the injection plane, a height chosen to be far enough from the injectors that the flow isn't dominated by the incoming jets, but still near enough to the reactants to capture detonation structure.

These images make apparent the much smaller pressure rise present in the constricted case, even though the average pressure is higher: at the instants examined, the constricted annulus pressure only increased from 0.8 MPa to 1.8 MPa across the wave, but in the unconstricted geometry the wave increased pressure from 0.3 MPa to 2.3 MPa. The larger pressure rise indicates that detonations in the unconstricted annulus were stronger, which is further indicated by the greater heat release behind the shock in the unconstricted case. The heat release seen in front of the wave in the straight-annulus case is likely due to deflagration where the fuel and oxidizer streams meet. In contrast, heat release in the constricted case seems to lag behind the pressure wave. This suggests that much of the constricted annulus

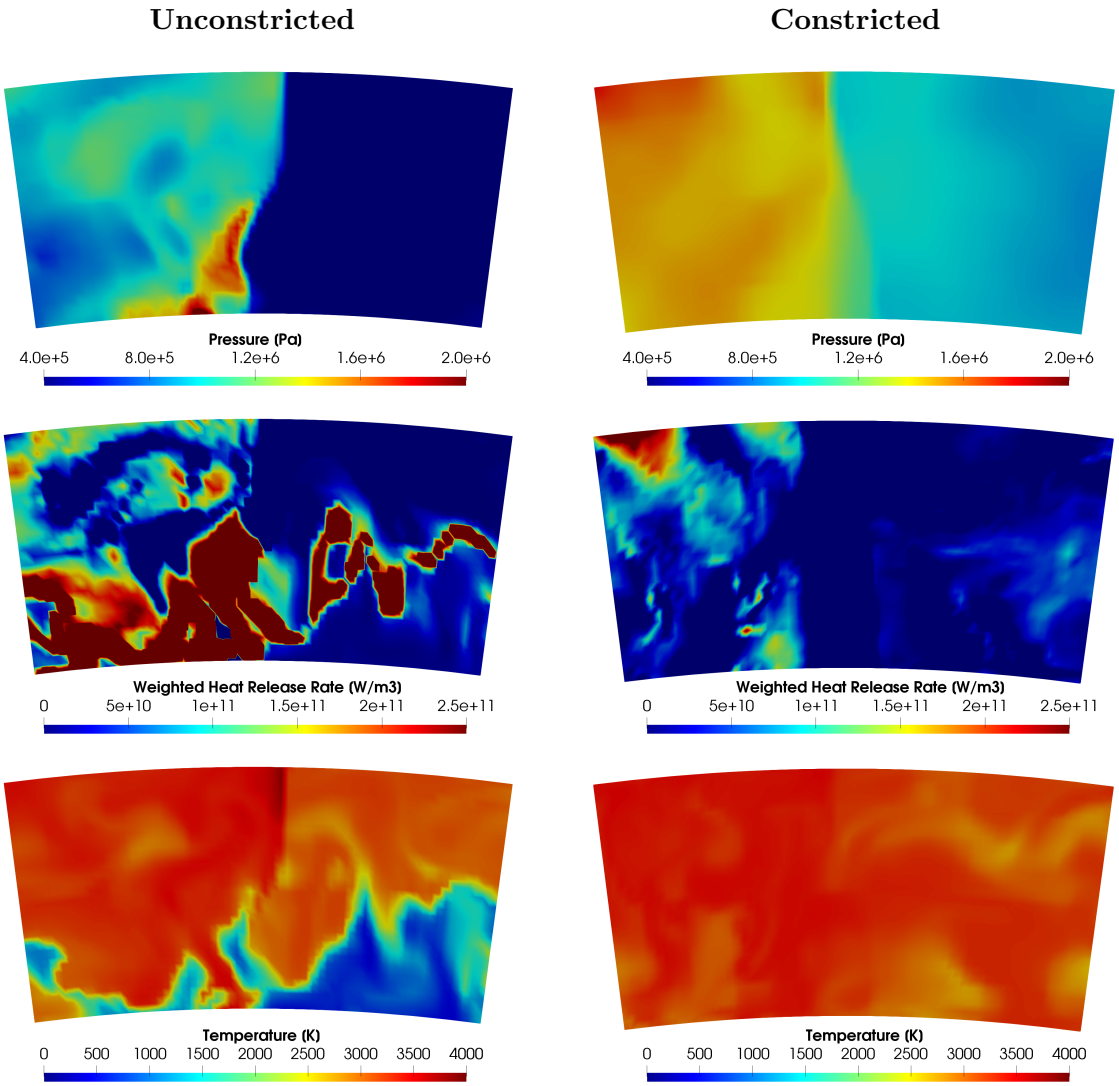

Figure 5.21: Measurements in the vicinity of the wave, taken in a slice 75 mm from the injection plane. Mixture fraction has a white contour overlaid to indicate stoichiometric. Images are oriented with wave traveling from left to right.

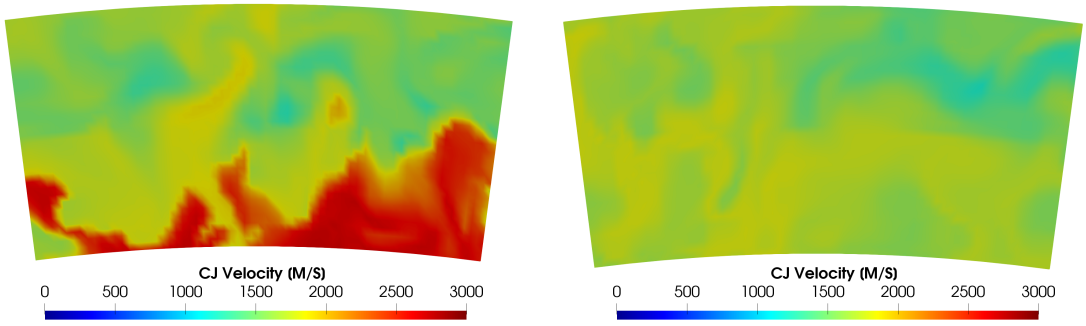

Figure 5.22: C-J velocity calculated locally for each simulation point using NASA's CEA utility.

heat release originates in deflagration triggered by an increased pressure, and not from a detonation wave. The existence of increased deflagrative combustion is in keeping with the discussion of section 5.5, in which it was shown that the energy released was closer to a purely deflagrative mode in the constricted simulation.

Idealized RDRE models suggest that the detonation wave should travel at close to the Chapman-Jouguet velocity, and so RDRE operating conditions are often compared to a theoretical C-J speed. However, the cited C-J condition is usually calculated assuming a mixture of the reactants used; it's useful as a first-order estimate, but does not take into account reactions that occur prior to the detonation wave. With simulation data it is possible to use NASA's Chemical Equilibrium with Applications (CEA) program to estimate C-J speed using conditions at any position within the chamber, and in so doing get a better estimate of conditions actually encountered by the detonation wave. An example of this is shown in Fig. 5.22, where CEA-calculated C-J velocity is shown in the vicinity of the detonation. These show that, in the constricted case, higher mixing leads to a nearly uniform C-J velocity field of 1650 m/s – much lower than the 2400 m/s CEA predicts for pure methane and oxygen. This updated value is also much closer to the measured wave speeds in Table 5.3, going a long way to explain the discrepancy between measurements and predicted C-J velocities.

5.7 Injection Behavior

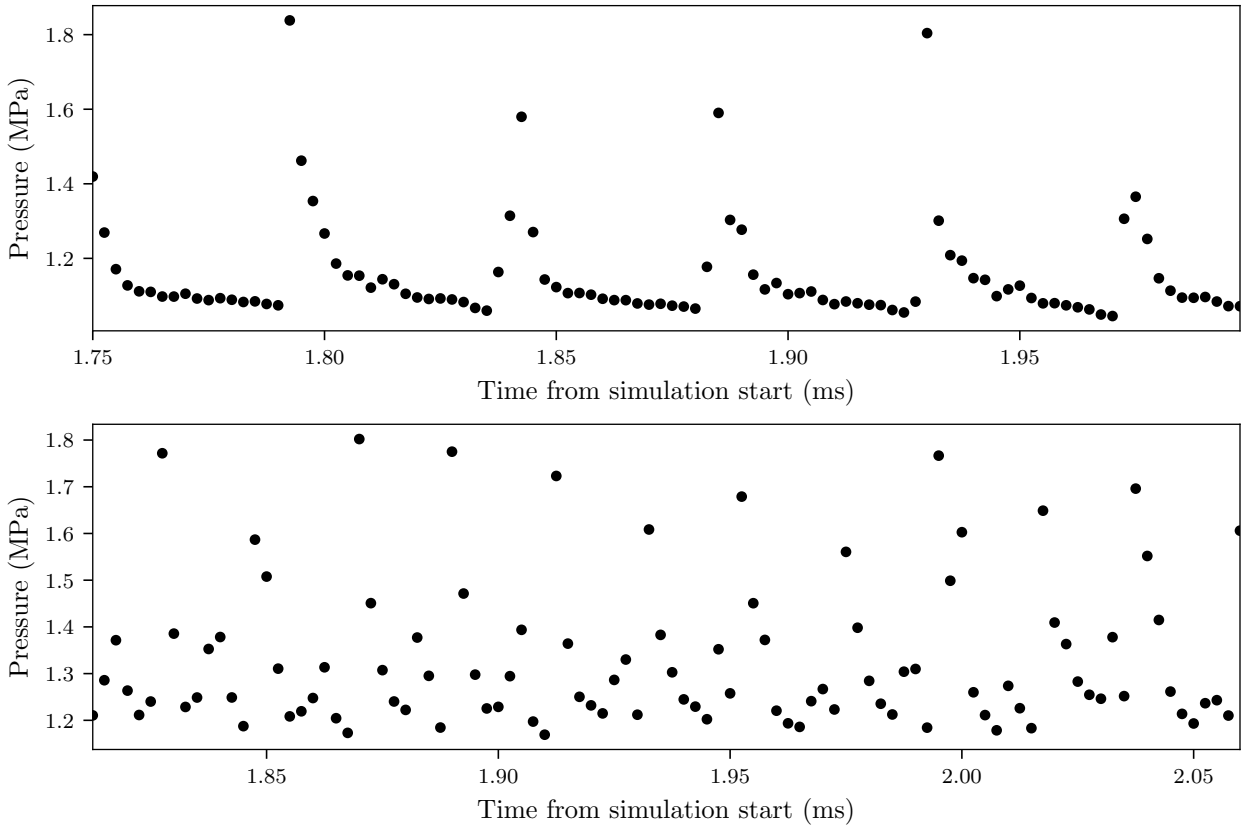

Figure 5.23: Static pressure at a fuel injector during quasi-steady operation, for the unconstricted (top) and constricted (bottom) simulations.

The mixing fields affecting detonation propagation, such as the scalar fields discussed in section 5.6, are directly connected to the injector behavior. Not only does the injector need to fill a region of the chamber with a detonable mixture in a short time, the injector must contend with large changes in pressure associated with the traveling shock structures. Static pressure at the chamber end of a fuel injector during engine operation for both the unconstricted and constricted simulation is shown in Fig. 5.23. This measurement was sampled in the simulation with a period of 2.5 μs, which is not a high enough resolution to guarantee multiple measurements for a single wave passing the injector; however, it does demonstrate large differences in the pressure signal experienced by the injectors in the two simulations. In the unconstricted simulation with three co-rotating waves the injectors saw a

sharp pressure rise as each detonation passed, followed by a qualitatively exponential decay. Waves in the constricted simulation resulted in similar peak pressures at the injection site, but the increased number of waves meant that the dominant-direction peak pressures occur more frequently, even though the wavespeeds were lower. The constricted simulation also had large-scale waves in the secondary direction, which prevented the pressure at the injection site from decaying back to a discernible background pressure.

Reactant injection was driven by the difference in pressure between the combustion chamber and injector plena. Because of this, the changing pressure on the chamber side resulted in a change in instantaneous flow rate through the injectors: the higher the local chamber pressure, the smaller the pressure gradient, leading to a reduction in the local reactant injection rate. This reveals an interdependency between the engine's operating mode and the injectors: stronger shock waves more greatly reduce reactant flow into the engine, leading to less well-mixed detonable regions in the chamber, potentially leading to weaker detonations.

In the simulation the effect on mass flow can be directly measured, as in Fig. 5.24. These measurements of flow rate are taken by instantaneously measuring the flow rate through the exit surface of the injector, $\int \rho \mathbf{u} \cdot d\mathbf{A}$. These are the same injector pairs for which the chamber-side fuel pressure is shown in Fig. 5.23, and so it can be seen by comparison that the instants where there were large pressure waves downstream of the injector coincided with dips in the injection rates for both the fuel and the oxidizer. The injector in the constricted geometry spent much less of its operating cycle near the targeted conditions, both because of the increased number of waves and because of the existence of large waves in the secondary direction; however, because the difference between highest pressure and lowest pressure was lower in the constricted simulation, and because the injector plena were initialized at a higher pressure, the drops in flow rate due to the passing waves were less severe in the constricted case.

Although the simulations targeted an overall equivalence ratio of 1.1, the unsteadiness in local flow rates meant that a given injector pair was not guaranteed to always inject at that targeted ratio. The larger area in the oxidizer side resulted in decreased stiffness when

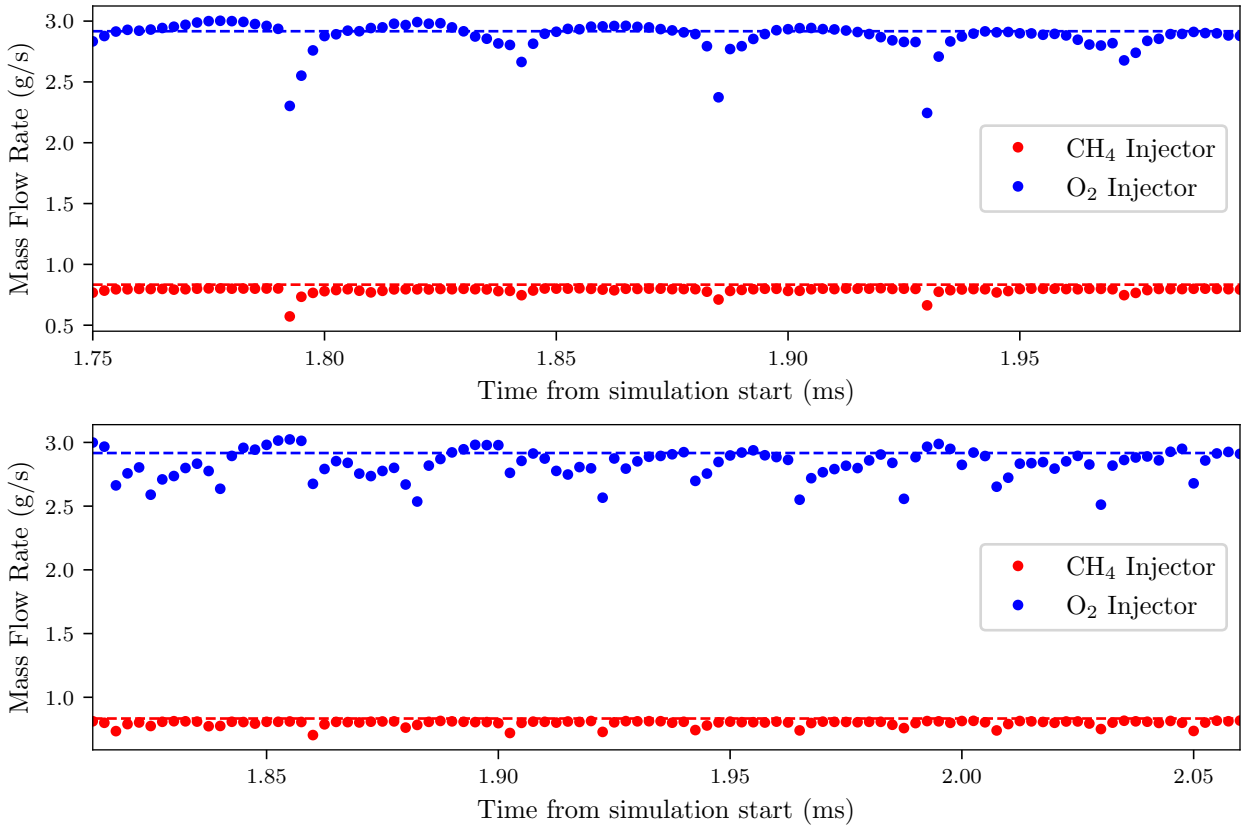

Figure 5.24: Response of mass flow rate for an injector pair, for the unconstricted (top) and constricted simulation (bottom). Dashed lines denote targeted flow rates as dictated by inflow conditions.

compared to the fuel injector, and as a consequence each pressure wave in the combustor increased the instantaneous equivalence ratio being injected; this effect can be seen in Fig. 5.25. The constricted simulation injector spent less of its operational cycle near the targeted equivalence ratio, and this non-ideal injection may have aided its ability to sustain counter-propagating waves by reducing the amount of reactant consumed by waves in the dominant direction. However, the increased number of shock waves also increased the amount of turbulent mixing inside the chamber, which suggests that, if this nonideal mixedness due to injection is a large part of what sustains counterpropagating combustion waves, these secondary waves are primarily fed near injection sites.

Although the drops in flow rate of Fig. 5.24 can be significant, in none of the sampled

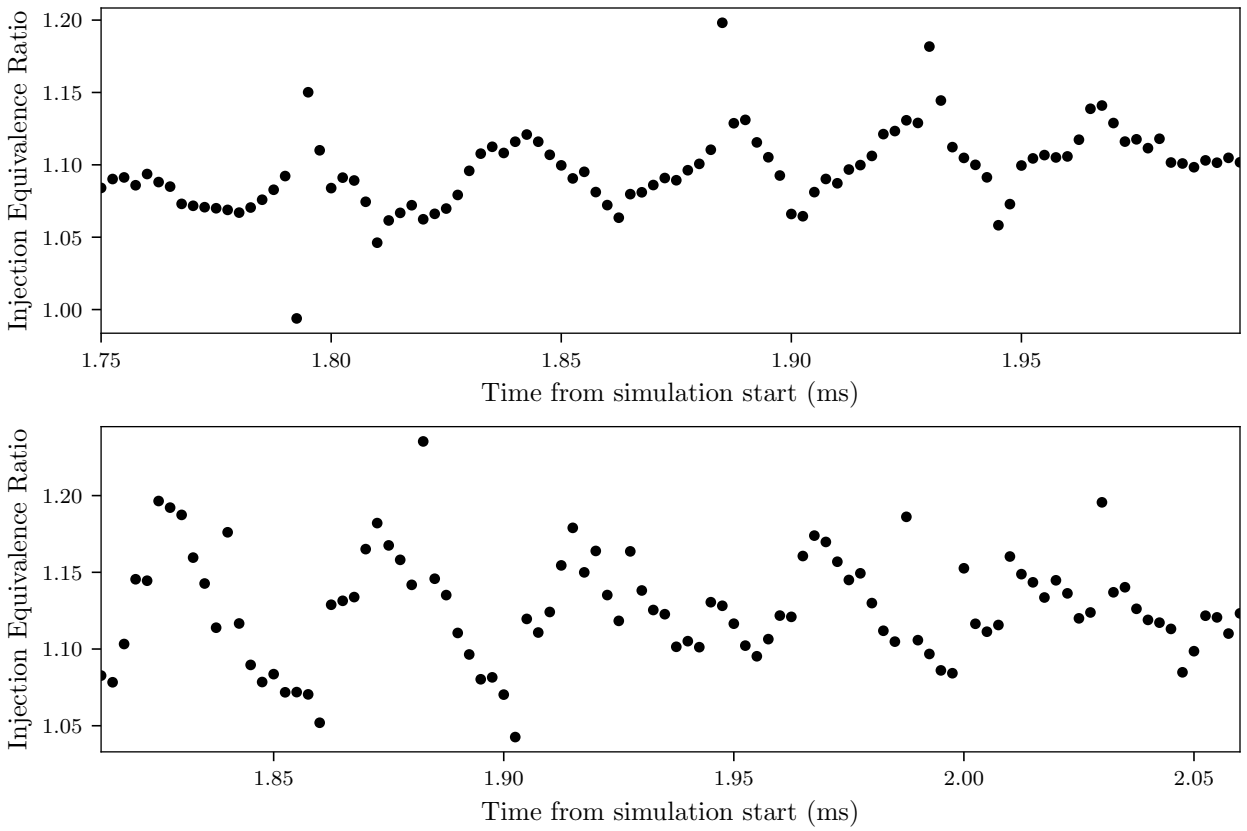

Figure 5.25: Response of equivalence ratio for an injector pair, for the unconstricted (top) and constricted simulation (bottom).

times did the flow reverse directions. This is a good thing: true flow reversal would further worsen the mixture detonability due to local injection, and in a worst case scenario could even trigger flashback, However, standard injectors are designed with thermally choked operating conditions in mind, and the drops in flow rate suggest that the injectors do not remain choked during the entire operation cycle. In the simulation, this can be further analyzed by directly measuring the Mach number at the exit of the injector, which would be unity in the case of perfectly choked injection. This measurement is shown in Fig. 5.26, where it can be seen that the injectors went well below mach 1 as waves passed in both simulations. In the unconstricted simulation, there was enough time to return to choked operation before the return of the next wave; however, in the constricted geometry only a very short period was spent at the choked conditions.

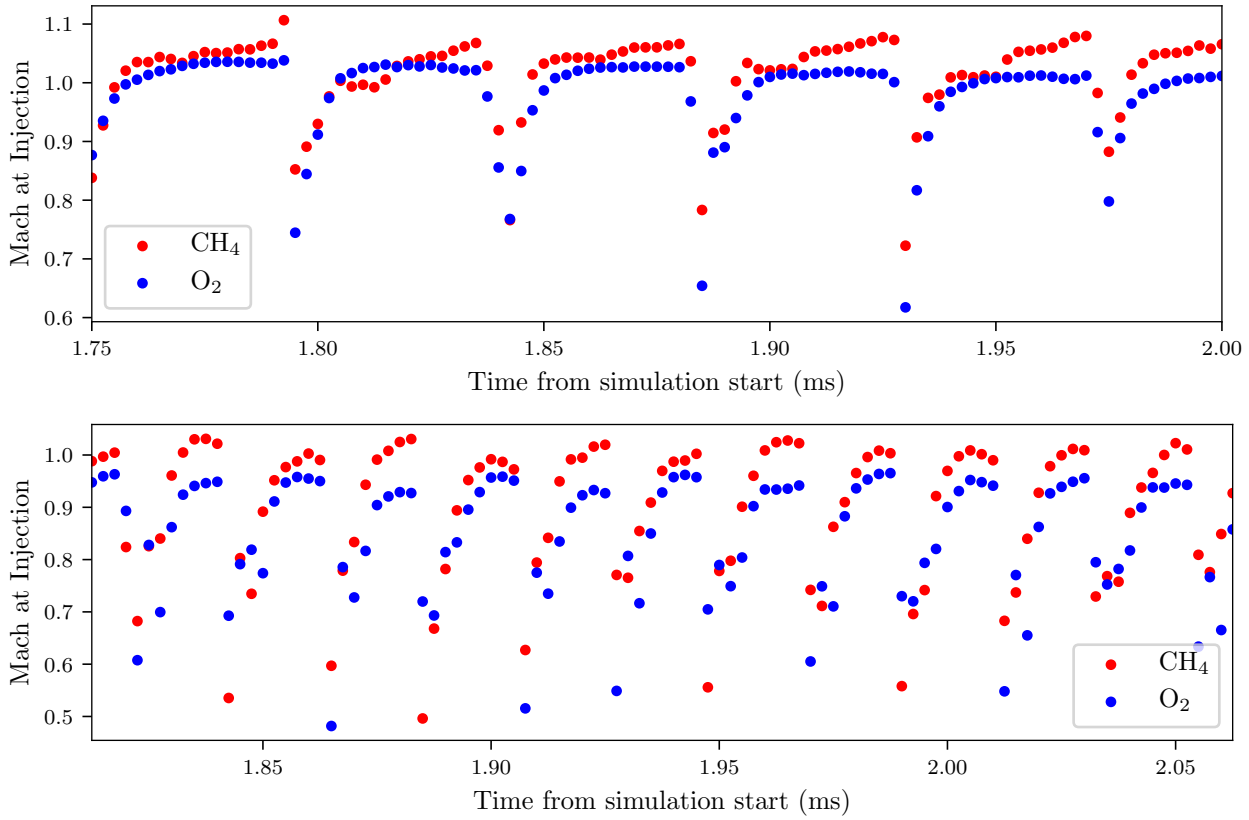

Figure 5.26: Response of Mach number at injection for an injector pair, for the unconstricted (top) and constricted simulation (bottom).

CHAPTER 6

Changing Chamber Length

One potentially useful characteristic of detonation engines is their ability to enable novel geometries. Specifically, there is a hope that, because the length scales required to fully combust propellant in a detonative mode are significantly shorter than comparable deflagrative length scales, it may be possible to create a smaller combustion chamber that still burns all the propellant. To that end, it becomes important to know how much the length of an RDRE affects engine operation.

Prior two-dimensional numerical work suggests that changing length has little effect on detonation structure for unconstricted engine geometries [50, 115]. However, experimental tests using a sudden exit constriction have been shown to operate with different modes depending on the chamber length, with certain lengths prone to longitudinal pulsing of the engine [58]. Experimental efforts to scale down airbreathing rotating detonation engines have been limited by the ability to sustain a detonative operating mode [116]. Using pure oxygen as an oxidizer significantly reduces detonation cell size, and ethylene-oxygen engines have been successfully tested with lengths of 36 mm [117].

This chapter describes simulations of experiments conducted at AFRL, in which a series of tests for a methane-oxygen RDRE were considered for chamber lengths of both 38 mm and 76 mm. It was observed that shortening the length of an unconstricted engine had very little effect on operating mode, both lengths operating with similar numbers of co-rotating waves. Changing the length of an engine with a chamber constriction was found to greatly affect the operating mode; an engine design that operated with significant counter-propagating behavior in the 76 mm configuration instead operated without counter-propagating waves in

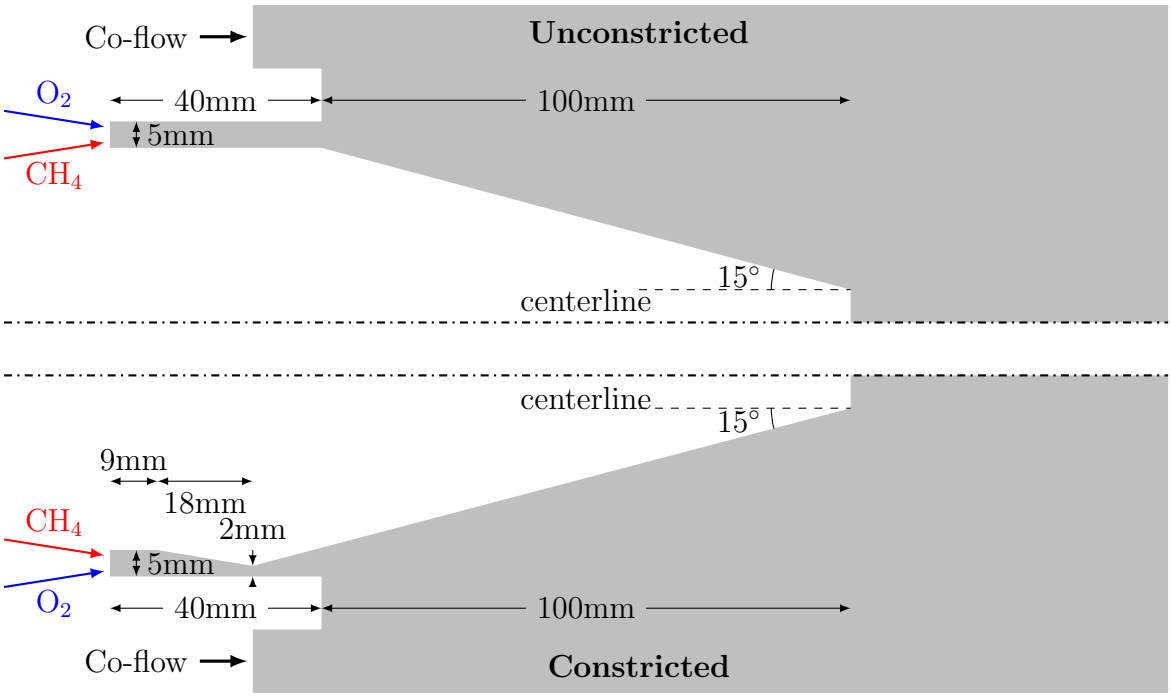

Figure 6.1: Domain diagram for simulated half-length geometries, represented with simplified injectors.

the 38 mm version. The change in operating mode resulted in a significant change in thrust, and the shorter engine demonstrated a higher I_{sp} at the same flow rates [110].

6.1 Case Description

Two shortened geometries were chosen to explore the effect changing length has on RDRE operation: one with, and one without, a chamber constriction. As this was an extension of the nozzle study of Ch. 5, most of the engine geometry remained the same as in previously discussed designs. Reactant was injected to the chamber through 72 discrete impinging injectors, and the annular channels were designed with a 76 mm outer diameter, and 5 mm channel width. Only the lengths differed from the designs of Ch. 5: the chamber length was shortened from 76 mm to 40 mm. For the unconstricted geometry this was a straightforward shortening of the inner and outer body, slightly more than half the previous length. In considering geometries with a constriction, the same contraction ratio was used, with a 2

mm gap at the throat. In order for the length of the chamber to change by the same amount in the constricted case, the converging section angle also had to change: the design used a 9.5° converging section, and a diverging aerospike at the same 15° angle. Further details on these designs are shown in Fig. 6.1.

Simulations were run using AHFM, as discussed in prior chapters. Targeted flow conditions matched the full-length simulations: an overall flow rate of 0.27 kg/s, with an equivalence ratio of 1.1. As such, boundary conditions were the same as those presented in Table 5.1.

6.2 Quasi-Steady Operation

	Unconstricted		Constricted	
	Simulation	Experiment	Simulation	Experiment
Number of Waves	3/-	3/-	6/9	9/-
Wavespeeds (m/s)	1618/-	1575/-	1472/1275	1244/-
Pressure 1 (MPa)	0.42	0.34	1.03	1.13
Thrust (N)	507	406	611	575
I_{sp} (s)	188	158	230	220

Table 6.1: Summary of quasi-steady modes achieved in both half-length simulations. Counter-propagating waves were sustained in the constricted simulations, and so number and wavespeeds are separated by direction in that case. Pressure 1 is a temporally averaged measurement taken 9 mm from the injection plane, a location chosen to coincide with experimental CTAP measurements taken by Bennewitz et al. [110].

Comparisons of the present simulations with global experimental results for the constricted and unconstricted cases are displayed in Table 6.1. The unconstricted half-length (40 mm) simulation operated in much the same way as the unconstricted full-length (76 mm) simulation discussed in chapter 5: three waves, with extremely similar wavespeed, thrust,

and I_{sp}. Comparable parameters in the unconstricted simulation closely matched what was seen experimentally, with exactly the same number of waves and wavespeeds. Adding a constriction to the 40 mm chamber resulted in an increased number of waves, as well as noticeable counter-propagating behavior, similar to what was seen in both simulations and experiments for the full-length geometries. However, unlike in the unconstricted geometries, changing the length of the constricted chamber did result in a different number of waves in both simulations and experiments. The half-length constricted simulation had fewer waves in the dominant direction than in the full-length simulation, but operated at very similar thrust and I_{sp}. This marks a departure from the trend seen in the experiments: the experimental half-length test exhibited very little counter-propagating behavior, and operated at higher I_{sp} than was seen in the full length chamber. The half-length constricted simulation also operated at lower chamber pressures than the experiment, which is surprising given the absence of thermal losses in the simulation. It is possible that the increased number of dominant-direction waves in the experiments resulted in a higher experimental CTAP pressure, but it is still generally expected that the adiabatic simulation would result in a higher chamber pressure.

6.2.1 θ-t Measurements of Detonation Region

Fig. 6.2 shows the temporal evolution of pressure during quasi-steady operation, in the 15 mm immediately downstream of injection for the two 40 mm chamber simulations. As indicated in Table 6.1, the unconstricted simulation stabilized with three co-rotating pressure waves. The constricted simulation operated with nine counter-propagating pressure waves, but Fig. 6.2 shows that the six dominant-direction waves had considerably higher pressures than the nine secondary-direction waves. This difference in strength between dominant and secondary directions is also visible in Fig. 6.3, where even though the nine-wave direction in the constricted simulation did account for some heat release, much more energy was released per dominant-direction wave.

The difference in wave strength for the two directions may provide an explanation for

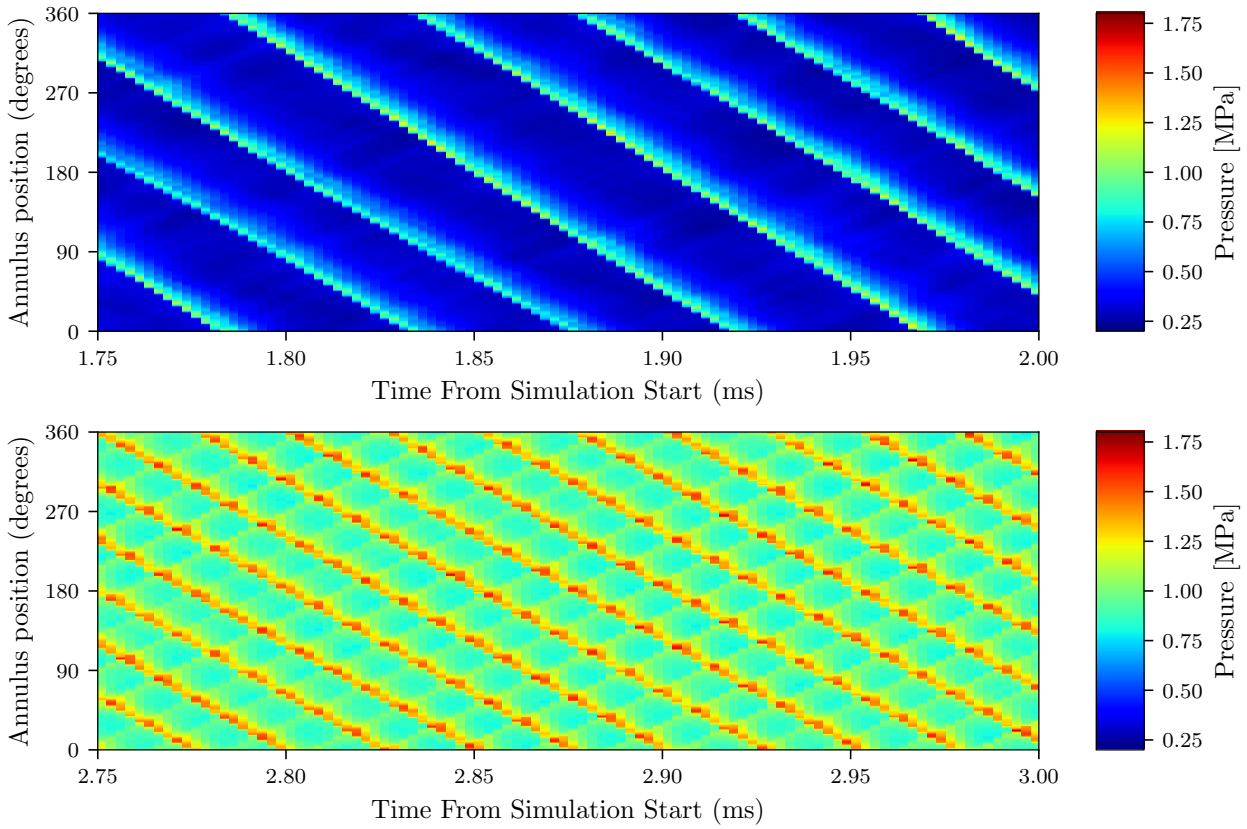

Figure 6.2: θ-t diagrams of pressure during quasi-steady operation, averaged over the 15 mm immediately downstream of injection in 1-degree wedges, for both the unconstricted simulation (top) and constricted simulation (bottom).

why the experiments did not detect any counter-propagating mode in the 40 mm constricted engine. In the simulation, the detection of waves comes directly from looking at the local pressure and heat release fields; however, experimentally the determination comes from chemiluminescence seen through the 2 mm channel gap. If the experimental engine exhibited a very weak counter-propagating mode it is possible that the chemiluminescence, as measured through the constricted channel, was not enough to stand out from background noise. However, even if there were some weak waves present in the experiment, there still seemed to be a significant difference in operating mode between experiment and simulation.

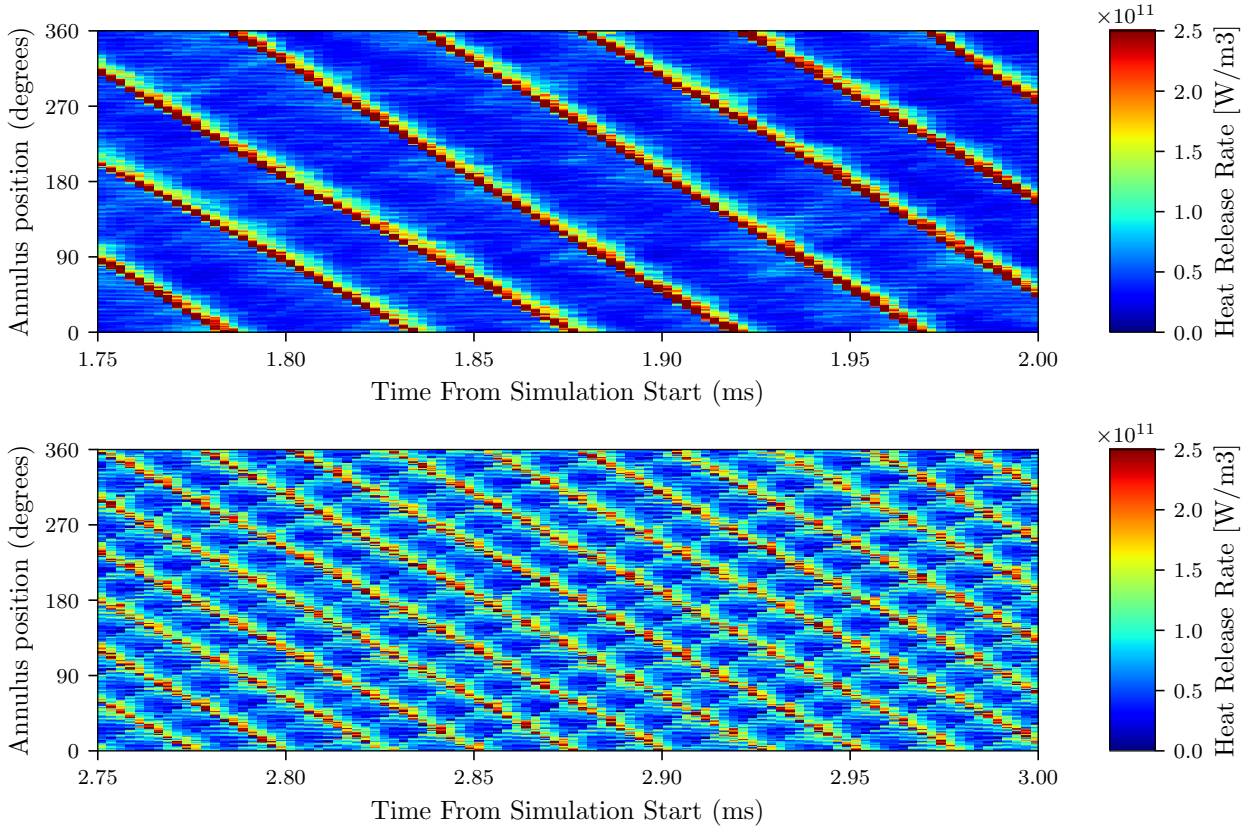

Figure 6.3: θ-t diagrams of heat release during quasi-steady operation, averaged over the 15 mm immediately downstream of injection in 1-degree wedges, for both the unconstricted simulation (top) and constricted simulation (bottom).

6.2.2 Flow Snapshots

Visualizations of instantaneous flowfields for the two half-length simulations are given in Figs. 6.4 and 6.5. In the unconstricted case, the pressure and temperature fields were extremely similar to the full-length simulations, with simply less of the oblique-shock region. In contrast, the change in wave number in the half-length constricted simulation resulted in several significant changes. With differing numbers of waves in both direction, the waves no longer all collide at the same time. Even though this is the case, at all instants the dominant six-wave direction demonstrated a flat detonation front, roughly perpendicular to the injection plane. The full-length constricted simulation did not have as clear a flat detonation region, the large number of strongly counter-propagating waves prevented the

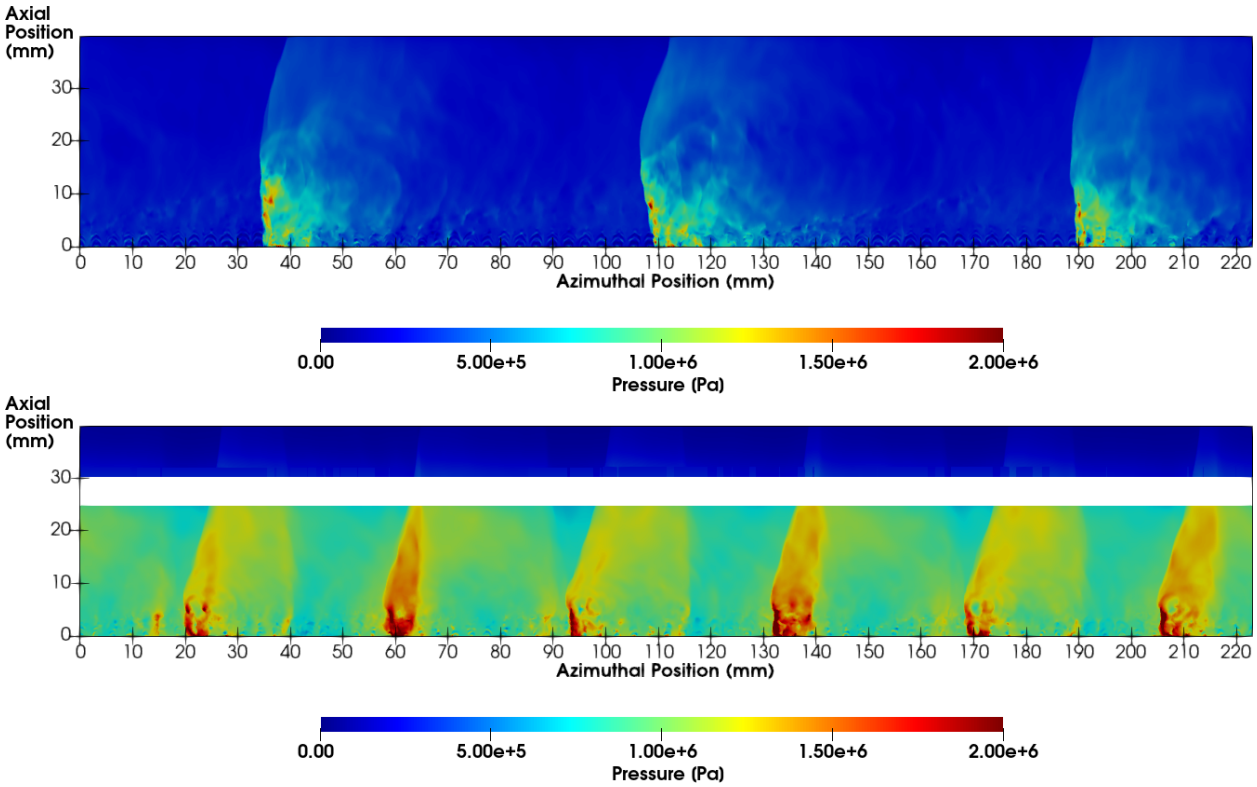

Figure 6.4: Flow snapshot of pressure for an unwrapped cylinder in the middle of the channel, for the half-length unconstricted (top) and constricted (bottom) simulations.

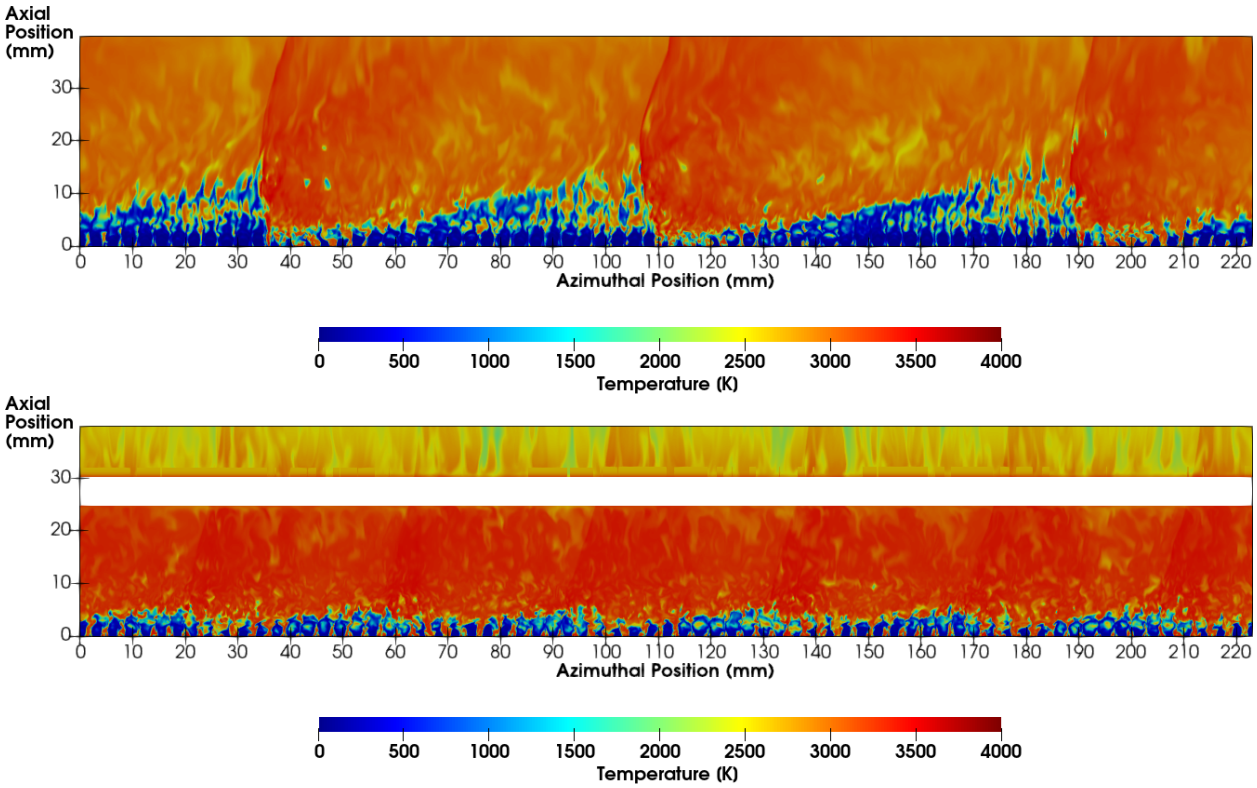

Figure 6.5: Flow snapshot of temperature for an unwrapped cylinder in the middle of the channel, for the half-length unconstricted (top) and constricted (bottom) simulations.

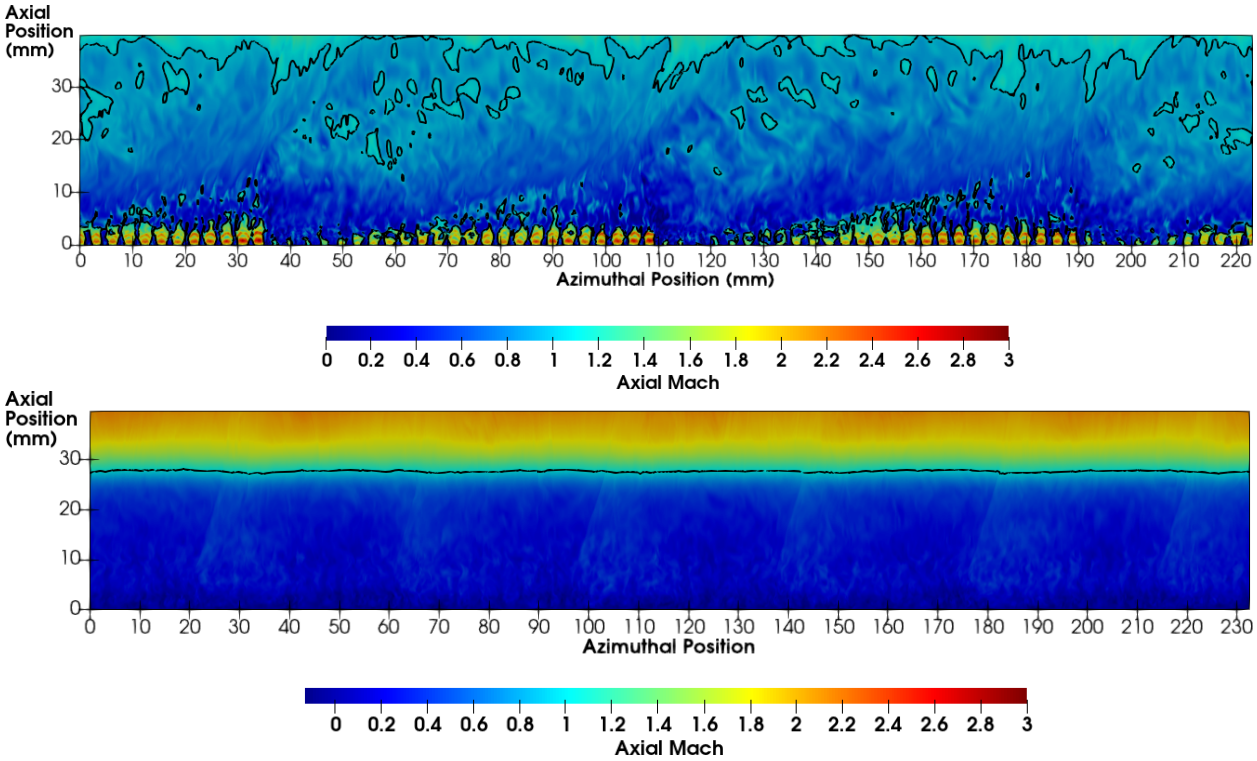

Figure 6.6: Instantaneous measurement of Mach number, for the half-length unconstricted (top) and constricted (bottom) simulations.

formation of a standard fill region.

Fig. 6.6 shows that the unconstricted engine was fully choked by the chamber exit, even though the chamber length was significantly less than the choking length of the full-length simulation. With detonations at a similar height but flow accelerating sooner, the half-length unconstricted simulation demonstrates less of the post-oblique supersonic turning than was seen in the full-length geometry. Instead, the flow thermally choked in pockets near the slip line, behavior that was also seen in the full-length simulation, but to a lesser extent. The constricted-simulation Mach field also behaved similarly to what was seen in the 76 mm simulation: flow was subsonic upstream of the geometric throat, and fully supersonic in the diverging section.

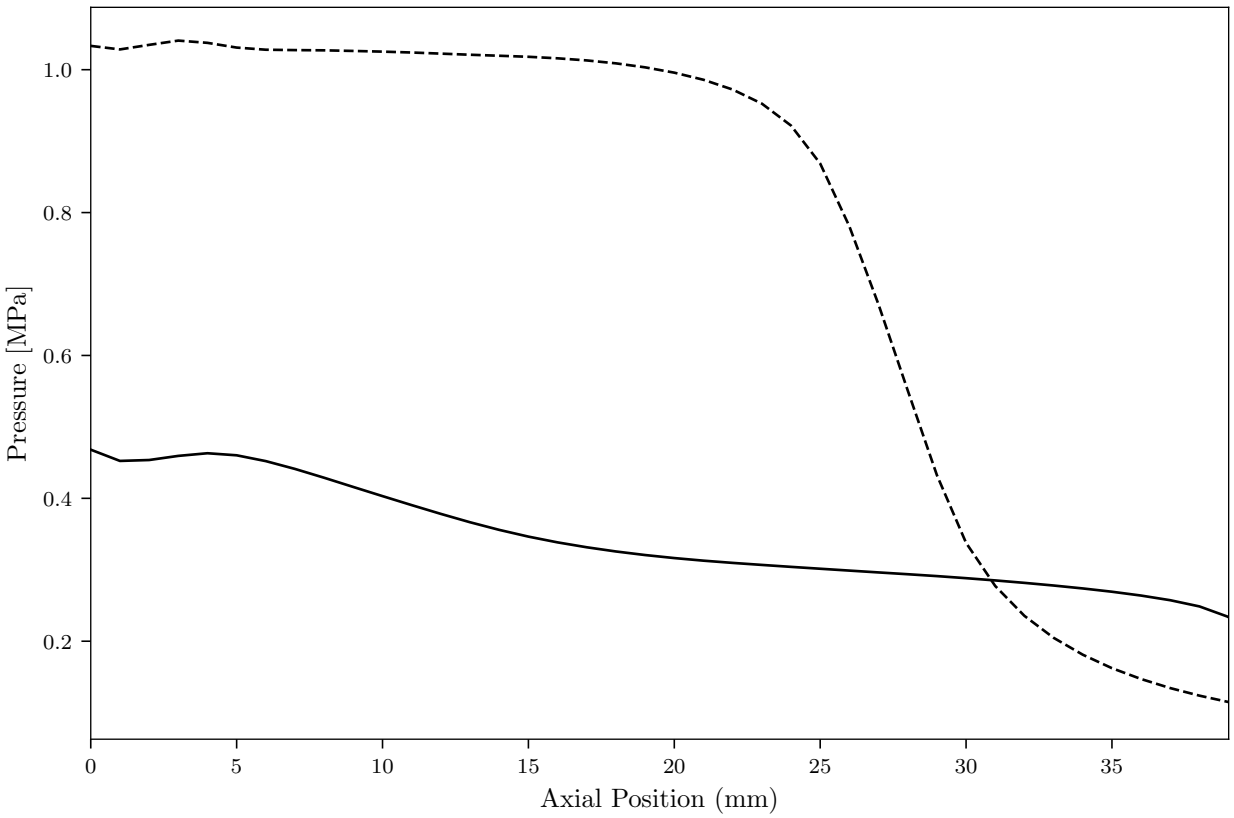

Figure 6.7: Time-averaged static pressure, as a function of axial distance from chamber injection. Dashed line denotes constricted geometry, and solid line denotes unconstricted geometry.

6.2.3 Axial Measurements

Axial trends in time-averaged pressure (Fig. 6.7) and temperature (Fig. 6.8 were similar in the 40 mm engines to what was seen in the full-length 76 mm chamber. The addition of the constriction increased average pressure inside the chamber, and even with the converging section starting at 9 mm the pressure did not decrease significantly until near the geometric throat at 27 mm. The unconstricted engine gradually decreased following the detonation region, similarly to the 76 mm unconstricted simulation.

Axial variations in composition, as in Fig. 6.8, were similar to what was seen in the full-length case. The detonation heights, as indicated by the presence of methane in the fill region, were again larger in the three-wave unconstricted simulation than in the constricted

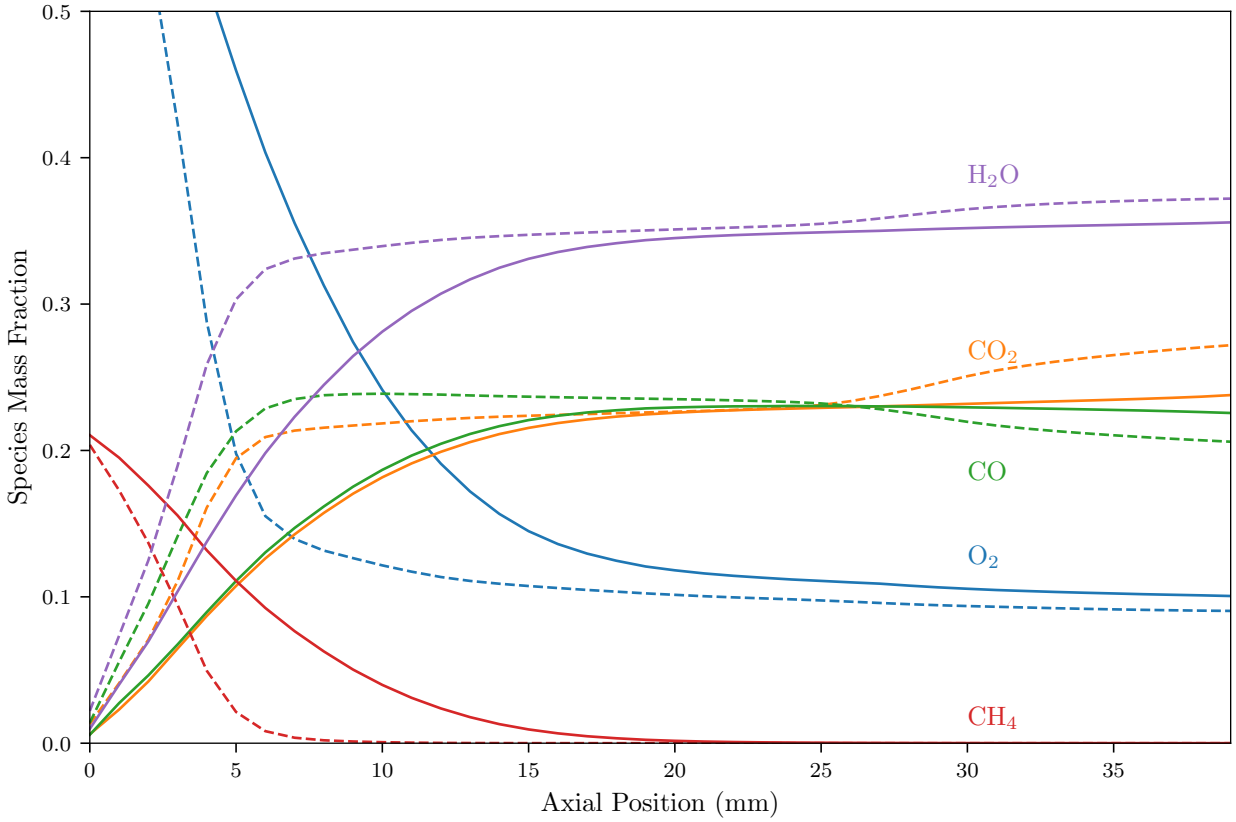

Figure 6.8: Time-averaged mass fractions for the most prevalent species inside the chamber, as a function of distance from injection plane. Dashed line indicates constricted geometry, solid lines denote the unconstricted chamber.

simulation. Equilibrium reactions due to the rapid expansion near the throat resulted in increased levels of CO_2 and H_2O, along with decreased CO, at a distance 25 mm from injection in the constricted simulation. However, compositions in the region between the detonation and the rapid expansion, 20 mm – 25 mm from injection, were quite similar in both simulations.

6.2.4 Energy Tracking

The flow compositions, as shown in Fig. 6.8, suggest that, at a distance 20 mm from injection, the same amount of energy had been released from the propellants in both engines. This was directly demonstrated by measuring the enthalpy of formation, as in Fig. 6.9. The

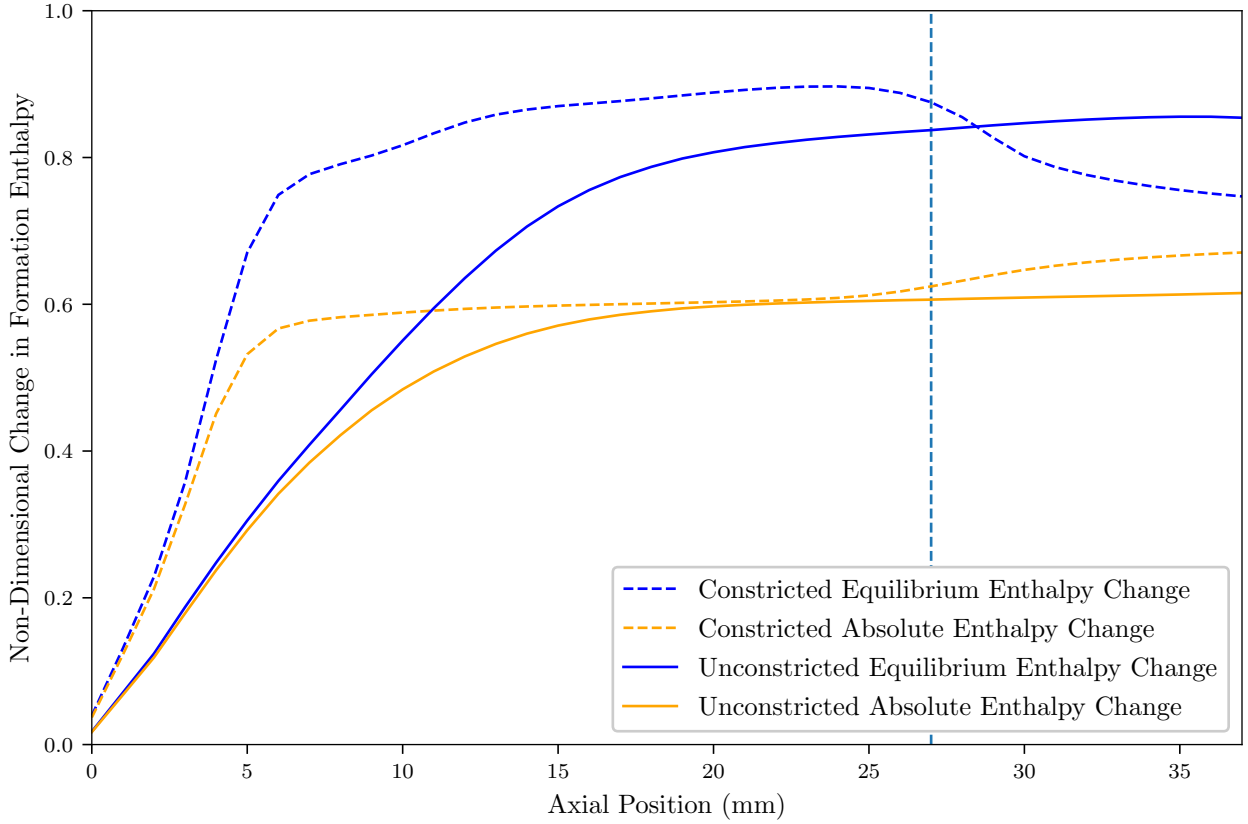

Figure 6.9: Change in enthalpy of formation of the two half-length geometries, given in non-dimensional forms scaled against idealized combustion and compared to equilibrium conditions. Vertical line at 27 mm indicates the geometric throat for the constricted simulation.

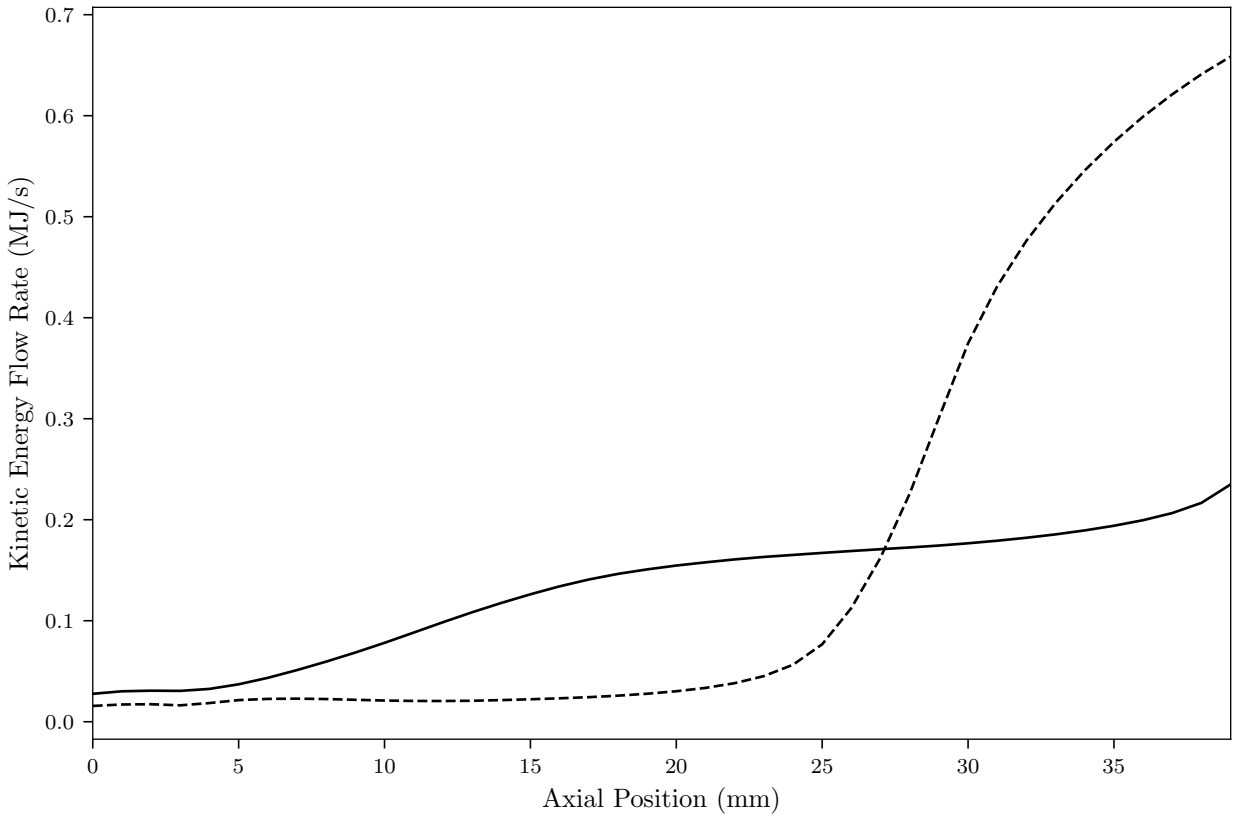

Figure 6.10: Kinetic energy flowing through axial planes, for the half-length unconstricted and constricted simulations, given as solid and dashed lines respectively.

change in enthalpy of formation, as given in this non-dimensionalized form, was 0.603 for the constricted simulation, as compared with 0.599 for the unconstricted simulation. Not only are these values measured from the two half-length simulations similar to one another, the values are very close to what was measured for the full-length simulations in section 5.5: 0.600 and 0.605. This suggests that RDRE combustion chambers can be made quite small; reducing the chamber length to 40 mm still extracted the same level of energy through combustion as was extracted in the 76 mm chamber.

Once the energy was released through combustion, the flow still needed to accelerate in order to be usefully converted to thrust. While enthalpy of formation makes it possible to track the energy contained in the composition, it is also possible to directly track how much energy energy has been converted to a kinetic form. This can be directly calculated in the

simulation by considering the kinetic energy flowing through a surface:

$$\text{Kinetic Energy Flow Rate} = \int_S \frac{1}{2}\rho|\mathbf{u}|^2\mathbf{u} \cdot d\mathbf{S} \tag{6.1}$$

Fig. 6.10 shows this prediction of the flow rate of kinetic energy for the two half-length simulations. In both simulations very little energy was converted to a kinetic form in the first 5 mm downstream of injection, an axial height where the propellant was burning (as demonstrated in Fig. 6.9), but the energy stored in temperature had not yet begun to accelerate the flow. That acceleration in the unconstricted case began around 5 mm from injection, corresponding in the model of Fig. 5.16 to post-detonation flow entering the expansion fan region. In the unconstricted case the flow continued to accelerate from 5 mm until the exit of the engine, with a change in slope in Fig. 6.10 occurring at the detonation height, 15 mm from injection. The constricted simulation showed very small amount of energy converted to a kinetic form in most of the chamber, with most of the flow acceleration occurring just upstream of the physical throat at 27 mm.

The expression in equation 6.1 can be changed to consider only axial or non-axial kinetic energy. This is a useful consideration, as only kinetic energy in the axial direction is directly used as thrust. Fig. 6.11 gives the measurement of kinetic energy in non-axial directions for both half-length simulations. The shape in the unconstricted case is as-expected based on a 2-D understanding of an RDRE: the detonations pull the flow azimuthally, but then the flow is turned by oblique shocks. It is unclear what is happening in the half-length constricted simulation; although the first 5 mm are consistent with detonations increasing the azimuthal velocity component, and the post-throat region corresponds to accelerating flow increasing both the non-axial and axial kinetic energies, some of the changes are surprisingly sudden for time-averaged measurements.

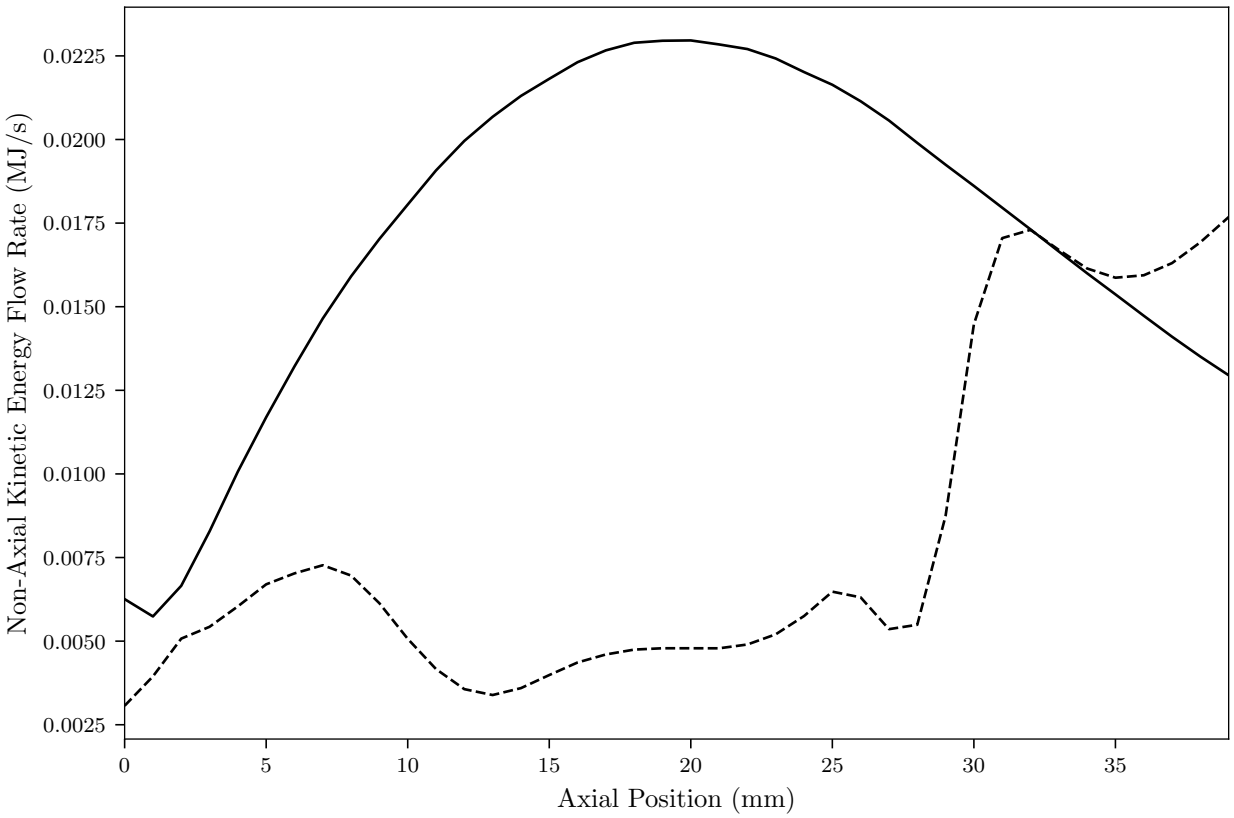

Figure 6.11: Non-Axial kinetic energy flowing through axial planes, for the half-length unconstricted and constricted simulations, given as solid and dashed lines respectively.

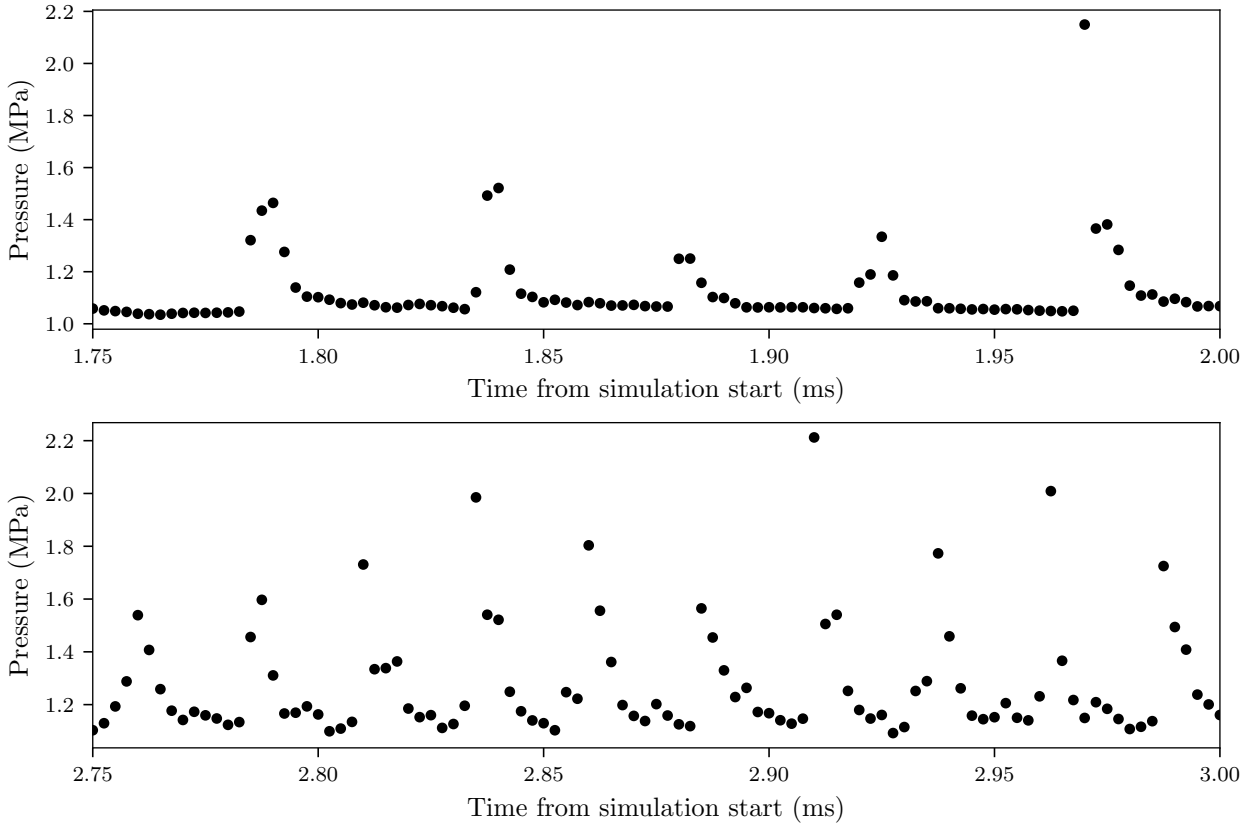

Figure 6.12: Static pressure at a fuel injector during quasi-steady operation, for the half-length unconstricted (top) and constricted (bottom) simulations.

6.3 Injection Behavior

During operation, the pressure waves traveling in the chamber were enough to change the injection pressure ratios, and impact injection rates. Fig. 6.12 shows the static pressure at the exit of a single fuel injector during quasi-steady operation, for the constricted and unconstricted simulations. As with the other characteristics of the unconstricted simulation, the pressure at injection for the unconstricted simulation behaved quite similarly to what was seen in the 76 mm unconstricted geometry in Fig. 5.23. However, the pressure signal at the exit of the fuel injector was noticeably different between the half-length and full-length constricted simulations. In the half-length simulation the peaks due to the dominant-direction waves were quite apparent, with dominant peaks every 0.024 ms corresponding to the six strong waves

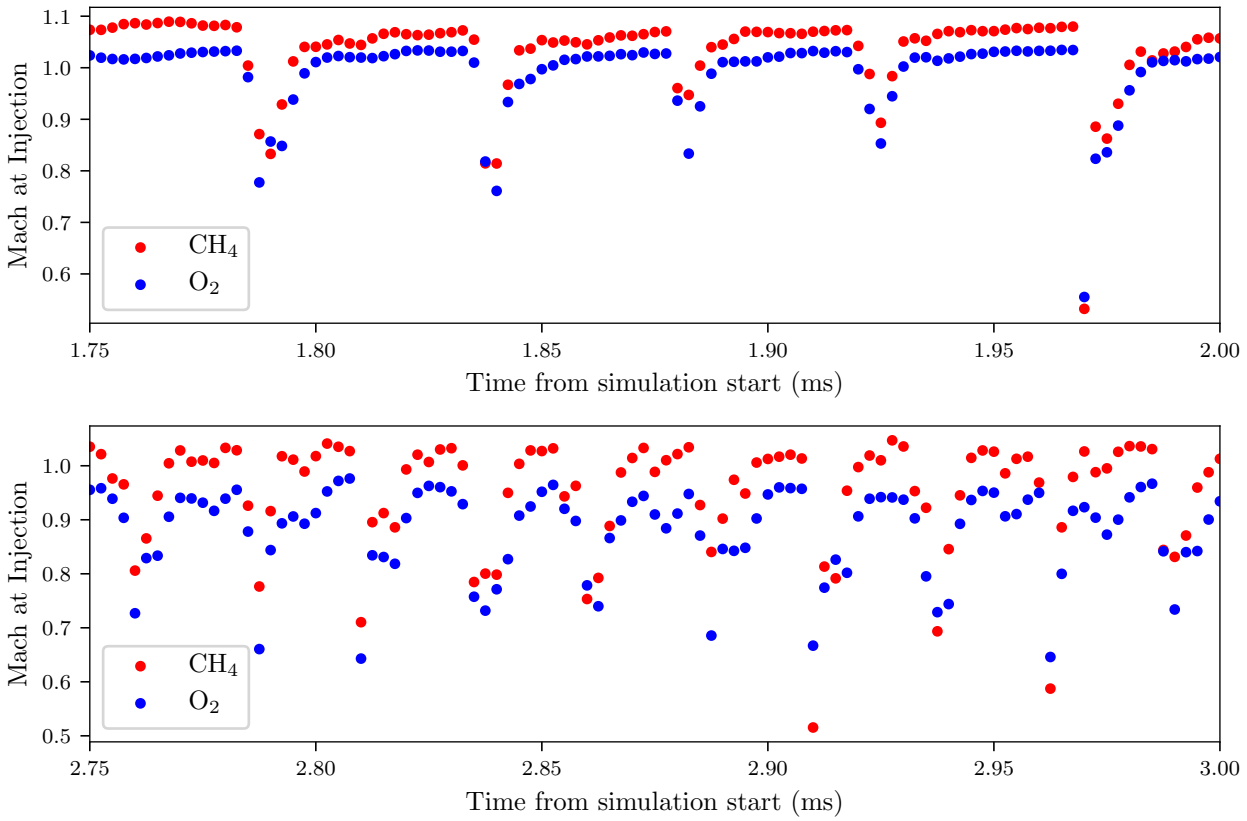

Figure 6.13: Response of Mach number at injection for an injector pair, for the half-length unconstricted (top) and constricted simulation (bottom).

For both simulations the waves were enough to unchoke the injection, as demonstrated by measurements of Mach number at injection, for an injection pair shown in Fig. 6.13. Although there were waves in both direction in the constricted simulation, only the pressure waves in the dominant direction were enough to fully unchoke the fuel injector. The measurement of average Mach number at injection suggests that the half-length constricted engine never operated with fully-choked oxygen injection.

The pressure wave's impact on the mass flow rates of methane and oxygen are shown in Fig. 6.14 for both 40 mm simulations. The effect on local injection equivalence ratio, calculated using the flow rates in Fig. 6.14, is shown in Fig. 6.15. In the unconstricted simulation this relationship was similar to the 76 mm simulation: as the wave passes there was a sharp drop in both methane and oxygen, in a ratio that resulted in a drop of the

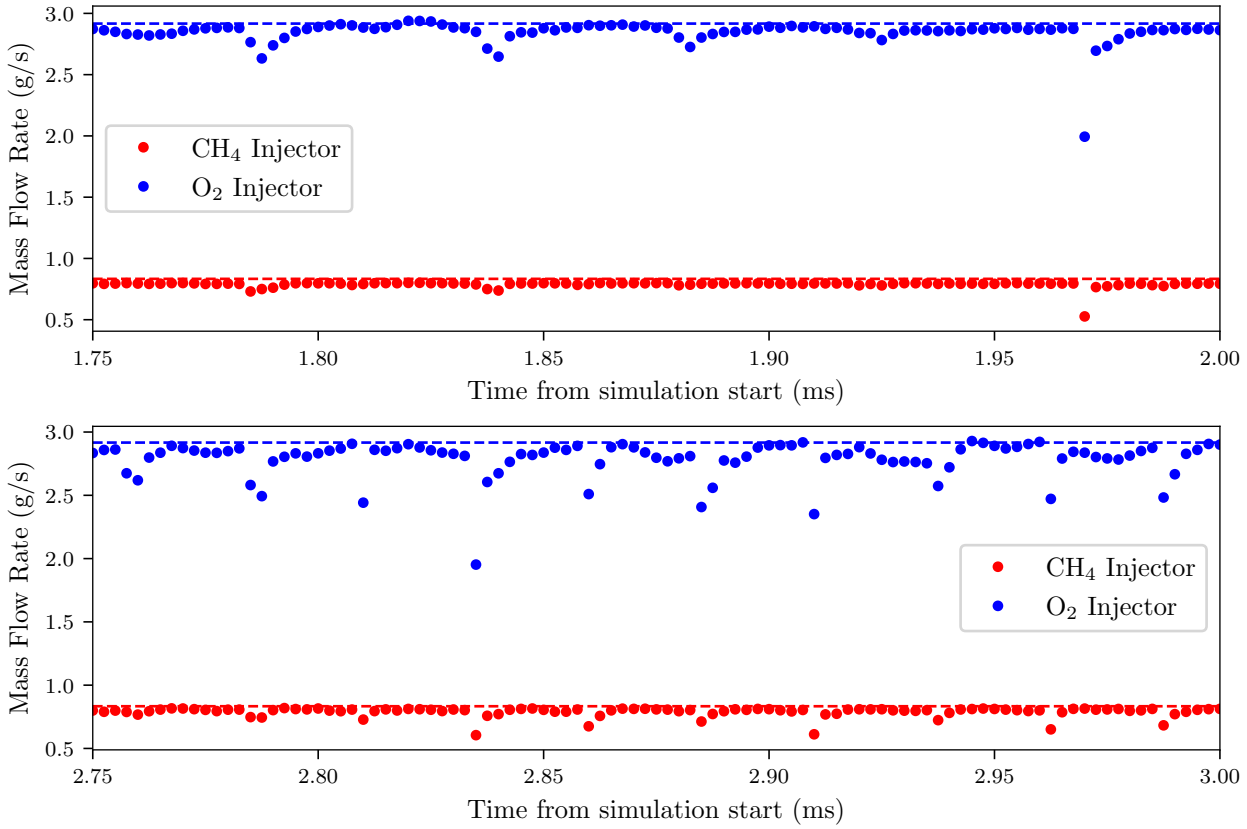

Figure 6.14: Response of mass flow rate for an injector pair, for half-length unconstricted (top) and constricted simulation (bottom). Dashed lines denote targeted flow rates as dictated by inflow conditions.

injected equivalence ratio. The equivalence ratio then increased, hitting a peak and then decreasing until the passing of the next wave.

The cycle in local equivalence ratio seen in the 40 mm constricted case is strikingly similar, even though the period corresponding to waves passing the injector is nearly halved. Instead of each wave resulting in a drop in injected equivalence ratio, the minima in injected equivalence ratio occurred for every other wave. Moreover, the same sort of peaks were seen in the unconstricted and constricted simulations, but instead of occurring between wave passes the peaks in locally injected equivalence ratio corresponded directly with the passage of every other wave in the constricted simulation.

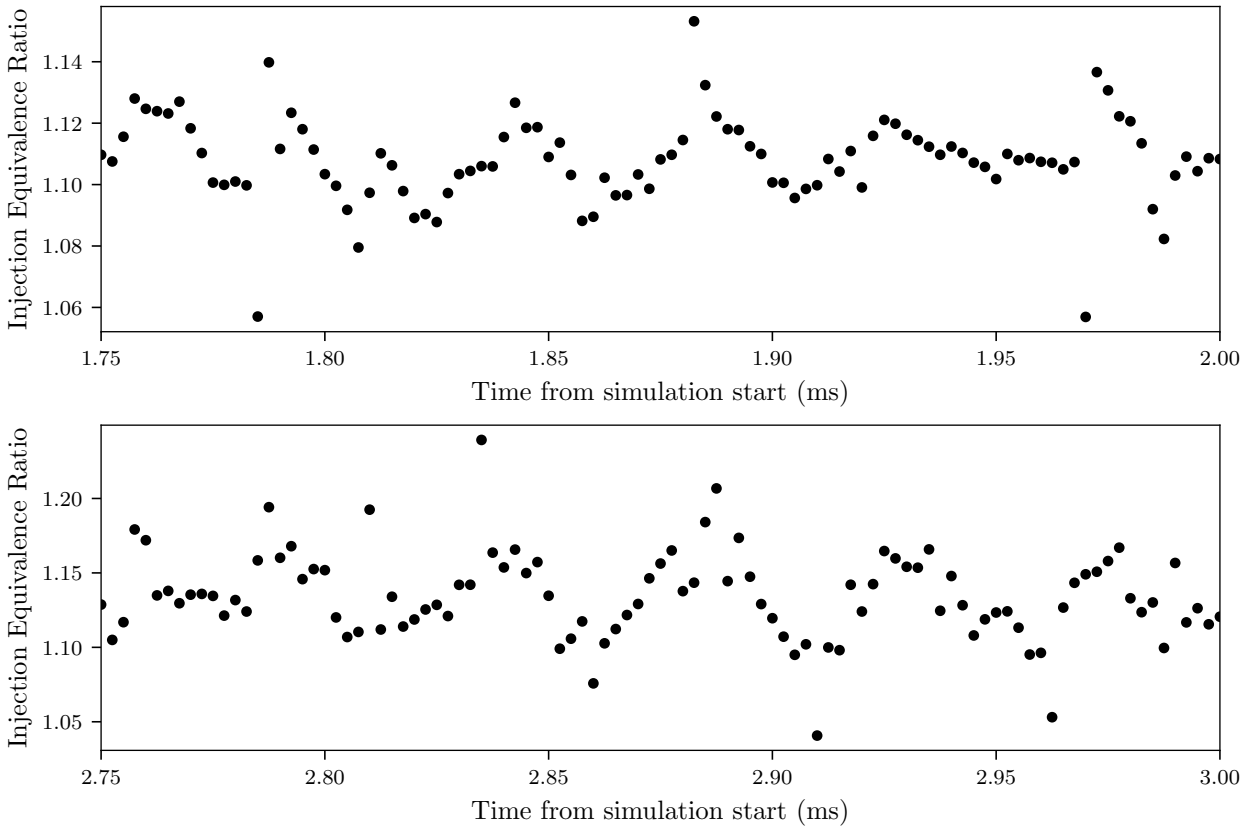

Figure 6.15: Response of equivalence ratio for an injector pair, for the half-length unconstricted (top) and constricted simulation (bottom).

CHAPTER 7

Summary and Conclusions

Although rotating detonation rocket engines are a promising propulsion technology, there remain many things that are not fully understood about the type of engine. This study uses numerical tools to examine flow features that cannot yet be measured experimentally, furthering understanding of phenomena that are encountered when modifying RDRE chamber geometry. Taken as a whole, the results demonstrate that modern numerical tools are able to predict a priori much of the complex behavior associated with RDREs; simulations will continue to be a powerful tool for developing improved engines, while at the same time reducing experimental testing requirements.

7.1 Validation Geometry

Chapters 3 and 4 discussed an engine geometry selected by the AIAA MVP workshop, and for which there is a growing body of work that can be used for comparison. A simulation of the engine was presented, for which the operating mode reached in the engine after startup was found to match the two-wave mode observed experimentally. General trends in the presented simulation matched other simulations of the engine: higher pressure and thrust than in experiments, but with lower wavespeeds. It was observed that the engine operated in a galloping regime, with the angular separation between the two waves varying by as much 70 degrees. The tendency of the engine to sustain galloping behavior provides one possible explanation for the range of wavespeeds reported by other simulations of the engine.

An examination of the instantaneous flowfields inside the engine demonstrated the existence of a double shock structure, likely enabled by the mixing field produced by the studied

injector design. It was further observed that, as in other simulations of this engine, the injected reactant remained near the inner wall of the annular chamber. This led to detonations existing only near the inner wall of the chamber. The shock structure produced by the detonation was found to propagate in the outer region ahead of the detonation itself, due to the different speeds of sound in the two regions.

Chapter 4 compared simulation results with experimental MHz-resolution measurements of the engine exhaust taken by Nair et al. [97]. Two approaches were presented for extracting LAS analogs from the simulation data: the first based on an instantaneous species-weighted integration, and the second using the Beer-Lambert law to evaluate the expected absorbance for simulated flowfields. It was shown by comparing the two models that the recirculation zone behind the simulated engine's outerbody was capable of greatly impacting LAS measurements of temperature, pressure, and CO column density. A comparison between simulation exhaust and experimental laser measurements reaffirmed that the simulated pressure in the chamber was higher than the experiment, and that the simulation also overestimated temperature.

The laser comparisons also showed that the double-peak structures observed experimentally in CO column density were present in the simulations, and corresponded to combustion occurring after the passage of the detonation. Simulation laser measurements inside the chamber suggested that the diagnostic design should be accurate inside the chamber, and that experimental measurements in the region may verify whether the double-shock structure seen in the simulation also exists in the experiments. An examination of the flowfield near the detonation fill zone suggests that the previous diagnostic approach will not work in that region of the engine, but that it may be useful to target absorbance of cold methane and hot H_2O separately.

7.2 Adding a Converging-Diverging Nozzle

Two high-fidelity simulations of a gaseous methane-oxygen RDRE were presented in chapter 5: one with, and one without, a converging-diverging nozzle. Simulation results were compared to experimental measurements of the same geometry and flow conditions, and it was found that the simulations captured experimental operating modes. Specifically, the addition of a chamber constriction caused the engine to operate in a counter-propagating mode, with a large number of waves in both directions. Inspection of the simulation flowfield revealed no large-scale shocks traveling in the upstream direction, demonstrating that counter-propagating behavior can occur without the influence of reflected shocks in the operating regime.

The constricted simulation exhibited flow choking precisely at the geometric throat, a contrast to the behavior usually seen in unconstricted RDREs. The RDRE flowfield followed the Mach-area relationship in the constricted simulation, demonstrating that even a gradual constriction can have a drastic effect on the RDRE flowfield. An idealized analysis showed that it is possible for an RDRE to operate without post-oblique supersonic regions in the presence of pre-detonative deflagration, which partially explains what changes occurred in the constricted simulation in order to allow the Mach-area relationship to hold in the converging section. The ability to dictate choking location may potentially be leveraged in future RDRE designs.

An analysis of the enthalpy of formation was conducted for both simulations. The enthalpy released through combustion in the unconstricted engine indicated higher combustive performance than for an equivalent constant-pressure device. The addition of a nozzle in the constricted simulation increased the thrust and I_{sp} of the engine; however, even with the large increase in chamber pressure, the constricted engine released similar amounts of enthalpy through combustion as was released by the unconstricted design. The similar magnitude of combustive energy release means that the changed detonation dynamics of the constricted simulation had a detrimental impact on the operation of the engine, bringing the device further away from the ideal detonative cycle. Future work on nozzles for RDREs will

need to take into account the interaction between nozzle and combustion dynamics.

Calculation of per-injection flowrates demonstrated that the passage of each shock reduced the amount of reactant being injected locally. The passing waves unchoked injection, but did not cause flow to reverse direction. Flowrate attenuation in fuel and oxidizer injectors were not symmetric, leading to variation in the locally injected equivalence ratio with each passage of the wave. An increased number of waves in the constricted geometry led to an increase in the number of unchoking events for each injector, and a corresponding reduction in time spent operating in a choked regime. The change in injector behavior may be connected to the ability of the constricted engine to sustain counter-propagating waves, but further research is required to understand whether unsteady injection is a necessary condition for the existence of sustained counter-propagating modes.

7.3 Changing Chamber Length

The constriction study of chapter 5 was extended in chapter 6 to consider chambers of reduced length. Reducing the length of an unconstricted annular RDRE was found to have no effect on the number of sustained detonation waves or overall engine thrust. The only observed differences in chamber flowfield in the unconstricted geometries were related to changes in thermal choke location, with the flow in both engines reaching sonic conditions at the exit of the chamber.

Counter-propagating waves were again observed in the shortened constricted geometry; however, as was observed in experiments at AFRL, the change in chamber length reduced the strength of the secondary-direction waves. This suggests that chamber length may be an important tunable parameter in future constricted engines designed to target a specific operating mode. However, overall I_{sp} was unchanged by the difference in length and operating mode.

Measurements of injector flowrates for the shortened unconstricted geometry were essentially equivalent to the same measurements in the full-length case. In the half-length

constricted geometry, attenuations in injector flow rate were caused primarily by the passages of the dominant-direction waves. This made it possible to observe that changes in equivalence ratio due to local injection had an operating period that was not purely caused by the passage of waves over the injectors. In both unconstricted cases each peaks in locally injected equivalence ratio coincided with the passage of a wave. However, for the half-length constricted geometry, a peak in injection equivalence ratio occurred every two waves.

7.4 Suggestions for Future Work

The wave galloping observed in chapter 3 is a phenomenon which may be closely tied to the number of waves an engine sustains, and would benefit from further investigation. Increasing the flowrate is known to increase the number of waves in an RDRE, so it is possible that the observed two-wave galloping could be stabilized by changes in engine flow rate. If this is the case, it would be important for the advancement of future engine designs to know whether such stabilization has an impact on I_{sp}.

As there are still many aspects of RDRE operation that are difficult to measure experimentally, there are many things to be gained by further considering LAS measurements using simulation data. One avenue for future exploration is the extension of the enthalpy analysis of chapter 5 to LAS measurements, to verify whether completeness-of-combustion and other composition-based efficiency measurements could be accurately measured using existing diagnostics. It would also be interesting to further verify that structures seen in the simulation, such as detonations which exhibit a paired-shock structure, are observable by experimental LAS measurements. Further, simulation data provide a next step toward designing diagnostics for CH_4 and H_2O measurements in the detonation region, which may enable direct measurements of detonation pressure rise or even help gauge physical reaction rates near the detonation.

Many of the questions connected to the development of nozzles for RDRE applications are still without answers. It's largely unknown how much the operational mode of the

engine is affected by changes in pressure, such as the increases associated with the addition of a constriction. Pressure effects could be isolated from geometric changes using a series of simulations with varying backpressure, an investigation which would also be useful in considering flight at differing altitudes.

It would also be interesting to further explore the development of sustained counter-propagating behavior in RDREs. One possible study is to consider a sweep of simulations with varying chamber constrictions, to find the transition point at which the engine stops operating in a purely co-rotating mode. To enable such a sweep, it would likely be necessary to further isolate what physics must be modeled in order to sustain counter-propagating behavior, since such behavior currently requires extremely expensive calculations. One step in such reduction may be to see whether the injection behavior is a necessary part of counter-propagating operation, possibly by using a chamber geometry that sustains such behavior to run simulations using simplified injection models (e.g. premixed injection, constant non-premixed injection, or non-premixed injection with constant equivalence ratio).

APPENDIX A

Methane-Oxygen Mechanism, FFCMy-12

```
!*****************************************************************************
!
! A skeletal model for methane oxygen combustion in rocket engine.
!
! Rui Xu, Hai Wang
! Stanford University
!
! October 31, 2018
!
! Please contact Hai Wang at haiwang@stanford.edu for questions and comments.
!
!*****************************************************************************
ELEMENTS
C H O
END
SPECIES
H2  H  O2  O  OH  HO2  H2O  CH3  CH4  CO  CO2  CH2O
END
REACTIONS
 H+O2=O+OH                  1.09E+14    0.       15310.
 O+H2=H+OH                  3.82E+12    0.        7950.
    DUPLICATE
 O+H2=H+OH                  8.79E+14    0.       19180.
    DUPLICATE
 OH+H2=H+H2O                2.16E+08    1.51      3437.
 2OH=O+H2O                  3.35E+04    2.42     -1928.
 H2+M=2H+M                  4.58E+19   -1.4     104390.
    H2/2.5/ CO/1.9/ CO2/3.8/ H2O/12./ CH4/2./ CH2O/2.5/
! 2O+M=O2+M                  6.16E+15   -0.5          0.
!    H2/2.5/ CO/1.9/ CO2/3.8/ H2O/12./ CH4/2./ CH2O/2.5/
 O+H+M=OH+M                 4.71E+18   -1.0          0.
    H2/2.5/ CO/1.9/ CO2/3.8/ H2O/12./ CH4/2./ CH2O/2.5/
 H2O+M=H+OH+M               6.06E+27   -3.322   120800.
    O2/1.5/ H2/3./ CO/1.9/ CO2/3.8/ H2O/0./ CH4/7./ CH2O/2.5/
 H2O+H2O=H+OH+H2O           1.01E+26   -2.44    120200.
!
 H+O2(+M)=HO2(+M)           4.65E+12    0.44         0.
    LOW                    /1.91E+21   -1.72       525./
    TROE/ 0.5    30.    90000.    90000./
    O2/.78/ H2/2./ CO/1.9/ CO2/3.8/ H2O/14./ CH4/2./ CH2O/2.5/
 HO2+H=H2+O2                3.68E+06    2.087    -1455.
 HO2+H=2OH                  7.08E+13    0.         300.
 HO2+H=O+H2O                1.45E+12    0.           0.
 HO2+O=OH+O2                1.63E+13    0.        -445.
 HO2+OH=H2O+O2              7.00E+12    0.       -1093.
    DUPLICATE
```

```
 HO2+OH=H2O+O2                4.50E+14    0.        10930.
    DUPLICATE
!
 CO+O(+M)=CO2(+M)             1.06E+13   -0.308     6943.
    LOW                      /1.40E+21   -2.1       5500./
    H2/2.5/ CO/1.9/ CO2/3.8/ H2O/12./ CH4/2./ CH2O/2.5/
 CO+O2=O+CO2                  2.53E+12    0.        47700.
 CO+OH=H+CO2                  8.46E+04    2.053      -356.
    DUPLICATE
 CO+OH=H+CO2                  8.64E+12   -0.664      332.
    DUPLICATE
 CO+HO2=OH+CO2                1.57E+05    2.18      17944.
!
 CH4+H=CH3+H2                 3.07E+06    2.5        7588.
 CH4+O=OH+CH3                 2.31E+08    1.56       8485.
 CH4+OH=CH3+H2O               1.00E+06    2.182      2446.
!
 CH3+H(+M)=CH4(+M)            1.41E+14    0.            0.
    LOW                      /6.35E+35   -5.57      3818./
    TROE/.37   3315.   61.   90000./
    H2/2./ CO/1.5/ CO2/2./ H2O/6./ CH4/2./ CH2O/2.5/
 CH3+O=H+CH2O                 1.08E+14    0.            0.
 CH3+O=>H+H2+CO               2.31E+13    0.            0.
 CH3+HO2=O2+CH4               1.16E+05    2.350     -1522.
 CH3+HO2=>OH+CH2O+H           2.08E+13    0.         -590.
 CH3+O2=>O+CH2O+H             2.51E+12    0.        28297.
 CH3+O2=OH+CH2O               2.28E+01    2.53       9768.
 CH3+CH2O=>H+CO+CH4           1.06E+01    3.36       4310.
!
 CH2O(+M)=H2+CO(+M)           3.70E+13    0.        71976.
    LOW                      /4.40E+38   -6.1       94000./
    TROE/.932   197.   1540.   10300./
    H2/2./ CO/1.5/ CO2/2./ H2O/6./ CH4/2./ CH2O/2.5/
 CH2O+H=>H2+CO+H              5.67E+12    0.361      4609.
    DUPLICATE
 CH2O+H=>H2+CO+H              1.14E+13    0.582     14395.
    DUPLICATE
 CH2O+O=>OH+H+CO              4.16E+11    0.57       2762.
 CH2O+OH=>H+CO+H2O            7.82E+07    1.63      -1055.
 CH2O+O2=>HO2+H+CO            2.44E+05    2.5       36460.
!
END
```

REFERENCES

[1] F. Abel, "Contributions to the history of explosive agents," *Philosophical Transactions of the Royal Society of London*, vol. 159, pp. 489–516, Dec. 1869.

[2] F. Abel, "Contributions to the history of explosive agents. —Second memoir," *Philosophical Transactions of the Royal Society of London*, vol. 164, pp. 337–395, Dec. 1874.

[3] M. Berthelot, "Sur la vitesse de propagation des phénomènes explosifs dans les gas," *Comptes rendus de l'Académie des Sciences*, vol. 93, pp. 18–22, 1881.

[4] M. Berthelot and P. Vieille, "L'onde Explosive," *Annales de Chimie et de Physique*, vol. 28, no. 5, pp. 289–332, 1883.

[5] E.-F. Mallard and H. Le Chatelier, "Combustion des Mélange Gazeux Explosifs," *Annales des Mines*, vol. 4, no. 8, pp. 274,618, 1883.

[6] M. Walton-Brown, W. J. Bird, and North of England Institute of Mining and Mechanical Engineers, *Report of the (French) commission on the use of explosives in the presence of fire-damp in mines ...* Newcastle-upon-Tyne: Lambert and Co., Ltd., 1890.

[7] P. Champion and H. Pellet, "Sur la théorie de l'explosion des composés détonants," *comptes rendus hebdomadaires des séances de l'académie des sciences*, vol. 75, p. 210, 1872.

[8] P. Vieille, "Rôle des discontinuités dans la propagation des phénomènes explosifs," *comptes rendus hebdomadaires des séances de l'académie des sciences*, vol. 131, pp. 413–416, 1900.

[9] W. J. M. Rankine, "On the thermodynamic theory of waves of finite longitudinal disturbance," *Philosophical Transactions of the Royal Society of London*, vol. 160, pp. 277–288, Jan. 1870. Publisher: Royal Society.

[10] P. Hugoniot, "Sur la propagation du mouvement dans les corps et spècialment dans le gaz parfaits," *Journal de l'École Polytechnique*, vol. 58, no. 1, pp. 1–125, 1889.

[11] D. L. Chapman, "On the rate of explosion in gases," *The London, Edinburgh, and Dublin Philosophical Magazine and Journal of Science*, vol. 47, pp. 90–104, Jan. 1899. Publisher: Taylor & Francis _eprint: https://doi.org/10.1080/14786449908621243.

[12] É. Jouguet, "Sur la propagation des réactions chimiques dans le gaz," *Journal de Mathématiques Pures et Appliquées*, vol. 60, no. 1, p. 347, 1904.

[13] V. Mikelson, *On the normal ignition velocity of explosive gaseous mixtures.* Ph.D. Thesis, Moscow University, 1890.

[14] J. D. Anderson, *Modern compressible flow: with historical perspective*. McGraw-Hill series in aeronautical and aerospace engineering, Boston: McGraw-Hill, 3rd ed ed., 2003.

[15] K. K. Kuo, *Principles of combustion*. Hoboken, NJ: John Wiley, 2nd ed ed., 2005.

[16] J. H. S. Lee, *The Detonation Phenomenon*. 32 Avenue of the Americas, New York, NY: Cambridge University Press, 2008.

[17] Y. B. Zeldovich, "On the theory of the propagation of detonation in gaseous systems," Nov. 1950. NTRS Author Affiliations: NTRS Report/Patent Number: NACA-TM-1261 NTRS Document ID: 19930093969 NTRS Research Center: Legacy CDMS (CDMS).

[18] J. Von Neuman, "Theory of Detonation Waves," tech. rep., INSTITUTE FOR ADVANCED STUDY PRINCETON NJ, May 1942. Section: Technical Reports.

[19] W. Döring, "Über den Detonationsvorgang in Gasen," *Annalen der Physik*, vol. 435, no. 6-7, pp. 421–436, 1943. _eprint: https://onlinelibrary.wiley.com/doi/pdf/10.1002/andp.19434350605.

[20] P. Clavin and G. Searby, *Combustion waves and fronts in flows: flames, shocks, detonations, ablation fronts and explosion of stars*. Cambridge, United Kingdom ; New York, NY: Cambridge University Press, 2016.

[21] G. B. Kistiakowsky and P. H. Kydd, "Gaseous Detonations. IX. A Study of the Reaction Zone by Gas Density Measurements," *The Journal of Chemical Physics*, vol. 25, pp. 824–835, Nov. 1956.

[22] D. H. Edwards, G. T. Williams, and J. C. Breeze, "Pressure and velocity measurements on detonation waves in hydrogen-oxygen mixtures," *Journal of Fluid Mechanics*, vol. 6, pp. 497–517, Nov. 1959.

[23] D. R. White, "Turbulent Structure of Gaseous Detonation," *Physics of Fluids*, vol. 4, no. 4, p. 465, 1961.

[24] J. A. Fay, "The structure of gaseous detonation waves," *Symposium (International) on Combustion*, vol. 8, pp. 30–40, Jan. 1961.

[25] F. Joubert, D. Desbordes, and H.-N. Presles, "Detonation cellular structure in NO2/N2O4–fuel gaseous mixtures," *Combustion and Flame*, vol. 152, pp. 482–495, Mar. 2008.

[26] M. I. Radulescu, G. J. Sharpe, C. K. Law, and J. H. S. Lee, "The hydrodynamic structure of unstable cellular detonations," *Journal of Fluid Mechanics*, vol. 580, pp. 31–81, June 2007.

[27] J. Verne, *De la Terre à la Lune*. Paris: J. Hetzel, 1865.

[28] W. J. M. Rankine, W. J. Millar, and P. G. Tait, *Miscellaneous scientific papers: from the transactions and proceedings of the Royal and other scientific and philosophical societies, and the scientific journals*. 1881. OCLC: 892151948.

[29] Y. B. Zeldovich, "To the question of energy use of detonation combustion," *Journal of Technical Physics*, vol. 10, no. 17, pp. 1453–1461, 1940.

[30] Y. B. Zeldovich, "To the Question of Energy Use of Detonation Combustion," *Journal of Propulsion and Power*, vol. 22, pp. 588–592, May 2006.

[31] B. R. Bigler, E. J. Paulson, and W. A. Hargus, "Idealized Efficiency Calculations for Rotating Detonation Engine Rocket Applications," in *53rd AIAA/SAE/ASEE Joint Propulsion Conference*, (Atlanta, GA), American Institute of Aeronautics and Astronautics, July 2017.

[32] M. Roy, "Propulsion par Statoréacteur à détonation," *comptes rendus hebdomadaires des séances de l'académie des sciences*, vol. 222, pp. 31–32, Jan. 1946.

[33] D. A. Rosato, M. Thornton, J. Sosa, C. Bachman, G. B. Goodwin, and K. A. Ahmed, "Stabilized detonation for hypersonic propulsion," *Proceedings of the National Academy of Sciences*, vol. 118, p. e2102244118, May 2021.

[34] J. A. Nicholls, H. R. Wilkinson, and R. B. Morrison, "Intermittent Detonation as a Thrust-Producing Mechanism," *Journal of Jet Propulsion*, vol. 27, pp. 534–541, May 1957.

[35] R. Goddard, "Reaction Combustion Chamber for Unconfined Charges of Detonative Fuel Fed Intermittently to the Combustion Chamber," Mar. 1949.

[36] R. Goddard, "Propulsion Apparatus Actuated By Successive Chages of Detonating Materials," Sept. 1953.

[37] R. Goddard, "Mechanism for Intermittent Feeding of Combustion liquids to a Combustion Chamber in Propulsion Apparatus," June 1955.

[38] F. Lu, E. Braun, L. Massa, and D. Wilson, "Rotating Detonation Wave Propulsion: Experimental Challenges, Modeling, and Engine Concepts (Invited)," in *47th AIAA/ASME/SAE/ASEE Joint Propulsion Conference & Exhibit*, (San Diego, California), American Institute of Aeronautics and Astronautics, July 2011.

[39] L. Barr, "Pulsed Detonation Engine Flies Into History," May 2008.

[40] B. V. Voitsekhovskii, "Statsionarnaya Dyetonatsiya," *Doklady Akademii Nauk SSSR*, vol. 129, no. 6, pp. 1254–1256, 1959.

[41] J. A. Nicholls, R. E. Cullen, and K. W. Ragland, "Feasibility studies of rotating detonation wave rocket motor," *Journal of Spacecraft and Rockets*, vol. 3, no. 6, pp. 893–898, 1966.

[42] F. Bykovskii, S. Zhdan, and E. Vedernikov, "Continuous Spin Detonations," *Journal of Propulsion and Power*, vol. 22, no. 6, pp. 1204–1216, 2006.

[43] K. Goto, K. Matsuoka, K. Matsuyama, A. Kawasaki, H. Watanabe, N. Itouyama, K. Ishihara, V. Buyakofu, T. Noda, J. Kasahara, A. Matsuo, I. Funaki, D. Nakata, M. Uchiumi, H. Habu, S. Takeuchi, S. Arakawa, J. Masuda, K. Maehara, T. Nakao, and K. Yamada, "Flight Demonstration of Detonation Engine System Using Sounding Rocket S-520-31: Performance of Rotating Detonation Engine," in *AIAA SCITECH 2022 Forum*, (San Diego, CA & Virtual), American Institute of Aeronautics and Astronautics, Jan. 2022.

[44] W. H. Heiser and D. T. Pratt, "Thermodynamic Cycle Analysis of Pulse Detonation Engines," *Journal of Propulsion and Power*, vol. 18, pp. 68–76, Jan. 2002.

[45] C. A. Nordeen, *Thermodynamics of a Rotating Detonation Engine*. PhD thesis, University of Connecticut, Dec. 2013.

[46] F. Chacon and M. Gamba, "Study of Parasitic Combustion in an Optically Accessible Continuous Wave Rotating Detonation Engine," in *AIAA Scitech 2019 Forum*, (San Diego, California), American Institute of Aeronautics and Astronautics, Jan. 2019.

[47] W. Anderson, D. Lim, and S. D. Heister, "Experimental Study of Liquid Injector Elements for Use in Rotating Detonation Engines," in *55th AIAA Aerospace Sciences Meeting*, (Grapevine, Texas), American Institute of Aeronautics and Astronautics, Jan. 2017.

[48] P. Wolanski, "Rotating Detonation Wave Stability," 23rd ICDERS, Irvine, USA, July 2011.

[49] C. A. Towery, A. Y. Poludnenko, and P. E. Hamlington, "Detonation initiation by compressible turbulence thermodynamic fluctuations," *Combustion and Flame*, vol. 213, pp. 172–183, Mar. 2020.

[50] S. A. Zhdan, F. A. Bykovskii, and E. F. Vedernikov, "Mathematical Modeling of a Rotating Detonation Wave in a Hydrogen-Oxygen Mixture," *Combustion, Explosion, and Shock Waves*, vol. 43, no. 4, pp. 449–459, 2007.

[51] M. Hishida, T. Fujiwara, and P. Wolanski, "Fundamentals of rotating detonations," *Shock Waves*, vol. 19, pp. 1–10, Apr. 2009.

[52] D. Schwer and K. Kailasanath, "Numerical investigation of the physics of rotating-detonation-engines," *Proceedings of the Combustion Institute*, vol. 33, pp. 2195–2202, Jan. 2011.

[53] D. A. Schwer, A. T. Corrigan, and K. Kailasanath, "Towards Efficient, Unsteady, Three-Dimensional Rotating Detonation Engine Simulations," in *52nd Aerospace Sciences Meeting*, (National Harbor, Maryland), American Institute of Aeronautics and Astronautics, Jan. 2014.

[54] S. M. Frolov, V. S. Aksenov, V. S. Ivanov, S. N. Medvedev, and I. O. Shamshin, "Flow Structure in Rotating Detonation Engine with Separate Supply of Fuel and Oxidizer: Experiment and CFD," in *Detonation Control for Propulsion*, Shock Wave and High Pressure Phenomena, pp. 39–59, Cham: Springer International Publishing, 2017. ISSN: 2197-9529.

[55] T. Sada, A. Matsuo, E. Shima, H. Watanabe, A. Kawasaki, K. Matsuoka, and J. Kasahara, "Numerical Investigation of Rotating Detonation Engine with Injection from the Combustor Side Wall," in *AIAA AVIATION 2022 Forum*, (Chicago, IL & Virtual), American Institute of Aeronautics and Astronautics, June 2022.

[56] G. Ge, L. Deng, H. Ma, X. Liu, L. Jin, and C. Zhou, "Effect of blockage ratio on the existence of multiple waves in rotating detonation engine," *Acta Astronautica*, vol. 164, pp. 230–240, Nov. 2019.

[57] J. Bennewitz, B. Bigler, S. Danczyk, W. Hargus, and R. Smith, "Performance of a Rotating Detonation Rocket Engine with Various Convergent Nozzles," AIAA Propulsion and Energy 2019 Forum, Aug. 2019.

[58] R. Bluemner, C. Paschereit, E. Gutmark, and M. Bohon, "Investigation of Longitudinal Operating Modes in Rotating Detonation Combustors," AIAA Scitech 2020 Forum, Jan. 2020.

[59] C. Lietz, M. Ross, Y. Desai, and W. Hargus, "Numerical investigation of operational performance in a methane-oxygen rotating detonation rocket engine," AIAA Scitech 2020 Forum, Jan. 2020.

[60] J. Codoni, K. Cho, J. Hoke, B. Rankin, and F. Schauer, "Simultaneous mid-IR emission and OH chemiluminesence measurements within a RDE operating with and without backpressure," 2018 AIAA Aerospace Sciences Meeting, Jan. 2018.

[61] B. McBride, S. Gordon, and M. Reno, "Coefficients for Calculating Thermodynamic and Transport Properties of Individual Species," Tech. Rep. 4513, NASA, 1993.

[62] G. P. Smith, Y. Tao, and H. Wang, "Foundational Fuel Chemistry Model Version 1.0 (FFCM-1)," 2016.

[63] F. A. Lindemann, S. Arrhenius, I. Langmuir, N. R. Dhar, J. Perrin, and W. C. M. Lewis, "Discussion on "the radiation theory of chemical action"," *Transactions of the Faraday Society*, vol. 17, pp. 598–606, Jan. 1922. Publisher: The Royal Society of Chemistry.

[64] J. Troe, "Theory of Thermal Unimolecular Reactions in the Fall-off Range. I. Strong Collision Rate Constants," *Berichte der Bunsengesellschaft für physikalische Chemie*, vol. 87, no. 2, pp. 161–169, 1983. _eprint: https://onlinelibrary.wiley.com/doi/pdf/10.1002/bbpc.19830870217.

[65] R. G. Gilbert, K. Luther, and J. Troe, "Theory of Thermal Unimolecular Reactions in the Fall-off Range. II. Weak Collision Rate Constants," *Berichte der Bunsengesellschaft für physikalische Chemie*, vol. 87, no. 2, pp. 169–177, 1983. _eprint: https://onlinelibrary.wiley.com/doi/pdf/10.1002/bbpc.19830870218.

[66] S. Prakash, V. Raman, C. F. Lietz, W. A. Hargus, and S. A. Schumaker, "Numerical simulation of a methane-oxygen rotating detonation rocket engine," *Proceedings of the Combustion Institute*, vol. 38, no. 3, pp. 3777–3786, 2021.

[67] C. Lietz, Y. Desai, W. Hargus, and V. Sankaran, "Parametric investigation of rotating detonation rocket engines using large eddy simulations," AIAA Propulsion and Energy 2019 Forum, Aug. 2019.

[68] M. Salvadori, P. Tudisco, D. Ranjan, and S. Menon, "Numerical investigation of mass flow rate effects on multiplicity of detonation waves within a H2/Air rotating detonation combustor," *International Journal of Hydrogen Energy*, vol. 47, pp. 4155–4170, Jan. 2022.

[69] W.-W. Kim, S. Menon, and H. C. Mongia, "Large-Eddy Simulation of a Gas Turbine Combustor Flow," *Combustion Science and Technology*, vol. 143, no. 1, pp. 25–62, 1999. Publisher: Taylor & Francis Group.

[70] W.-W. Kim and S. Menon, "An unsteady incompressible Navier–Stokes solver for large eddy simulation of turbulent flows," *International Journal for Numerical Methods in Fluids*, vol. 31, no. 6, pp. 983–1017, 1999. _eprint: https://onlinelibrary.wiley.com/doi/pdf/10.1002/%28SICI%291097-0363%2819991130%2931%3A6%3C983%3A%3AAID-FLD908%3E3.0.CO%3B2-Q.

[71] F. Génin and S. Menon, "Studies of shock/turbulent shear layer interaction using Large-Eddy Simulation," *Computers & Fluids*, vol. 39, pp. 800–819, May 2010.

[72] M. Masquelet and S. Menon, "Large-Eddy Simulation of Flame-Turbulence Interactions in a Shear Coaxial Injector," *Journal of Propulsion and Power*, vol. 26, pp. 924–935, Sept. 2010.

[73] S. Srinivasan, R. Ranjan, and S. Menon, "Flame Dynamics During Combustion Instability in a High-Pressure, Shear-Coaxial Injector Combustor," *Flow, Turbulence and Combustion*, vol. 94, pp. 237–262, Jan. 2015.

[74] S. Yang, R. Ranjan, V. Yang, W. Sun, and S. Menon, "Sensitivity of predictions to chemical kinetics models in a temporally evolving turbulent non-premixed flame," *Combustion and Flame*, vol. 183, pp. 224–241, Sept. 2017.

[75] C. F. Lietz, Y. Desai, R. Munipalli, S. A. Schumaker, and V. Sankaran, "Flowfield analysis of a 3D simulation of a rotating detonation rocket engines," AIAA Paper 2019-1009, Jan. 2019.

[76] R. Maccormack, "The effect of viscosity in hypervelocity impact cratering," in *4th Aerodynamic Testing Conference*, (Cincinnati,OH,U.S.A.), American Institute of Aeronautics and Astronautics, Apr. 1969.

[77] B. van Leer, "Towards the ultimate conservative difference scheme. V. A second-order sequel to Godunov's method," *Journal of Computational Physics*, vol. 32, pp. 101–136, July 1979.

[78] P. Colella and P. R. Woodward, "The Piecewise Parabolic Method (PPM) for gas-dynamical simulations," *Journal of Computational Physics*, vol. 54, pp. 174–201, Apr. 1984.

[79] E. F. Toro, M. Spruce, and W. Speares, "Restoration of the contact surface in the HLL-Riemann solver," *Shock Waves*, vol. 4, pp. 25–34, July 1994.

[80] F. M. Genin, *Study of compressible turbulent flows in supersonic environment by large-eddy simulation*. PhD thesis, Feb. 2009. Accepted: 2009-06-08T18:43:08Z Publisher: Georgia Institute of Technology.

[81] M. W. Chase and National Institute of Standards and Technology, *NIST-JANAF thermochemical tables*. Journal of physical and chemical reference data. Monograph ; no. 9, Washington, D.C: American Chemical Society, 4th ed ed., 1998.

[82] A. Harten, P. D. Lax, and B. v. Leer, "On Upstream Differencing and Godunov-Type Schemes for Hyperbolic Conservation Laws," *SIAM Review*, vol. 25, pp. 35–61, Jan. 1983. Publisher: Society for Industrial and Applied Mathematics.

[83] P. Batten, N. Clarke, C. Lambert, and D. M. Causon, "On the Choice of Wavespeeds for the HLLC Riemann Solver," *SIAM Journal on Scientific Computing*, vol. 18, pp. 1553–1570, Nov. 1997. Publisher: Society for Industrial and Applied Mathematics.

[84] J. J. Quirk, "A contribution to the great Riemann solver debate," *International Journal for Numerical Methods in Fluids*, vol. 18, no. 6, pp. 555–574, 1994. _eprint: https://onlinelibrary.wiley.com/doi/pdf/10.1002/fld.1650180603.

[85] B. Einfeldt, "On Godunov-Type Methods for Gas Dynamics," *SIAM Journal on Numerical Analysis*, vol. 25, pp. 294–318, Apr. 1988. Publisher: Society for Industrial and Applied Mathematics.

[86] B. Einfeldt, C. D. Munz, P. L. Roe, and B. Sjögreen, "On Godunov-type methods near low densities," *Journal of Computational Physics*, vol. 92, pp. 273–295, Feb. 1991.

[87] P. Pal, S. Demir, and S. Som, "Numerical Analysis of Combustion Dynamics in a Full-Scale Rotating Detonation Rocket Engine using Large Eddy Simulations," *Journal of Energy Resources Technology*, pp. 1–31, Aug. 2022.

[88] P. Strakey and D. H. Ferguson, "Validation of a Computational Fluid Dynamics Model of a Methane-Oxygen Rotating Detonation Engine," in *AIAA SCITECH 2022 Forum*, (San Diego, CA & Virtual), American Institute of Aeronautics and Astronautics, Jan. 2022.

[89] J. W. Bennewitz, B. R. Bigler, W. A. Hargus, S. A. Danczyk, and R. D. Smith, "Characterization of detonation wave propagation in a rotating detonation rocket engine using direct high-speed imaging," AIAA Paper 2018-4688, July 2018.

[90] P. Virtanen, R. Gommers, T. E. Oliphant, M. Haberland, T. Reddy, D. Cournapeau, E. Burovski, P. Peterson, W. Weckesser, J. Bright, S. J. van der Walt, M. Brett, J. Wilson, K. J. Millman, N. Mayorov, A. R. J. Nelson, E. Jones, R. Kern, E. Larson, C. J. Carey, İ. Polat, Y. Feng, E. W. Moore, J. VanderPlas, D. Laxalde, J. Perktold, R. Cimrman, I. Henriksen, E. A. Quintero, C. R. Harris, A. M. Archibald, A. H. Ribeiro, F. Pedregosa, P. van Mulbregt, SciPy 1.0 Contributors, A. Vijaykumar, A. P. Bardelli, A. Rothberg, A. Hilboll, A. Kloeckner, A. Scopatz, A. Lee, A. Rokem, C. N. Woods, C. Fulton, C. Masson, C. Häggström, C. Fitzgerald, D. A. Nicholson, D. R. Hagen, D. V. Pasechnik, E. Olivetti, E. Martin, E. Wieser, F. Silva, F. Lenders, F. Wilhelm, G. Young, G. A. Price, G.-L. Ingold, G. E. Allen, G. R. Lee, H. Audren, I. Probst, J. P. Dietrich, J. Silterra, J. T. Webber, J. Slavič, J. Nothman, J. Buchner, J. Kulick, J. L. Schönberger, J. V. de Miranda Cardoso, J. Reimer, J. Harrington, J. L. C. Rodríguez, J. Nunez-Iglesias, J. Kuczynski, K. Tritz, M. Thoma, M. Newville, M. Kümmerer, M. Bolingbroke, M. Tartre, M. Pak, N. J. Smith, N. Nowaczyk, N. Shebanov, O. Pavlyk, P. A. Brodtkorb, P. Lee, R. T. McGibbon, R. Feldbauer, S. Lewis, S. Tygier, S. Sievert, S. Vigna, S. Peterson, S. More, T. Pudlik, T. Oshima, T. J. Pingel, T. P. Robitaille, T. Spura, T. R. Jones, T. Cera, T. Leslie, T. Zito, T. Krauss, U. Upadhyay, Y. O. Halchenko, and Y. Vázquez-Baeza, "SciPy 1.0: fundamental algorithms for scientific computing in Python," *Nature Methods*, vol. 17, pp. 261–272, Mar. 2020.

[91] J. W. Bennewitz, B. R. Bigler, J. J. Pilgram, and W. A. Hargus, "Modal Transition in Rotating Detonation Rocket Engines," *International Journal of Energetic Materials and Chemical Propulsion*, vol. 18, no. 2, pp. 91–109, 2019.

[92] G. Paniagua and R. Dénos, "Digital compensation of pressure sensors in the time domain," *Experiments in Fluids*, vol. 32, pp. 417–424, Apr. 2002.

[93] Z. Liu, J. Braun, J. Saavedra, and G. Paniagua, "Numerical analysis on the effect of CTAP measurements in pulse and rotating detonation combustors," in *AIAA Propulsion and Energy 2019 Forum*, (Indianapolis, IN), American Institute of Aeronautics and Astronautics, Aug. 2019.

[94] S. Badillo-Rios, *Effect of Chemical Kinetic Mechanisms on Turbulent Combustion*. PhD thesis, UCLA, 2020.

[95] R. M. Spearrin, C. S. Goldenstein, J. B. Jeffries, and R. K. Hanson, "Quantum cascade laser absorption sensor for carbon monoxide in high-pressure gases using wavelength modulation spectroscopy," *Applied Optics*, vol. 53, p. 1938, Mar. 2014.

[96] W. Y. Peng, S. J. Cassady, C. L. Strand, C. S. Goldenstein, R. M. Spearrin, C. M. Brophy, J. B. Jeffries, and R. K. Hanson, "Single-ended mid-infrared laser-absorption sensor for time-resolved measurements of water concentration and temperature within the annulus of a rotating detonation engine," *Proceedings of the Combustion Institute*, vol. 37, no. 2, pp. 1435–1443, 2019.

[97] A. P. Nair, D. D. Lee, D. I. Pineda, J. Kriesel, W. A. Hargus, J. W. Bennewitz, S. A. Danczyk, and R. M. Spearrin, "MHz laser absorption spectroscopy via diplexed RF modulation for pressure, temperature, and species in rotating detonation rocket flows," *Applied Physics B*, vol. 126, p. 138, Aug. 2020.

[98] A. P. Nair, D. D. Lee, D. I. Pineda, J. Kriesel, W. A. Hargus, J. W. Bennewitz, B. Bigler, S. A. Danczyk, and R. M. Spearrin, "Methane-oxygen rotating detonation exhaust thermodynamics with variable mixing, equivalence ratio, and mass flux," *Aerospace Science and Technology*, vol. 113, p. 106683, June 2021.

[99] L. Rothman, I. Gordon, R. Barber, H. Dothe, R. Gamache, A. Goldman, V. Perevalov, S. Tashkun, and J. Tennyson, "HITEMP, the high-temperature molecular spectroscopic database," *Journal of Quantitative Spectroscopy and Radiative Transfer*, vol. 111, pp. 2139–2150, Oct. 2010.

[100] J. M. Hartmann, L. Rosenmann, M. Y. Perrin, and J. Taine, "Accurate calculated tabulations of CO line broadening by H_2o, N_2, O_2, and CO_2 in the 200–3000-K temperature range," *Applied Optics*, vol. 27, p. 3063, Aug. 1988.

[101] R. Sur, K. Sun, J. B. Jeffries, and R. K. Hanson, "Multi-species laser absorption sensors for in situ monitoring of syngas composition," *Applied Physics B*, vol. 115, pp. 9–24, Apr. 2014.

[102] S. G. Johnson, "Fadeeva W function implementation."

[103] E. Bach, C. Paschereit, P. Stathopoulos, and M. D. Bohon, "An empirical model for stagnation pressure gain in rotating detonation combustors," *Proceedings of the Combustion Institute*, vol. 38, no. 3, pp. 3807–3814, 2021.

[104] T. A. Kaemming and D. E. Paxson, "Determining the Pressure Gain of Pressure Gain Combustion," in *2018 Joint Propulsion Conference*, (Cincinnati, Ohio), American Institute of Aeronautics and Astronautics, July 2018.

[105] B. A. Rankin, J. Hoke, and F. Schauer, "Periodic Exhaust Flow through a Converging-Diverging Nozzle Downstream of a Rotating Detonation Engine," in *52nd Aerospace Sciences Meeting*, (National Harbor, Maryland), American Institute of Aeronautics and Astronautics, Jan. 2014.

[106] C. A. Nordeen, D. Schwer, A. T. Corrigan, and B. Cetegen, "Radial Effects on Rotating Detonation Engine Swirl," in *51st AIAA/SAE/ASEE Joint Propulsion Conference*, (Orlando, FL), American Institute of Aeronautics and Astronautics, July 2015.

[107] D. E. Paxson, "Impact of an Exhaust Throat on Semi-Idealized Rotating Detonation Engine Performance," in *54th AIAA Aerospace Sciences Meeting*, (San Diego, California, USA), American Institute of Aeronautics and Astronautics, Jan. 2016.

[108] K. Miki, D. E. Paxson, D. Perkins, and S. Yungster, "RDE Nozzle Computational Design Methodology Development and Application," AIAA Propulsion and Energy 2020 Forum, Aug. 2020.

[109] A. J. Harroun, S. D. Heister, and J. H. Ruf, "Computational and Experimental Study of Nozzle Performance for Rotating Detonation Rocket Engines," *Journal of Propulsion and Power*, vol. 37, pp. 660–673, Sept. 2021.

[110] J. W. Bennewitz, B. R. Bigler, M. C. Ross, S. A. Danczyk, W. A. Hargus, and R. D. Smith, "Performance of a Rotating Detonation Rocket Engine with Various Convergent Nozzles and Chamber Lengths," *Energies*, vol. 14, p. 2037, Jan. 2021. Number: 8 Publisher: Multidisciplinary Digital Publishing Institute.

[111] R. D. Smith and S. B. Stanley, "Experimental Investigation of Rotating Detonation Rocket Engines for Space Propulsion," *Journal of Propulsion and Power*, vol. 37, pp. 463–473, May 2021.

[112] S. A. Schumaker, A. M. Knisely, J. L. Hoke, and K. D. Rein, "Methane–oxygen detonation characteristics at elevated pre-detonation pressures," *Proceedings of the Combustion Institute*, vol. 38, no. 3, pp. 3623–3632, 2021.

[113] J. Ahrens, B. Geveci, and C. Law, "ParaView: An End-User Tool for Large-Data Visualization," in *Visualization Handbook*, pp. 717–731, Elsevier, 2005.

[114] R. T. Fievisohn and K. H. Yu, "Steady-State Analysis of Rotating Detonation Engine Flowfields with the Method of Characteristics," *Journal of Propulsion and Power*, vol. 33, pp. 89–99, Jan. 2017.

[115] D. Schwer and K. Kailasanath, "Numerical Study of the Effects of Engine Size n Rotating Detonation Engines," in *49th AIAA Aerospace Sciences Meeting including the New Horizons Forum and Aerospace Exposition*, Aerospace Sciences Meetings, American Institute of Aeronautics and Astronautics, Jan. 2011.

[116] J. R. Dechert, M. D. Polanka, F. R. Schauer, S. A. Schumaker, B. Sell, and M. L. Fotia, "Development of a Small Scale Rotating Detonation Engine," in *AIAA Scitech 2020 Forum*, AIAA SciTech Forum, American Institute of Aeronautics and Astronautics, Jan. 2020.

[117] H. Law, T. Baxter, C. N. Ryan, and R. Deiterding, "Design and testing of a small-scale laboratory rotating detonation engine running on ethylene-oxygen," in *AIAA Propulsion and Energy 2021 Forum*, AIAA Propulsion and Energy Forum, American Institute of Aeronautics and Astronautics, July 2021.